



**Ashutosh Goel**

**VIDROS E VITRO-CERÂMICOS Á BASE DE  
CLINOPIROXENAS PARA APLICAÇÕES  
FUNCIONAIS**

**CLINOPYROXENE BASED GLASSES AND GLASS-  
CERAMICS FOR FUNCTIONAL APPLICATIONS**



**Ashutosh Goel**

**VIDROS E VITRO-CERÂMICOS À BASE DE  
CLINOPIROXENAS PARA APLICAÇÕES FUNCIONAIS**

**CLINOPYROXENE BASED GLASSES AND GLASS-  
CERAMICS FOR FUNCTIONAL APPLICATIONS**

Dissertação apresentada à Universidade de Aveiro para cumprimento dos requisitos necessários à obtenção do grau de Doutor em Ciência e Engenharia de Materiais, realizada sob a orientação científica do Doutor José Maria da Fonte Ferreira, Professor Associado com Agregação do Departamento de Engenharia Cerâmica e do Vidro da Universidade de Aveiro, e do Doutor Dilshat U. Tulyaganov, Professor Associado com Agregação da Universidade Politécnica de Turim em Tachkent, Uzbequistão.

Apoio financeiro da FCT e do FSE no âmbito do III Quadro Comunitário de Apoio.

Dedicated to my parents

**o júri**  
Presidente

**Prof. Doutor Helmuth Robert Malonek**  
professor catedrático do Departamento de Matemática da Universidade de Aveiro, Portugal

**Prof. Doutor Tanguy Rouxel**  
professor catedrático do LARMAUR da Universidade de Rennes 1, França

**Prof. Doutor Federico Smeacetto**  
professor auxiliar do Departamento de Engenharia Química e Ciência dos Materiais do Politécnico de Turim, Itália

**Prof. Doutor Luís Filipe da Silva dos Santos**  
professor auxiliar do Departamento de Engenharia de Materiais/ICEMS do Instituto Superior Técnico/Universidade Técnica de Lisboa, Portugal

**Prof. Doutor Jorge Ribeiro Frade**  
professor catedrático do Departamento de Engenharia Cerâmica e do Vidro da Universidade de Aveiro, Portugal

**Prof. Doutor José Maria da Fonte Ferreira**  
professor associado c/ agregação do Departamento de Engenharia Cerâmica e do Vidro da Universidade de Aveiro, Portugal

## Agradecimientos

First and foremost, I would like to bow in full thankfulness and humbleness to the Almighty, God, who has given me the ability and strength to complete this research work. At this momentous occasion of compiling my Ph.D. dissertation, I would like to acknowledge the contribution of all those benevolent people, I have been blessed to associate with. The foundation for the successful completion of this research work, leading to my Ph.D. dissertation has been laid by a myriad of people whose help and contribution have made things successful. Since such a list can be prohibitively long, I may be excused for any omissions.

In 2003-2004, I carried out my first small research as masters' student in the area of glasses under Professor Kulwant S. Thind in India. Therefore, I would like to extend my foremost gratitude to him because it was under his able guidance that I got introduced to an amazing world of glass science and research. Also, I am indebted to Dr. Kulvir Singh and Professor O.P. Pandey from Thapar University, India for introducing me to a fascinating field of glass-ceramics and their application as sealants in solid oxide fuel cells (SOFC). It was during my stay at Thapar University that I learnt the basics of materials science which further played a significant role while accomplishing my Ph.D. work.

This Ph.D. dissertation came into being because of the immense faith shown by my supervisor, Professor José M.F. Ferreira, in me and my capabilities. It has been an honour to be his Ph.D. student. He was the person who gave me an opportunity to prove my potential and was always there by my side as a guiding torch during all odds. He taught me, both consciously and unconsciously, how good experimental materials science is done. I appreciate all his contributions of time, ideas and funding to make my Ph.D. experience productive and stimulating. The joy and enthusiasm he has for his research was contagious and motivational for me, even during tough times in the Ph.D. pursuit. I am thankful for an excellent example he has provided as a successful scientist and professor.

I also wish to express my appreciation to my co-supervisor, Professor Dilshat U. Tulyaganov, who taught me the fundamentals of crystallization in glasses, designing of glass compositions, investigating microstructure-property relationships and introduced me to the mesmerizing world of the applications of glass-ceramics in different technological areas. In the absence of his moral support and scientific guidance, it would have been really difficult to complete this odyssey with success.

Sincere thanks are extended to Dr. Simeon Agathopoulos for his moral support and close collaboration which indeed helped me to cope up with the stress that I felt of being away from my family and to learn various experimental characterization and testing techniques during my initial days in Aveiro. The electrical conductivity measurements and thermal shock resistance studies discussed in this dissertation would not have been possible without the support of Dr. V.V. Kharton and Dr. A.A. Yaremchenko and their research group. I very much appreciate their enthusiasm, intensity and willingness to perform these experiments for me in their laboratory.

## palavras-chave

Vitro-cerâmicos, clinopiroxenas, diopsídio, enstatite, células de combustível de óxido sólido (SOFC), selantes.

## Resumo

As piroxenas são um vasto grupo de silicatos minerais encontrados em muitas rochas ígneas e metamórficas. Na sua forma mais simples, estes silicatos são constituídas por cadeias de  $\text{SiO}_3$  ligando grupos tetrahédricos de  $\text{SiO}_4$ . A fórmula química geral das piroxenas é  $\text{M}_2\text{M}_1\text{T}_2\text{O}_6$ , onde M2 se refere a cationes geralmente em uma coordenação octaédrica distorcida ( $\text{Mg}^{2+}$ ,  $\text{Fe}^{2+}$ ,  $\text{Mn}^{2+}$ ,  $\text{Li}^+$ ,  $\text{Ca}^{2+}$ ,  $\text{Na}^+$ ), M1 refere-se a cationes numa coordenação octaédrica regular ( $\text{Al}^{3+}$ ,  $\text{Fe}^{3+}$ ,  $\text{Ti}^{4+}$ ,  $\text{Cr}^{3+}$ ,  $\text{V}^{3+}$ ,  $\text{Ti}^{3+}$ ,  $\text{Zr}^{4+}$ ,  $\text{Sc}^{3+}$ ,  $\text{Zn}^{2+}$ ,  $\text{Mg}^{2+}$ ,  $\text{Fe}^{2+}$ ,  $\text{Mn}^{2+}$ ), e T a cationes em coordenação tetrahédrica ( $\text{Si}^{4+}$ ,  $\text{Al}^{3+}$ ,  $\text{Fe}^{3+}$ ). As piroxenas com estrutura monoclinica são designadas de clinopiroxenas. A estabilidade das clinopiroxenas num espectro de composições químicas amplo, em conjugação com a possibilidade de ajustar as suas propriedades físicas e químicas e a durabilidade química, têm gerado um interesse mundial devido a suas aplicações em ciência e tecnologia de materiais. Este trabalho trata do desenvolvimento de vidros e de vitro-cerâmicos baseadas de clinopiroxenas para aplicações funcionais. O estudo teve objectivos científicos e tecnológicos; nomeadamente, adquirir conhecimentos fundamentais sobre a formação de fases cristalinas e soluções sólidas em determinados sistemas vitro-cerâmicos, e avaliar a viabilidade de aplicação dos novos materiais em diferentes áreas tecnológicas, com especial ênfase sobre a selagem em células de combustível de óxido sólido (SOFC). Com este intuito, prepararam-se vários vidros e materiais vitro-cerâmicos ao longo das juntas Enstatite ( $\text{MgSiO}_3$ ) - diopsídio ( $\text{CaMgSi}_2\text{O}_6$ ) e diopsídio ( $\text{CaMgSi}_2\text{O}_6$ ) - Ca - Tschermak ( $\text{CaAlSi}_2\text{O}_6$ ), os quais foram caracterizados através de um vasto leque de técnicas. Todos os vidros foram preparados por fusão-arrefecimento enquanto os vitro-cerâmicos foram obtidos quer por sinterização e cristalização de fritas, quer por nucleação e cristalização de vidros monolíticos. Estudaram-se ainda os efeitos de várias substituições iónicas em composições de diopsídio contendo Al na estrutura, sinterização e no comportamento durante a cristalização de vidros e nas propriedades dos materiais vitro-cerâmicos, com relevância para a sua aplicação como selantes em SOFC. Verificou-se que Foi observado que os vidros/vitro-cerâmicos à base de enstatite não apresentavam as características necessárias para serem usados como materiais selantes em SOFC, enquanto as melhores propriedades apresentadas pelos vitro-cerâmicos à base de diopsídio qualificaram-nos para futuros estudos neste tipo de aplicações. Para além de investigar a adequação dos vitro-cerâmicos à base de clinopiroxene como selantes, esta tese tem também como objetivo estudar a influência dos agentes de nucleação na nucleação em volume dos vitro-cerâmicos resultantes à base de diopsídio, de modo a qualificá-los como potenciais materiais hoppedeiros de resíduos nucleares radioactivos.

**keywords**

glass-ceramic, clinopyroxene, diopside, enstatite, solid oxide fuel cell, sealant.

**abstract**

The pyroxenes are a wide spread group rock-forming silicate minerals found in many igneous and metamorphic rocks. They are silicates that, in their simplest form, contain single  $\text{SiO}_3$  chains of linked  $\text{SiO}_4$  tetrahedra. The general chemical formula for pyroxenes is  $\text{M}_2\text{M}_1\text{T}_2\text{O}_6$ , where M2 refers to cations in a generally distorted octahedral coordination ( $\text{Mg}^{2+}$ ,  $\text{Fe}^{2+}$ ,  $\text{Mn}^{2+}$ ,  $\text{Li}^+$ ,  $\text{Ca}^{2+}$ ,  $\text{Na}^+$ ), M1 to cations in a regular octahedral coordination ( $\text{Al}^{3+}$ ,  $\text{Fe}^{3+}$ ,  $\text{Ti}^{4+}$ ,  $\text{Cr}^{3+}$ ,  $\text{V}^{3+}$ ,  $\text{Ti}^{3+}$ ,  $\text{Zr}^{4+}$ ,  $\text{Sc}^{3+}$ ,  $\text{Zn}^{2+}$ ,  $\text{Mg}^{2+}$ ,  $\text{Fe}^{2+}$ ,  $\text{Mn}^{2+}$ ), and T to tetrahedrally coordinated cations ( $\text{Si}^{4+}$ ,  $\text{Al}^{3+}$ ,  $\text{Fe}^{3+}$ ). Monoclinic pyroxenes are called clinopyroxenes. The stability of clinopyroxenes over a broad spectrum of chemical compositions, in conjunction with the possibility of achieving desired physical properties and high chemical durability, has generated a worldwide interest due to their applications in material science and technology. The present work deals with the development of clinopyroxene based glasses and glass-ceramics for functional applications. The objective of the study was dual, both scientific and technological; particularly to gain fundamental knowledge on the formation of crystalline phases and solid solutions in selected glass-ceramic systems, and to evaluate the feasibility for application of new materials in different technological areas with emphasis on sealing in solid oxide fuel cells (SOFC). In this pursuit, various glasses and glass-ceramics along Enstatite ( $\text{MgSiO}_3$ ) - Diopside ( $\text{CaMgSi}_2\text{O}_6$ ) and Diopside ( $\text{CaMgSi}_2\text{O}_6$ ) - Ca - Tschermak ( $\text{CaAlSi}_2\text{O}_6$ ) joins have been prepared and characterized by a wide array of characterization techniques. All the glasses were prepared by melt-quenching technique while glass-ceramics were produced either by sintering and crystallization of glass powders or by nucleation and crystallization in monolithic glasses. Furthermore, influence of various ionic substitutions/additions in Al-containing diopside on the structure, sintering and crystallization behaviour of glasses and properties of resultant glass-ceramics has been investigated, in relevance with final application as sealants in SOFC. It has been observed that enstatite based glasses/glass-ceramics do not exhibit requisite characteristics in order to qualify for the job of sealing in SOFC while the superior properties exhibited by diopside based glass-ceramics qualify them for further experimentation as SOFC sealants. Apart from investigating the suitability of clinopyroxene based glass-ceramics as sealants, this thesis also aims to study the influence of nucleating agents on the volume nucleation in the resultant diopside based glass-ceramics so as to qualify them for further experimentation as hosts for radioactive nuclear wastes.

# Contents

Page no.

|                                                                                                                                                                                 |    |
|---------------------------------------------------------------------------------------------------------------------------------------------------------------------------------|----|
| Abstract                                                                                                                                                                        |    |
| Acknowledgements                                                                                                                                                                |    |
| List of tables                                                                                                                                                                  |    |
| List of figures                                                                                                                                                                 |    |
| List of publications                                                                                                                                                            |    |
| 1. Introduction                                                                                                                                                                 | 1  |
| 2. State of the art                                                                                                                                                             | 5  |
| 2.1 Ca-Mg-Fe pyroxenes                                                                                                                                                          | 6  |
| 2.1.1 Magnesium metasilicate ( $\text{MgSiO}_3$ ): polymorphism, possibilities for production of glasses and glass-ceramics                                                     | 6  |
| 2.1.2 Diopside ( $\text{CaMgSi}_2\text{O}_6$ ): structure, isomorphism, technological applications                                                                              | 10 |
| 2.1.3 Diopside ( $\text{CaMgSi}_2\text{O}_6$ )-Ca-Tschermak ( $\text{CaAl}_2\text{SiO}_6$ ) join: structural features, feasibility for production of glasses and glass-ceramics | 15 |
| 2.2 Sealing in solid oxide fuel cells                                                                                                                                           | 16 |
| 3. Experimental procedure                                                                                                                                                       | 19 |
| 3.1 Preparation of glasses and glass-ceramics                                                                                                                                   | 20 |
| 3.1.1 Glass preparation                                                                                                                                                         | 20 |
| 3.1.2 Preparation of glass-ceramics                                                                                                                                             | 20 |
| 3.1.2.1 Nucleation and crystallization in monolithic glasses                                                                                                                    | 20 |
| 3.1.2.2 Sintering and crystallization of glass powder compacts                                                                                                                  | 21 |
| 3.2 Characterization of glasses                                                                                                                                                 | 21 |
| 3.2.1 Amorphous nature and phase separation in glasses                                                                                                                          | 21 |
| 3.2.2 Structural characterization of samples                                                                                                                                    | 21 |
| 3.2.2.1 Infrared spectroscopy (FTIR)                                                                                                                                            | 21 |
| 3.2.2.2 Nuclear magnetic resonance (MAS-NMR)                                                                                                                                    | 22 |

|         |                                                                                                                                                          |    |
|---------|----------------------------------------------------------------------------------------------------------------------------------------------------------|----|
| 3.2.3   | Density measurements                                                                                                                                     | 22 |
| 3.2.4   | Thermal analysis                                                                                                                                         | 22 |
| 3.2.4.1 | Dilatometry                                                                                                                                              | 22 |
| 3.2.4.2 | Differential thermal analysis (DTA)/Differential scanning calorimetry (DSC)                                                                              | 23 |
| 3.2.4.3 | Hot stage microscopy (HSM)                                                                                                                               | 24 |
| 3.3     | Characterization of glass-ceramics                                                                                                                       | 24 |
| 3.3.1   | Crystalline phase analysis and microstructure                                                                                                            | 24 |
| 3.3.2   | Linear shrinkage, density and mechanical strength                                                                                                        | 25 |
| 3.3.3   | Measurements of electrical properties and oxygen permeability                                                                                            | 25 |
| 3.3.4   | Joining behaviour and chemical interaction between electrolyte - glass-ceramic sealant - metallic interconnect in air and humidified reducing atmosphere | 28 |
| 3.3.5   | Thermal shock resistance                                                                                                                                 | 29 |
| 4.      | Results and discussion                                                                                                                                   | 30 |
| 4.1     | Enstatite-Diopside join: Magnesium-metasilicate ( $\text{MgSiO}_3$ ) based glasses and glass-ceramics                                                    | 31 |
| 4.1.1   | Designing of compositions                                                                                                                                | 31 |
| 4.1.2   | Casting ability of glasses                                                                                                                               | 31 |
| 4.1.3   | Structure of glasses                                                                                                                                     | 34 |
| 4.1.4   | Dilatometry                                                                                                                                              | 35 |
| 4.1.5   | Sintering and crystallization kinetics of glass powders                                                                                                  | 36 |
| 4.1.6   | Crystallization behaviour of glass powder compacts                                                                                                       | 42 |
| 4.2     | Diopside-Ca-Tschermak join                                                                                                                               | 46 |
| 4.2.1   | Designing of compositions                                                                                                                                | 46 |
| 4.2.2   | Casting ability of glasses                                                                                                                               | 46 |
| 4.2.3   | Structure of glasses                                                                                                                                     | 47 |
| 4.2.4   | Dilatometry                                                                                                                                              | 48 |

|         |                                                                                                                                                                                    |    |
|---------|------------------------------------------------------------------------------------------------------------------------------------------------------------------------------------|----|
| 4.2.5   | Glass transition                                                                                                                                                                   | 49 |
| 4.2.6   | Crystallization kinetics by DTA                                                                                                                                                    | 53 |
| 4.2.7   | Crystallization behaviour of glass powder compacts                                                                                                                                 | 54 |
| 4.2.7.1 | Non-isothermal conditions, 850–1000 °C (1 h)                                                                                                                                       | 54 |
| 4.2.7.2 | Isothermal conditions, 900 °C (1 h - 300 h)                                                                                                                                        | 59 |
| 4.2.8   | Properties of glass-ceramics                                                                                                                                                       | 59 |
| 4.2.8.1 | Shrinkage, density and bending strength                                                                                                                                            | 59 |
| 4.2.8.2 | Adherence to zirconia (8YSZ)                                                                                                                                                       | 60 |
| 4.3     | Influence of ZnO and BaO on the crystallization behaviour and properties of Di-CaTs based glasses                                                                                  | 63 |
| 4.3.1   | Designing of compositions                                                                                                                                                          | 63 |
| 4.3.2   | Casting ability of glasses                                                                                                                                                         | 63 |
| 4.3.3   | Density measurements                                                                                                                                                               | 66 |
| 4.3.3.1 | ZnO-containing glasses                                                                                                                                                             | 66 |
| 4.3.3.2 | BaO-containing glasses                                                                                                                                                             | 66 |
| 4.3.4   | Glass transition and Coefficient of thermal expansion (CTE)                                                                                                                        | 68 |
| 4.3.5   | Crystallization kinetics by DTA                                                                                                                                                    | 68 |
| 4.3.6   | Crystallization behaviour of glass powder compacts                                                                                                                                 | 71 |
| 4.3.6.1 | Non-isothermal conditions, 850 – 1000 °C (1 h)                                                                                                                                     | 71 |
| 4.3.6.2 | Heat treatment of BaO-containing GCs under isothermal conditions, 900 °C (300 h)                                                                                                   | 77 |
| 4.3.7   | Properties of BaO-containing sintered glass-ceramics                                                                                                                               | 78 |
| 4.4     | Influence of MO (M = Ba, Sr) and R <sub>2</sub> O <sub>3</sub> (R = B, Cr, La) on sintering, crystallization behaviour and properties of diopside based glasses and glass-ceramics | 86 |
| 4.4.1   | Designing of glass compositions                                                                                                                                                    | 86 |
| 4.4.2   | Casting ability of glasses                                                                                                                                                         | 88 |
| 4.4.3   | Density measurements                                                                                                                                                               | 89 |

|         |                                                                                                                                                     |     |
|---------|-----------------------------------------------------------------------------------------------------------------------------------------------------|-----|
| 4.4.4   | Dilatometry                                                                                                                                         | 90  |
| 4.4.5   | Structure of glasses                                                                                                                                | 92  |
| 4.4.5.1 | FTIR analysis                                                                                                                                       | 92  |
| 4.4.5.2 | NMR structural characterization                                                                                                                     | 96  |
| 4.4.6   | Sintering and crystallization behaviour by HSM and DTA                                                                                              | 97  |
| 4.4.6.1 | Effect of $\text{La}_2\text{O}_3$                                                                                                                   | 99  |
| 4.4.6.2 | Effect of $\text{B}_2\text{O}_3$                                                                                                                    | 101 |
| 4.4.6.3 | Effect of replacement of BaO by SrO                                                                                                                 | 101 |
| 4.4.7   | Crystallization kinetics of glasses by DTA                                                                                                          | 102 |
| 4.4.8   | Crystalline phase analysis, microstructure and properties of sintered glass powder compacts                                                         | 103 |
| 4.4.8.1 | $\text{B}_2\text{O}_3$ -free compositions                                                                                                           | 103 |
| 4.4.8.2 | $\text{B}_2\text{O}_3$ -containing compositions                                                                                                     | 109 |
| 4.4.9   | Interfacial adhesion, stability and electrical resistivity in contact with solid electrolyte and interconnect materials under different atmospheres | 117 |
| 4.4.9.1 | In air                                                                                                                                              | 117 |
| 4.4.9.2 | In humidified reducing atmosphere                                                                                                                   | 123 |
| 4.4.10  | Thermal shock resistance                                                                                                                            | 127 |
| 4.5     | Optimization of diopside based glass-ceramic sealants for sealing applications in SOFC                                                              | 128 |
| 4.5.1   | Designing of glass compositions                                                                                                                     | 128 |
| 4.5.2   | Casting ability of glasses                                                                                                                          | 129 |
| 4.5.3   | Density and dilatometry                                                                                                                             | 129 |
| 4.5.4   | FTIR analysis                                                                                                                                       | 131 |
| 4.5.5   | Crystallization kinetics by DTA                                                                                                                     | 132 |
| 4.5.6   | Sintering and crystallization process of glasses                                                                                                    | 134 |
| 4.5.7   | Isothermal heat treatment, 800 °C (300 h)                                                                                                           | 140 |

|         |                                                                                                                                                                               |     |
|---------|-------------------------------------------------------------------------------------------------------------------------------------------------------------------------------|-----|
| 4.5.8   | Properties of sintered glass powder compacts                                                                                                                                  | 141 |
| 4.6     | Influence of nucleating agents ( $\text{Cr}_2\text{O}_3$ , $\text{Fe}_2\text{O}_3$ and $\text{CaF}_2$ ) on the crystallization kinetics of diopside and Di-CaTs based glasses | 148 |
| 4.6.1   | Designing of glass compositions                                                                                                                                               | 148 |
| 4.6.2   | Casting ability of glasses                                                                                                                                                    | 150 |
| 4.6.3   | Density and dilatometry measurements                                                                                                                                          | 150 |
| 4.6.3.1 | CaF <sub>2</sub> containing glasses                                                                                                                                           | 150 |
| 4.6.3.2 | Di-CaTs based glasses containing $\text{Fe}_2\text{O}_3$ and $\text{Cr}_2\text{O}_3$                                                                                          | 151 |
| 4.6.4   | FTIR analysis                                                                                                                                                                 | 152 |
| 4.6.4.1 | CaF <sub>2</sub> containing glasses                                                                                                                                           | 152 |
| 4.6.4.2 | Di-CaTs based glasses containing $\text{Fe}_2\text{O}_3$ and $\text{Cr}_2\text{O}_3$                                                                                          | 153 |
| 4.6.5   | Crystallization kinetics by DTA, XRD and SEM                                                                                                                                  | 154 |
| 4.6.5.1 | CaF <sub>2</sub> containing glasses                                                                                                                                           | 154 |
| 4.6.5.2 | Di-CaTs based glasses containing $\text{Fe}_2\text{O}_3$ and $\text{Cr}_2\text{O}_3$                                                                                          | 156 |
| 5.      | Conclusions                                                                                                                                                                   | 162 |
| 5.1     | Enstatite-Diopside join: Magnesium-metasilicate ( $\text{MgSiO}_3$ ) based glasses and glass-ceramics                                                                         | 163 |
| 5.2     | Diopside-Ca-Tschermak join                                                                                                                                                    | 164 |
| 5.3     | Influence of ZnO and BaO on the crystallization behaviour and properties of Di-CaTs based glasses                                                                             | 165 |
| 5.4     | Influence of MO (M = Ba, Sr) and $\text{R}_2\text{O}_3$ (R = B, Cr, La) on sintering, crystallization behaviour and properties of diopside based glasses and glass-ceramics   | 167 |
| 5.5     | Optimization of diopside based glass-ceramic sealants for sealing applications in SOFC                                                                                        | 169 |
| 5.6     | Influence of nucleating agents ( $\text{Cr}_2\text{O}_3$ , $\text{Fe}_2\text{O}_3$ and $\text{CaF}_2$ ) on the crystallization kinetics of diopside and Di-CaTs based glasses | 171 |
|         | Future directions                                                                                                                                                             | 172 |
|         | References                                                                                                                                                                    | 174 |

---

List of tables

---

- Table 2.1 Details about Mg-Fe pyroxenes and Ca-pyroxenes.
- Table 3.1 Chemical composition of metallic interconnects (wt.%).
- Table 4.1 Composition of glasses along Di-En join (wt. %).
- Table 4.2 Thermal parameters obtained for the investigated glasses ( $\beta = 5 \text{ K min}^{-1}$ ).
- Table 4.3 Properties of glass-ceramics (GCs) produced after firing at different temperatures.
- Table 4.4 Influence of heating rate on the thermal parameters of both the glasses.
- Table 4.5 Thermal parameters showing the thermal stability and crystallization mechanism in glasses 2a and 3a.
- Table 4.6 Evolution of crystalline phases assemblages in the investigated glasses over increasing temperature, determined by the high temperature X-ray diffraction (HT-XRD) and room temperature X-ray diffraction (RT-XRD) analysis.
- Table 4.7 Composition of Di-CaTs based glasses (wt. %).
- Table 4.8 Thermal properties of Di-CaTs based glasses.
- Table 4.9 Values of properties of the GCs produced from GPCs after heat treatment at different temperatures for 1 h.
- Table 4.10 Thermal expansion coefficients ( $\text{CTE} \times 10^6 \text{ K}^{-1}$ ) of the GCs produced under different conditions together with the CTE of yttria stabilized cubic zirconia (8YSZ), ( $\beta = 5 \text{ K min}^{-1}$ ).
- Table 4.11 Composition of ZnO-containing Di-CaTs based glasses (wt. %).

- Table 4.12 Composition of BaO-containing Di-CaTs based glasses (wt. %).
- Table 4.13 Properties of glasses.
- Table 4.14 Results of Rietveld-R.I.R quantitative analysis (wt.%).
- Table 4.15 Batch compositions of the glasses (wt.%).
- Table 4.16 Properties of the glasses.
- Table 4.17 Properties of the sintered glass-ceramics produced from GPC heat treatment at different temperatures for 1 h.
- Table 4.18  $\text{CTE} \times 10^6 \text{ (K}^{-1}\text{)}$  of the GCs produced at different conditions together with the CTE of yttria stabilized cubic zirconia (8YSZ).
- Table 4.19 Activation energy for the total conductivity of glass-ceramics in air.
- Table 4.20 Properties of the sintered GCs produced from GPCs after heat treatment at different temperatures for 1 h.
- Table 4.22  $\text{CTE} \times 10^6 \text{ (K}^{-1}\text{)}$  (200-600 °C) of the GCs produced under different conditions.
- Table 4.23 Activation energy for the total conductivity of GCs in air.
- Table 4.24 Batch compositions of the glasses.
- Table 4.25 Properties of the glasses
- Table 4.26 Properties of the sintered GCs produced from GPCs after heat treatment at different temperatures for 1 h.
- Table 4.27 Results of Rietveld-R.I.R quantitative analysis.
- Table 4.28  $\text{CTE} \times 10^6 \text{ K}^{-1}$  (200-600 °C) of the GCs produced under different conditions.

Table 4.29    Activation energy for the total conductivity (730-830 °C) of GCs in air.

Table 4.30    Batch compositions of glasses 8 and 8A (wt.%).

Table 4.31    Batch compositions of CaF<sub>2</sub> containing glasses (wt.%).

Table 4.32    Properties of CaF<sub>2</sub> -containing glasses.

Table 4.33    Variation in T<sub>p</sub> (°C) with heating rate.

---

.....

---

List of figures

---

- Fig. 2.1 Composition ranges of Ca-Mg-Fe clinopyroxenes with accepted names.
- Fig. 2.2 Structural scheme of planar SOFC stack.
- Fig. 3.1 Schematic outline of experimental setup for measurements of oxygen permeability.
- Fig. 4.1 Photograph of as-casted and annealed bulk glasses 1, 2a and 3a.
- Fig. 4.2 Inclusions observed at the opaque skin layer of as-cast bulk glass 1 obtained after melting at 1600 °C for 1 h and subsequent annealing.
- Fig. 4.3 FTIR spectra of the investigated glass powders.
- Fig. 4.4 Dilatometry curves obtained from as-cast and annealed bulk glasses.
- Fig. 4.5 DTA scans of glass powders (mean particle size of 2.8-3.0  $\mu\text{m}$ ), obtained from frits of the investigated glasses.
- Fig. 4.6 Photographs of glass powder compacts of composition (a) 2a heat treated at 1000 °C (b) 3a heat treated at 1100 °C, (c) 2b and 3b heat treated at 900 °C for 1 h, respectively.
- Fig. 4.7 DSC thermographs of the glass powder (a) 2a and (b) 3a at different heating rates.
- Fig. 4.8 Plot for determination of activation energy for viscous flow ( $E_{\eta}$ ) for glasses 2a and 3a.
- Fig. 4.9 Plot of activation energy for crystallization ( $E_c$ ) for glasses 2a and 3a.
- Fig. 4.10 FTIR spectra of Di-CaTs based glasses.
- Fig. 4.11 DTA thermographs of Di-CaTs glasses at  $\beta = 5 \text{ K min}^{-1}$ .
- Fig. 4.12 DTA thermograph of glass DT1 at  $\beta = 40 \text{ K min}^{-1}$ .
- Fig. 4.13 SEM image of glasses (a) DT1a and (b) DT1b (revealed after chemical etching of polished glass surfaces by 2 vol.% HF for 10 s).
- Fig. 4.14 Plot for determination of activation energy for (a) structural relaxation ( $E_{\text{relax.}}$ ) (b) viscous flow ( $E_{\eta}$ ) for the investigated glasses.
- Fig. 4.15 Plot for activation energy of crystallization of Di-CaTs glasses.

- Fig. 4.16 SEM images (revealed after chemical etching with 2 vol.% HF for 20 s) of bulk glasses (fractured) heat treated at (a) 900 °C, (b) 1000 °C for 1 h, respectively.
- Fig. 4.17 XRD diffractograms of glass powder compacts of compositions (a) DT1, (b) DT1a, (c) DT1b, (d) DT1c, sintered at different temperatures in temperature range 850 - 1000 °C, for 1 h, respectively. XRD spectra have not been normalised. Full scale intensity: 5000cps.
- Fig. 4.18 Microstructure (revealed after chemical etching of polished surfaces with HF solution) of the GCs DT1a heat treated at (a) 850 °C, (b) 900 °C, and (c) 950 °C; DT1b at 950 °C (d) and DT1c at 900 °C (e).
- Fig. 4.19 X-ray diffractograms of glass-powder compacts of DT1, DT1a, and DT1b, after heat treatment at 900 °C for 1 h, 50 h, 100 h, and 300 h. (Au: Augite ICDD card 01-078-1392; W: Wollastonite 00-042-0550; C: Cristobalite 00-039-1425. The spectra have not been normalized. Full scale of intensity axes 15000 cps).
- Fig. 4.20 SEM image of the interface between 8YSZ and GC DT1b.
- Fig. 4.21 DTA thermographs of parent glass DT and ZnO-containing glasses.
- Fig. 4.22 DTA thermographs of BaO-containing glasses.
- Fig. 4.23 DTA thermographs of glass DT-Zn2 at different heating rates.
- Fig. 4.24 Observed (crosses), calculated (continuous line), and difference curve from the Rietveld refinement of the GC DT treated at 900 °C for 1 h in air. Markers representing the phase reflections correspond to corundum and augite (from bottom to top).
- Fig. 4.25 X-ray diffractograms of glass-powder compacts, after heat treatment at different temperatures for 1 h. (Au: Augite, ICDD card 01-078-1391; HC: Hexacelsian, 01-077-0185; OC: Orthocelsian, 00-012-0725; C: Monocelsian, 01-074-1677. The spectra have not been normalized. Full scale of intensity axes 6000 cps).
- Fig. 4.26 Microstructure (revealed after chemical etching of polished surfaces with HF solution) of the glass-ceramics BaCMAS2 heat treated at (a) 850 °C, (b) 900 °C for 1 h.
- Fig. 4.27 X-ray diffractograms of glass-powder compacts of (a) DT, (b) DT-Zn1, (c) DT-Zn2 and (d) DT-Zn3 after heat treatment at different temperatures for 1 h (Aug: Augite, ICDD card: 01-078-1392; W\*: CaSiO<sub>3</sub>, 01-084-0655; OE: Orthoenstatite, 00-019-0768; W; Wollastonite, 01-072-2284; Hy: Hardystonite, 00-035-0745. The spectra have not been normalized. Full scale of intensity axes 21000 cps).

- Fig. 4.28 Microstructure (revealed after chemical etching of polished surfaces with HF solution) of the GCs: (a) DT heat treated at 900 °C, (b) 950 °C (c) DT-Zn1 heat treated at 950 °C, (d) and (e) DT-Zn2 heat treated at 950 °C and (f) DT-Zn3 heat treated at 950 °C for 1 h, respectively.
- Fig. 4.29 X-ray diffractograms of glass-powder compacts after heat treatment at 900 °C for 300 h. (Please see the comments in the legend of [Fig. 4.25](#)).
- Fig. 4.30 Density (a) and bending strength (b) of glass-powder compacts sintered at different temperatures for 1 h.
- Fig. 4.31 Microstructure of solidified interface between zirconia (8YSZ) and glass BaCMAS1, developed after heat treatment at 900 °C for 100 h in air.
- Fig. 4.32 Total conductivity of the investigated glass-ceramics in air. The inset shows a typical example of impedance spectrum for BaCMAS1.
- Fig. 4.33 Ion transference numbers, ratio between the observed and the theoretical e.m.f. values, and  $R_{\eta}/R_i$  ratio for BaCMAS1 glass-ceramics with Pt electrodes under air / (H<sub>2</sub>-H<sub>2</sub>O-N<sub>2</sub>) gradient.
- Fig. 4.34 Oxygen permeation flux and the corresponding permeate-side oxygen partial pressure for dense BaCMAS1 membrane (thickness of 1.0 mm), under air / (H<sub>2</sub>+H<sub>2</sub>O+N<sub>2</sub>) gradient at 820 °C.
- Fig. 4.35 SEM images of glasses (a) 7-2B, (b) 7-5B, (c) 7-10B after heat treatment at 700 °C for 1 h, respectively and (d) 7-20B (as casted and annealed at 550°C for 1h).
- Fig. 4.36 FTIR spectra of the investigated glasses
- Fig. 4.37 (a) <sup>29</sup>Si MAS-NMR spectra, (b) <sup>11</sup>B MAS-NMR spectra, (c) <sup>27</sup>Al MAS-NMR spectra of the investigated glasses.
- Fig. 4.38 Comparison of DTA and HSM curves on the same temperature scale for compositions (a) 7A, (b) 7B, (c) 7-2B, (d) 7(Sr)-2B.
- Fig. 4.39 HSM images of glasses on alumina substrates at various stages of heating cycle.
- Fig. 4.40 X-ray diffractograms of glass-powder compacts of (a) 7A, (b) 7A-Cr, (c) 7B and (d) 7B-Cr after heat treatment at different temperatures for 1 h and at 900 °C for 300 h. (The spectra have not been normalized. Full scale of intensity axes 7500 cps).
- Fig. 4.41 Microstructure (revealed via SEM imaging after chemical etching of polished surfaces with 2 vol.% HF solution) of the glass-ceramics 7A heat treated at (a) 900 °C and (b) 1000 °C; 7B at 900 °C and (d) 1000 °C.

- Fig. 4.42 X-ray diffractograms of glass-powder compacts sintered at (a) 800 °C, (b) 850 °C, for 1 h.
- Fig. 4.43 Microstructure (revealed via SEM imaging after chemical etching of polished surfaces with 2 vol.% HF solution) of the GCs (a) 7-5B heat treated at 850 °C (b) 7-10B heat treated at 800 °C (c) 7-15B heat treated at 800 °C and (d) 7(Sr)-2B heat treated at 850 °C for 1 h, respectively.
- Fig. 4.44 X-ray diffractograms of sintered GCs (850 °C, 1 h) after heat treatment at 800 °C for 300 h.
- Fig. 4.45 Thermal expansion curve of GCs 7-5B and 7-10B after sintering and crystallization at 850 °C for 1h. Inserts: (a) *In-situ* HT-XRD for GC 7-10B at 700 °C, (b) XRD for GC 7-5B after dilatometry at room temperature.
- Fig. 4.46 Total conductivity of dense GCs in air. The data on 7A are shown for comparison. The error bars are smaller than the data point symbols.
- Fig. 4.47 (a) Microstructure (SEM) and EDS element mapping of Ba, Cr and Fe at the interface between Crofer22 APU/glass 7-2B (b) EDS line profile for diffusion of various elements from glass 7-2B to Crofer22 APU and vice versa at their interface (c) microstructure (SEM) and EDS element mapping of Ba, Cr and Fe at the interface between Crofer22 APU/glass 7-5B (d) microstructure (SEM) and EDS element mapping of Ba, Cr and Fe at the interface between Crofer22 APU/glass 7(Sr)-2B (e) EDS line profile for diffusion of various elements from glass 7(Sr)-2B to Crofer22 APU and vice versa at their interface (f) microstructure (SEM) and EDS element mapping of Ba, Cr and Fe at the interface between Sanergy HT/glass 7-2B developed after heat treatment at 850 °C for 1 h and 800 °C for 300 h in air.
- Fig. 4.48 Total electrical resistance of a model cell comprising Crofer 22 APU and YSZ plates joined by the 7A GC sealant.
- Fig. 4.49 (a) Microstructure (SEM) and EDS element mapping of Ba, Mn, Cr and Fe at interface between glass 7-2B and Crofer22 APU (b) EDS line profile for diffusion of Cr, Ba and Mn at the interface between glass 7-2B and Crofer22 APU developed after heat treatment at 850 °C for 1 h and 800 °C for 300 h in humidified reducing atmosphere. (The term ‘unoxidized’ refers to the usage of interconnect material in as received form. The alloy was not pre-oxidized).
- Fig. 4.50 SEM micrographs of the interface between (a) glass 7A and Sanergy HT, (b) glass 7-2B and Sanergy HT, (c) glass 7-5B and Sanergy HT developed after heat treatment at 850 °C for 1 h and 800 °C for 300 h in humidified reducing atmosphere. (The term ‘unoxidized’ refers to the usage of interconnect material in as received form. The alloy was not pre-oxidized.).
- Fig. 4.51 SEM image of the 8YSZ-GC 7-5B pseudo cell after thermal shock

resistance experiments in (a) air, (b) water, after 15 quenching cycles.

- Fig. 4.52 FTIR of investigated glasses.
- Fig. 4.53 DTA thermographs of glass powders at  $\beta = 20 \text{ K min}^{-1}$ .
- Fig. 4.54 Comparison of DTA and HSM curves on the same temperature scale for compositions (a) 10, (b) 10B and (c) 10D.
- Fig. 4.55 HSM images of glasses on alumina substrates at various stages of heating cycle.
- Fig. 4.56 Powder X-ray diffractograms of GCs sintered at  $850 \text{ }^\circ\text{C}$  for 1 h mixed with corundum (internal standard). (Label: C: Corundum)
- Fig. 4.57 Observed (crosses), calculated (continuous line), and difference curve from the Rietveld refinement of the GC 10B treated at  $850 \text{ }^\circ\text{C}$  for 1 h in air. Markers representing the phase reflections correspond to corundum, diopside, and augite (from bottom to top).
- Fig. 4.58 Microstructure (revealed via SEM imaging after chemical etching of polished surfaces with 2 vol.% HF solution) of the GCs (a) 10A heat treated at  $800 \text{ }^\circ\text{C}$  (b) 10B heat treated at  $850 \text{ }^\circ\text{C}$  for 1 h, respectively.
- Fig. 4.59 X-ray diffractograms of GPCs sintered at  $850^\circ\text{C}$  for 1 h followed by  $800 \text{ }^\circ\text{C}$  for 300 h.
- Fig. 4.60 Total conductivity of dense GCs in air. The data on 7-2B are shown for comparison. The error bars are smaller than the data point symbols.
- Fig. 4.61 SEM image of the 8YSZ-GC 10B pseudo cell after thermal shock resistance experiments in air after 15 quenching cycles.
- Fig. 4.62 (a) Microstructure (SEM) and EDS element mapping of Cr, Mn, and Ti at interface between GC 10 and Crofer22 APU developed after heat treatment at  $850 \text{ }^\circ\text{C}$  for 1 h and  $800 \text{ }^\circ\text{C}$  for 300 h in air.
- Fig. 4.63 (a) Microstructure (SEM) and EDS element mapping of Ba, Cr, Mn and Ti at the interface between GC 10B and Crofer22 APU (b) EDS line profile for diffusion of Ba, Cr, Mn and Ti from GC 10B to Crofer22 APU and vice versa at their interface developed after heat treatment at  $850 \text{ }^\circ\text{C}$  for 1 h and  $800 \text{ }^\circ\text{C}$  for 300 h in air.
- Fig. 4.64 FTIR spectra of  $\text{CaF}_2$  containing glasses.
- Fig. 4.65 FTIR spectra of glasses 8 and 8A.
- Fig. 4.66 DTA thermographs of  $\text{CaF}_2$ -containing glasses.
- Fig. 4.67 Microstructure of the glass-ceramics (a) 7-8 (step1), (b) 7-5 (step 2), (c) 7-3

(step 5) (d) 7-5 (step 6) after etching in 2 vol% HF for 2 min.

- Fig. 4.68 Plot of  $\ln(T_p^2/\beta)$  v/s  $1/T_p$  in order to calculate the  $E_c$  for the investigated glasses.
- Fig. 4.69 Plot of  $\ln(T_p^2/\beta)$  v/s  $1/T_p$  in order to calculate the  $E_c$  for the investigated glasses 8 and 8A.
- Fig. 4.70 X-ray diffractograms of GCs (a) 8 and (b) 8A heat treated at different temperatures
- Fig. 4.71 SEM images of GCs (revealed after etching in 2 vol.% HF) (a) 8A after heat treatment at 700 °C for 2 h followed by heat treatment at 800 °C for 1 h, (b) 8A after heat treatment at 700 °C for 2 h followed by 850 °C, (c) 8 after heat treatment at 700 °C for 2 h followed by heat treatment at 900 °C for 1 h (d) 8A after heat treatment at 700 °C for 2 h followed by heat treatment at 900 °C for 1 h (e) 8A after heat treatment at 700 °C for 2 h followed by heat treatment at 950 °C for 1 h (f) 8A after heat treatment at 700 °C for 2 h followed by heat treatment at 1000 °C for 1 h.
- 

.....

---

List of publications

---

Ph.D thesis

1. **A. Goel**, D.U. Tulyaganov, S. Agathopoulos, M.J. Ribeiro, R.N. Basu, J.M.F. Ferreira, Diopside-Ca-Tschermak clinopyroxene based glass-ceramics processed via sintering and crystallization of glass powder compacts, *J. Eur. Ceram. Soc.* 27 [5] (2007) 2325.
2. **A. Goel**, D.U. Tulyaganov, S. Agathopoulos, M.J. Ribeiro, J.M.F. Ferreira, Synthesis and characterization of MgSiO<sub>3</sub> containing glass-ceramics, *Ceram. Int.* 33 [8] (2007) 1481.
3. **A. Goel**, D.U. Tulyaganov, S. Agathopoulos, M. Ribeiro, J.M.F. Ferreira, Crystallization behaviour of the glasses, structure and properties of sintered glass-ceramics in the Diopside-Ca-Tschermak system, *J. Eur. Ceram. Soc.* 27 [10] (2007) 3231.
4. **A. Goel**, D.U. Tulyaganov, V.V. Kharton, A.A. Yaremchenko, S. Agathopoulos, J.M.F. Ferreira, The influence of BaO on the phase formation and properties of aluminous clinopyroxenes in the Diopside-Ca-Tschermak system, *J. Am. Ceram. Soc.* 90 [7] (2007) 2236.
5. **A. Goel**, D.U. Tulyaganov, S. Agathopoulos, J.M.F. Ferreira, The role of Al<sub>2</sub>O<sub>3</sub> on the sintering and crystallization of MgSiO<sub>3</sub> based glasses, *Ceram. Int.* 34 (2008) 505.
6. **A. Goel**, D.U. Tulyaganov, V.V. Kharton, A.A. Yaremchenko, J.M.F. Ferreira, The effect of Cr<sub>2</sub>O<sub>3</sub> on the crystallization behaviour and properties of La<sub>2</sub>O<sub>3</sub> containing diopside glasses and glass-ceramics. *Acta Mater.* 56 [13] (2008) 3065.
7. **A. Goel**, E.R. Shaaban, D.U. Tulyaganov, J.M.F. Ferreira, Study of crystallization kinetics on the glasses along the Diopside-Ca-Tschermak join, *J. Am. Ceram. Soc.* 91 [8] (2008) 2690.
8. **A. Goel**, D.U. Tulyaganov, E.R. Shaaban, R.N. Basu, J.M.F. Ferreira, Influence of ZnO on the crystallization kinetics and properties of the Diopside-Ca-Tschermak based glasses and glass-ceramics, *J. Appl. Phys.* 104 (2008) 043529.
9. **A. Goel**, D.U. Tulyaganov, I. Kansal, E.R. Shaaban, J.M.F. Ferreira, Effect of BaO on the crystallization kinetics of the Diopside-Ca-Tschermak based glasses and glass-ceramics, *J. Non-Cryst. Solids* 355 (2009) 193.
10. **A. Goel**, D.U. Tulyaganov, E.R. Shaaban, S. Eriksson, C. S. Knee, J.M.F. Ferreira, Structure and crystallization behaviour of some

MgSiO<sub>3</sub> based glasses, *Ceram. Int.* 35 (2009) 1529.

11. **A. Goel**, D.U. Tulyaganov, V.V. Kharton, A.A. Yaremchenko, S. Eriksson, J.M.F. Ferreira, Optimization of La<sub>2</sub>O<sub>3</sub>-containing diopside based glass-ceramic sealants for fuel cell applications, *J. Power Sources* 189 (2009) 1032.
12. **A. Goel**, D.U. Tulyaganov, I. Kansal, E.R. Shaaban, J.M.F. Ferreira, Crystallization kinetics of Diopside-Ca-Tschermak based glasses nucleated with Fe<sub>2</sub>O<sub>3</sub> and Cr<sub>2</sub>O<sub>3</sub>, *Int. J. Mater. Eng. Innov.* 1 (2009) 40.
13. I. Kansal, **A. Goel**, D.U. Tulyaganov, E.R. Shaaban, M.J. Ribeiro, J.M.F. Ferreira, The effect of fluoride ions on the structure and crystallization kinetics of La<sub>2</sub>O<sub>3</sub>-containing diopside based oxyfluoride glasses, *Ceram. Int.* 35 (2009) 3489-3493.
14. I. Kansal, **A. Goel**, D.U. Tulyaganov, J.M.F. Ferreira, Effect of some rare-earth oxides on structure, devitrification and properties of diopside based glasses, *Ceram. Int.* 35 (2009) 3221-3227.
15. **A. Goel**, D.U. Tulyaganov, V.V. Kharton, A.A. Yaremchenko, J.M.F. Ferreira, Electrical behaviour of aluminosilicate glass-ceramic sealants and their interaction with metallic SOFC interconnects, *J. Power Sources* 195 (2010) 522-526.
16. **A. Goel**, D.U. Tulyaganov, A.M. Ferrari, E.R. Shaaban, A. Prange, F. Bondioli, J.M. F. Ferreira, Structure, sintering process and crystallization kinetics of alkaline-earth aluminosilicate glasses suitable for sealing solid oxide fuel cells, *J. Am. Ceram. Soc.* (2009) **In press.**
17. **A. Goel**, D.U. Tulyaganov, M.J. Pascual, F. Munoz, E.R. Shaaban, J.M.F. Ferreira, Development and performance of La<sub>2</sub>O<sub>3</sub>-containing diopside based glass-ceramics for sealing applications in solid oxide fuel cells, *J. Non-Cryst. Solids* (2009) **Accepted.**

#### Others

18. K. Singh, **A. Goel**, S. Mohan, A. Arora, G. Sharma, Lead-and Bismuth Borate Fly Ash Glasses as Radiation Shielding Materials, *Nucl. Sci. Engg.* 154 [2] (2006) 233.
19. **A. Goel**, E.R. Shaaban, F.C.L. Melo, M.J. Ribeiro, and J.M.F. Ferreira, Non-isothermal crystallization kinetic studies on MgO-Al<sub>2</sub>O<sub>3</sub>-SiO<sub>2</sub>-TiO<sub>2</sub> glass, *J. Non-Cryst. Solids* 353 [24&25] (2007) 2383.
20. **A. Goel**, E.R. Shaaban, F.C.L. Melo, M.J. Ribeiro, J.M.F. Ferreira, Influence of NiO on the crystallization kinetics of near

stoichiometric-cordierite glasses nucleated with  $\text{TiO}_2$ , J. Phys: Condens. Matter. 19 (2007) 386231.

21. A. Arora, **A. Goel**, E.R. Shaaban, K. Singh, O.P. Pandey, J.M.F. Ferreira, Crystallization kinetics of  $\text{BaO-ZnO-Al}_2\text{O}_3\text{-B}_2\text{O}_3\text{-SiO}_2$  glass, Physica B: Cond. Mater. 403 (2008) 1738.
  22. **A. Goel**, A.M. Ferrari, I. Kansal, M.J. Pascual, L. Barbieri, F. Bondioli, I. Lancellotti, M.J. Ribeiro, J.M.F. Ferreira, Sintering and crystallization behavior of  $\text{CaMgSi}_2\text{O}_6\text{-NaFeSi}_2\text{O}_6$  based glass-ceramics, J. Appl. Phys. 106 (2009) 093502.
-

# **CHAPTER I: Introduction**

Science and technology in today's era constantly requires new materials with special properties to achieve breathtaking innovations. This development centres on the improvement of scientific and technological fabrication and working procedures. Glass-ceramics (GCs) are one such category of materials which offer the possibility of combining the special properties of conventional sintered ceramics with distinctive characteristics of glasses. GCs are ceramic materials formed either through the controlled nucleation and crystallization of glass or sintering and crystallization of powdered glass. It is however, possible to develop modern GC materials with features unknown, thus far, in either ceramics or glasses or in other materials such as metals or organic polymers.

The pyroxenes are a wide spread group rock-forming silicate minerals found in many igneous and metamorphic rocks. They are silicates that, in their simplest form, contain single  $\text{SiO}_3$  chains of linked  $\text{SiO}_4$  tetrahedra. Generally small amount of Si are replaced by Al and other small cations. The name 'pyroxene' is derived from the Greek words for *fire* and *stranger*. They were named this way because of their presence in volcanic lavas, where they are sometimes seen as crystals embedded in volcanic glass. They were considered to be impurities in the glass, hence the name "fire strangers". The general chemical formula for pyroxenes is  $\text{M}_2\text{M}_1\text{T}_2\text{O}_6$ , where M2 refers to cations in a generally distorted octahedral coordination ( $\text{Mg}^{2+}$ ,  $\text{Fe}^{2+}$ ,  $\text{Mn}^{2+}$ ,  $\text{Li}^+$ ,  $\text{Ca}^{2+}$ ,  $\text{Na}^+$ ), M1 to cations in a regular octahedral coordination ( $\text{Al}^{3+}$ ,  $\text{Fe}^{3+}$ ,  $\text{Ti}^{4+}$ ,  $\text{Cr}^{3+}$ ,  $\text{V}^{3+}$ ,  $\text{Ti}^{3+}$ ,  $\text{Zr}^{4+}$ ,  $\text{Sc}^{3+}$ ,  $\text{Zn}^{2+}$ ,  $\text{Mg}^{2+}$ ,  $\text{Fe}^{2+}$ ,  $\text{Mn}^{2+}$ ), and T to tetrahedrally coordinated cations ( $\text{Si}^{4+}$ ,  $\text{Al}^{3+}$ ,  $\text{Fe}^{3+}$ ).

Any pyroxene belongs to either the orthorhombic or the monoclinic crystal system. There are two types of orthorhombic pyroxene: orthopyroxene (*Pbca*) and orthopyroxene (*Pbcn*). However, only the former has been found in nature, for example: enstatite ( $\text{Mg}_2[\text{SiO}_3]_2$ ) and ferrosilite ( $\text{Fe}^{2+}\text{MgSi}_2\text{O}_6$ ) while orthopyroxene (*Pbcn*) is stable only at elevated temperatures for limited compositions near  $\text{MgSiO}_3$ . Monoclinic pyroxenes are called clinopyroxenes. Their space groups are *C2/c*, *P2<sub>1</sub>/c*, and *P2/n*, depending on their chemical composition and petrogenetic history. The chain silicate structure of the pyroxenes offers much flexibility in the incorporation of various cations and the names of the pyroxene minerals are primarily defined by their chemical composition. Pyroxene minerals are named according to the chemical species occupying the M2 site, the M1 site, and the tetrahedral T site. Twenty mineral names for pyroxenes have been recognised by

the International Mineralogical Association's Commission on New Minerals and Mineral Names and 105 previously used names have been discarded [1].

The stability of clinopyroxenes over a broad spectrum of chemical compositions, in conjunction with the possibility of achieving desired physical properties and high chemical durability, has generated a worldwide interest due to their possible applications in material science and technology for example: biomedicine [2-5], fuel cells [6-9], nuclear waste immobilization [10-12], electrical insulators [13-16] and many more. Despite the interesting features and practical applications as mentioned above, the literature survey reveals that clinopyroxene based ceramics, especially, GCs have received less attention and hence, poor documentation in literature. Therefore, the aim of this work was to investigate the influence of various ionic substitutions/additions on sintering behaviour, crystallization kinetics, microstructure and other properties of GCs produced in enstatite (En;  $\text{MgSiO}_3$ ), diopside (Di;  $\text{CaMgSi}_2\text{O}_6$ ) and diopside-Ca-Tschermak (Di-CaTs;  $\text{CaMgSi}_2\text{O}_6 - \text{CaAl}_2\text{SiO}_6$ ) systems. The objective of the study was dual, both scientific and technological; particularly to gain the fundamental knowledge on the formation of crystalline phases and solid solutions in selected GCs systems, and to evaluate the feasibility for application of new materials in different technological areas with emphasis on sealing in solid oxide fuel cells (SOFCs).

In the light of the above mentioned perspective, this dissertation comprises of five chapters. While the first chapter, i.e. *Introduction* provides an outlook of the content of each chapter; the second chapter will focus on the literature survey in the field of pyroxene based glasses, ceramics and mainly GCs, with special emphasis on magnesium metasilicates and Di based systems. The second chapter has been divided into two different subsections; the first section aims at providing an insight to the recent advances and shortcomings in the science and technology of clinopyroxenes while the second section provides an overview about the current status of sealing technology in SOFC and draws attention towards the existing lacuna in the existing glass/GC sealants. In other words, chapter two lays the foundation of our work. The third chapter deals with the experimental procedure and methodology used in accomplishing this work. It provides details about all the experimental techniques and procedures employed in order to synthesise, characterize and test our samples. Chapter four is the most important part of this work as it presents all the experimental results obtained on clinopyroxene based glasses and GCs during past 3

years along with pertaining discussion while, in chapter five we have tried to conclude all the results obtained during this work and provide future directions in order to produce technologically useful materials.

.....

## **CHAPTER II: State of the art**

## 2.1 Ca-Mg-Fe pyroxenes

The pyroxenes form extensive solid solutions by various types of ionic substitutions. The Mg-Fe pyroxenes and some Ca pyroxenes (Table 2.1) are the most common rock-forming pyroxenes and form wide solid solutions that cover the pyroxene quadrilateral of the ternary  $\text{Ca}_2\text{Si}_2\text{O}_6$  (Wollastonite, Wo) –  $\text{Mg}_2\text{Si}_2\text{O}_6$  (En) –  $\text{Fe}_2\text{Si}_2\text{O}_6$  (Ferrosilite, Fs) system. Therefore, these pyroxenes are better treated together as the Ca-Mg-Fe or “quadrilateral” pyroxenes [1]. The Ca-Mg-Fe pyroxenes include varieties that have orthorhombic symmetry. These orthopyroxenes consist essentially of a simple chemical series  $(\text{Mg, Fe})_2\text{Si}_2\text{O}_6$  and thus contrast with Ca-Mg-Fe clinopyroxenes, which have wide range of chemical composition. Therefore, the Ca-Mg-Fe pyroxenes are defined on the basis of symmetry and relative amounts of  $\text{Ca}_2\text{Si}_2\text{O}_6$  (Wo),  $\text{Mg}_2\text{Si}_2\text{O}_6$  (En) and  $\text{Fe}^{2+}_2\text{Si}_2\text{O}_6$  (Fs). The composition ranges of clinopyroxenes and orthopyroxenes are indicated in Fig. 2.1. Since, in the present study, the focus of our investigation will be on glasses and GCs developed along En-Di and Di-CaTs join and their possible technological applications; therefore, the following literature review will be confined to these clinopyroxene systems and recent developments pertaining to these systems in different applications.

### 2.1.1 Magnesium metasilicate ( $\text{MgSiO}_3$ ): polymorphism, possibilities for production of glasses and glass-ceramics

Magnesium metasilicate ( $\text{MgSiO}_3$ ) has been extensively studied due to its abundance in the Earth’s lower crust and upper mantle [17]. According to the review of Smith [18] and later by Lee and Heuer [14],  $\text{MgSiO}_3$  occurs in three well characterised structures. Orthoenstatite (OE) and protoenstatite (PE) having orthorhombic symmetry and clinoenstatite (CE) with monoclinic crystal symmetry. The influence of the temperature and the time of annealing, the preparation route, the chemical nature and the amount of chemical dopants and the particle size of precursors on the phase transformations and the properties of  $\text{MgSiO}_3$  have been comprehensively investigated [14, 15, 19].

Ceramic and GC materials based on magnesium metasilicates ( $\text{MgSiO}_3$ ) are ideal for high frequency low loss high voltage insulators, surge arrestors, standoffs, spacers, resistor and coil forms due to their good mechanical and low loss electrical properties [13-16].

Table 2.1 Details about Mg-Fe pyroxenes and Ca-pyroxenes

| Mineral names          | Composition as end member               | Main composition as solid solution              | Space group             |
|------------------------|-----------------------------------------|-------------------------------------------------|-------------------------|
| <b>Mg-Fe pyroxenes</b> |                                         |                                                 |                         |
| 1. Enstatite (En)      | $\text{Mg}_2\text{Si}_2\text{O}_6$      | $(\text{Mg, Fe})_2\text{Si}_2\text{O}_6$        | <i>Pbca</i>             |
| 2. ferrosilite (Fs)    | $\text{Fe}^{2+}_2\text{Si}_2\text{O}_6$ |                                                 |                         |
| 3. Clinoenstatite      |                                         | $(\text{Mg, Fe})_2\text{Si}_2\text{O}_6$        | <i>P2<sub>1</sub>/c</i> |
| 4. Clinoferrosilite    |                                         |                                                 |                         |
| 5. Pigeonite           |                                         | $(\text{Mg, Fe, Ca})_2\text{Si}_2\text{O}_6$    | <i>P2<sub>1</sub>/c</i> |
| <b>Ca pyroxenes</b>    |                                         |                                                 |                         |
| 6. diopside (Di)       | $\text{CaMgSi}_2\text{O}_6$             | $\text{Ca}(\text{Mg, Fe})\text{Si}_2\text{O}_6$ | <i>C2/c</i>             |
| 7. hedenbergite (Hd)   | $\text{CaFe}_{2+}\text{Si}_2\text{O}_6$ |                                                 |                         |
| 8. Augite              |                                         | $(\text{Ca, Mg, Fe})\text{Si}_2\text{O}_6$      | <i>C2/c</i>             |
| 9. Johannsenite (Jo)   | $\text{CaMnSi}_2\text{O}_6$             |                                                 | <i>C2/c</i>             |
| 10. petedunnite (Pe)   | $\text{CaZnSi}_2\text{O}_6$             |                                                 | <i>C2/c</i>             |
| 11. esseneite (Es)     | $\text{CaFe}^{3+}\text{AlSiO}_6$        |                                                 | <i>C2/c</i>             |

Enstatite (En) is a low temperature modification of  $\text{MgSiO}_3$ , which, during a thermal cycle, transforms into PE (during heating) and CE (during cooling of PE) [13-15, 20]. The presence of metastable PE can result in electrical loss and weakening of mechanical strength during operation conditions. This drawback is known from the technology of steatite ceramics [14, 19, 20]. Another striking disadvantage of steatite ceramics is the narrow sintering range due to the rapid formation of liquid phase during firing. [20].

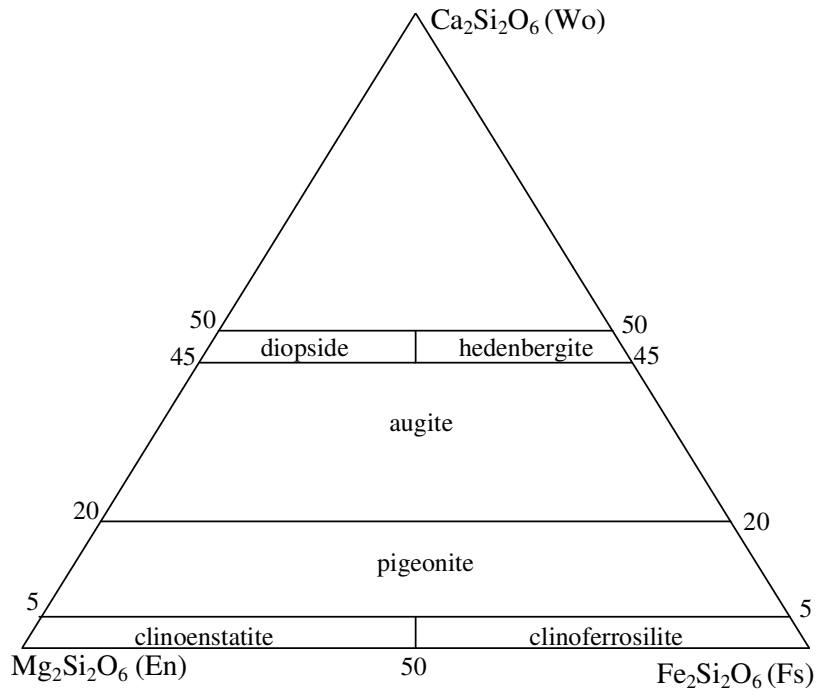


Fig. 2.1 Composition ranges of Ca-Mg-Fe clinopyroxenes with accepted names [1].

The production of  $\text{MgSiO}_3$  based materials via the GC route features particular peculiarities because the precise stoichiometric composition of En does not result in a stable glass. Several attempts have been addressed in producing  $\text{MgSiO}_3$  based materials using GC route. Lee and Heuler [14] had made an attempt to produce stoichiometric  $\text{MgSiO}_3$  glass by quenching of glass melt into water where liquid  $\text{N}_2$  was bubbling. Heat treatment of powder from that glass with particle's diameter of about  $180 \mu\text{m}$  in temperature range of  $800\text{--}1000 \text{ }^\circ\text{C}$  caused crystallization of OE, which was invariably associated with CE, independent of annealing time and cooling conditions (air, or water, or slow cooling of  $5 \text{ K min}^{-1}$ ). At temperatures  $\geq 1200 \text{ }^\circ\text{C}$ , PE was formed at the expense of OE while during cooling, CE was formed. The sintered GC samples were highly porous, even after many hours of heat treatment at temperatures close to melting point.

Cooper *et al.* [21] melted and re-melted stoichiometric  $\text{MgSiO}_3$  composition at  $1650 \text{ }^\circ\text{C}$  for 16 h to get high homogeneity. Nevertheless, during pouring into cold water the melt got an opalescence appearance, which, according to subsequent X-ray analysis, was due to traces of PE and OE. The produced cullet was pulverised to fine powder, sieved and annealed at temperatures between  $1150 \text{ }^\circ\text{C}$  and  $1200 \text{ }^\circ\text{C}$  for 24 h in air. The microstructure

of annealed powder particles suggested columnar grain growth and surface crystallization mechanism (due to formation of centre voids).

In 1974, Takher *et al.* [22-24] developed steatite-based GCs with a wide sintering range using glass powder of MgO-BaO-Al<sub>2</sub>O<sub>3</sub>-SiO<sub>2</sub> system [22, 23]. The glass was melted in quartz crucibles at 1520 °C. Using glass powders with surface area of 0.5-0.7 m<sup>2</sup> g<sup>-1</sup>, the sintering range was widened up to 80 degrees (between 1080 °C and 1160 °C), while the optimum firing temperature was 1120 °C. The dielectric performance of the sintered steatite GCs was improved by adding BaO and ZnO in the initial glass batch [22, 24]. Finally, the resultant GC from that particular composition exhibited reduced dielectric loss angle ( $\tan \delta$  at 1 MHz decreased down to 0.0008-0.0009) [24].

In 1991, Beall [25] successfully developed En-GCs in the ternary MgO-Al<sub>2</sub>O<sub>3</sub>-SiO<sub>2</sub> system using tetragonal zirconia as nucleating agent. In the base glass, tetragonal zirconia was formed as a primary crystal phase in temperature interval of 800–900 °C. PE was subsequently formed after heat treatment above 900 °C and transformed into fine crystals of twinned CE (but not OE) during cooling. Since proto-to-clino inversion was accompanied by 4% volume shrinkage, toughening was not based on the metastable presence of PE form. The toughening mechanism involved crack deflection and slippage along twinned crystals. It was shown that splintering due to the intersection of cleavage (110) and twin (100) planes in clinoenstatite was a factor of toughening. The resultant GCs had fracture toughness of approximately 5 MPa m<sup>0.5</sup>. Compositions with high content of zirconia also exhibited excellent refractoriness. Beyond bulk nucleation processing, Echeverria and Beall [26] have also produced En-GCs via surface as well as bulk nucleation mechanism and sol-gel route, achieving toughness of ca. 4 MPa m<sup>0.5</sup>.

Different types of En-GC materials have been produced by Partridge *et al.* and Budd [13, 27-29] for application in electronic circuits. In order to avoid cracking of GCs due to high surface stress as was observed for composition 43.7 SiO<sub>2</sub>-22.2 Al<sub>2</sub>O<sub>3</sub>-22.3 MgO-11.8 ZrO<sub>2</sub> (wt.%), En-type GCs having both ZrO<sub>2</sub> and TiO<sub>2</sub> as nucleating agents were prepared from glass powders using the surface nucleation and crystallization mechanisms. The sintered GCs had flexural strength of 250 MPa, fracture toughness of 3.3 MPa m<sup>0.5</sup>, Weibull modulus of 11.2, flexural modulus of 160 GPa and fracture surface energy of 51 J m<sup>-2</sup>.

In the crystalline lattice of Mg-metasilicate there are two non-equivalent chains, where one half of Mg cations occupy symmetrical (or regular) octahedral positions, while the second half occupy irregular octahedral positions [30-33]. This feature allows half of  $\text{Mg}^{2+}$  to be replaced by  $\text{Ca}^{2+}$ , despite the significant difference of their ion size (40%). Such a substitution can result in formation of a more stable diopside structure. Intermediate compositions of synthetic clinopyroxenes in the Di-En join form continuous solid solutions with a general formula of  $\text{Ca}_x\text{Mg}_{1-x}\text{SiO}_3$  (Di-En). Tribaudino *et al.* [34] refined the structures of six clinopyroxenes along the Di-En join ( $\text{Di}_{80}\text{En}_{20}$ ,  $\text{Di}_{70}\text{En}_{30}$ ,  $\text{Di}_{59}\text{En}_{41}$ ,  $\text{Di}_{52}\text{En}_{46}\text{CaTs}_2$ ,  $\text{Di}_{40}\text{En}_{60}$ , and  $\text{Di}_{20}\text{En}_{80}$ ) by Rietveld analysis of powder diffraction patterns obtained with synchrotron radiation. It is noteworthy that CaTs refers to Ca-Tschermak ( $\text{CaAl}_2\text{SiO}_6$ ) which is a representative of clinopyroxene group where Al is both at octahedral and tetrahedral sites [35]. According to Vereshchagin *et al.* [33], compositions with less than 12 mol.% of Di in the Di-En joint are prone to polymorphism.

Apart from there above mentioned electrical applications, En based ceramics have also been investigated for their potential applicability in the development of machinable prosthesis for dental applications [36]. Goeriot *et al.* [36] developed biosteatites (En materials sintered with added glass in order to lower the sintering temperature) from the sintering of talc powders after dehydration and milling in order to achieve PE phase and studied the bioactive properties and mechanical strength of these ceramics. In comparison to some GCs used in dentistry, the mechanical properties of En ceramics presented higher toughness ( $\sim 2.4 \text{ MPa m}^{-1}$  instead of  $0.8 \text{ MPa m}^{-1}$ ) for the same flexural strength while machinability and biocompatibility tests proved them to be potential candidates for bio-restorations (crowns and bones).

### **2.1.2 Diopside ( $\text{CaMgSi}_2\text{O}_6$ ): structure, isomorphism, technological applications.**

Diopside (Di) belongs to the group of inosilicates and is an important member of clinopyroxene group with composition  $\text{CaMgSi}_2\text{O}_6$ . It forms complete solid solution series with hedenbergite ( $\text{CaFeSi}_2\text{O}_6$ ) and augite, and partial solid solutions with orthopyroxenes and pigeonite (Table 2.1, Fig. 2.1). The structure of Di consists of chains of  $\text{SiO}_3$  held together by magnesium in octahedral sites, and calcium in eight-coordinated sites. The replacement of  $\text{Si}^{4+}$  by  $\text{Al}^{3+}$  ions within  $\text{SiO}_3$  chains permit inclusion of trivalent and tetravalent ions outside the chains. The pyroxene mineral augite, which arises from such

replacement, may adopt a variety of compositions with in general formula (Ca, Na, Mg, Fe<sup>2+</sup>, Mn, Fe<sup>3+</sup>, Al, Ti)<sub>2</sub>[(Si, Al)<sub>2</sub>O<sub>6</sub>] [1].

The stoichiometric Di glasses and resultant GCs have been investigated by many researchers for several properties and mechanisms due to their wide applicability in different practical applications. Nascimento *et al.* [37] collected an extensive data on the viscosity, covering 15 orders of magnitude, and crystal growth rate, covering seven orders of magnitude, of liquid Di (CaO•MgO•2SiO<sub>2</sub>) in a wide range of undercoolings from 1.10T<sub>g</sub> to 0.99T<sub>m</sub> (T<sub>g</sub> is the glass transition temperature and T<sub>m</sub> is the melting point) while Reinsch *et al.* [38] measured and collected crystal growth rate,  $U(T)$ , data of Di (CaO•MgO•2SiO<sub>2</sub>) in its isochemical glass forming melt in the temperature range of 750-1378 °C. The maximum of  $U(T)$  was found to occur at 1250 °C and the experimental  $U(T)$  for fitted well to the 2D surface nucleation model and also to the screw dislocation growth mechanism. Recently, Conradt [39] calculated the residual entropy of Di glass at zero Kelvin as  $S_{\text{glass}}(0) = 24.8 \pm 3 \text{ J mol}^{-1} \text{ K}^{-1}$  while entropy difference  $S_{\text{glass}} - S_{\text{crystal}}$  reached  $42.5 \pm 2 \text{ J mol}^{-1} \text{ K}^{-1}$  at 298 K and  $45.5 \pm 3 \text{ J mol}^{-1} \text{ K}^{-1}$  at the glass transition temperature, T<sub>g</sub> = 981 K.

Branda *et al.* [40] studied the non-isothermal crystallization kinetics of the stoichiometric Di glass and evaluated the crystal growth activation energy to be 573 kJ mol<sup>-1</sup>. They concluded that mechanism of devitrification in diopside glass is dependant on the particle size of the glass as devitrification occurs in bulk samples through a surface nucleation mechanism while surface nuclei behave as bulk nuclei in very finely powdered samples sintered before devitrifying. Öveçoğlu *et al.* [41] investigated the crystallization kinetics of a Di based GC developed from glass industry raw materials blended with 10 wt.% TiO<sub>2</sub> in the glass system SiO<sub>2</sub>-MgO-Al<sub>2</sub>O<sub>3</sub>-CaO-(Na<sub>2</sub>O,K<sub>2</sub>O). The resultant GC revealed the presence of Di as major crystalline phase comprising about 74 vol.% while electron microscopy investigations revealed the formation of conical shaped diopside crystals as a result of surface nucleation, thus, re-confirming the results of Branda *et al.* [40].

Barbieri *et al.* [42, 43] investigated the crystallization kinetics of a MgO-CaO-Al<sub>2</sub>O<sub>3</sub>-SiO<sub>2</sub> glass corresponding to the composition of 25 wt.% anorthite (An; CaO•Al<sub>2</sub>O<sub>3</sub>•2SiO<sub>2</sub>) – 75 wt.% Di (CaO•MgO•2SiO<sub>2</sub>) and calculated the activation energy of crystallization as 773 kJ mol<sup>-1</sup> which decreased to 589 kJ mol<sup>-1</sup> with the addition of 2

wt.% steel fly ash to the parent glass [44]. This decrease in activation energy of crystallization was attributed to the nucleating effect of  $\text{Fe}_2\text{O}_3$  present in the steel fly ash added to the parent glass composition and surface nucleation was found to be predominant in all the investigated glasses. Further, Baldi *et al.* [45] studied the effect of nucleating agents ( $\text{TiO}_2$ ,  $\text{P}_2\text{O}_5$  and  $\text{ZrO}_2$ ; 0-10 wt.%) on Di crystallization in new glass-ceramics for tile-glaze application. They found that devitrification process was independent of thermal treatment and Di crystalline phase was more thermodynamically favourable than other phases. The effect of the nucleating agent was observed to depend on its nature:  $\text{TiO}_2$  decreased the activation energy while  $\text{P}_2\text{O}_5$  and  $\text{ZrO}_2$  did not.

Recently, Barbieri *et al.* [46] and Corradi *et al.* [47] made detailed investigations on the atomistic description of the structure of glasses in the An – Di glass forming system (amount of An varying between 0–100 wt.%) using molecular dynamic (MD) simulations. The MD simulations confirmed the role of aluminium ions as network former and network modifier behaviour of magnesium ions in these glasses [46]. Further, it was shown that glass materials with compositions close to two extremes, corresponding to the pure glass anorthite or pure glass diopside, display the typical structural features of the tectosilicates and inosilicates subclass of minerals, respectively, to which An and Di crystals belong [47]. Also, it was concluded that the local environment of the Ca atoms in the 3D network is strongly influenced by the increasing  $\text{Al}_2\text{O}_3$  concentration as well as by the decrease in Mg content in the glass formulation. In particular, the Ca-based octahedral were progressively distorted due to transformation of the “inosilicate”-like glass structure (diopside rich) in a “tectosilicate” – like configuration (An rich). Further, they studied the devitrification behaviour of these glasses and made a quantitative analysis of crystalline phases in the resultant GCs by employing Rietveld-R.I.R (reference intensity ratio) technique on x-ray data [48]. Marques *et al.* [49, 50] and Leonelli *et al.* [51] have produced sintered GCs along An-Di glass forming system for their potential application as low temperature co-fired ceramics.

During 1980s, developments at Imperial College, London (UK) were aimed at reducing the production cost of GCs from slag by simplifying the heat treatments required for crystallization [52-54]. The composition of the starting batch was adjusted by mixing the blast-furnace slag with up to 30 wt.% colliery shale (another waste product) and small amounts of pure oxide components. A typical composition of parent glass (in wt.%) was:

48.3 SiO<sub>2</sub>–0.6 TiO<sub>2</sub>–13.3 Al<sub>2</sub>O<sub>3</sub>–0.8 Cr<sub>2</sub>O<sub>3</sub>–4.0 Fe<sub>2</sub>O<sub>3</sub>–0.4 MnO–5.7 MgO–24.7 CaO–1.2 Na<sub>2</sub>O–1.1 K<sub>2</sub>O. The heat treatments of the parent glass at its nucleation and crystallization temperature resulted in the formation of a bulk nucleated GC with Di as the main crystalline phase with minor amount of An. This GC produced was called “Silceram” and has been extensively studied for its potential application in structural applications including thermal shock, erosion, impact, and abrasion resistant components [52, 55-58]. The bulk nucleation in Di based GCs may be attributed to the combined presence and amount of Cr<sub>2</sub>O<sub>3</sub> and Fe<sub>2</sub>O<sub>3</sub> present in the parent glass. Although, either oxide alone is capable of initiating nucleation but there is a synergistic effect if they both are present together. These oxides promote the formation of spinel, which in turn act as nucleation sites for the main crystal phase, a pyroxene [59].

GCs containing Di as the major crystalline phase have been produced at Hahn-Meitner Institute (HMI), Berlin for the purpose of nuclear waste immobilisation [60] while GCs based on the calcium magnesium silicate system containing Di, powellite (CaMoO<sub>4</sub>) and perovskite have also been reported by workers in Japan at the Nippon Electric Glass Co. [61]. Simulated waste loading of up to 30 wt.% were achieved using these materials. The glasses were melted at 1300 °C and crystallization was carried out at temperatures in the range 800-1100 °C, usually during controlled cooling of the melt, without the inclusion of a separate nucleation stage. A bulk Di GC sample has been prepared with a diameter of 30 cm and weighing 65 kg. Relatively low leach rates have been noted for these GCs, making them useful for potential candidates for immobilisation of high level radioactive wastes [10]. Similarly, Karnis and Gautron [62] synthesized Di based GCs for the immobilization of cadmium and lead as Di can incorporate large cations, especially in 8-fold coordinated M2 site. Di crystals were shown to incorporate significant amount of Cd (9 wt.% CdO or 1.5 at.% Cd), thus proving themselves to be potential candidates for this job. In another study, Wood *et al.* [63] demonstrated the capability of Di based clinopyroxenes to accept uranium in 8-fold coordinated M2 site.

In the last decade, Di based ceramics and GCs have generated significant interest among scientific community due to their potential application as bioactive materials. Nonami and Tsutsumi [3] fabricated a composite of Di and hydroxyapatite (HAp) in order to increase the fracture toughness of pure sintered HAp. It was shown that the bending strength and fracture toughness of diopside-HAp composite was 2-3 times higher in

comparison to sintered HAp. Further, it was revealed that Di has no general toxicity in cell culture and it helps in bone regeneration. Similarly, Aza *et al.* [4] soaked Di based ceramic pellets in human parotid saliva (HPS) over different time intervals, to investigate the behaviour of the material in a natural medium of high protein content. The results showed the formation of HAp like layer on the surface of the ceramic, and suggested that the mechanism of HAp layer formation in saliva was similar to that showed *in vitro* tests by other silica based materials.

Yoganand *et al.* [64] developed bioactive GCs with transferred arc plasma technique in the system CaO-MgO-SiO<sub>2</sub> with diopside as the major crystalline phase. HAp formation on the GC surface was observed after 12 days of immersion in simulated body fluid (SBF) while fibroblast culture results showed that the GCs were non-toxic to human fibroblasts and promote cell growth. It has been reported that GC system with the eutectic composition of 38 wt.% TCP (3CaO • P<sub>2</sub>O<sub>5</sub>) • 62 wt.% diopside shows a flexural strength of more than 200 MPa [65]. Unfortunately, the bioactivity of this material has not yet been examined. Kamitakahara *et al.* [66] synthesised porous GCs containing TCP and Di and evaluated their bioactivity by examining *in vitro* apatite formation in SBF and proposed the porous GCs as scaffold materials for bone repair.

Recently, Goel *et al.* [67] investigated Di (CaMgSi<sub>2</sub>O<sub>6</sub>) – aegirine (NaFeSi<sub>2</sub>O<sub>6</sub>) based GC compositions. A glass with nominal composition 16.64 MgO–23.15 CaO–1.42 Na<sub>2</sub>O–3.66 Fe<sub>2</sub>O<sub>3</sub>–55.12 SiO<sub>2</sub> (wt.%), corresponding to theoretical formula Ca<sub>0.9</sub>Mg<sub>0.9</sub>Na<sub>0.1</sub>Fe<sub>0.1</sub>Si<sub>2</sub>O<sub>6</sub>, was prepared in bulk and frit form by conventional melt-quenching technique. The glass composition was prone for easy casting after 1 h of soaking time at 1580 °C resulting in homogeneous, amorphous and transparent frits with brown colour (probably due to Fe<sub>2</sub>O<sub>3</sub>). On the contrary, it was difficult to produce a stable monolithic bulk glass as the surface of glass rod, which was in direct contact with air, crystallized immediately after pouring the melt on the bronze mould while the remaining part of the sample did not show any tendency towards crystallization. The microstructure of the crystallized layer revealed the presence of uniformly grown crystals of two different sizes with a rosette like morphology. XRD and EDS mapping of these crystals exhibited the formation of Di (CaMgSi<sub>2</sub>O<sub>6</sub>) and magnesium iron oxide (Mg<sub>1.55</sub>Fe<sub>1.6</sub>O<sub>4</sub>) on the surface of the glass.

### 2.1.3 Diopside ( $\text{CaMgSi}_2\text{O}_6$ )-Ca-Tschermak ( $\text{CaAl}_2\text{SiO}_6$ ) join: structural features, feasibility for production of glasses and glass-ceramics

As mentioned above, CaTs is an aluminium-bearing clinopyroxene. Aluminium bearing pyroxenes can be used to calibrate geothermometers and geobarometers [68-71]. Flemming and Luth [35] studied short range cation ordering across the Di-CaTs solid solution in samples synthesised at 1400 °C and 2 GPa, for 24 h. However, a complication that arises in attempting to calibrate or apply these geobarometers is the potential for cation ordering to displace reactions. Etzel *et al.* [72] measured the unit cell parameters and heat capacities of a series of synthetic clinopyroxenes along Di-CaTs join using X-ray and calorimetric methods, respectively while in another study they calculated the heat of mixing for the binary solid solution Di-CaTs at  $T = 980$  K by lead borate solution calorimetry [73]. Recently, they investigated the structure of Di-CaTs clinopyroxenes by powder infra-red spectroscopy in the wave number range 80-2000  $\text{cm}^{-1}$  [74].

Kushiro [75], and Schairer and Yoder [76] have demonstrated that the maximum concentration of CaTs, which can be accommodated in Di, is 20%. Salama *et al.* [77] synthesised GCs based on Di-CaTs-fluorapatite (FA) system and studied the effect of increasing CaTs/Di ratio with constant FA content, on the crystallization behaviour of glasses. They observed a preferential tendency of Di to capture CaTs in its structure forming a Di based solid solution. The maximum concentration of CaTs that could be accommodated in the Di structure was found to be 25 wt.%, above which, gehlenite ( $\text{Ca}_2\text{Al}_2\text{SiO}_7$ ) was also observed. However, no solid solution formation was observed between pyroxene and FA. In an another study, Salama *et al.* [78] investigated the bioactivity of the GCs in the system Di-CaTs-FA by *in vitro* (immersion in SBF) analysis and observed that increasing CaTs content in the GCs decreases the bioactivity by hindering the growth of apatite layer on the surface of GCs due to increasing  $\text{Al}_2\text{O}_3$  in the system. It has already been reported by Hench and Anderson [79] that high contents of  $\text{Al}_2\text{O}_3$  in Bioglass® reduce its bioactivity by reducing the activity of  $\equiv\text{Si-OH}$ -rich layer.

Vasilopoulos *et al.* [80] prepared Di-CaTs based GCs from low-silica fly ash and  $\text{SiO}_2$ ,  $\text{Al}_2\text{O}_3$  and  $\text{MgCO}_3$  additives, via two-step thermal heat treatment (nucleation and crystallization) and obtained mono-mineral GCs with augite as the crystalline phase. It was observed that addition of  $\text{Cr}_2\text{O}_3$  (up to 0.75 wt.%), as a nucleating agent, favours volume nucleation and crystallization in the glasses and the composition containing the highest

amount of  $\text{Cr}_2\text{O}_3$  (0.75 wt.%) exhibited the highest degree of crystallinity. Méndez *et al.* [81] synthesized Al-containing diopside based GCs from solid industrial wastes generated in Northeast Mexico and reported surface crystallization mechanism in those glasses. In another study, Torres and Alarcon [82] studied the mechanism of crystallization of a powdered glass with composition in the pyroxene crystallization primary field within the  $\text{CaO-MgO-Al}_2\text{O}_3\text{-SiO}_2$  quaternary system in order to develop GC glazes. Gomes *et al.* [83] produced clinopyroxene based GCs from steelwork slag, limestone, sand, bauxite, and ilmenite nucleated with  $\text{TiO}_2$  *via* conventional melt-quenching method. Di ( $\text{CaMgSi}_2\text{O}_6$ ) and augite ( $(\text{Ca,Na})(\text{Mg,Fe,Al})(\text{Al,Si})_2\text{O}_6$ ) crystallized to be the primary phases in the resultant GCs. Augite is an intermediary member between Di and CaTs, representing a mineral midway between these two minerals along this series, where  $\text{Al}^{3+}$  occupies both octahedral ( $\text{AlO}_6$ ) and tetrahedral ( $\text{AlO}_4$ ) positions in the structure [84]. Similar studies using two Turkish fly ashes and the conventional two-stage method have been carried out by Erol and co-workers [85, 86]. The main crystalline phase in the GCs so produced was Di-alumina ( $\text{Ca}(\text{Mg,Al})(\text{Si,Al})_2\text{O}_6$ ). An interesting feature of the investigation was the correlation found between heat treatment and microstructure, hardness and wear resistance.

## 2.2 Sealing in solid oxide fuel cells

Over the past several decades, there has been an exigent need to develop alternative methods of power generation so as to meet the ever-increasing demand of the rising population. Development of fuel cell (FC) technology is one such attempt to cater the rising energy demands in the coming era. The primary function of any FC is to convert the chemical energy of the incoming fuel directly into the electrical energy, via an electrochemical reaction. Among different categories of FC, solid oxide fuel cell (SOFC) is currently in demand due to its better output with ease of handling and manufacturing and is considered to be the most efficient and versatile power generation system, particularly for dispersed power generation [87].

Since its invention, different modifications in SOFC design have been suggested and implemented. This has brought a complete change into its stacking sequence and ultimately, a change in design of complete system. Among different designs of SOFC, flat plate (planar) design is the most promising due to its cheap and simple fabrication along with improved performance and power density relative to other designs. However, the

planar design must overcome a significant challenge i.e. the need for an effective, high temperature seal to prevent fuel leakage and air mixing at high temperature along with to seal the electrolyte against the metallic body of the device, in order to create a hermetic, rugged and stable stack (Fig. 2.2). Any leakage of fuel into the air (or air into the fuel) will lead to direct combustion of fuel and may cause local overheating (hot spots) and sometimes may burst. Therefore, the seals must be stable in a wide range of oxygen partial pressure (air and fuel) and be chemically compatible with other FC components, while minimizing thermal stresses during high-temperature operation which creates a major challenge in the development of planar SOFCs [88, 89].

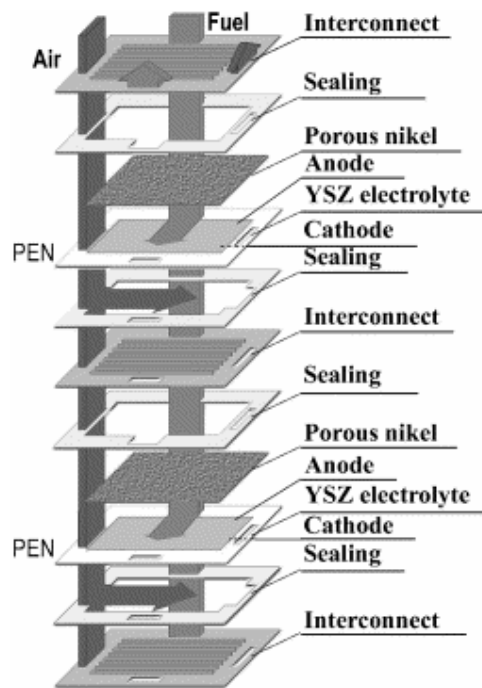


Fig. 2.2 Structural scheme of planar SOFC stack [90].

At present, five main approaches are being studied for sealing SOFCs: brazing [91], compressive seals [92], glass [93, 94], GC [95, 96] and glass-composite seals [97]. However, among all the sealing approaches proposed until today, glasses and GCs proved out to be the promising candidates for this job. The glass seals are designed to soften, and viscously flow above the SOFC operating temperature to provide hermetic seals by mechanical/chemical bonding. On cooling back down to operating temperature, the glass crystallizes to form a rigid, bonded seal. A principal advantage of glass seals is that the

glass composition can be tailored to optimize the properties like coefficient of thermal expansion (CTE), mechanical strength, electrical resistance, etc.

Most of the GC based sealants proposed so far are alkali or alkaline-earth aluminosilicate based; borate based, phosphate based or borosilicate GCs [98, 99]. However, every material has some advantages which are coupled along with some drawbacks. Alkali silicate glasses or GCs, in principle are not suitable as sealants because alkali cations tend to react with other FC components [100] and can lead to chromium poisoning. Further, most of the researchers have searched sealing materials on Ba-aluminosilicate GC system and its derivatives [93, 98, 100-102]. Most of these glass compositions contain high amount of BaO (30-35 mol.%), leading to the crystallization of monoclinic celsian ( $\text{BaAl}_2\text{Si}_2\text{O}_8$ ) after long term heat treatments [98] and formation of detrimental crystalline phase  $\text{BaCrO}_4$  when in contact Cr-based metallic interconnect materials in air at operating temperatures [103]. Significant content of BaO may also promote interaction with water vapour, leading to slow sealant degradation under SOFC operating conditions. Also,  $\text{B}_2\text{O}_3$  forms volatile compounds with water vapour leading to seal degradation [98]. Glasses with  $\text{B}_2\text{O}_3$  as the only glass former have shown up to 20% weight loss in the humidified  $\text{H}_2$  environment and extensive interactions with cell component materials both in air and wet fuel gas [104]. Thus, high amount of  $\text{B}_2\text{O}_3$  in the sealants is not seen with alacrity. Some  $\text{P}_2\text{O}_5$ -based glasses have also been investigated for the job of sealing in SOFCs. However, these compositions face a severe problem of volatilization of phosphate component leading to easy crystallization of pyro- or metaphosphates. These phases show poor stability at high temperature in wet fuel gas atmosphere [99, 105]. Therefore, still there is a need to fill in this lacuna by developing a suitable sealing material for SOFC technology.

.....

## **CHAPTER III: Experimental**

### 3.1 Preparation of glasses and glass-ceramics

#### 3.1.1 Glass preparation

High purity powders of  $\text{SiO}_2$ ,  $\text{CaCO}_3$ ,  $\text{Al}_2\text{O}_3$ ,  $\text{MgCO}_3$ ,  $\text{BaCO}_3$ ,  $\text{H}_3\text{BO}_3$ ,  $\text{La}_2\text{O}_3$ ,  $\text{Y}_2\text{O}_3$ ,  $\text{Cr}_2\text{O}_3$ ,  $\text{Fe}_2\text{O}_3$ ,  $\text{ZnO}$ ,  $\text{CaF}_2$ , and  $\text{NiO}$  were used. Homogeneous mixtures of batches (~100 g), in accordance with the designed compositions, obtained by ball milling, were calcined at 900 °C for 1 h and then melted in Pt / $\text{Al}_2\text{O}_3$  crucibles in temperature range 1500–1600 °C for 1 h, in air. Glasses in bulk form were produced by pouring the melts on preheated bronze moulds following by annealing in temperature range 500–550 °C for 1 h, depending on glass composition. The glasses in frit form were obtained by quenching of glass melts in cold water. The frits were dried and then milled in a high-speed agate mill resulting in fine glass powders with mean particle sizes of 3–20  $\mu\text{m}$  (determined by light scattering technique; Coulter LS 230, UK; Fraunhofer optical model).

#### 3.1.2 Preparation of glass-ceramics

##### 3.1.2.1 Nucleation and crystallization in monolithic glasses

This crystallization technique was followed on glasses investigated in Chapter 4 (*section 4.6*). Two series of glasses with different nucleating agents (i.e.  $\text{Cr}_2\text{O}_3 + \text{Fe}_2\text{O}_3$  containing and  $\text{CaF}_2$  containing) were evaluated for their crystallization behaviour under different nucleation and crystallization heating conditions, which are as follow:

##### *Cr<sub>2</sub>O<sub>3</sub> + Fe<sub>2</sub>O<sub>3</sub> containing glasses*

The bulk glasses were cut into small pieces and heat treated in an electric furnace, in air, up to 700 °C for a dwell time of 2 h followed by heating at different crystallization temperatures varying between 800–1000 °C for 1 h, respectively. The heating rate from room temperature to 700 °C was 5 K min<sup>-1</sup> while from 700 °C to crystallization temperature it was 2 K min<sup>-1</sup>.

##### *CaF<sub>2</sub> containing glasses*

The crystallization behaviour of the glasses was investigated by heat treating the small pieces of bulk glasses in an electric furnace, in air, in accordance with the following thermal cycles: (1) Room Temperature (RT) → 700 °C for a dwell time of 1 h at 700 °C; (2) RT → 800 °C for a dwell time of 1 h at 800 °C; (3) RT → 900 °C for a dwell time of 1

h at 900 °C (4) RT → 1000 °C for a dwell time of 1 h at 1000 °C; (5) RT → 600 °C for a dwell time of 2 h at nucleating temperature ( $T_n$ ), i.e. 600 °C, and then 600 °C → 900 °C for a dwell time of 1 h at 900 °C; (6) RT → 700 °C (973 K) for a dwell time of 2 h at nucleating temperature, i.e. 700 °C, and then 700 °C → 900 °C for a dwell time of 1 h at 900 °C. The heating rate in all the thermal cycles was 5 K min<sup>-1</sup>.

### *3.1.2.2 Sintering and crystallization of glass powder compacts*

The results presented in Chapter 4 (*section 4.1 – 4.5*) have been obtained on the GCs prepared via sintering and crystallization of glass powder compacts (GPCs). Rectangular bars with dimensions of 4x5x50 mm<sup>3</sup> or circular disc shaped pellets with Ø 20 mm and thickness ~3 mm were prepared from fine glass powders by uniaxial pressing (80 MPa). The GPCs were sintered under non-isothermal conditions for 1 h in the temperature range of 800-1100 °C, respectively. A slow heating rate ( $\beta$ ) of 2 K min<sup>-1</sup> was maintained in order to prevent deformation of the samples. Further, GPCs already sintered at 900 °C for 1 h, were heat treated under isothermal conditions at 900 °C for different time durations varying between 1 h - 300 h (Chapter 4, *section 4.2 and 4.3*) while in *section 4.4 and 4.5*, GPCs already sintered at 850 °C for 1 h, were heat treated under isothermal conditions at 800 °C for 300 h in order to evaluate their thermal expansion behaviour and stability of crystalline phase assemblage during long term operation at SOFC operation temperature.

## **3.2 Characterization of glasses**

### *3.2.1 Amorphous nature and phase separation in glasses*

The amorphous nature of glasses was confirmed by x-ray diffraction (XRD) and scanning electron microscopy (SEM). In order to examine the possibility of existence of liquid-liquid amorphous phase separation, glasses in bulk form were heat treated at 700 °C for 1 h at heating rate of 5 K min<sup>-1</sup> and were observed under SEM in polished (mirror-finishing) form.

### *3.2.2 Structural characterization of glasses*

#### *3.2.2.1 Infrared spectroscopy (FTIR)*

Infrared spectra for the glass powders were obtained using an infrared Fourier spectrometer (FT-IR, model Mattson Galaxy S-7000, USA). For this purpose each sample

was mixed with KBr in the proportion of 1/150 (by weight) for 15 min and pressed into a pellet using a hand press.

### 3.2.2.2 Magic angle spinning - Nuclear magnetic resonance (MAS-NMR)

<sup>29</sup>Si MAS NMR spectra were recorded on a Bruker ASX 400 spectrometer operating at 79.52 MHz (9.4 T) using a 7 mm probe at a spinning rate of 5 kHz. The pulse length was 2 μs and 60 seconds delay time was used. Kaolinite was used as the chemical shift reference. <sup>27</sup>Al MAS NMR spectra were recorded on a Bruker ASX 400 spectrometer operating at 104.28 MHz (9.4 T) using a 4 mm probe at a spinning rate of 15 kHz. The pulse length was 0.6 μs and 4 seconds delay time was used. Al(NO<sub>3</sub>)<sub>3</sub> was used as the chemical shift reference. <sup>11</sup>B MAS NMR spectra were recorded on a Bruker ASX 400 spectrometer operating at 128.36 MHz (9.4 T) using a 4 mm probe at a spinning rate of 12 kHz. The pulse length was 3.6 μs and 2 seconds delay time was used. H<sub>3</sub>BO<sub>3</sub> was used as the chemical shift reference.

### 3.2.3 Density measurements

Archimedes' method (i.e. immersion in diethyl phthalate) was employed to measure the apparent density of the bulk annealed glasses. Molar Volume ( $V_m$ ), oxygen molar volume ( $V_o$ ) and excess volume ( $V_e$ ) were calculated using the density data for the bulk glasses using following relations:

$$V_m = \frac{M}{\rho} \quad (3.1),$$

where M is the molar mass of the glass and  $\rho$  is the apparent density of the bulk glasses. Similarly, excess volume of the glasses can be expressed as:

$$V_e = V_m - \sum_i x_i V_m(i) \quad (3.2),$$

Here,  $x_i$  is the molar concentration of every oxide and  $V_m(i)$  is the molar volume of every oxide.

### 3.2.4 Thermal analysis

#### 3.2.4.1 Dilatometry

Dilatometry measurements were done with prismatic samples with cross section of 4x5 mm<sup>2</sup> (Bahr Thermo Analyse DIL 801 L, Hüllhorst, Germany GmbH; heating rate 5 K

min<sup>-1</sup>). The mean values and the standard deviations (SD) presented for coefficient of thermal expansion (CTE) (both glasses and GCs), dilatometric glass transition temperature (T<sub>dg</sub>), and softening temperature (T<sub>s</sub>) have been obtained from (at least) three different samples for each glass and GC.

#### 3.2.4.2 Differential thermal analysis (DTA)/Differential scanning calorimetry (DSC)

DTA/DSC experiments on glass powders were carried out in three different equipments (i.e. DTA-TG, Labsys Setaram, Caluire, France; DTA, NETZSCH 402 EP, Germany; DSC-TG, NETZSCH STA 409 PC Luxx thermal analyzer) with  $\alpha$ -alumina as a reference material. Glass transition temperature (T<sub>g</sub>), temperature for onset of crystallization (T<sub>c</sub>) and peak temperature of crystallization (T<sub>p</sub>) were obtained from DTA/DSC thermographs. In order to investigate the non-isothermal crystallization kinetics of glasses, 50 mg of glass powders were heated from room temperature up to 1000 °C with different heating rates ( $\beta$ ) varying between 2–40 K min<sup>-1</sup>. The crystallization kinetics of the glasses was studied using the formal theory of transformation kinetics as developed by Johnson and Mehl [106] and Avrami [107], for non-isothermal processes that has already been obtained in our previous work [108, 109]:

$$\ln\left(\frac{T_p^2}{\beta}\right) = \frac{E_c}{RT_p} - \ln q = 0 \quad (3.3)$$

which is the equation of a straight line, whose slope and intercept give the activation energy,  $E_c$ , and the pre-exponential factor,  $q = Q^n K_0$ , respectively and the maximum crystallization rate by the relationship:

$$\left.\frac{dx}{dt}\right|_p = 0.37 \beta E_c n (RT_p^2)^{-1} \quad (3.4)$$

which makes it possible to obtain, for each heating rate, a value of the kinetic exponent,  $n$ .

In Eq. 3.4,  $\chi$  corresponds to the crystallization fraction and  $\left.\frac{d\chi}{dt}\right|_p$  corresponds to the crystallization rate, which may be calculated by the ratio between the ordinates of the DTA curve and the total area of the crystallization curve.

### 3.2.4.3 Hot-stage microscopy

A side-view hot-stage microscope (HSM) EM 201 equipped with image analysis system and electrical furnace 1750/15 Leica was used. The microscope projects the image of the sample through a quartz window and onto the recording device. The computerized image analysis system automatically records and analyzes the geometry changes of the sample during heating. The image analyzer takes into account the thermal expansion of the alumina substrate while measuring the height of the sample during firing, with the base as a reference. The HSM software calculates the percentage of decrease in height, width and area of the sample images. The measurements were conducted in air with a heating rate of  $5 \text{ K min}^{-1}$ . The cylindrical shaped samples with height and diameter of  $\approx 3 \text{ mm}$  were prepared by cold-pressing the glass powders. The cylindrical samples were placed on a  $10 \times 15 \times 1 \text{ mm}$  alumina ( $>99.5 \text{ wt.}\% \text{ Al}_2\text{O}_3$ ) support. The temperature was measured with a Pt/Rh (6/30) thermocouple contacted under the alumina support. The temperatures corresponding to the characteristic viscosity points (first shrinkage, maximum shrinkage, softening, half ball and flow) were obtained from the photographs taken during the hot-stage microscopy experiment following Scholze's definition [110] and [111, 112].

## 3.3 Characterization of glass-ceramics

### 3.3.1 Crystalline phase analysis and microstructure

The crystalline phases in GCs were determined by XRD analysis (Rigaku Geigerflex D/Max, C Series;  $\text{CuK}_\alpha$  radiation;  $2\theta$  angle range  $10^\circ$ - $80^\circ$ ; step  $0.02 \text{ deg s}^{-1}$ ). The quantitative analysis of crystalline phases in GCs (crushed to particle size  $< 25 \mu\text{m}$ ) were determined by XRD analysis using a conventional Bragg-Brentano diffractometer (Philips PW 3710, Eindhoven, The Netherlands) with Ni-filtered  $\text{Cu-K}_\alpha$  radiation. The quantitative phase analysis of the GCs was made by combined Rietveld-R.I.R method. A 10 wt.% of corundum (NIST SRM 674a, annealed at  $1500^\circ\text{C}$  for 1 day to increase the crystallinity to 100%) was added to all the GC samples as an internal standard. The mixtures, ground in an agate mortar, were side loaded in aluminium flat holder in order to minimize the preferred orientation problems. Data were recorded in  $2\theta$  range =  $5$ - $140^\circ$  (step size  $0.02^\circ$  and 6 seconds of counting time for each step). The phase fractions were extracted by Rietveld-R.I.R refinements, using GSAS software [113] and EXPGUI [114] as graphical interface, were rescaled on the basis of the absolute weight of corundum

originally added to their mixtures as an internal standard, and therefore, internally renormalized. The background was successfully fitted with a Chebyshev function with a variable number of coefficients depending on its complexity. The peak profiles were modelled using a pseudo-Voigt function with one Gaussian and one Lorentzian coefficient. Lattice constants, phase fractions, and coefficients corresponding to sample displacement and asymmetry were also refined.

The phase transformations occurring in glass powders/ GCs over increasing temperature were monitored by *in situ* high temperature X-ray diffraction (HT-XRD) analysis (Philips, X'pert, The Netherlands, equipped with a Pt hot stage).

Microstructure observations were done at polished (mirror finishing) and then etched (by immersion in 2 vol.% HF solution for 2 min) surfaces of samples by field emission scanning electron microscopy (FE-SEM, Hitachi S-4100, Japan/SU-70, Hitachi, Japan) under secondary electron mode.

### ***3.3.2 Linear shrinkage, density and mechanical strength***

Archimedes' method (i.e. immersion in diethyl phthalate) was employed to measure the apparent density of the samples. The mechanical properties were evaluated by measuring the three-point bending strength of rectified parallelepiped bars ( $3 \times 4 \times 50 \text{ mm}^3$ ) of sintered GCs (Shimadzu Autograph AG 25 TA;  $0.5 \text{ mm min}^{-1}$  displacement). The linear shrinkage during sintering was calculated from the difference of the dimensions between the green and the sintered bars. The mean values and the standard deviations (SD) presented for shrinkage, density, and bending strength have been obtained from (at least) 10 different samples.

### ***3.3.3 Measurements of electrical properties and oxygen permeability***

The sintered GCs were checked for gas-tightness, by the absence of gas leakage through samples placed under a pressure gradient of 2-3 atm at room temperature. The total conductivity was studied by AC impedance spectroscopy (HP4284A precision LCR meter, 20 Hz–1 MHz, Technologies, Palo Alto, CA), using dense disk- or bar-shaped samples with porous Pt electrodes. In the course of impedance measurements, the magnitude of AC voltage was fixed at 1.00 V; the equilibration time after each temperature change was 2-4 h. The same method was used in Chapter 4, *section 4.4* in order to test the

total electrical resistance of a model cell comprising metallic interconnect (Crofer 22 APU) and electrolyte (zirconia stabilized by 8 mol.% yttria, 8YSZ) plates joined by the GC sealant, with Pt electrodes deposited onto the metal and zirconia plates (for further details regarding the preparation of model cell, please refer to *section 3.3.4*).

The ion transference numbers were determined by the modified electromotive-force (e.m.f.) technique, as described elsewhere [115, 116]. Gas mixtures of 10% H<sub>2</sub>-90% N<sub>2</sub> or O<sub>2</sub>-Ar were supplied at the anode of a Pt|GC|Pt cell, where the oxygen partial pressure ( $p_1$ ) was determined using a 8YSZ sensor. The cathode was exposed to atmospheric air ( $p_2 = 21$  kPa). The e.m.f. of the cell was measured at 820-860 °C as a function of an external resistance,  $R_M$ . The ion transference numbers were calculated using regression model of eq. (3.5) in combination with eq. (3.6):

$$\frac{E_{th}}{E_{obs}} - 1 = A \left( \frac{1}{R_M} \right) + B, \quad R_e = \frac{A}{B} \quad (3.5),$$

$$t_i = 1 - \frac{R_{bulk}}{R_e} \quad (3.6),$$

where  $A$  and  $B$  are regression parameters,  $E_{obs}$  the measured e.m.f.,  $E_{th}$  the theoretical Nernst voltage,  $R_{bulk}$  the bulk resistance determined from the impedance spectra, and  $R_e$  the partial electronic resistance of the sample.

The determination of oxygen permeation fluxes through GCs under air/(H<sub>2</sub>-H<sub>2</sub>O-N<sub>2</sub>) gradients was based on the analysis of the oxygen activity in the gas flowing over the sample permeate side ( $p_1$ ). The experimental set-up, sketched in Fig. 3.1, comprised a dense GCs membrane disk (1.00 mm thickness) hermetically sealed onto the 8YSZ tube with a commercial Aremco Products sealant, and two 8YSZ oxygen sensors at the cell inlet (sensor 1) and outlet (sensor 2). The third sensor (sensor 3) was used to control the oxygen chemical potential at the feed-side of membrane. A (H<sub>2</sub>-H<sub>2</sub>O)-N<sub>2</sub> gas mixture flow was supplied onto the GC permeate side, where hydrogen interacted with oxygen permeating through the membrane. For all data presented in this work, the partial pressures of oxygen, hydrogen, and water vapor at the membrane permeate side were fixed at  $3.2 \times 10^{-16}$ ,  $9.5 \times 10^3$  and  $5.8 \times 10^2$  Pa, respectively. In order to minimize possible effects due to water vapour permeation, the partial pressures of oxygen and vapour in the feed gas mixture were at 19.2 and 10.2 kPa, respectively. The gases were supplied with a constant flow rate of 20 ml min<sup>-1</sup>, fixed with Bronkhorst mass-flow controllers (MFC) and additionally measured

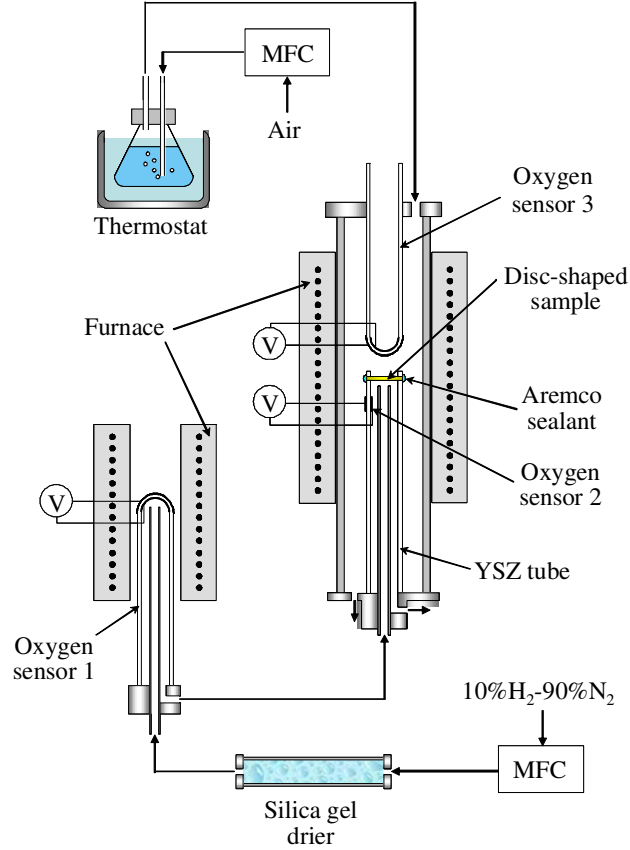


Fig. 3.1 Schematic outline of experimental setup for measurements of oxygen permeability.

at the outlets by a soap-film flow meter. The oxygen permeation flux density ( $j$ ) through a membrane under steady-state conditions was calculated as

$$j = \frac{V}{RT_V S} \cdot \frac{p(\text{H}_2)_{\text{in}} - p(\text{H}_2)_{\text{out}}}{2} \quad (3.7),$$

where  $T_V$  is the flow meter temperature,  $S$  the membrane surface area, and  $p(\text{H}_2)_{\text{in}}$  and  $p(\text{H}_2)_{\text{out}}$  the inlet and outlet hydrogen partial pressures, respectively. The hydrogen pressure was calculated from the oxygen chemical potential and volume fraction of H-containing species ( $\text{H}_2 + \text{H}_2\text{O}$ ) using available thermodynamic data [117].

**3.3.4 Joining behaviour and chemical interaction between electrolyte - glass-ceramic sealant - metallic interconnect in air and humidified reducing atmosphere.**

In order to investigate the adhesion and chemical interaction of the glasses with SOFC components, wetting experiments between glass (powder) - 8YSZ (Tosoh, Japan) and glass (powder) - metallic interconnect were carried out under different conditions. Two different metallic interconnect materials, namely, Crofer22 APU (Thyssen Krupp, VDM, Werdohl, Germany) and Sanergy HT (Sandvik AB, Sandviken, Sweden) were employed for wetting and interaction experiments with the glasses. Table 3.1 presents the composition of the two interconnect materials [118, 119]. The glass powders were deposited on electrolyte and interconnect by slurry coating. Joined interconnect-glass-electrolyte samples were obtained by sandwiching the glass coated YSZ wafer and the interconnect plate.<sup>1</sup> Heat treatment was performed in a tubular furnace, without applying any dead load, in air as well as humidified reducing atmosphere (95% Ar + 5% H<sub>2</sub> passed through water bath), respectively. The diffusion couples were heated to 850 °C with a relatively slow heating rate (2 K min<sup>-1</sup>) and kept at that temperature for 1 h. Finally, the temperature was brought down to SOFC operating temperature (i.e. 800 °C) and maintained at this temperature for 300 h.

Table 3.1 Chemical composition of metallic interconnects (wt.%)

| Crofer22 APU |      |      |             |              |              |      |      |       |       |      |      |
|--------------|------|------|-------------|--------------|--------------|------|------|-------|-------|------|------|
|              | Cr   | Fe   | C           | Mn           | Si           | Cu   | Al   | S     | P     | Ti   | La   |
| Min.         | 20.0 | Bal. | -           | 0.30         | -            | -    | -    | -     | -     | 0.03 | 0.04 |
| Max.         | 24.0 |      | 0.03        | 0.80         | 0.50         | 0.50 | 0.50 | 0.020 | 0.050 | 0.20 | 0.20 |
| Sanergy HT   |      |      |             |              |              |      |      |       |       |      |      |
|              |      |      | C<br>(max.) | Si<br>(max.) | Mn<br>(max.) | Cr   | Mo   | Nb    | Other |      |      |
|              |      |      | 0.05        | 0.30         | 0.50         | 22   | 1.0  | 0.75  | Ti    |      |      |

Energy dispersive spectroscopy (EDS; Bruker Quantax, Germany) was employed to study the distribution of elements along the glass-interconnect diffusion couples.

<sup>1</sup> In section 4.2 and 4.3, the glass was applied on 8YSZ pellets (sintered and polished) and heat treated at 900 °C for 100 h in air. No interconnect materials were used.

### ***3.3.5 Thermal shock resistance***

In order to evaluate thermal shock resistance of the GC sealants in contact with stabilized zirconia electrolyte, a series of cells were made of 8YSZ by sealing dense ceramic tubes onto the disks. Hermetic sealing was performed using powdered GCs, with final annealing at 1250 °C for 0.5 h. Then each pseudo-cell was heated in the furnace up to 800 °C, kept at this temperature for 0.5 h, and quenched in air or in water. After subsequent checking of the gas-tightness, each cell was rapidly heated again, and the quenching cycle was repeated. The YSZ pseudo-cells were successfully tested in 15 air-quenching cycles.

.....

## **CHAPTER IV: Results and discussion**

## 4.1 Enstatite-Diopside join: Magnesium-metasilicate (MgSiO<sub>3</sub>) based glasses and glass-ceramics

### 4.1.1 Designing of compositions

Partial substitutions in cation and anion sublattice of Mg-metasilicate were attempted and their influence on crystallization process and the properties of the resultant GCs was investigated. Table 4.1 presents the scheme of substitutions; type of crucibles used and detailed compositions of the investigated glasses. The composition with 25 wt.% Di and 75 wt.% En (Ca<sub>0.125</sub>Mg<sub>0.875</sub>SiO<sub>3</sub>, composition 1) was considered as the starting point, aiming at reducing the tendency of Mg-metasilicate for polymorphism. Substitutions of 0.125Ca<sup>2+</sup> + 0.125Si<sup>4+</sup> ↔ 0.125Y<sup>3+</sup> + 0.125B<sup>3+</sup> were attempted in the composition 2a. Composition 3a features a more complex substitution of 0.125Ca<sup>2+</sup> + 0.125Si<sup>4+</sup> ↔ 0.125Y<sup>3+</sup> + 0.125B<sup>3+</sup> and 0.15Mg<sup>2+</sup> ↔ 0.15Ba<sup>2+</sup>. The incorporation of B<sub>2</sub>O<sub>3</sub> in compositions 2a and 3a had a dual aim: To satisfy the overall charge balance of the system, and, under the perspective of technology, to decrease the viscosity of glass melts and facilitate diffusion. Further, the influence of Al<sub>2</sub>O<sub>3</sub> addition on sintering and crystallization behaviour of En-based glasses was studied by incorporating 8 wt.% Al<sub>2</sub>O<sub>3</sub> in glasses 2a and 3a, respectively, thus deriving compositions 2b and 3b. In order to enhance the potential application of the resultant GCs, we incorporated in the batches small amount of NiO (1 wt.%), considering that NiO will favour adhesion of the resultant GCs with metals.

### 4.1.2 Casting ability of glasses

The compositions 2 (2a and 2b) and 3 (3a and 3b) were prone for easy casting after only 1 h of melting (at 1600 °C), resulting in a homogenous transparent glass with dark brown colour and with no crystalline inclusions, as was also confirmed by X-ray and SEM analyses afterwards. The brown colour of the experimental glasses is probably due to the addition of NiO. Nickel is one of the elements that impart oxide glasses the widest range of coloration: green, yellow, brown, purple, and blue. These modifications of the glass colour have been interpreted in the past as arising from two kinds of sites, octahedral and tetrahedral, the proportion of which varies as a function of glass composition [120]. The origin of this brown coloration in the glasses is due to the presence of nickel in five-coordination, in trigonal bipyramids [121].

Table 4.1 Composition of glasses along Di-En join (wt. %)

| Label                                                                                                                         | Scheme of substitutions in accordance with parent glass composition                                                                                                                                                                                              | Type of crucible | MgO   | CaO   | BaO   | SiO <sub>2</sub> | B <sub>2</sub> O <sub>3</sub> | Al <sub>2</sub> O <sub>3</sub> | Y <sub>2</sub> O <sub>3</sub> |
|-------------------------------------------------------------------------------------------------------------------------------|------------------------------------------------------------------------------------------------------------------------------------------------------------------------------------------------------------------------------------------------------------------|------------------|-------|-------|-------|------------------|-------------------------------|--------------------------------|-------------------------------|
| <i>Parent glass composition: 25 mol.% Diopside (CaMgSi<sub>2</sub>O<sub>6</sub>) – 75 mol.% Enstatite (MgSiO<sub>3</sub>)</i> |                                                                                                                                                                                                                                                                  |                  |       |       |       |                  |                               |                                |                               |
| 1                                                                                                                             | 25 mol.% Diopside – 75 mol.% Enstatite<br>(Ca <sub>0.125</sub> Mg <sub>0.875</sub> SiO <sub>3</sub> )                                                                                                                                                            | Alumina          | 34.45 | 6.85  | –     | 58.70            | –                             | –                              | –                             |
| 2a                                                                                                                            | 0.125Ca <sup>2+</sup> + 0.125Si <sup>4+</sup> ↔ 0.125Y <sup>3+</sup> + 0.125B <sup>3+</sup><br>(Y <sub>0.125</sub> Mg <sub>0.875</sub> Si <sub>0.875</sub> B <sub>0.125</sub> O <sub>3</sub> )                                                                   | Pt               | 33.17 | –     | –     | 49.45            | 4.09                          | –                              | 13.27                         |
| 2b                                                                                                                            | 8 wt.% Al <sub>2</sub> O <sub>3</sub> added to glass 2a                                                                                                                                                                                                          |                  | 30.52 | –     | –     | 45.49            | 3.76                          | 8.00                           | 12.21                         |
| 3a                                                                                                                            | 0.125Ca <sup>2+</sup> + 0.125Si <sup>4+</sup> ↔ 0.125Y <sup>3+</sup> + 0.125B <sup>3+</sup><br>0.15Mg <sup>2+</sup> ↔ 0.15Ba <sup>2+</sup><br>(Y <sub>0.125</sub> Mg <sub>0.725</sub> Ba <sub>0.15</sub> Si <sub>0.875</sub> B <sub>0.125</sub> O <sub>3</sub> ) |                  | 23.70 | –     | 18.65 | 42.65            | 3.52                          | –                              | 11.44                         |
| 3b                                                                                                                            | 8 wt.% Al <sub>2</sub> O <sub>3</sub> added to glass 3a                                                                                                                                                                                                          | 21.80            | –     | 17.16 | 39.24 | 3.24             | 8.00                          | 10.52                          |                               |



Fig. 4.1 Photograph of as-casted and annealed bulk glasses 1, 2a and 3a.

We met, however, some difficulties to produce a stable glass of composition 1, because dwell of 1 h at 1600 °C resulted in a non-homogeneously coloured opaque glass (Fig. 4.1). In particular, the core of the cast bulk glass had a similar aspect to the glasses 2 and 3 but the thick skin layer was opaque brown. SEM observation revealed that the skin layer contained large number of round shaped (300-400 nm) inclusions (Fig. 4.2) of amorphous nature (confirmed by XRD analysis), which tended to disappear gradually when moving from the skin toward the core of the samples. Prolongation of dwell time to 1.5-2 h eliminated the problem and homogenous transparent glass 1 was obtained.

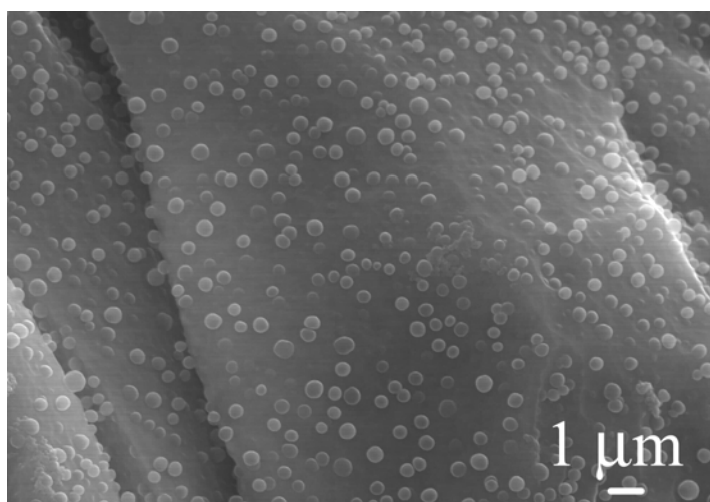


Fig. 4.2 Inclusions observed at the opaque skin layer of as-cast bulk glass 1 obtained after melting at 1600 °C for 1 h and subsequent annealing.

### 4.1.3 Structure of glasses

The room temperature FTIR transmittance spectra of the investigated glasses are shown in Fig. 4.3. All the spectra exhibit four broad transmittance bands in the region of 300-1500  $\text{cm}^{-1}$ . The most intense bands lie in the 800-1300  $\text{cm}^{-1}$  region, the next between 300-600  $\text{cm}^{-1}$  and 1350-1500  $\text{cm}^{-1}$ , while the least intensive lies between 650-800  $\text{cm}^{-1}$ . This lack of sharp features is indicative of the general disorder in the silicate network mainly due to a wide distribution of  $Q^n$  units (polymerization in the glass structure, where  $n$  denotes the number of bridging oxygen) occurring in these glasses. The broad band in the 800-1300  $\text{cm}^{-1}$  is assigned to the stretching vibrations of the  $\text{SiO}_4$  tetrahedron with different number of bridging oxygen atoms [122, 123]. For glasses 2a and 3a, this band is around 1050-1070  $\text{cm}^{-1}$  indicating the distribution of  $Q^n$  units centred on the  $Q^3$  and possibly  $Q^4$ , while for glasses 2b and 3b, this band shifts towards lower wave numbers with addition of  $\text{Al}_2\text{O}_3$ , implying towards the decrease in the connectivity of the silicate glass network. Al is known to create  $Q^3$  bands at the expense of  $Q^2$  and  $Q^4$  units in the silicate glasses [124].

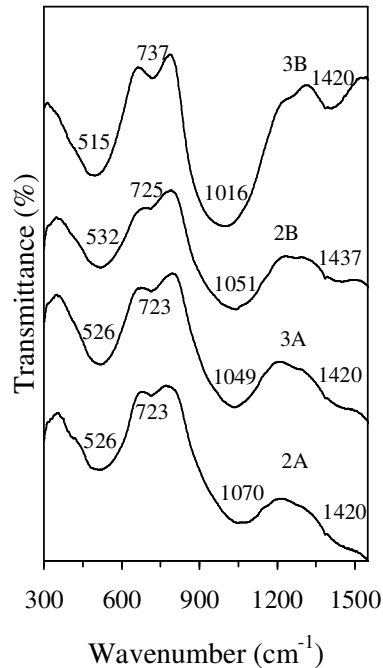


Fig. 4.3 FTIR spectra of the investigated glass powders.

The transmittance band in the region 800-1300  $\text{cm}^{-1}$  for glass 2a is centred on 1070  $\text{cm}^{-1}$  while for BaO- containing glass (3a), it is centred at 1049  $\text{cm}^{-1}$ . This shows that BaO

effectively depolymerises the silicate glass network. The bands in the 300-600  $\text{cm}^{-1}$  region are due to bending vibrations of Si-O-Si linkages. The transmittance band in the 650-800  $\text{cm}^{-1}$  region in the glasses 2a and 3a is attributed to the bending vibrations of bridging oxygen between trigonal boron atoms while in glasses 2b and 3b, it is also related to the stretching vibrations of the Al-O bonds with  $\text{Al}^{3+}$  ions in four-fold coordination. The band in the region 1350-1500  $\text{cm}^{-1}$  corresponds to B-O vibrations in  $[\text{BO}_3]$  triangle. Borate glasses show two characteristic bands derived from the B-O bonds in the  $[\text{BO}_3]$  triangles (about 1300-1500  $\text{cm}^{-1}$ ) and the  $[\text{BO}_4]$  tetrahedra (about 1000  $\text{cm}^{-1}$ ) [125]. These bands get shifted under the influence of surrounding cations, the extent and the direction of this shift depending on the type of cation. FTIR spectra of the glasses under investigation show that in these glasses boron primarily occurs in the form of  $[\text{BO}_3]$  triangles (1396  $\text{cm}^{-1}$ ). However, the presence of  $[\text{BO}_4]$  tetrahedron in the glass structure can not be neglected. Since the IR band for  $[\text{BO}_4]$  tetrahedron (about 1000  $\text{cm}^{-1}$ ) overlaps with that of stretching vibrations of  $\text{SiO}_4$ , therefore, it could not be observed in the present investigation. No other band could be resolved in the spectra of the glasses.

#### 4.1.4 Dilatometry

From the dilatometry curves of the cast-annealed bulk glasses, plotted in Fig. 4.4, the dilatometric transition temperatures ( $T_{\text{dg}}$ ) and the dilatometric softening points ( $T_{\text{s}}$ ) of the glasses were determined. The results, presented in Table 4.2, suggest that the presence of  $\text{Al}_2\text{O}_3$  in the glasses (i.e. compositions 2b and 3b) causes a considerable decrease in  $T_{\text{dg}}$  and  $T_{\text{s}}$ , respectively, as compared to the  $\text{Al}_2\text{O}_3$ -free compositions (2a and 3a). The CTE of the glasses was observed to decrease with the addition of  $\text{Al}_2\text{O}_3$  in BaO-free glasses (2a and 2b) while it increased for glass 3b in comparison to glass 3a (Table 4.2). However, CTE for BaO-containing glasses (3a and 3b) was observed to be higher in comparison to BaO-free glasses (2a and 2b). Addition of BaO is known to increase the CTE of silicate glasses [126] as it favours the formation of non-bridging oxygens (NBO) in the silicate glass network (Fig. 4.2).

The CTE values of all the investigated glasses are lower than the clinopyroxene based Di-CaTs glasses [126]. This may be attributed to the higher degree of polymerization in the silicate glass network of En based glasses and also, to the presence of  $\text{B}_2\text{O}_3$  in the

glasses. According to Ojovan and Lee [124],  $B_2O_3$  when present in less than 15 wt. %, decreases the CTE of the silicate glasses.

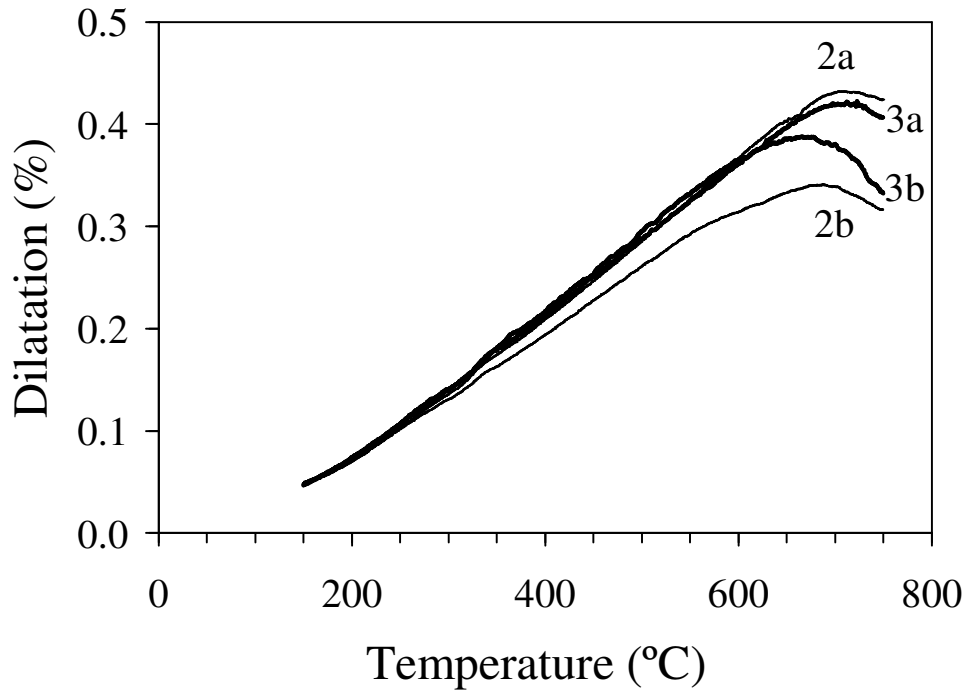


Fig. 4.4 Dilatometry curves obtained from as-cast and annealed bulk glasses.

Table 4.2 Thermal parameters obtained for the investigated glasses ( $\beta = 5 \text{ K min}^{-1}$ )

| Glass | $T_{dg}$ (°C) | $T_s$ (°C) | $T_c$ (°C) | $T_p$ (°C) | $T_c - T_{dg}$ (°C) | CTE <sup>#</sup> |
|-------|---------------|------------|------------|------------|---------------------|------------------|
| 2a    | 670           | 710        | 835        | 862        | 165                 | 7.14             |
| 2b    | 590           | 670        | 870        | 898        | 280                 | 6.29             |
| 3a    | 670           | 698        | 860        | 890        | 190                 | 7.19             |
| 3b    | 610           | 653        | 895        | 928        | 285                 | 7.38             |

<sup>#</sup>CTE $\times 10^6 \text{ K}^{-1}$  (200 - 500 °C)

#### 4.1.5 Sintering and crystallization kinetics of glass powders

Figure 4.5 presents the DTA thermographs (Labsys setaram, France) of fine powders with mean particle size of 2.8-3.0  $\mu\text{m}$ , obtained from glass frits. In comparison to  $Al_2O_3$ -free glasses (2a and 3a), the presence of  $Al_2O_3$  (2b and 3b) shifted  $T_p$  and  $T_c$  to higher

temperatures and increased the intensity of the exothermic crystallization peak. Table 4.2 lists the  $T_c$  and  $T_p$  values for the glasses at  $\beta = 5 \text{ K min}^{-1}$ .

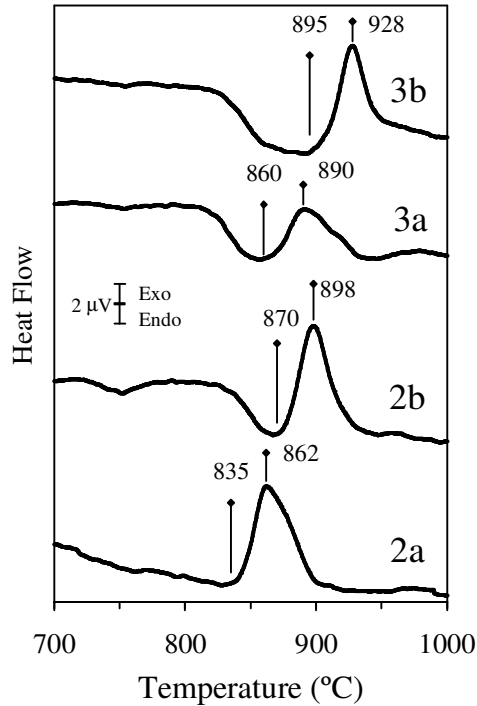


Fig. 4.5 DTA scans of glass powders (mean particle size of 2.8-3.0  $\mu\text{m}$ ), obtained from frits of the investigated glasses.

The effect of  $\text{Al}_2\text{O}_3$  was also evident on the properties of the sintered GPCs. In particular, the GPCs of the  $\text{Al}_2\text{O}_3$ -free compositions 2a and 3a were very poorly sintered after heat treatment at 900 °C and 1000 °C (Fig. 4.6a). The resultant samples of white colour were highly porous and extensively fractured. Heat treatment at 1100 °C for 1 h slightly improved densification, but over-firing effect became evident because randomly distributed globules of grey-yellowish colour on the surface of the samples developed (Fig. 4.6b).

In the contrast, the sintering ability of the  $\text{Al}_2\text{O}_3$ -containing samples 2b and 3b was very good. Well sintered and dense samples were obtained after heat treatment at 900 °C and 950 °C for 1 h (Fig. 4.6c). The values of the properties, listed in Table 4.3, evidence the sound influence of  $\text{Al}_2\text{O}_3$  on improving the properties of the produced GCs. The experimental results of this study agree fairly well with earlier studies outlined in the ‘State of the art’ (Chapter II) and summarized in the difficulties of producing stable glass with

composition of  $\text{MgSiO}_3$  and the remarkable delay of densification of the  $\text{Al}_2\text{O}_3$ -free

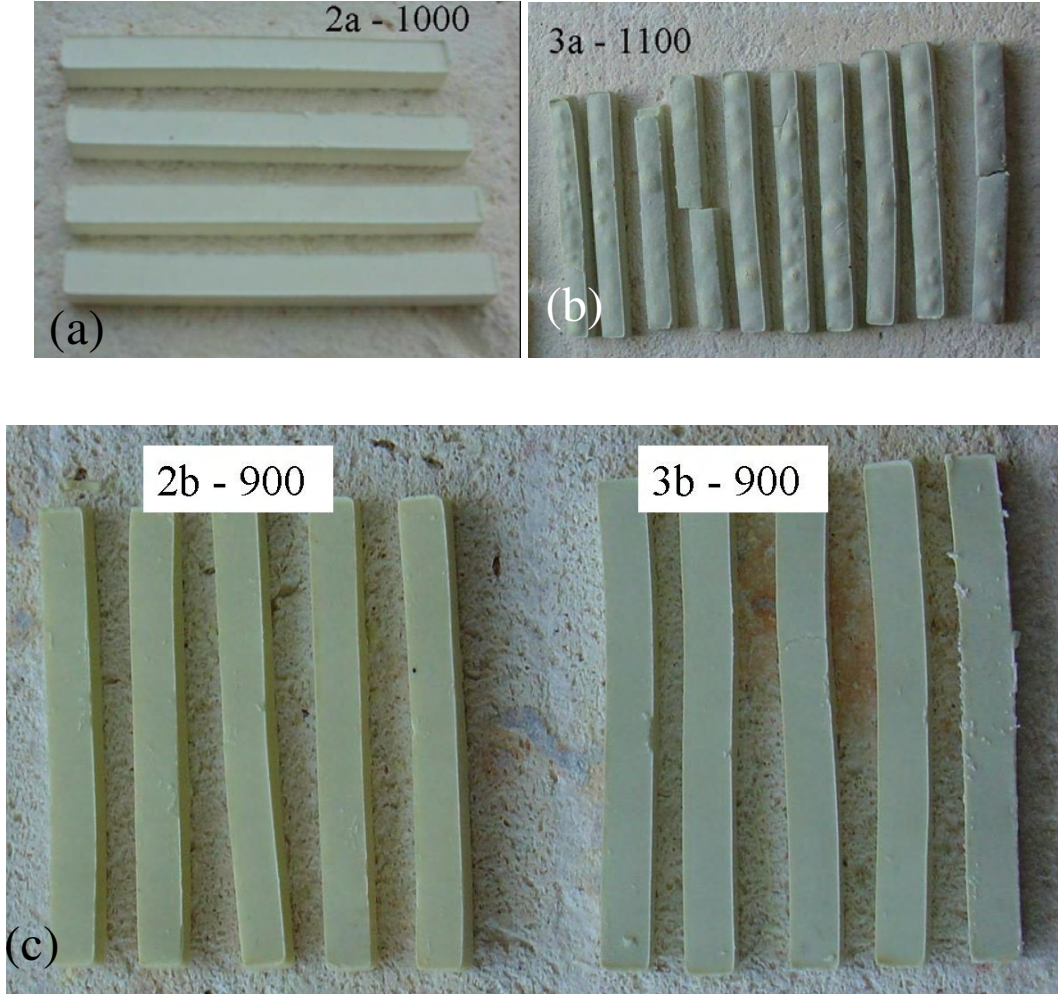


Fig. 4.6 Photographs of glass powder compacts of composition (a) 2a heat treated at 1000 °C (b) 3a heat treated at 1100 °C, (c) 2b and 3b heat treated at 900 °C for 1 h, respectively.

$\text{MgSiO}_3$ . This was the main reason that many researches have shifted their interest in the  $\text{MgO-Al}_2\text{O}_3\text{-SiO}_2$  system to produce sintered  $\text{MgSiO}_3$  GCs. Indeed, high quality  $\text{MgSiO}_3$  GCs have been produced from glass powders via surface nucleation and crystallization mechanisms with batches based on  $\text{MgO-Al}_2\text{O}_3\text{-SiO}_2$  system and additions of  $\text{ZrO}_2$ ,  $\text{TiO}_2$ ,  $\text{ZnO}$ , and  $\text{BaO}$  [13, 21, 23-29].

In quest for the reason behind poor sintering ability of  $\text{Al}_2\text{O}_3$ -free glasses, we investigated the non-isothermal crystallization kinetics and thermal stability of glasses 2a and 3a using DSC (NETZSCH STA 409 PC Luxx thermal analyzer). Representative DSC thermographs for both the glasses (2a and 3a), taken at different heating rates (Fig. 4.7),

Table 4.3 Properties of GCs produced after firing at different temperatures

| GC | T (°C) | Shrinkage (%) | Density (g cm <sup>-3</sup> ) | Flexural strength (MPa) |
|----|--------|---------------|-------------------------------|-------------------------|
| 2a | 1100   | 5.61 ± 0.18   | -                             | 19.64 ± 1.94            |
| 3a | 1100   | 9.49 ± 0.34   | 2.31 ± 0.002                  | 49.64 ± 1.52            |
| 2b | 900    | 16.64 ± 0.47  | 3.07 ± 0.005                  | 149.53 ± 34.79          |
| 3b | 900    | 15.91 ± 0.30  | 3.20 ± 0.005                  | 105.11 ± 24.41          |

Table 4.4 Influence of heating rate on the thermal parameters of both the glasses

| $\beta$ (K min <sup>-1</sup> ) | Glass 2a            |                     |                     |                            | Glass 3a            |                     |                     |                            |
|--------------------------------|---------------------|---------------------|---------------------|----------------------------|---------------------|---------------------|---------------------|----------------------------|
|                                | T <sub>g</sub> (°C) | T <sub>c</sub> (°C) | T <sub>p</sub> (°C) | Area* (J g <sup>-1</sup> ) | T <sub>g</sub> (°C) | T <sub>c</sub> (°C) | T <sub>p</sub> (°C) | Area* (J g <sup>-1</sup> ) |
| 2                              | 758                 | 829                 | 858                 | 219.2                      | 753                 | 858                 | 880                 | 126.6                      |
| 5                              | 767                 | 838                 | 872                 | 233.7                      | 762                 | 867                 | 895                 | 132.0                      |
| 15                             | 783                 | 856                 | 888                 | 249.0                      | 778                 | 883                 | 917                 | 161.1                      |
| 20                             | 788                 | 860                 | 893                 | 252.7                      | 783                 | 885                 | 922                 | 203.3                      |

\*Area under the crystallization curve of the DTA thermograph.

exhibit an endothermic dip before the onset of crystallization and a single well defined crystallization exotherm. The values of T<sub>g</sub>, T<sub>c</sub> and T<sub>p</sub> shifted towards higher side with increase in heating rate (Table 4.4).

Since the densification of glass powder compacts is initially obtained through viscous flow at temperatures slightly higher than T<sub>g</sub>, the activation energy of viscous flow occurring around glass transition (E<sub>η</sub>) was calculated using the equation (4.1) [127, 128]:

$$\ln(T_g^2 / \beta) = E_\eta / RT_g + const. \quad (4.1)$$

where,  $\beta$  is the heating rate, R is the Gas constant. From Fig. 4.8 and Table 4.5, it is clear that glass 2a shows higher E<sub>η</sub> in comparison to glass 3a. The E<sub>η</sub> for glass 2a and 3a is much higher than for Al<sub>2</sub>O<sub>3</sub>-containing Di-CaTs glasses [129]. Moreover, it has been reported that E<sub>η</sub> decreases with increasing the Al<sub>2</sub>O<sub>3</sub> content in the glasses and the GCs obtained from Di-CaTs GPCs showed good sintering behaviour and exhibited high mechanical

strength. Therefore, higher temperature is required to achieve good sintering in Al<sub>2</sub>O<sub>3</sub>-free enstatite glasses in comparison to Al<sub>2</sub>O<sub>3</sub>-containing glasses. However, at higher temperature, crystallization process starts, which further hinders the sintering of the GPCs.

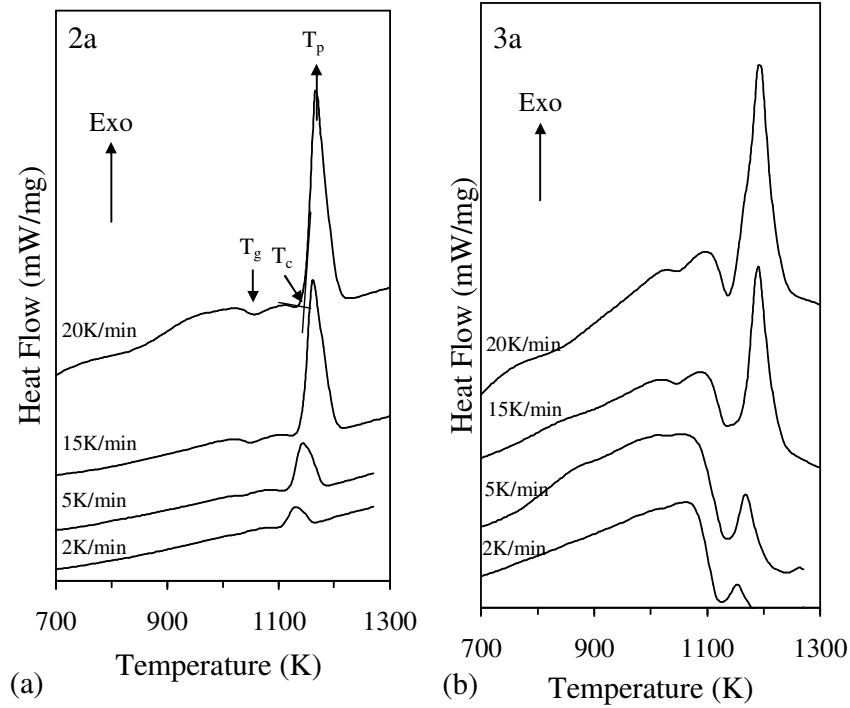


Fig. 4.7 DSC thermographs of the glass powder (a) 2a and (b) 3a at different heating rates.

Further, as also mentioned in *section 4.1.2*, we faced some serious difficulties in casting the glass with composition corresponding to 75% En - 25% Di. Therefore, glass forming ability of the glasses 2a and 3a was determined by calculating the kinetic fragility index,  $F$ , because it is a measure of the rate at which the relaxation time decreases with increasing temperature around  $T_g$  and is given by equation (2) [130, 131]:

$$F = \frac{E_\eta}{RT_g \ln 10} \quad (4.2)$$

According to Vilgis [132], glass forming liquids that exhibit an approximate Arrhenius temperature dependence of their relaxation times are defined as strong and specified with low value of  $F$  ( $F \approx 16$ ), while the limit for fragile glass-forming liquids is characterized by

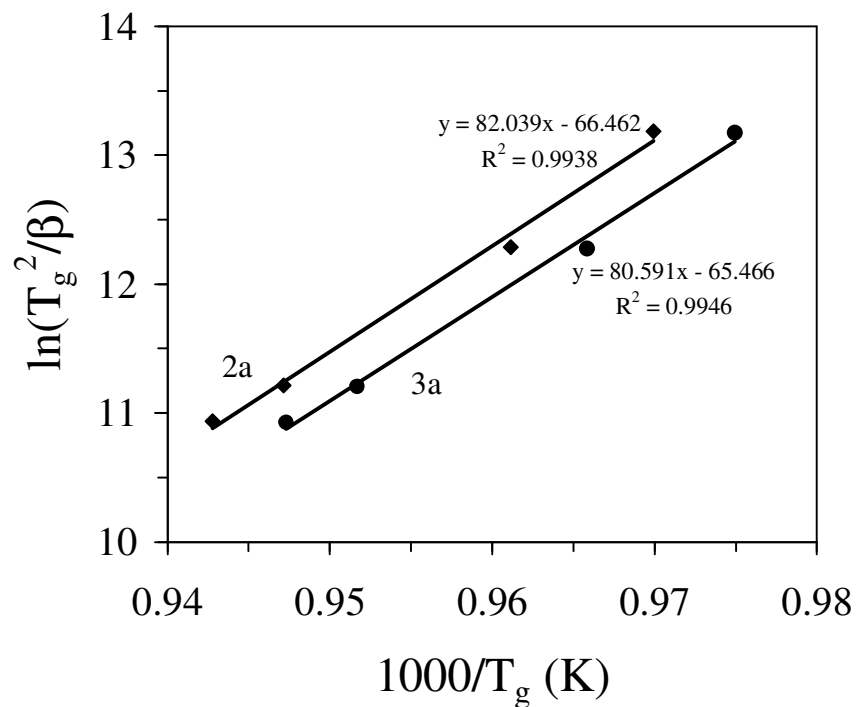


Fig. 4.8 Plot for determination of activation energy for viscous flow ( $E_{\eta}$ ) for glasses 2a and 3a.

Table 4.5 Thermal parameters showing the thermal stability and crystallization mechanism in glasses 2a and 3a

|                                       | 2a                     | 3a                      |
|---------------------------------------|------------------------|-------------------------|
| $E_{\eta}$ (kJ mol <sup>-1</sup> )    | 682                    | 670                     |
| $F^{\S}$                              | 34.55                  | 34.12                   |
| Avrami parameter, $\langle n \rangle$ | 1.07 ± 0.014           | 1.11 ± 0.017            |
| $q$ (sec <sup>-1</sup> )              | 1.2 × 10 <sup>30</sup> | 2.65 × 10 <sup>24</sup> |
| $E_c$ (kJ mol <sup>-1</sup> )         | 718                    | 604                     |

<sup>§</sup>β = 2 K min<sup>-1</sup>

a high value of  $F$  ( $F \approx 200$ ) [133]. As is evident from Table 4.5, glass 3a has slightly lower value of  $F$  in comparison to glass 2a. However, considering that the values of  $F$  for both the glasses are within the above mentioned limit, it is reasonable to state that both the glasses are obtained from strong glass forming liquids. It is noteworthy that the value of  $F$

for the glasses under investigation is significantly higher in comparison to the clinopyroxene based Di-CaTs glasses [133], which explain the cause of the difficulties met by us in preparing the En based glasses.

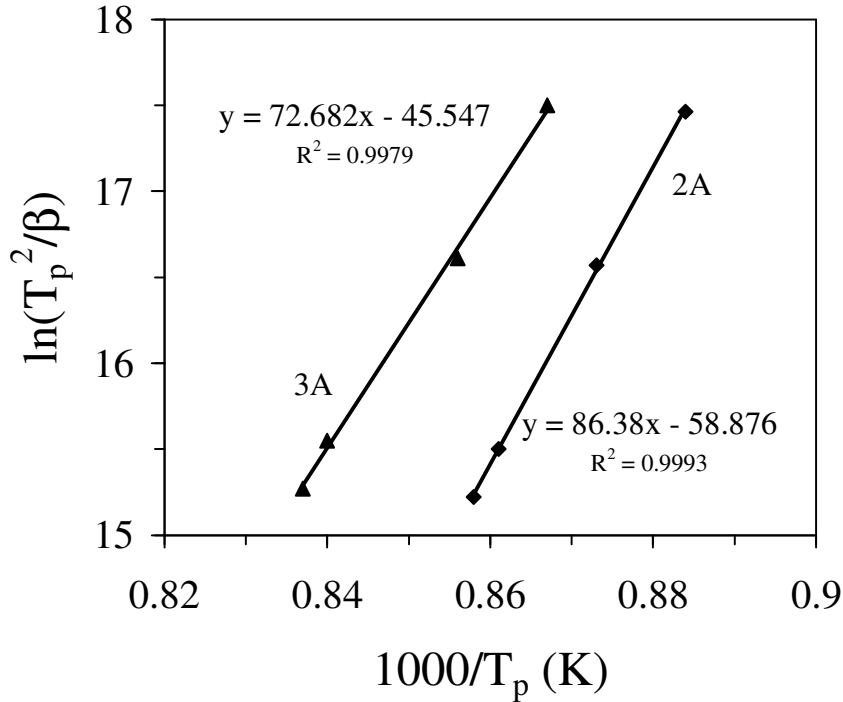


Fig. 4.9 Plot of activation energy for crystallization ( $E_c$ ) for glasses 2a and 3a.

The values of activation energy of crystallization ( $E_c$ ) and Avrami parameter,  $n$  for both the glasses are listed in Table 4.5 and presented in Fig. 4.9. The  $E_c$  value for glass 3a is considerably lower than glass 2a, while the value of  $n$  has been obtained to be near to 1 for both the glasses, which depicts the existence of surface crystallization in both the glasses. The lower  $E_c$  for glass 3a may be attributed to the presence of BaO, as this oxide tends to increase the crystalline volume fraction in silicate glasses. This is supported by the decrease in the area under the DTA crystallization curve for glass 3a in comparison to glass 2a at a particular heating rate (Table 4.4).

#### 4.1.6 Crystallization behaviour of glass powder compacts

In order to follow the crystalline phase assemblage in the resultant GCs at different temperatures (900 °C and 1000 °C, respectively), XRD data collected at room temperature (RT-XRD) from the sintered GCs is summarized in Table 4.6, along with the in-situ high

Table 4.6. Evolution of crystalline phases assemblages in the investigated glasses over increasing temperature, determined by the high temperature X-ray diffraction (HT-XRD) and room temperature X-ray diffraction (RT-XRD) analysis

(Note: The phases indicated are listed in the order of their decreasing intensities in the respective XRD spectra.)

| Glass |        | 800 °C                        | 900 °C         | 1000 °C        | 1100 °C       |
|-------|--------|-------------------------------|----------------|----------------|---------------|
| 2a    | HT-XRD | -                             | CE, OE         | CE, OE         | CE, OE, PE, K |
|       | RT-XRD | Amorphous with some CE and OE | CE, OE, Q      | CE, OE, Q      | -             |
| 2b    | HT-XRD | -                             | CE, OE         | CE, OE         | -             |
|       | RT-XRD | Amorphous with some CE        | CE, OE         | CE, OE         | -             |
| 3a    | HT-XRD | -                             | PE, Q          | PE, Q          | PE, Q         |
|       | RT-XRD | Amorphous                     | CE, PE, YS, K  | PE, YBSi, BaSi | -             |
| 3b    | HT-XRD | -                             | HC, CE, OE, PE | HC, CE, PE, OE | -             |
|       | RT-XRD | Amorphous with some CE and HC | HC, CE, OE, PE | HC, CE, PE, OE | -             |

CE, Clinoenstatite; OE, Orthoenstatite; PE, Protoenstatite ; Q, Quartz ; YS, Yttrium silicate; K, Keivyite; HC, Hexacelsian; YBSi, Yttrium oxide borate silicate; BaSi, Barium silicon oxide (For ICDD card nos. and chemical formulas of the respective phases, please refer to the text).

temperature XRD (HT-XRD) data. The schedule of the hot stage was as follows: Heating up to 600 °C with a rate of 10 K min<sup>-1</sup>, heating with a rate of 5 K min<sup>-1</sup> up to 900 °C, dwell for 30 min before recording the diffractogram, and then a similar ramp (5 Kmin<sup>-1</sup>) and dwell (30 min) for obtaining the diffractograms at 1000 °C and 1100 °C, respectively.

In order to be consistent with the work of Lee and Heuer [14], we have used the ICDD cards 00-019-0768 for OE and 00-011-273 for PE. ICDD card 00-035-0610 was used for CE instead of 00-019-0769 as the latter has been replaced by former in the new ICDD classification. It should be also mentioned that since the diffractograms of synthetic CE and OE are quite similar, we have considered the peak corresponding to  $2\theta = 29.999^\circ$  for securing the presence of CE.

According to the RT-XRD results, CE and OE crystallized out from glass 2a at 800 °C while quartz precipitated out as secondary phase after sintering at 900 °C and 1000 °C. Since, no peak for quartz was observed in HT-XRD results of glass 2a at 900 °C and 1000 °C; it can be assumed that the latter precipitated from liquid phase during cooling. According to HT-XRD results, CE and OE precipitated in composition 2a at 900 °C and 1000 °C (Table 4.6), however, the intensity of the peaks slightly increased at 1000 °C. With further increase in temperature to 1100 °C, PE and keivyite (designated as K;  $Y_2Si_2O_7$ , ICDD card: 00-038-0440,) precipitated out in the GC along with CE and OE. PE predominantly crystallized from the glass 3a at all the investigated temperatures, along with quartz (ICDD card 01-081-1665, marked as Q) as secondary phase. The intensity of the XRD peaks of PE and quartz were reduced at 1100 °C, likely due to dissolution effect in liquid phase.

Glass 3a was XRD amorphous after heat treatment at 800 °C, while PE and CE were the predominant phases after heat treatment at 900 °C along with yttrium silicate ( $Y_2Si_2O_7$ , ICDD card 00-045-0043, marked as YS) and keivyite as secondary phases. The conversion of PE to CE during cooling has been well documented in literature [14]. It is worth noting that YS is orthorhombic while K is monoclinic polymorph of  $Y_2Si_2O_7$ . A complex XRD pattern was obtained for GC 3a after heat treatment at 1000 °C. CE no more existed at this temperature and PE was the only predominant phase along with the presence of yttrium oxide borate silicate ( $Y_{9.73}Y_6((SiO_4)_{4.8}(BO_4)_{1.2})O_2$ , ICDD card 00-053-0055, marked as YBSi) and barium silicon oxide ( $Ba_2Si_2O_5$ , ICDD card 04-009-3348, marked as BaSi) as secondary phases. In addition to the crystalline phases identified, there were some unidentified XRD peaks in GCs 2a ( $2\theta = 31.68^\circ$ ) and 3a ( $2\theta = 27.93^\circ$  and  $30.88^\circ$ ) after heat treatment at 1000 °C. Assuming that no barium or boron containing phases were observed by HT- XRD analysis of composition 3a, precipitation of YBSi and BaSi may be suggested to occur from the liquid phase components and at the expense of CE.

The RT-XRD spectrum of composition 2b was highly amorphous after heat treatment at 800 °C, with the presence of very low intensity peaks attributed to CE. However, in accordance with the HT-XRD results, both CE and OE were registered at 900 °C and 1000 °C with no significant alterations in the peak intensities of the MgSiO<sub>3</sub>-polymorphs. In case of composition 3b, low intensity peaks for hexacelsian (ICDD: 01-088-1051, designated as HC) and CE registered among amorphous halo after heat treatment at 800 °C. However, with further increase in temperature to 900 °C, HC crystallized out extensively from the glassy matrix along with all the three MgSiO<sub>3</sub> polymorphs (CE, OE and PE), featuring peaks of less intensity (particularly PE). No major differences were observed in the XRD diffractograms of glass 3b after heat treatment at 1000 °C. These results are in agreement with data received from the HT-XRD analysis in which the same crystalline phase assemblage was registered.

From the technological application point of view, En based glasses/GCs are not suitable candidates for the job of sealing in SOFCs due to their low CTE. However, they can be potential candidates for the job of ceramic insulators and standoff resistors. Particularly, compositions 2b and 3b seem to be more promising as the GCs produced from these composition show good sintering ability and mechanical strength. Specially, the absence of metastable PE in GC 2b may be considered as an important step towards the prevention from aging of steatite ceramics and the increasing stability of the system during exploitation. The suggested Y-substitution for Mg in 2b causes stabilization of OE and CE while Al<sub>2</sub>O<sub>3</sub> affects the diffusion mechanism in the glass powder compacts resulting in well sintered MgSiO<sub>3</sub>-based GCs. However, further experimentation, especially electrical resistivity measurements, on these two GCs compositions is required in order to validate our claims.

.....

## 4.2 Diopside – Ca-Tschermak join

### 4.2.1 Designing of glass compositions

Di forms solid solution with CaTs with a general formula of  $\text{Ca}[\text{Mg}_{1-x}\text{Al}_x](\text{Si}_{1-x/2}\text{Al}_{x/2})_2\text{O}_6$ , where the square brackets and the parentheses denote the octahedral and the tetrahedral sublattices, respectively [35]. Cation substitution is governed by Tschermak's substitution, concisely represented by the scheme  $(\text{Si}^{4+}) + [\text{Mg}^{2+}] \leftrightarrow (\text{Al}^{3+}) + [\text{Al}^{3+}]$ . In this study, four novel glass compositions based on varying Di/CaTs mole ratio were investigated. The glass compositions have been labelled as DT1, DT1a, DT1b and DT1c. Table 4.7 presents their detailed scheme of substitutions, chemical composition and type of crucibles used to prepare the glasses. In brief, the composition DT1 comprised 80 mol.% Di and 20 mol.% CaTs. With regard to the design of this composition, it actually derives from Di if we substitute  $0.2 (\text{Si}^{4+} + \text{Mg}^{2+}) \leftrightarrow 0.4 \text{Al}^{3+}$ . Furthermore, in compositions DT1a, DT1b and DT1c, the Di/CaTs mole ratio was varied as described in Table 4.7. In order to enhance the potential applications of the produced GCs, and particularly towards the possibility of using the produced materials as SOFC-sealants we incorporated in the batches a small amount of NiO (1 wt.%), considering that NiO will favour the adhesion of the resultant GCs to metals. The experimental results aim to study the:

- (a) Influence of the above substitutions on the crystallization and the properties of the resultant GCs.
- (b) Threshold limit of CaTs solubility in Di and existence of solid solutions in Di-CaTs system leading to formation of mono-mineral GCs.
- (c) Structure and properties of glasses and resultant GCs in order to qualify them as potential candidates for further experimentation as sealants in SOFC.

### 4.2.2 Casting ability of glasses

For all the investigated compositions, melting at 1580 °C for 1 h was adequate to obtain bubble-free, transparent and amorphous (confirmed by XRD analysis) glasses with brown colour. The brown colour of the glasses was due to the presence of NiO [120, 121].

Table 4.7 Composition of Di-CaTs based glasses (wt. %)

| Label | Scheme of substitutions in accordance with diopside ( $\text{CaMgSi}_2\text{O}_6$ )                                                              | Type of crucible | MgO   | CaO   | $\text{SiO}_2$ | $\text{Al}_2\text{O}_3$ |
|-------|--------------------------------------------------------------------------------------------------------------------------------------------------|------------------|-------|-------|----------------|-------------------------|
| DT-1  | 80 mol.% $\text{CaMgSi}_2\text{O}_6$ – 20 mol.% $\text{CaAl}_2\text{SiO}_6$<br>( $\text{CaMg}_{0.8}\text{Al}_{0.4}\text{Si}_{1.8}\text{O}_6$ )   |                  | 14.87 | 25.86 | 49.87          | 9.40                    |
| DT-1a | 75 mol.% $\text{CaMgSi}_2\text{O}_6$ – 25 mol.% $\text{CaAl}_2\text{SiO}_6$<br>( $\text{CaMg}_{0.75}\text{Al}_{0.5}\text{Si}_{1.75}\text{O}_6$ ) | Alumina          | 13.93 | 25.85 | 48.47          | 11.75                   |
| DT-1b | 70 mol.% $\text{CaMgSi}_2\text{O}_6$ – 30 mol.% $\text{CaAl}_2\text{SiO}_6$<br>( $\text{CaMg}_{0.7}\text{Al}_{0.6}\text{Si}_{1.7}\text{O}_6$ )   |                  | 13.00 | 25.84 | 47.06          | 14.09                   |
| DT-1c | 65 mol.% $\text{CaMgSi}_2\text{O}_6$ – 35 mol.% $\text{CaAl}_2\text{SiO}_6$<br>( $\text{CaMg}_{0.65}\text{Al}_{0.6}\text{Si}_{1.65}\text{O}_6$ ) |                  | 12.07 | 25.83 | 45.66          | 16.44                   |

1 wt.% NiO was added to the batches

#### 4.2.3 Structure of glasses

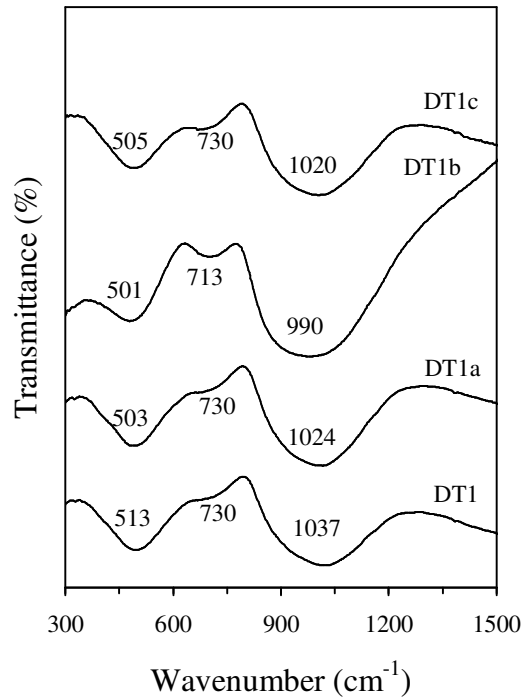


Fig. 4.10 FTIR spectra of Di-CaTs based glasses.

The influence of varying Di/CaTs ratio on the structure of glasses was studied by infrared spectroscopy. The room temperature FTIR transmittance spectra of four glasses (DT1, DT1a, DT1b and DT1c) are shown in Fig. 4.10. All spectra exhibit three broad transmittance bands in the region of 300-1300  $\text{cm}^{-1}$ . This lack of sharp features is indicative of the general disorder in the silicate network mainly due to a widely distribution of  $Q^n$  units occurring in these glasses. The broad bands in the 800-1300  $\text{cm}^{-1}$  are assigned to the stretching vibrations of the  $\text{SiO}_4$  tetrahedron with a different number of bridging oxygen atoms [122, 123]. For all the four glasses, this band is on 990-1040  $\text{cm}^{-1}$  indicating the distribution of  $Q^n$  units centred on  $Q^2$  and  $Q^3$  units. Al is known to create  $Q^3$  bands at the expense of  $Q^2$  and  $Q^4$  units in the silicate glasses [124]. In particular case with the change in Di/CaTs ratio from 80/20 to 70/30 this band shifted towards lower wave number while further increase in CaTs content at the expense of Di in composition DT1c (D/CaTs = 65/35) resulted in higher wave number (Fig. 4.10). The lowering of wave number in FTIR spectra with the increase in CaTs content up to 30 mol.% suggests that gradual occupancy of tetrahedral sites by Al resulted in depolymerization of the silicate glass network. The transmittance bands in the 300-650  $\text{cm}^{-1}$  region (Fig. 4.10) are due to bending vibrations of Si-O-Si and Si-O-Al linkages [122, 123]. This band is centred around 505-513  $\text{cm}^{-1}$  for all the four glasses and shifted to lower values when CaTs amount increases from 20 to 30 mol.%. However, a slight increase is revealed for glass DT1c when D/CaTs ratio is 65/35. The transmittance bands in the 650-800  $\text{cm}^{-1}$  region (centred at  $\sim 730 \text{ cm}^{-1}$ ) are related to the stretching vibrations of the Al-O bonds with  $\text{Al}^{3+}$  ions in four-fold coordination [123]. However, in glass DT1b, this band is very sharp and is centred at 713  $\text{cm}^{-1}$  seemingly indicating distinct structural arrangement in the Al-O bonds.

#### 4.2.4 Dilatometry

The values of  $T_{\text{dg}}$  and  $T_s$  were determined together with the CTE from the slope of the linear part of the curves (200-500  $^{\circ}\text{C}$ ). The results, presented in Table 4.8, indicate that both  $T_{\text{dg}}$  and  $T_s$  range within narrow temperature intervals (660-670  $^{\circ}\text{C}$  and 700-720  $^{\circ}\text{C}$ , respectively), but there is no evidence of systematic influence of Di/CaTs mole ratio on these values.

Table 4.8 Thermal properties of Di-CaTs based glasses

|                                      | DT1              | DT1a             | DT1b             | DT1c             |
|--------------------------------------|------------------|------------------|------------------|------------------|
| $\beta = 5 \text{ K min}^{-1}$       |                  |                  |                  |                  |
| $T_{dg}$ (°C)                        | 667              | 668              | 660              | 670              |
| $T_s$ (°C)                           | 710              | 715              | 700              | 720              |
| $CTE \times 10^6$ (K <sup>-1</sup> ) | 7.22             | 7.89             | 7.31             | 7.66             |
| $T_g$ (°C)                           | 747              | 727              | 729              | 739              |
| $T_c$ (°C)                           | 907              | 910              | 931              | 939              |
| $T_p$ (°C)                           | 926              | 940              | 947              | 956              |
| $\Delta T$ (K)                       | 160              | 183              | 202              | 200              |
| $E_{relax}$ (kJmol <sup>-1</sup> )   | 669              | 428              | 391              | 473              |
| $E_\eta$ (kJmol <sup>-1</sup> )      | 652              | 411              | 374              | 456              |
| F                                    | 33.40            | 21.47            | 19.48            | 24.42            |
| $E_c$ (kJmol <sup>-1</sup> )         | 439              | 493              | 444              | 473              |
| $n$                                  | $2.11 \pm 0.032$ | $2.11 \pm 0.019$ | $2.08 \pm 0.047$ | $1.96 \pm 0.112$ |

#### 4.2.5 Glass transition

Fig. 4.11 presents the typical DTA (Labsys, SETARAM, France) thermographs for all the four investigated compositions at  $\beta = 5 \text{ K min}^{-1}$ . The DTA plots of all the glasses feature two endothermic dips ( $T_{g1}$  and  $T_{g2}$ ) before the onset of crystallization ( $T_c$ ), indicating the existence of two glass transition temperatures, which is followed by an exothermic crystallization curve (Fig. 4.12). The existence of two  $T_g$  values suggests the possible occurrence of phase separation in the glasses. The SEM images of the glasses DT1a and DT1b shown in Fig. 4.13 reveal that some segregation has occurred, thus supporting our claim for phase separation. The existence of phase separation in Di based glasses has been well documented in literature [13, 82]. According to De Veckey *et al.* [134], in glasses located in the CaO-MgO-Al<sub>2</sub>O<sub>3</sub>-SiO<sub>2</sub> quaternary system, the phase separation is caused by the segregation of calcium and magnesium ions. Since, the glass

transition took place during its first  $T_g$ ,  $T_{g1}$  will be considered as the transition temperature in the following discussion of the present results.

The glass transition temperature  $T_g$  (Table 4.8) for all the glasses vary between 727– 747 °C for  $\beta = 5 \text{ K min}^{-1}$ . The value of  $T_g$  shifted towards higher side with the increase in heating rate for all the glasses and is highest for the glass DT1. This may be attributed to the stronger connectivity in the glass network structure as is evident from the FTIR spectra (Fig. 4.10). Further, it diminished sharply with the initial decrease in Di/CaTs ratio from 80/20 (DT1) to 75/25 (DT1a). The values of  $T_g$  for glasses DT1a and DT1b are almost similar. However,  $T_g$  increases for glass DT1c most probably due to the increasing connectivity in the glass structure. The activation energy for the structural relaxation ( $E_{\text{relax}}$ ) of the glass occurring around the glass transition was calculated by using the equation (4.3) [127, 135]:

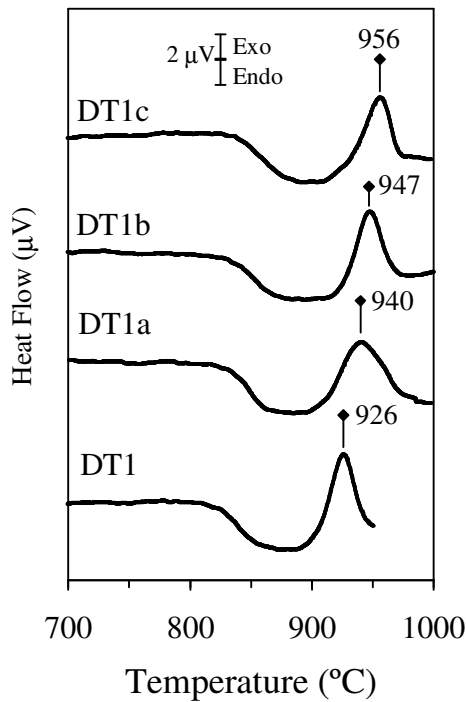


Fig. 4.11 DTA thermographs of Di-CaTs glasses at  $\beta = 5 \text{ K min}^{-1}$ .

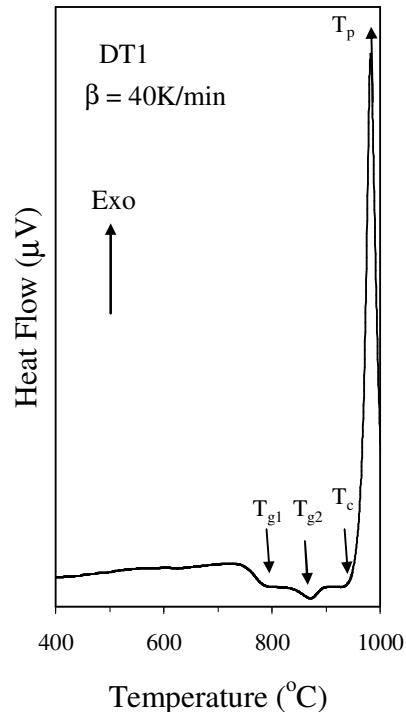


Fig. 4.12 DTA thermograph of glass DT1 at  $\beta = 40 \text{ K min}^{-1}$ .

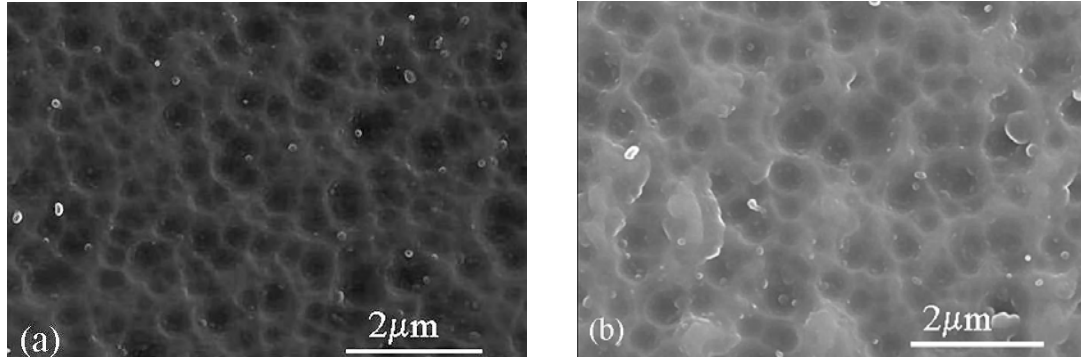


Fig. 4.13 SEM image of glasses (a) DT1a and (b) DT1b (revealed after chemical etching of polished glass surfaces by 2 vol.% HF for 10 s).

$$\ln \beta = \frac{-E_{relax}}{RT_g} \quad (4.3)$$

while the activation energy for viscous flow,  $E_\eta$  was calculated from equation (4.1). It is evident from Fig. 4.14 and Table 4.8 that both the calculated activation energies are in good agreement with each other and the highest values of  $E_{relax}$  and  $E_\eta$  have been obtained for glass DT1, while the lowest were obtained for glass DT1b. The  $E_{relax}$  and  $E_\eta$  decrease with decreasing the Di/CaTs ratio from Di/CaTs = 80/20 until Di/CaTs = 70/30.  $E_{relax}$  and  $E_\eta$  increase with further decreasing this ratio to Di/CaTs = 65/35 (DT1c). It has already been reported that both  $E_{relax}$  and  $E_\eta$  are responsible for the molecular motion and rearrangement of the atoms around  $T_g$  and the glass with lowest activation energy values is the most stable one [128, 136].

From the point of view of technological applications, the glass should be thermally stable. This thermal stability of glasses has been ascertained on the basis of thermal analysis using DTA. Usually, unstable glasses show crystallization peak close to the glass transition temperature. Therefore, difference between onset temperature of crystallization,  $T_c$  and glass transition temperature,  $T_g$  i.e.  $\Delta T = T_c - T_g$  is a good indication of thermal stability because the higher the value of this difference, more will be the delay in the nucleation process [137]. Table 4.8 presents the values of  $\Delta T$  for all the four investigated compositions at  $\beta = 5 \text{ K min}^{-1}$  and the highest value of  $\Delta T$  has been calculated for Di/CaTs = 70/30 (DT1b).

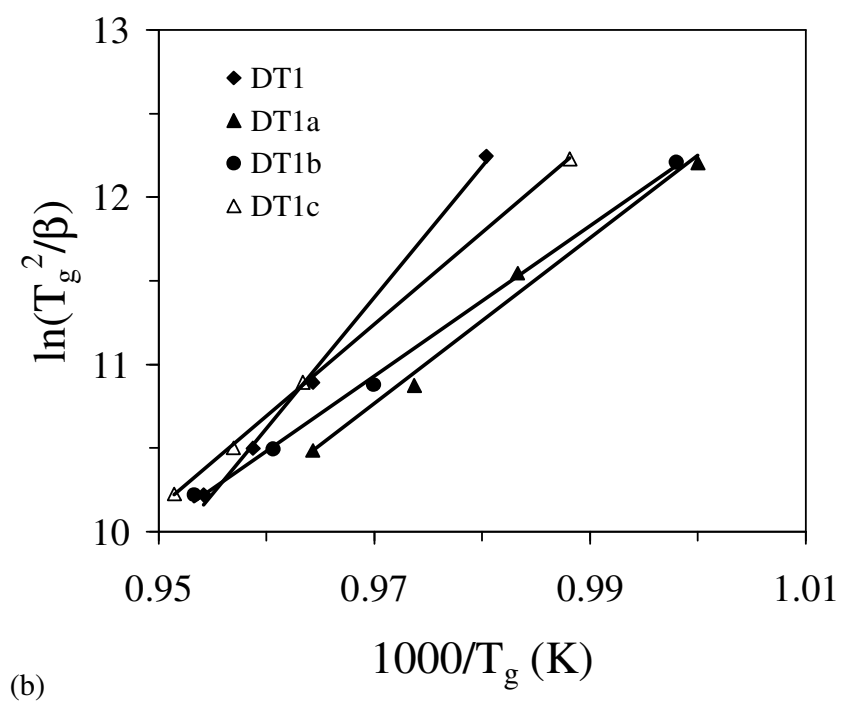
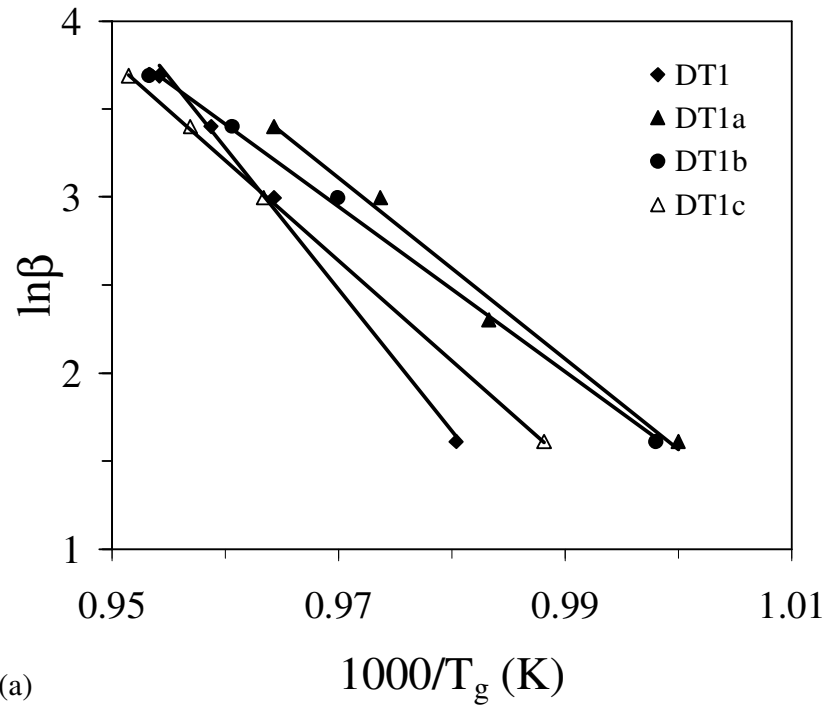


Fig. 4.14. Plot for determination of activation energy for (a) structural relaxation ( $E_{relax.}$ ) (b) viscous flow ( $E_{\square}$ ) for the investigated glasses.

The kinetic fragility index ( $F$ ) of all the four glasses was calculated using eq. 4.2. The values of  $F$  for all the glasses are listed in Table 4.8 at  $\beta = 5 \text{ K min}^{-1}$ . Since all these values of  $F$  are within the above mentioned limit, it is reasonable to state that all the glasses are obtained from strong glass forming liquids. However, the value of  $F$  is maximum for glass DT1 and minimum for glass DT1b, confirming higher thermal stability of the latter.

#### 4.2.6 Crystallization kinetics by DTA

The DTA plots of all the four glasses exhibit single exothermic effects at all the heating rates which shifted towards higher temperatures with increase in heating rate. This signifies that the GC is formed either as a result of single phase crystallization or of an almost simultaneous precipitation of different crystalline phases. The value of  $T_p$  increases from Di/CaTs = 80/20 (DT1) to Di/CaTs = 65/35 (DT1c) as presented in Table 4.8. The values of  $E_c$  and  $n$  for all the four glasses are listed in Table 4.8 and Fig. 4.15. The value of the kinetic exponent, so called, Avrami parameter for all the glasses suggests that the crystallization did not occur on the fixed number of nuclei and with the increase in CaTs content, the tendency for surface crystallization increases. It is also important to note that complications appear with systems where  $n$  is a non-integer value and the deviation from the integer value of the Avrami exponent might originate from impurities influencing crystal growth and the simultaneous appearance of different growth mechanisms as well as from the density of the growing phases [138].

In order to visualize the effects of crystallization mechanism in the bulk glasses, bulk annealed glass DT1 was heat treated at 900 °C and 1000 °C for 1 h at heating rate of 5 K min<sup>-1</sup> in a box furnace. Fig. 4.16 shows the SEM images of the fractured GCs. Augite crystals can be seen in Fig. 4.16a while Fig. 4.16b shows that the crystallization initiates from the edge or surface of the glass. These results are in accordance with the study of Branda *et al.* [40], according to whom, crystallization mechanism in diopside glass shifts from surface to bulk nucleation with the decrease in the particle size. However, considering that in the present investigation we are not dealing with stoichiometric diopside glass, such a deviation from  $\langle n \rangle = 3$  to  $\langle n \rangle = 2$  in the powdered glasses is expected due to the influence of CaTs content. Moreover, the glass powders in present study have much lower particle size in comparison to those studied by Branda *et al.* [40], which will further alter the crystallization mechanism in the glasses.

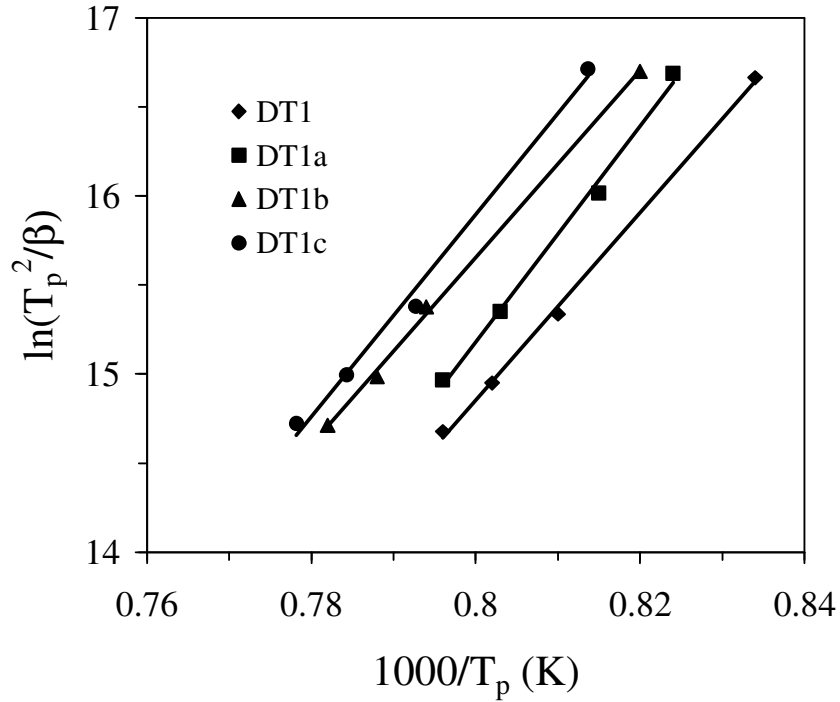


Fig. 4.15 Plot for activation energy of crystallization of Di-CaTs glasses.

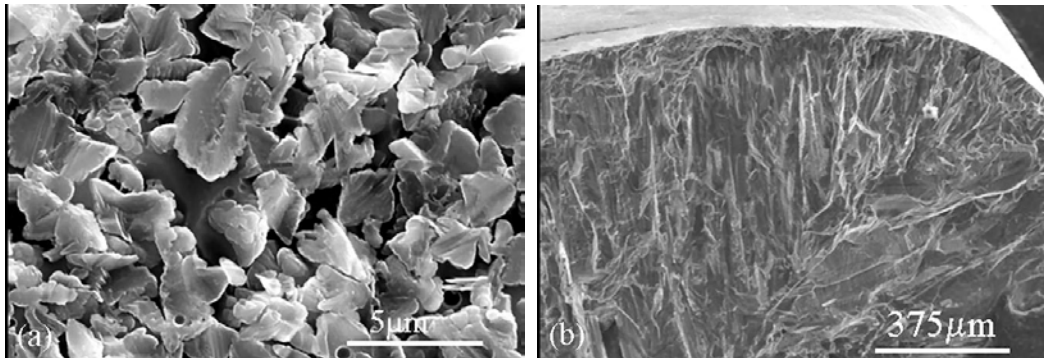


Fig. 4.16 SEM images (revealed after chemical etching with 2 vol.% HF for 20 s) of bulk glasses (fractured) heat treated at (a) 900 °C, (b) 1000 °C for 1 h, respectively.

#### 4.2.7 Crystallization behaviour of glass-powder compacts

##### 4.2.7.1 Non-isothermal conditions, 850-1000 °C (1 h)

The evolution of crystalline regime of the GPCs over increasing temperature (always for 1 h) is demonstrated in the X-ray diffractograms of Fig. 4.17, while characteristic microstructures (observed by SEM) are shown in Fig. 4.18. There were evidences of crystallization in the bars of DT1a (Fig. 4.17b), DT1b (Fig. 4.17c), and DT1c (Fig. 4.17d)

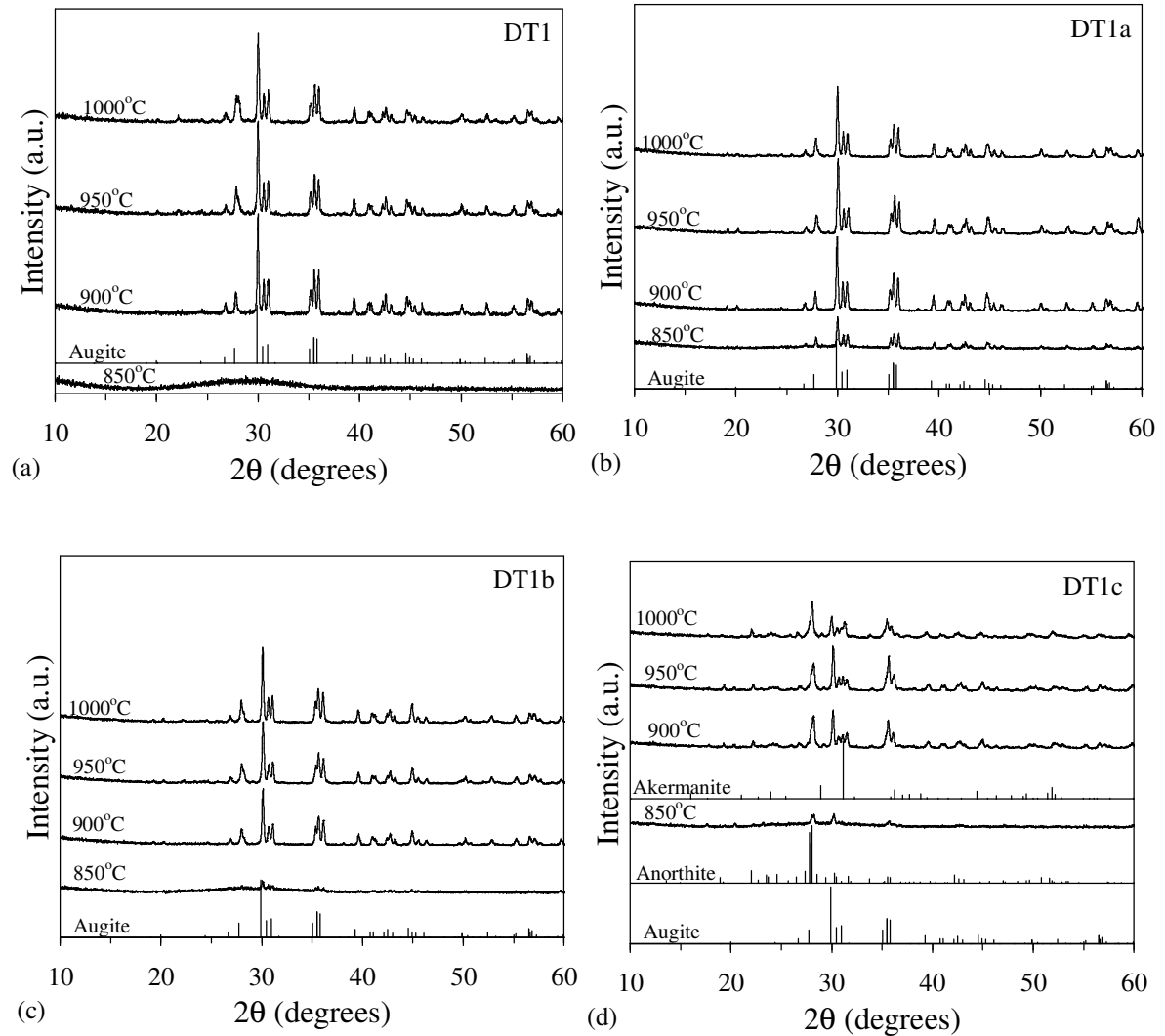


Fig. 4.17 XRD diffractograms of glass powder compacts of compositions (a) DT1, (b) DT1a, (c) DT1b, (d) DT1c, sintered at different temperatures in temperature range 850 - 1000 °C, for 1 h, respectively. XRD spectra have not been normalised. Full scale intensity: 5000cps.

compositions sintered at 850 °C, whereas DT1 samples remained amorphous at the same temperature (Fig. 4.17a). Augite (ICDD card: 01-078-1392,  $\text{CaMg}_{0.70}\text{Al}_{0.30}\text{Si}_{1.70}\text{Al}_{0.30}\text{O}_6$ ) was identified in DT1a and DT1b. Devitrification was seemingly more intensive in the case of DT1a, enough to have an impact on the microstructure where first crystals embedded in the glassy matrix can be observed (Fig. 4.18a). In the composition DT1c

calcium plagioclase anorthite (ICDD card 00-041-1486,  $\text{CaAl}_2\text{Si}_2\text{O}_8$ ) was also registered. Heat treating at higher temperatures 900-1000 °C significantly improved the crystallinity in all investigated compositions concluded from the increasing intensity of the XRD peaks (Fig. 4.17). Monomineral GCs composed exclusively of augite were obtained for the case of DT1, DT1a, and DT1b evidencing solubility of CaTs molecule in the structure of Di and formation of Di-CaTs solid solutions. Microstructure of GCs DT1a, and DT1b (Fig 4.18b, c, d) resembles the microstructure of GC DT1 where the oval shaped crystals of augite phase (2-3  $\mu\text{m}$  in length) are closely bordering each other. From the inserted images in the Fig.4.18(c and d) the finer augite crystals (less than 1  $\mu\text{m}$  in length) can be observed in the inner part of the GCs.

Augite is the most widespread member of pyroxenes and represents a group of closely related minerals with chemical formula of  $\text{Ca}(\text{Mg,Fe,Al})(\text{SiAl})\text{O}_6$ , identical in structure, but containing different percentages of certain elements [84]. In the light of the experimental results of the present study, augite (that was obviously Fe-free) seemingly acts as an intermediary member between Di and CaTs, representing a mineral midway between these two minerals along this series, where  $\text{Al}^{3+}$  occupies both octahedral ( $\text{AlO}_6$ ) and tetrahedral ( $\text{AlO}_4$ ) positions in the structure.

The above mentioned ICDD card 01-078-1392, which had the most precise fitting to the diffractograms of Fig. 4.17, corresponds to augite crystallized in monoclinic structure with lattice parameters  $a=9.717$  nm,  $b=8.882$  nm,  $c=5.266$  nm, and  $\beta=106.16^\circ$  (ICDD: 01-078-1392). However, there is also another ICDD card of augite (01-078-1391) whose formula,  $\text{Ca}(\text{Mg}_{0.85}\text{Al}_{0.15})(\text{Si}_{1.70}\text{Al}_{0.30})\text{O}_6$ , corresponds to 22.5 mol.% CaTs dissolved in Di, which matches fairly well to the Di/CaTs solid solutions of the parent glasses of the present study. Since the differences between the patterns of the two ICDD cards are very small, therefore, only one ICDD card 01-078-1392 has been used in XRD diffractograms. However, to investigate the distribution of aluminium in the tetrahedral and octahedral sublattices of Di/CaTs solid solutions, other experimental techniques (e.g. Mossbauer, MAS NMR, etc.), or statistical-thermodynamic models need to be applied.

The above experimental results (obtained by studying glass crystallization between 850 °C and 1000 °C for 1 h) suggest a solubility limit of CaTs in Di at about 30 mol.% CaTs. This limit was justified by the behaviour of the glass DT1c (i.e. Di/CaTs=65/35) in

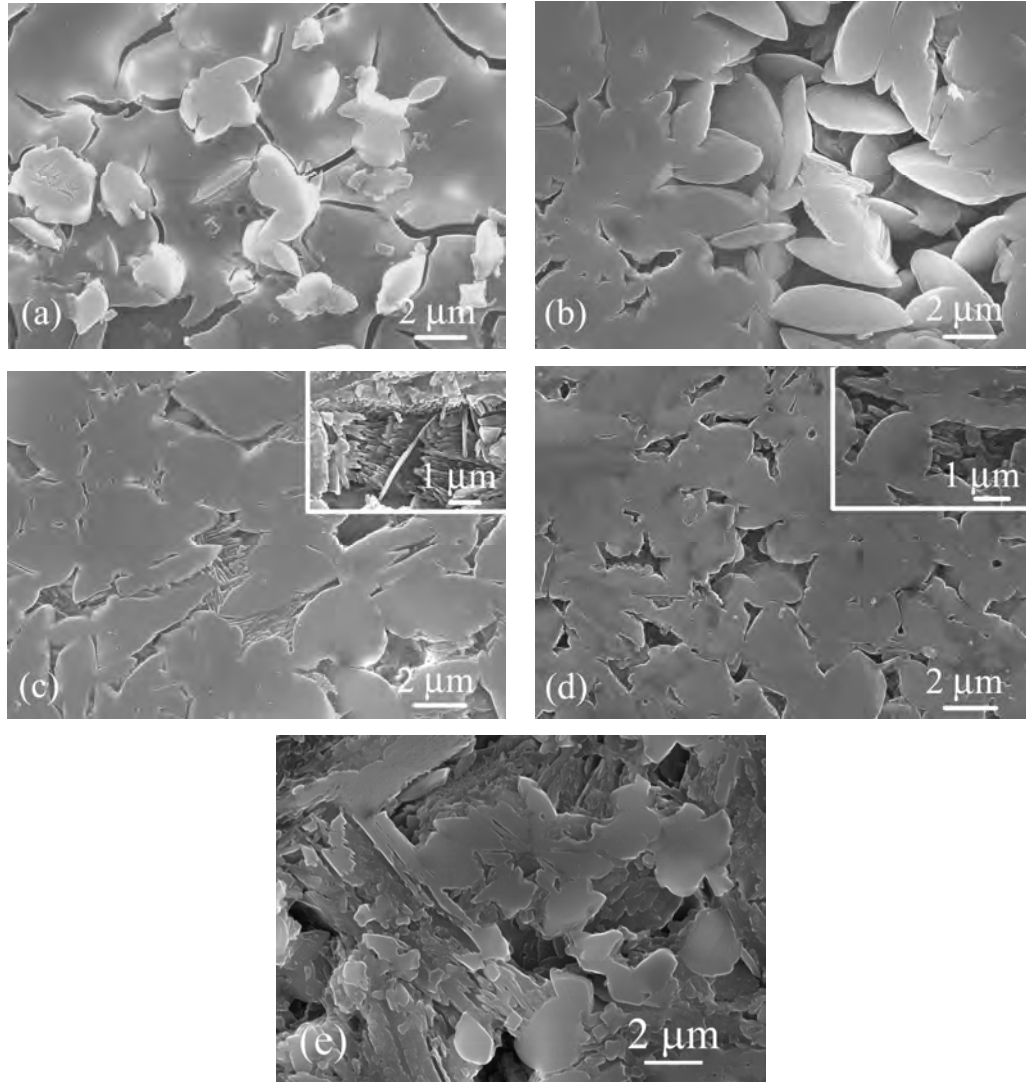


Fig. 4.18 Microstructure (revealed after chemical etching of polished surfaces with HF solution) of the GCs DT1a heat treated at (a) 850 °C, (b) 900 °C, and (c) 950 °C; DT1b at 950 °C (d) and DT1c at 900 °C (e).

which anorthite and akermanite (designated as Ak, ICDD card 00-035-592  $\text{Ca}_2\text{MgSi}_2\text{O}_7$ ) precipitated along with augite, at temperatures 850 °C and 900 °C respectively. The SEM image of GC DT1c (Fig.4.18e) is noticeably different from those of GCs DT1, DT1a, and DT1b: apart from augite, prismatic blade shaped crystals, a typical characteristic of anorthite phase are presented. It is noteworthy that the range of Di/CaTs solid solutions is more spread in the natural Si-poor pyroxene rocks that can contain even 50 mol.% CaTs

[35]. Continuous Di-CaTs solid solutions have been obtained when glass crystallization was achieved by applying pressure of 2 GPa at 1400 °C for 24 h [35].

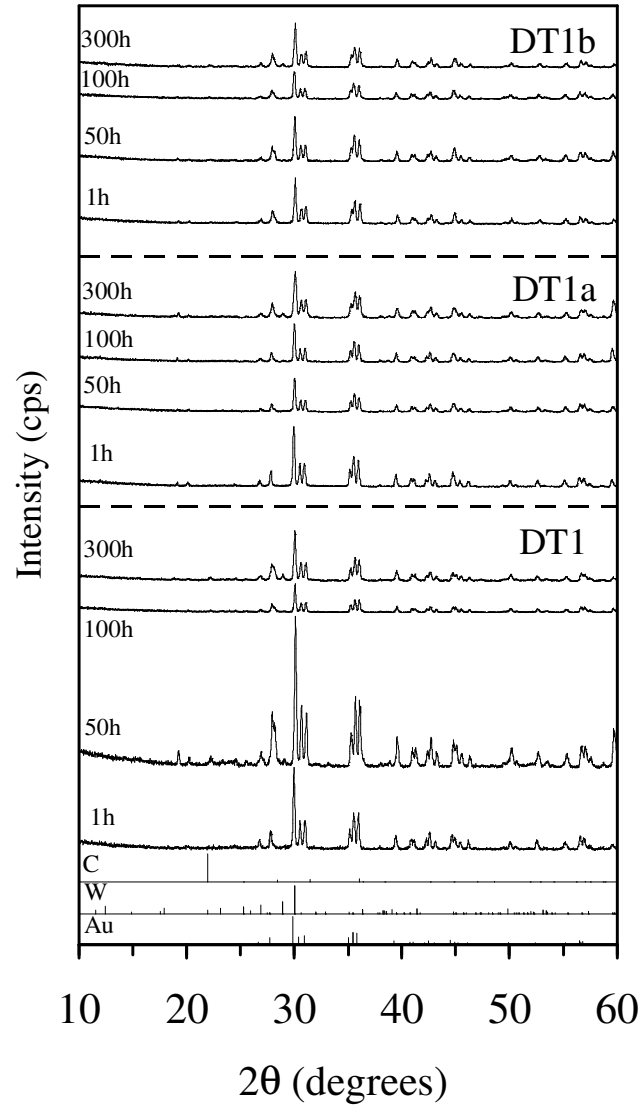


Fig. 4.19 X-ray diffractograms of glass-powder compacts of DT1, DT1a, and DT1b, after heat treatment at 900 °C for 1 h, 50 h, 100 h, and 300 h. (Au: Augite ICDD card 01-078-1392; W: Wollastonite 00-042-0550; C: Cristobalite 00-039-1425. The spectra have not been normalized. Full scale of intensity axes 15000 cps).

#### 4.2.7.2 Isothermal conditions, 900 °C (1 -300 h)

The stability of crystalline regime of the monomineral GCs DT1, DT1a, and DT1b, under prolong isothermal heat treatment at 900 °C (that is about 100 °C higher than the operation temperature of SOFC) for 50 h, 100 h, and 300 h, is demonstrated in X-ray diffractograms of Fig. 4.19. Comparison of the intensity of the peaks suggest that exposure of the samples beyond 50 h at 900 °C causes a decay of their crystallinity, which is striking in DT1, less pronounce in DT1b, and negligible in DT1a. Augite, which probably dissolves in the glassy phase, seemingly re-crystallizes after 300 h, since the intensity of peaks increase. Careful observation of diffractograms may suggest evidence of partial destabilization of augite since low intensity peaks of cristobalite after 100 h for DT1 and DT1b, and wollastonite (designated as W, ICDD card 00-042-0550  $\text{CaSiO}_3$ ) after 300 h for all compositions were developed.

### 4.2.8 Properties of glass-ceramics

#### 4.2.8.1 Shrinkage, density, and bending strength

Sintering generally starts at temperatures slightly higher than  $T_g$  and occurs due to viscous flow, which instigates coalescence of powder and removes the pores from the bulk of materials. In the case of the four investigated compositions (Table 4.7), the GPCs resulted in mostly amorphous (Fig. 4.17) but highly dense sintered samples of dark brown colour after heat treatment at 850 °C. Sintering preceded crystallization (Fig. 4.17) suggesting that densification was complete at 900 °C, where the investigated samples exhibited white colour. The values of linear shrinkage, density, and bending strength of GPCs sintered at different temperatures for 1 h, summarized in Table 4.9, support fairly well the above suggested stages, occurring over increasing temperature. Further increase of temperature up to 950 °C or 1000 °C had negligible influence on density, but shrinkage showed a tendency to decrease.

A general trend of decreasing the values of density and bending strength with increasing the amount of CaTs can be suggested. The high crystallinity of GC DT1 (Fig. 4.17) that correlates with its respectively low  $E_c$  value should be responsible for the best mechanical performance along the heat treatment at 900-1000 °C for 1 h. Furthermore, the results of Table 4.9 underline the importance of producing monomineral GCs. The

properties of DT1c GCs were significantly poorer than all the other monomineral investigated GCs. The simultaneous presence of 3 crystalline phases in DT1c GCs (An, augite, akermanite, Fig. 4.17) anticipates a detrimental impact (with regard to the structural integrity of GC) of the mismatch of CTE of each phase during cooling.

Table 4.9 Values of properties of the GCs produced from GPCs after heat treatment at different temperatures for 1 h.

| Composition                        | 850 °C         | 900 °C         | 950 °C         | 1000 °C        |
|------------------------------------|----------------|----------------|----------------|----------------|
| <i>Shrinkage (%)</i>               |                |                |                |                |
| DT1                                | 15.20 ± 0.31   | 15.88 ± 0.39   | 15.90 ± 0.90   | 15.74 ± 0.16   |
| DT1a                               | 15.92 ± 0.27   | 16.37 ± 0.13   | 16.12 ± 0.45   | 16.18 ± 0.05   |
| DT1b                               | 15.86 ± 0.22   | 16.29 ± 0.06   | 16.18 ± 0.38   | 15.67 ± 0.08   |
| DT1c                               | 15.22 ± 0.57   | 16.20 ± 0.37   | 15.61 ± 0.19   | 16.03 ± 0.08   |
| <i>Density (g cm<sup>-3</sup>)</i> |                |                |                |                |
| DT1                                | 2.80 ± 0.01    | 2.96 ± 0.01    | 2.95 ± 0.01    | 2.94 ± 0.01    |
| DT1a                               | 2.91 ± 0.01    | 2.94 ± 0.01    | 2.94 ± 0.01    | 2.94 ± 0.01    |
| DT1b                               | 2.86 ± 0.01    | 2.94 ± 0.01    | 2.93 ± 0.01    | 2.93 ± 0.01    |
| DT1c                               | 2.85 ± 0.01    | 2.86 ± 0.01    | 2.86 ± 0.01    | 2.86 ± 0.01    |
| <i>Bending strength (MPa)</i>      |                |                |                |                |
| DT1                                | 90.56 ± 16.77  | 189.06 ± 10.28 | 165.30 ± 17.13 | 165.18 ± 2.90  |
| DT1a                               | 77.34 ± 7.84   | 170.01 ± 18.49 | 154.65 ± 17.53 | 158.24 ± 12.20 |
| DT1b                               | 91.77 ± 26.77  | 137.97 ± 19.45 | 126.69 ± 14.16 | 155.45 ± 7.64  |
| DT1c                               | 105.13 ± 20.97 | 69.92 ± 6.37   | 51.78 ± 5.24   | 113.40 ± 8.40  |

#### 4.2.8.2 Adherence to zirconia (8YSZ)

The good matching of the CTE values (200-700 °C) between the GCs and cubic zirconia, calculated from the slope of these lines (not shown) and presented in Table 4.10, qualify the GCs DT1, DT1a and DT1b for further experimentation as candidate SOFC sealant materials. However, as has been observed with other GCs applied for sealing SOFC, prolong isothermal heat treatment at 900 °C for 300 h caused a decrease of CTE

values, as shown in Table 4.10 (except DT1c). In the present study, this reduction can be attributed to the above suggested dissolution-recrystallization processes (Fig. 4.19).

A characteristic microstructure of the interface formed between 8YSZ pellet and glass-powder DT1b after heat treatment at 900 °C for 100 h in air is shown in Fig. 4.20. Similar interfaces were observed with the glasses DT1 and DT1a. The good matching of CTE of 8YSZ and DT1b resulted in a generally continuous interface with no cracks or gaps. There is no evidence of formation of a reaction zone at the interface which if existed should be quite wide due to the long heat treatment.

Table 4.10 Thermal expansion coefficients ( $CTE \times 10^6 \text{ K}^{-1}$ ) of the GCs produced under different conditions together with the CTE of yttria stabilized cubic zirconia (8YSZ), ( $\beta = 5 \text{ K min}^{-1}$ ).

| Composition | 950 °C, 1 h | 900 °C, 300 h |
|-------------|-------------|---------------|
| DT1         | 9.57        | 8.16          |
| DT1a        | 8.67        | 8.21          |
| DT1b        | 9.78        | 8.41          |
| DT1c        | 7.28        | 8.01          |
| 8YSZ        | 10.01       |               |

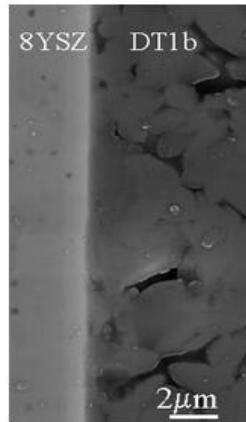


Fig. 4.20 SEM image of the interface between 8YSZ and GC DT1b.

The absence of reaction product between the glasses and zirconia was also confirmed by X-ray analysis of samples made of powder mixtures of glasses and 8YSZ similarly heat treated (i.e. 900 °C, 100 h), where only augite and 8YSZ (ICDD card 01-082-1245) were

identified. The above features, in conjunction with the fact of the prolong heat treatment, do not allow the presentation of a certain contact (wetting) angle value, but the *in situ* observed wetting angle generally indicated a good wetting regime (i.e.  $\theta < 90^\circ$ ).

.....

### **4.3 Influence of ZnO and BaO on the crystallization behaviour and properties of Di-CaTs based glasses**

#### ***4.3.1 Designing of compositions***

This part of work derives from the results obtained in *section 4.2*. The addition of BaO is known to increase CTE of the glasses and resultant GCs [98] while ZnO enhances sintering and crystallization processes over MgO and CaO in GCs, thus resulting into dense sintered GPCs and mechanically strong GCs [139]. Moreover, it has been observed that ZnO acts in a manner similar to B<sub>2</sub>O<sub>3</sub> with regard to the viscosity and thermal expansion. In a number of alkaline earth aluminosilicate glasses, addition of 10 mol.% ZnO decreased viscosity in the transition temperature range, lowering T<sub>g</sub> by around 50 °C while at the same time slightly increasing the CTE [140, 141]. Also, unlike B<sub>2</sub>O<sub>3</sub>, ZnO remains stable in wet H<sub>2</sub> conditions and does not form any volatile compounds [142]. Therefore, in order to tailor the properties of Di-CaTs based GCs for their suitability as sealants in SOFC, two series of glasses were synthesized with theoretical partial substitution of ZnO for MgO and BaO for CaO in glass composition corresponding to 80 mol.% Di – 20 mol.% CaTs, as described in [Table 4.11](#) and [Table 4.12](#), respectively. In order to be consistent with the studies described in *section 4.2* and to enhance the potential application of resultant glasses for sealing applications in SOFC, 1 wt.% NiO was added to all the glass batches.

#### ***4.3.2 Casting ability of glasses***

For all the investigated compositions ([Table 4.11](#) and [Table 4.12](#)), melting at 1580 °C for 1 h was adequate to obtain bubble-free, transparent glasses with brown colour. The brown colour of the glasses was due to the presence of NiO [120, 121].

Table 4.11 Composition of ZnO-containing Di-CaTs based glasses (wt. %)

| Label                                                                                                                                          | Scheme of substitutions in accordance with parent glass composition                                                                          | Type of crucible | MgO   | CaO   | ZnO  | SiO <sub>2</sub> | Al <sub>2</sub> O <sub>3</sub> |
|------------------------------------------------------------------------------------------------------------------------------------------------|----------------------------------------------------------------------------------------------------------------------------------------------|------------------|-------|-------|------|------------------|--------------------------------|
| <i>Parent glass composition: 80 mol.% Diopside (CaMgSi<sub>2</sub>O<sub>6</sub>) – 20 mol.% Ca-Tschermak (CaAl<sub>2</sub>SiO<sub>6</sub>)</i> |                                                                                                                                              |                  |       |       |      |                  |                                |
| DT                                                                                                                                             | 80 mol.% Diopside – 20 mol.% Ca-Tschermak<br>(CaMg <sub>0.8</sub> Al <sub>0.4</sub> Si <sub>1.8</sub> O <sub>6</sub> )                       |                  | 14.87 | 25.86 | –    | 49.87            | 9.40                           |
| DT-Zn1                                                                                                                                         | 0.05Mg <sup>2+</sup> ↔ 0.05Zn <sup>2+</sup><br>(CaMg <sub>0.75</sub> Zn <sub>0.05</sub> Al <sub>0.4</sub> Si <sub>1.8</sub> O <sub>6</sub> ) | Pt               | 13.81 | 25.62 | 1.86 | 49.40            | 9.31                           |
| DT-Zn2                                                                                                                                         | 0.1Mg <sup>2+</sup> ↔ 0.1Zn <sup>2+</sup><br>(CaMg <sub>0.7</sub> Zn <sub>0.1</sub> Al <sub>0.4</sub> Si <sub>1.8</sub> O <sub>6</sub> )     |                  | 12.77 | 25.38 | 3.68 | 48.94            | 9.23                           |
| DT-Zn3                                                                                                                                         | 0.2Mg <sup>2+</sup> ↔ 0.2Zn <sup>2+</sup><br>(CaMg <sub>0.6</sub> Zn <sub>0.2</sub> Al <sub>0.4</sub> Si <sub>1.8</sub> O <sub>6</sub> )     |                  | 10.74 | 24.91 | 7.23 | 48.05            | 9.06                           |

1 wt.% NiO was added to all the glasses.

Table 4.12 Composition of BaO-containing Di-CaTs based glasses (wt. %)

| Label                                                                                                                                          | Scheme of substitutions in accordance with parent glass composition                                                                                                                                                  | Type of crucible | MgO   | CaO   | BaO   | SiO <sub>2</sub> | B <sub>2</sub> O <sub>3</sub> | Al <sub>2</sub> O <sub>3</sub> |
|------------------------------------------------------------------------------------------------------------------------------------------------|----------------------------------------------------------------------------------------------------------------------------------------------------------------------------------------------------------------------|------------------|-------|-------|-------|------------------|-------------------------------|--------------------------------|
| <i>Parent glass composition: 80 mol.% Diopside (CaMgSi<sub>2</sub>O<sub>6</sub>) – 20 mol.% Ca-Tschermak (CaAl<sub>2</sub>SiO<sub>6</sub>)</i> |                                                                                                                                                                                                                      |                  |       |       |       |                  |                               |                                |
| BaCMAS1                                                                                                                                        | 0.05Ca <sup>2+</sup> ↔ 0.05Ba <sup>2+</sup><br>(Ca <sub>0.95</sub> Ba <sub>0.05</sub> Mg <sub>0.8</sub> Al <sub>0.4</sub> Si <sub>1.8</sub> O <sub>6</sub> )                                                         | Pt               | 14.54 | 24.03 | 3.46  | 48.78            | -                             | 9.20                           |
| BaCMAS2                                                                                                                                        | 0.1Ca <sup>2+</sup> ↔ 0.1Ba <sup>2+</sup><br>(Ca <sub>0.9</sub> Ba <sub>0.1</sub> Mg <sub>0.8</sub> Al <sub>0.4</sub> Si <sub>1.8</sub> O <sub>6</sub> )                                                             |                  | 14.23 | 22.27 | 6.77  | 47.73            | -                             | 9.00                           |
| BaCMAS3                                                                                                                                        | 0.2Ca <sup>2+</sup> ↔ 0.2Ba <sup>2+</sup><br>(Ca <sub>0.8</sub> Ba <sub>0.2</sub> Mg <sub>0.8</sub> Al <sub>0.4</sub> Si <sub>1.8</sub> O <sub>6</sub> )                                                             |                  | 13.64 | 18.98 | 12.98 | 45.76            | -                             | 8.63                           |
| BaCMAS4                                                                                                                                        | 0.2Ca <sup>2+</sup> + 0.2Al <sup>3+</sup> ↔ 0.2Ba <sup>2+</sup> + 0.2B <sup>3+</sup><br>(Ca <sub>0.8</sub> Ba <sub>0.2</sub> Mg <sub>0.8</sub> Al <sub>0.2</sub> B <sub>0.2</sub> Si <sub>1.8</sub> O <sub>6</sub> ) |                  | 13.83 | 19.24 | 13.15 | 46.40            | 2.98                          | 4.37                           |

1 wt.% NiO was added to all the glasses.

### 4.3.3 Density of glasses

The values of apparent density for BaO- and ZnO-containing glasses are presented in [Table 4.13](#).

#### 4.3.3.1 ZnO-containing glasses

The experimental results showed that substitution of MgO by ZnO caused an increase in the density of the glasses due to the higher density of ZnO ( $5.6 \text{ g cm}^{-3}$ ) with respect to MgO ( $3.6 \text{ g cm}^{-3}$ ). The molar volume ( $V_m$ ) and excess volume ( $V_e$ ) for all the investigated glasses was calculated using eq. 3.1 and 3.2, respectively. The highest value of  $V_m$  was obtained for glass DT-Zn1 and the lowest for glass DT-Zn2. The highest value of  $V_e$  was calculated for glasses DT and DT-Zn1, while a significant decrease of  $V_e$  was observed with further addition of ZnO. An initial increase in the value of  $V_m$  and a constant value of  $V_e$ , with the addition of ZnO indicates that the topology of the network does not significantly change with the change in glass composition [143, 144]. However, decrease in the value of  $V_m$  along with a considerable decrease in the value of  $V_e$  for glass DT-Zn2 indicates towards increasing ionic character in the glasses, thus leading to a collapse of structural skeleton.

#### 4.3.3.2 BaO-containing glasses

The experimental results showed an increase in the apparent density of the glasses with increasing BaO contents because BaO has higher density ( $\rho = 5.72 \text{ g cm}^{-3}$ ) than CaO ( $\rho = 3.34 \text{ g cm}^{-3}$ ) ([Table 4.13](#)). The decrease in density of glass BaCMAS4 is because  $\text{Al}_2\text{O}_3$  ( $\rho = 3.98 \text{ g cm}^{-3}$ ) has been substituted by  $\text{B}_2\text{O}_3$  ( $\rho = 2.55 \text{ g cm}^{-3}$ ). The higher value of  $V_m$  for BaO-containing glasses in comparison to parent glass (DT) and ZnO-containing Di-CaTs glasses may be explained on the basis of higher ionic radii (and lower field strength) of the  $\text{Ba}^{2+}$  compared to  $\text{Ca}^{2+}$  and  $\text{Zn}^{2+}$ . As a result of higher  $V_m$ , the  $V_e$  for BaO-containing glasses is higher than BaO-free and ZnO containing glasses. The decrease in  $V_e$  with increase in BaO content may be attributed to the collapse of the glass structural skeleton into a closer packing, thus, decreasing the excess volume of the glass [145]. However, the value of  $V_e$  for glass BaCMAS4 is higher in comparison to glass BaCMAS3 which can be explained on the basis of increasing covalent nature of the glass structure with addition of  $\text{B}_2\text{O}_3$ .

Table 4.13 Properties of glasses

|                                            | DT            | DT-Zn1        | DT-Zn2        | DT-Zn3        | BaCMAS1      | BaCMAS2      | BaCMAS3      | BaCMAS4      |
|--------------------------------------------|---------------|---------------|---------------|---------------|--------------|--------------|--------------|--------------|
| $\rho$ (g cm <sup>-3</sup> )               | 2.90 ± 0.001  | 2.92 ± 0.007  | 2.99 ± 0.007  | 3.02 ± 0.008  | 2.90 ± 0.007 | 2.94 ± 0.003 | 3.03 ± 0.001 | 3.01 ± 0.002 |
| $V_m$ (cm <sup>3</sup> mol <sup>-1</sup> ) | 19.70 ± 0.004 | 19.75 ± 0.051 | 19.50 ± 0.047 | 19.64 ± 0.050 | 20.16 ± 0.04 | 20.31 ± 0.03 | 20.33 ± 0.01 | 20.40 ± 0.01 |
| $V_e$ (cm <sup>3</sup> mol <sup>-1</sup> ) | 0.40 ± 0.004  | 0.40 ± 0.051  | 0.11 ± 0.047  | 0.16 ± 0.050  | 0.82 ± 0.04  | 0.75 ± 0.03  | 0.51 ± 0.01  | 0.54 ± 0.01  |
| $\beta = 5 \text{ K min}^{-1}$             |               |               |               |               |              |              |              |              |
| $T_{dg}$ (°C)                              | -             | -             | -             | -             | 654          | 677          | 681          | 642          |
| $T_s$ (°C)                                 | -             | -             | -             | -             | 704          | 707          | 709          | 676          |
| CTE x10 <sup>6</sup> (K <sup>-1</sup> )    | 8.31          | 7.61          | 7.82          | 7.95          | 8.02         | 8.08         | 8.11         | 7.65         |
| $T_g$ (°C)                                 | 753           | 749           | 737           | 735           | -            | -            | -            | -            |
| $T_p$ (°C)                                 | 910           | 909           | 906           | 904           | 924          | 932          | 930          | 904          |
| $E_c$ (kJ mol <sup>-1</sup> )              | 405           | 394           | 359           | 341           | 437          | 426          | 378          | 400          |
| $N$                                        | 1.68 ± 0.01   | 1.88 ± 0.01   | 2.06 ± 0.01   | 2.08 ± 0.01   | 2.03 ± 0.04  | 2.12 ± 0.02  | 2.10 ± 0.05  | 2.11 ± 0.02  |

#### 4.3.4 Glass transition and Coefficient of thermal expansion (CTE)

The dilatometric glass transition temperature ( $T_{dg}$ ) and softening temperature ( $T_s$ ) for BaO- containing glasses along with glass transition temperature ( $T_g$ ) for ZnO-containing glasses is presented in Table 4.13. The value of  $T_{dg}$  and  $T_s$  for BaO-containing glasses increased with an increase in BaO content while they decreased with introduction of  $B_2O_3$  (BaCMAS4). On the contrary, an increase in ZnO content in the glasses led to decrease in  $T_g$  values of the investigated glasses. Both BaO-containing and ZnO-containing glasses showed similar trend with regard to the variation in CTE of the glasses (Table 4.13). The CTE of glasses decreased with introduction of ZnO and BaO in the parent glass DT, respectively. However, with further increase in the concentration of ZnO and BaO, the CTE of the glasses was observed to increase. Among all the eight investigated compositions lowest CTE was obtained for glass DT-Zn1 and highest for glass DT. This variation in CTE of glasses with change in BaO and ZnO concentration may be explained on the basis of excess volume ( $V_e$ ) in the glasses. As depicted in Table 4.13, the  $V_m$  and  $V_e$  for glasses BaCMAS1 and DT-Zn1 are higher in comparison to their parent glass DT. An increase in excess volume of the glass implies towards an increasing directional bonding in the glass network, thus, leading to decrease in CTE of the respective glasses. However, further increase in BaO and ZnO content led to a decrease in value of  $V_e$ , thus, pointing towards a collapse of glass structural skeleton due to increasing non-directional (ionic) nature, which further leads to an increase in CTE. The decrease in CTE of glass BaCMAS4 may be explained on the basis of increasing covalent character in the glass due to addition of  $B_2O_3$  which is also supported by an increase in  $V_m$  and  $V_e$  for glass BaCMAS4 in comparison to glass BaCMAS3 (Table 4.13).

#### 4.3.5 Crystallization kinetics by DTA

Fig. 4.21 presents the DTA (Labsys SETARAM, France) thermographs of parent glass DT along with ZnO-containing glasses DT-Zn1, DT-Zn2 and DT-Zn3, respectively while Fig. 4.22 presents the DTA thermographs of the BaO-containing glasses at  $\beta = 5 \text{ K min}^{-1}$ . The DTA plots of all the glasses exhibit a single exothermic effect at all the heating rates which shifted towards higher temperatures with increasing the heating rate (Fig. 4.23). This signifies that the GC is formed either as a result of single phase crystallization or of an almost simultaneous precipitation of different crystalline phases.

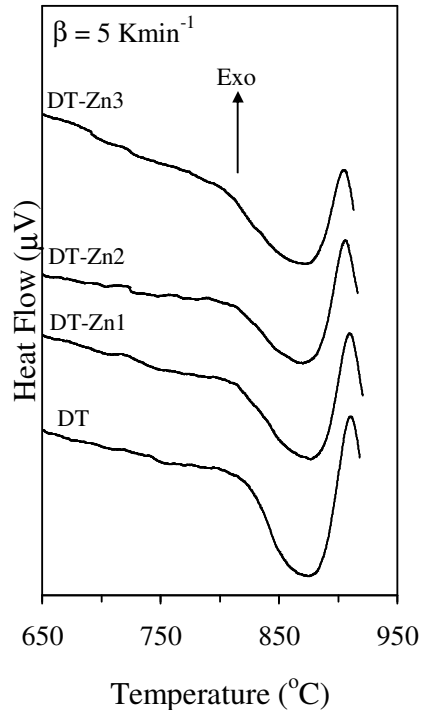


Fig. 4.21 DTA thermographs of parent glass DT and ZnO-containing glasses.

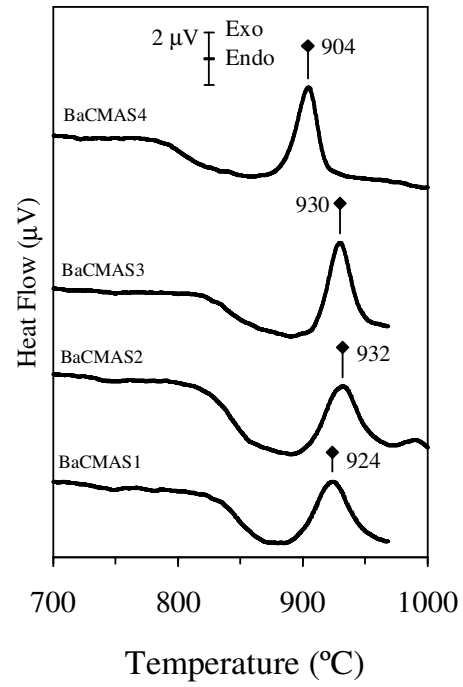


Fig. 4.22 DTA thermographs of BaO-containing glasses.

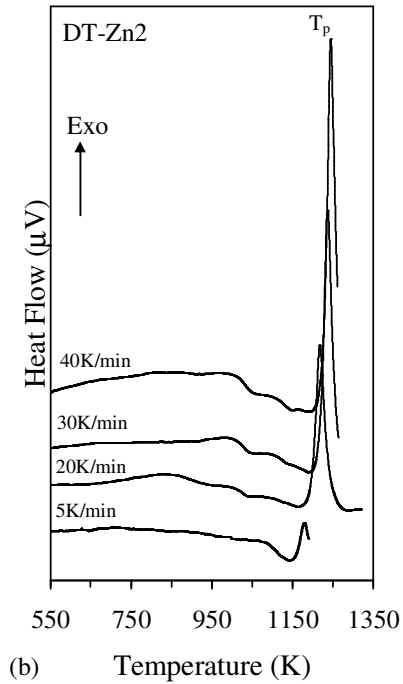


Fig. 4.23 DTA thermographs of glass DT-Zn2 at different heating rates.

The addition of ZnO did not show any significant effect on the crystallization temperature as  $T_p$  decreased slightly with an increase in ZnO content (Table 4.13). The value of  $T_p$  increased with introduction of BaO (BaCMAS1) while a slight increase was observed for glass BaCMAS2 in comparison to glass BaCMAS1. No further increase was observed with increase in BaO content in glass BaCMAS3 (Table 4.13). The value of  $T_p$  for BaO-containing glasses was observed to be higher than ZnO-containing glasses. The  $T_p$  for glass BaCMAS4 decreased considerably with the addition of  $B_2O_3$  and shares the lowest  $T_p$  value with glass DT-Zn3 among all the eight investigated glasses. The values of activation energy of crystallization,  $E_c$  and Avrami parameter,  $n$ , for all the investigated glasses are listed in Table 4.13. It was observed that that  $E_c$  value decreased with increase in ZnO as well as BaO content in the glasses and  $E_c$  for ZnO-containing glasses is much lower in comparison to BaO-containing glasses. The value of Avrami parameter for all the glasses suggests that the crystallization did not occur on a fixed number of nuclei and the mechanism of crystallization is intermediate (i.e. both bulk and surface). It is noteworthy that  $E_c$  for glass DT1 (Table 4.8) is higher than glass DT (Table 4.13), even though, both correspond to the same composition (80 mol.% Di – 20 mol.% CaTs) and crystallize as mono-mineral augite GC with same crystalline phase, augite (01-078-1392). This may be explained on the basis of unwanted uptake of alumina from crucible during the synthesis of glass DT1. In fact, the results obtained from the quantitative analysis of the amount of crystalline and amorphous content in the GCs (GPCs heat treated at 900 °C for 1 h) from both the compositions (DT1 and DT) calculated by XRD studies adjoined with Rietveld-R.I.R analysis (Fig. 4.24) support these results. Owing to lower activation energy of crystallization ( $E_c$ ), composition DT crystallized extensively in comparison to composition DT1, as is evident from Table 4.14.

Table 4.14 Results of Rietveld-R.I.R quantitative analysis (wt.%)

| GPC sintered at 900 °C for 1 h | Augite (01-078-1392)<br>$Ca(Mg_{0.70}Al_{0.30})(Si_{1.70}Al_{0.30})O_6$ | Glass     | Total | $\chi^2$ | $R_{wp}$ | $R_p$ |
|--------------------------------|-------------------------------------------------------------------------|-----------|-------|----------|----------|-------|
| DT                             | 74.21 (1)                                                               | 25.79 (1) | 100   | 7.68     | 0.080    | 0.059 |
| DT1                            | 54.26 (1)                                                               | 45.74 (1) | 100   | 4.97     | 0.066    | 0.050 |

R.I.R, reference intensity ratio

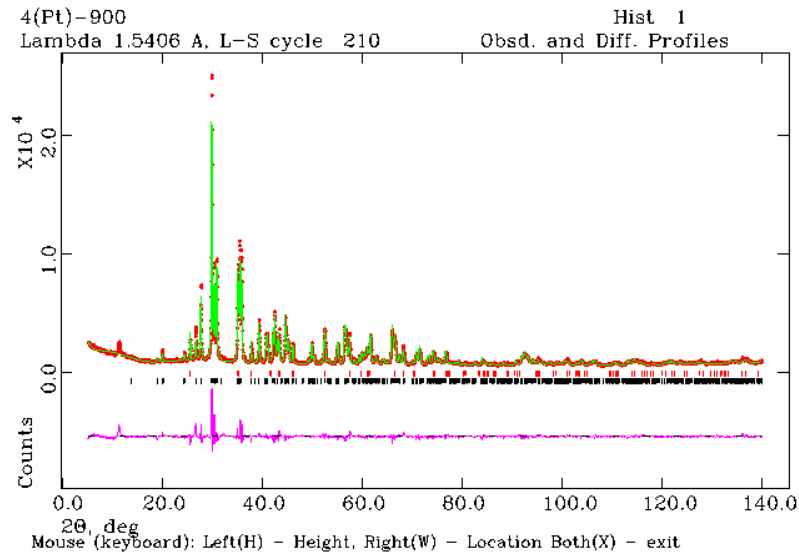


Fig. 4.24 Observed (crosses), calculated (continuous line), and difference curve from the Rietveld refinement of the GC DT treated at 900 °C for 1 h in air. Markers representing the phase reflections correspond to augite and corundum (from bottom to top).

### 4.3.6 Crystallization behaviour of glass powder compacts

#### 4.3.6.1 Non-isothermal conditions, 850-1000 °C (1 h)

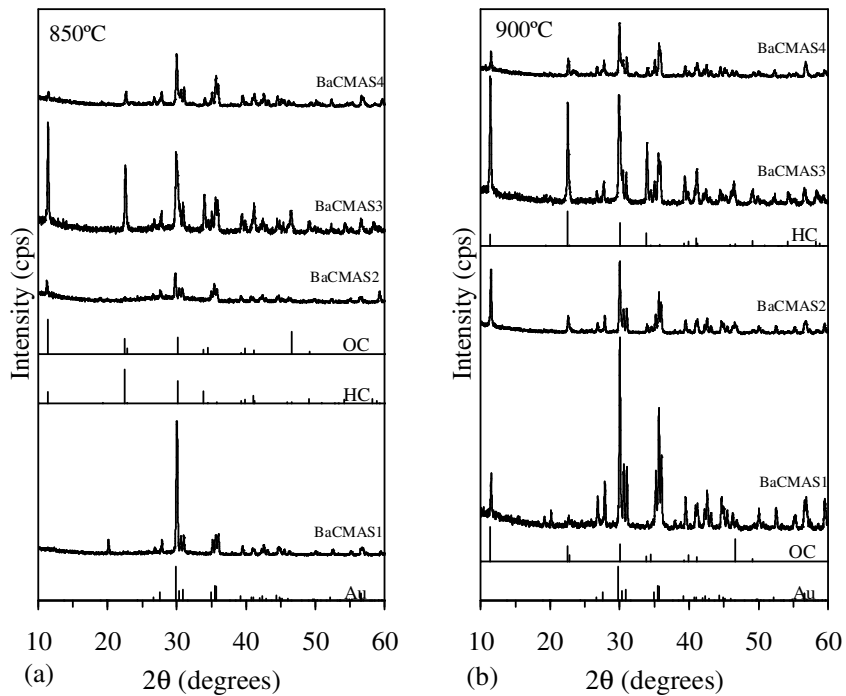
##### *BaO-containing glasses*

Figure 4.25 shows the evolution of crystalline phases in GPCs between 850 °C and 1000 °C (1 h). The composition of BaCMAS1 developed only augite after heat treatment at 850 °C, while modifications of  $\text{BaAl}_2\text{Si}_2\text{O}_8$ , orthocelsian (OC) and hexacelsian (HC), were further registered in the diffractograms of the other three compositions (Fig. 4.25a). SEM analysis of BaCMAS2 samples (Fig. 4.26a) showed crystals embedded in glass matrix, which agrees fairly well to the low intensity of the X-ray peaks in the respective diffractogram of Fig. 4.25a.

The phases of OC, HC, and augite were registered with higher peaks' intensities in the diffractograms of the three B-free compositions at 900 °C (Fig. 4.25b), indicating improvement of crystallinity, as Fig. 4.26b also confirms for the case of BaCMAS2 samples. The same phases were identified in the B-containing composition BaCMAS4, but the negligible change of peaks' intensities with temperature suggests a rather sluggish crystallization. A similar crystalline regime is generally suggested for the diffractograms at

950 °C (Fig. 4.25c), but in BaCMAS3, the most intensive peak of OC (at  $2\theta = 11.35^\circ$ ) was almost vanished, while intensive patterns of HC appeared, together with peaks of newly developed phases of monocelsian (C) and silica (S). Monocelsian (C) formed in the B-containing composition BaCMAS4, as well.

After heat treatment at 1000 °C (Fig. 4.25d), the intensity of crystalline phases in the BaCMAS1 and BaCMAS2 compositions considerably decayed likely due to dissolution effect, but low intensity peaks of C appeared in the diffractogram of BaCMAS1. In the composition BaCMAS3, the peaks of C and S disappeared while the ratio of OC/HC intensities changed and was apparently similar to that at 900 °C. In the diffractogram of BaCMAS4, the peak heights and widths remained unaltered, suggesting that B likely suppresses crystallization in that complex system.



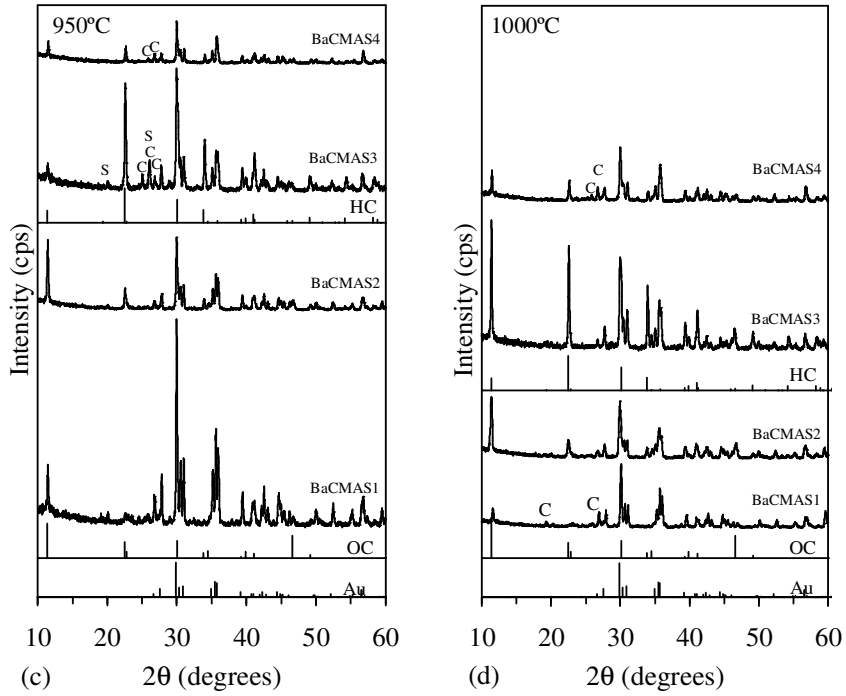


Fig 4.25 X-ray diffractograms of glass-powder compacts, after heat treatment at different temperatures for 1 h. (Au: Augite, ICDD card 01-078-1391; HC: Hexacelsian, 01-077-0185; OC: Orthocelesian, 00-012-0725; C: Monocelsian, 01-074-1677. The spectra have not been normalized. Full scale of intensity axes 6000 cps).

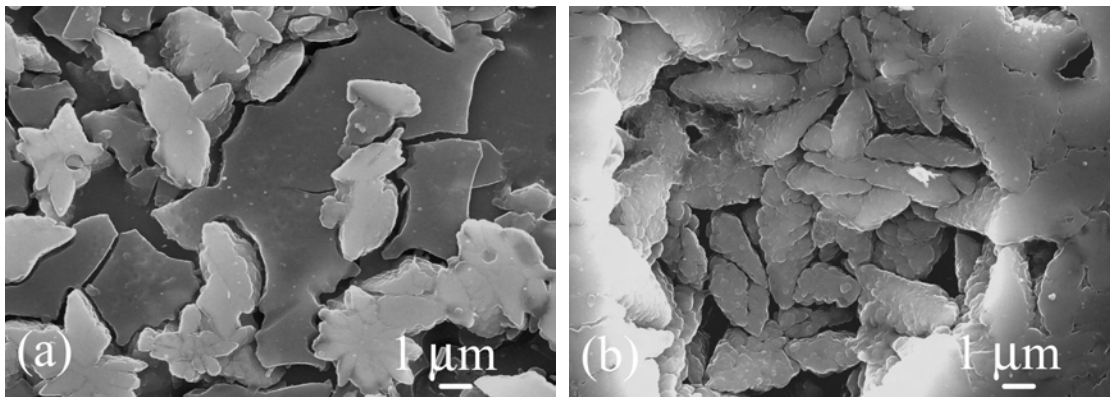


Fig. 4.26 Microstructure (revealed after chemical etching of polished surfaces with HF solution) of the glass-ceramics BaCMAS2 heat treated at (a) 850 °C, (b) 900 °C for 1 h.

### ZnO-containing glasses

According to XRD results (Fig. 4.27) monomineral GCs of augite (Aug; ICDD card: 01-078-1392) were developed in the composition DT after sintering at 850 °C and 900 °C. The intensity of the XRD peaks for augite increased significantly with increasing sintering temperature and reached a maximum at 950 °C, and decreased upon thermal heat treatment at 1000 °C due to partial dissolution in the liquid phase. The wollastonite (W\*; CaSiO<sub>3</sub>; ICDD: 01-084-0655) and orthoenstatite (OE; ICDD card: 00-019-0768) appeared as minor phases in GC DT, along with augite as the dominant crystalline phase, after heat treatment at both 950 °C and 1000 °C (Fig. 4.27a).

The composition DT-Zn1, containing the lowest amount of ZnO (1.86 wt.%), showed a similar crystalline phase assemblage and their sequential precipitation order as was observed for composition DT. The formation of monomineral GCs of augite at 850 °C and 900 °C followed by appearance of wollastonite (W; CaSiO<sub>3</sub>; ICDD card: 01-072-2284) and OE at 950 °C and 1000 °C were recorded (Fig. 4.27b). It is noteworthy that wollastonite (W), which precipitated in ZnO containing GCs had a different XRD pattern from that detected for ZnO-free GCs (DT). No ZnO-associated crystalline phases were observed for the GCs DT-Zn1 in the temperature interval 850-1000 °C.

The GC DT-Zn2 was mono-mineral after sintering at 850 °C with augite as the only crystalline phase (Fig. 4.27c). Hardystonite (Hs; Ca<sub>2</sub>ZnSi<sub>2</sub>O<sub>7</sub>; ICDD: 00-035-0745) was revealed in GC DT-Zn2 at elevated temperatures (900–1000 °C) suggesting that the limit for substitution of Mg by Zn has probably been exceeded.

Earlier Zhunina *et al.* [146] proposed existence of limited isomorphous substitution of Mg for Zn and consequently formation of solid solutions of general formula Ca(Mg,Zn)Si<sub>2</sub>O<sub>6</sub>. According to their study, apart from Di solid solution, villemite (Zn<sub>2</sub>SiO<sub>4</sub>) and Hs (Ca<sub>2</sub>ZnSi<sub>2</sub>O<sub>7</sub>) might also be formed due to the higher polarization effect of Zn cation on surrounding oxygen anions.

In the GC DT-Zn3, featuring highest ZnO content (7.23 wt.%), OE crystallized out as a minor phase after sintering at 850 °C, along with augite as the dominant crystalline phase (Fig. 4.27d). Further, with an increase in temperature to 900 °C, Hs and W joined the phase assemblage as minor phases. However, with increasing temperature to 950 °C and 1000 °C, no change in crystalline phase assemblage could be observed.

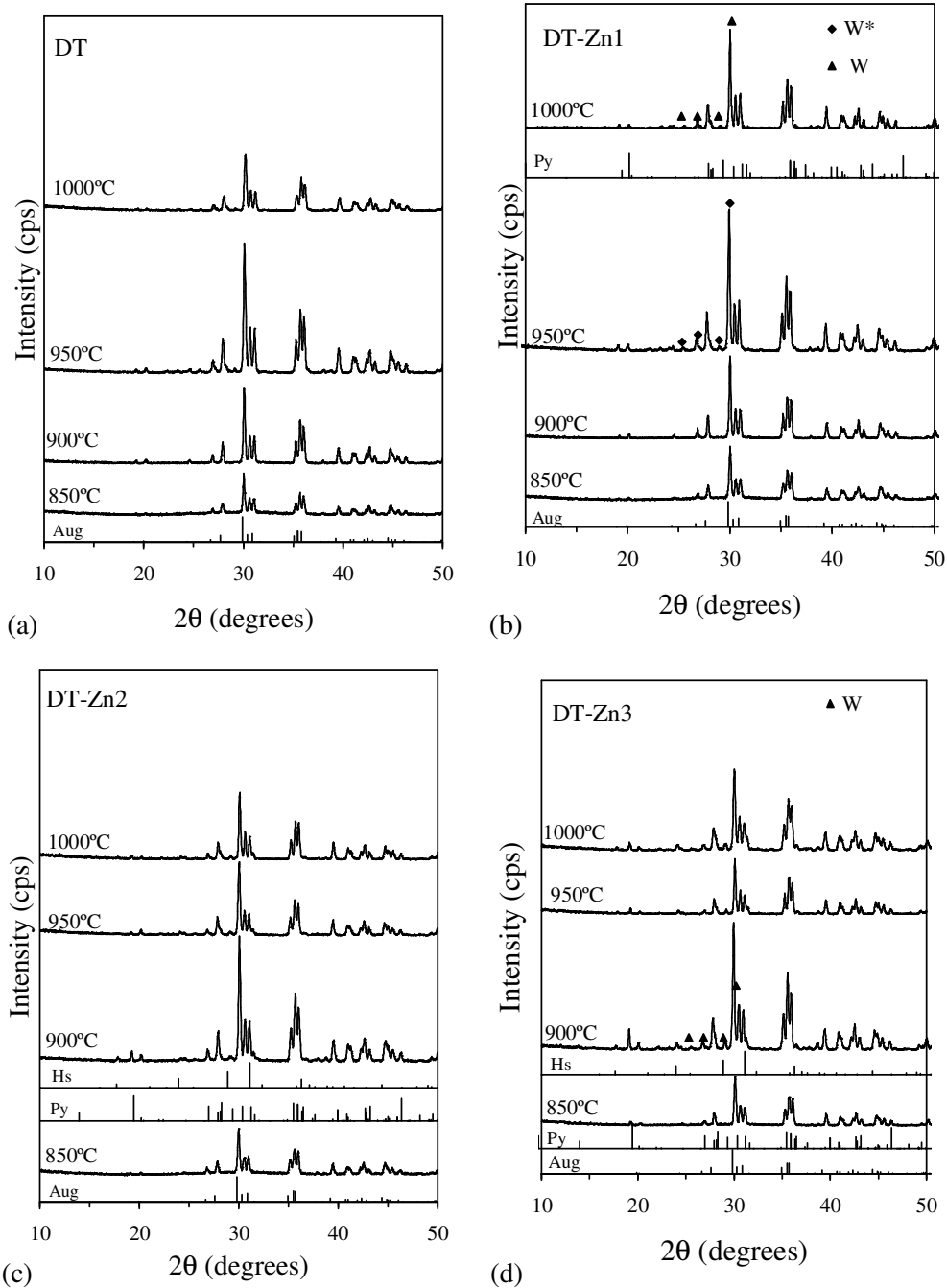


Fig. 4.27 X-ray diffractograms of glass-powder compacts of (a) DT, (b) DT-Zn1, (c) DT-Zn2 and (d) DT-Zn3 after heat treatment at different temperatures for 1 h (Aug: Augite, ICDD card: 01-078-1392; W\*:  $\text{CaSiO}_3$ , 01-084-0655; OE: Orthoenstatite, 00-019-0768; W; Wollastonite, 01-072-2284; Hy: Hardystonite, 00-035-0745). The spectra have not been normalized. Full scale of intensity axes 21000 cps).

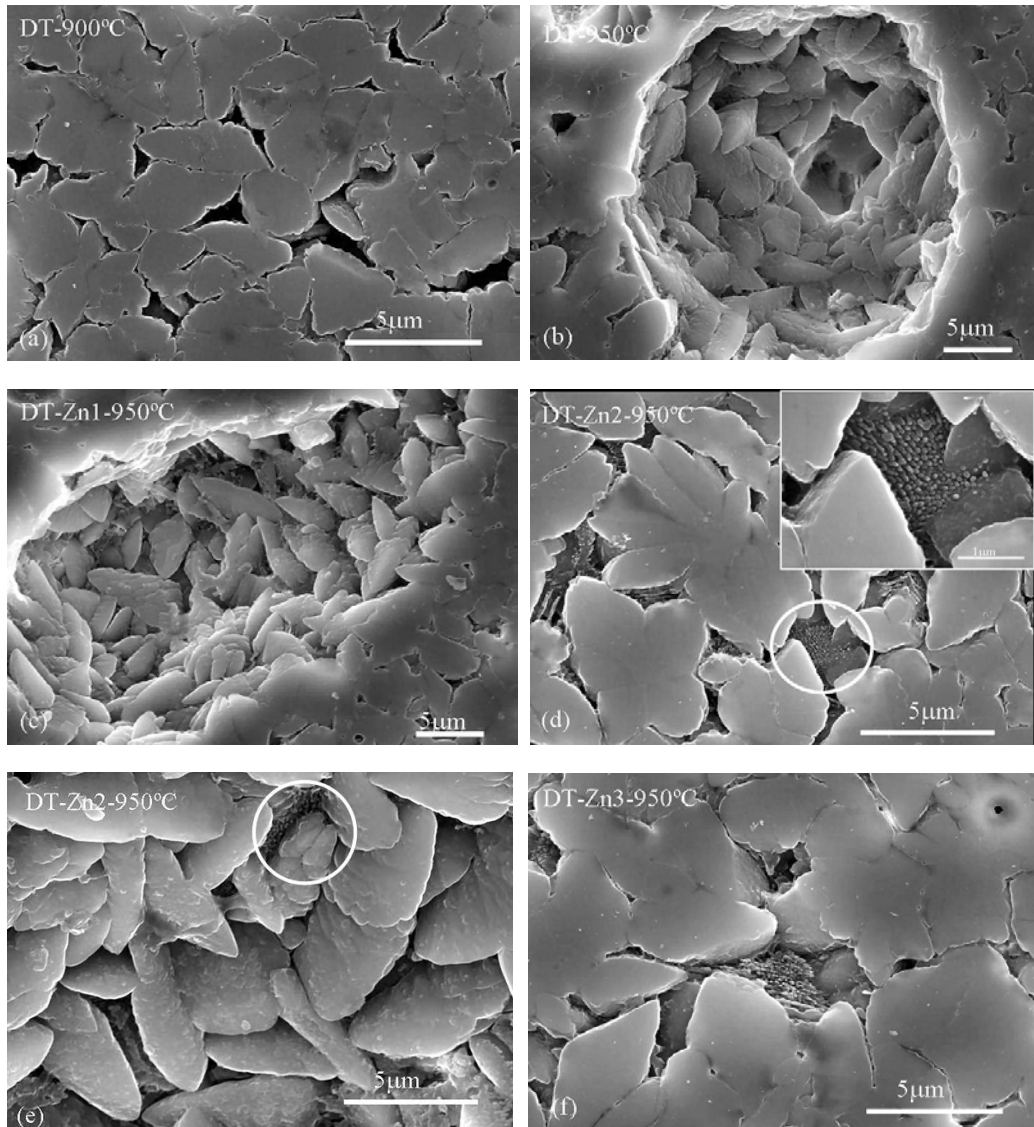


Fig. 4.28 Microstructure (revealed after chemical etching of polished surfaces with HF solution) of the GCs: (a) DT heat treated at 900 °C, (b) 950 °C (c) DT-Zn1 heat treated at 950 °C, (d) and (e) DT-Zn2 heat treated at 950 °C and (f) DT-Zn3 heat treated at 950 °C for 1 h, respectively.

The particular attention should be addressed to the minor peak varying between  $2\theta = 19.24^\circ$ - $19.28^\circ$  which was revealed in the XRD patterns of the experimental GCs. Since, augite possess peak of very low intensity at  $2\theta = 19.002^\circ$  (ICDD card 01-078-1392), we believe that the observed peaks ( $2\theta = 19.24^\circ$ - $19.28^\circ$ ) peaks belong to augite. The

differences in  $2\theta$  values can be attributed to the formation of solid solution of complex nature, slightly different from augite (ICDD card 01-078-1392). Earlier, it was around  $2\theta = 19^\circ$  [147]. This phenomenon can be explained by effect of  $\text{Cr}_2\text{O}_3$  during nucleation stage due to increasing bulk effect with Cr, and thus formation of Cr-spinel, content [148]. Further, crystallographic studies are needed to investigate phenomenon that occurred upon precipitation of pyroxene solid solutions with emphasis on quantitative determination of cation substitutions in both octahedral and tetrahedral sub-lattices.

Fig. 4.28 shows the SEM images of the sintered GCs. The disc shaped crystals of augite can be seen in all the experimental GCs, as major crystalline phase. However, as revealed (also by XRD data), Fig. 4.28 (d, e, f) shows the presence of some dendritic crystals (see white circles in Fig. 4.28d and 4.28e) along with the augite phase in the GC DT-Zn2 and DT-Zn3. These dendritic structures may be due to the appearance of Zn containing Hs phase in these GCs.

#### 4.3.6.2 Heat treatment of BaO-containing GCs under isothermal conditions, 900 °C (300 h)

The phase stability of GCs heat treated at 900 °C (that is close to the operation temperatures of SOFC) was investigated with X-ray diffraction of GPCs after prolonged isothermal heat treatment for 300 h (Fig. 4.29). With respect to the diffractograms of Fig. 4.25b, Fig. 4.29 shows augite as the predominant phase in BaCMAS1, with OC as secondary phase. In BaCMAS2, the strongest peaks of augite and OC have similar intensities, but in BaCMAS3, OC peaks are stronger than augite peaks. Prolonged heat treatment caused a pronounced decrease of augite peaks' intensities in the diffractograms of BaCMAS4, but the formation of monoclinic celsian was sound.

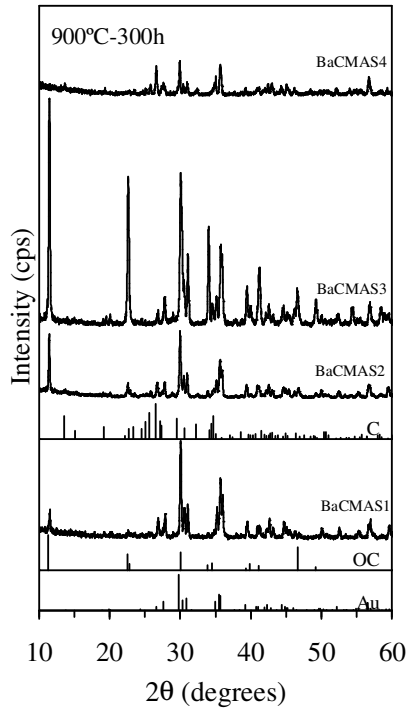
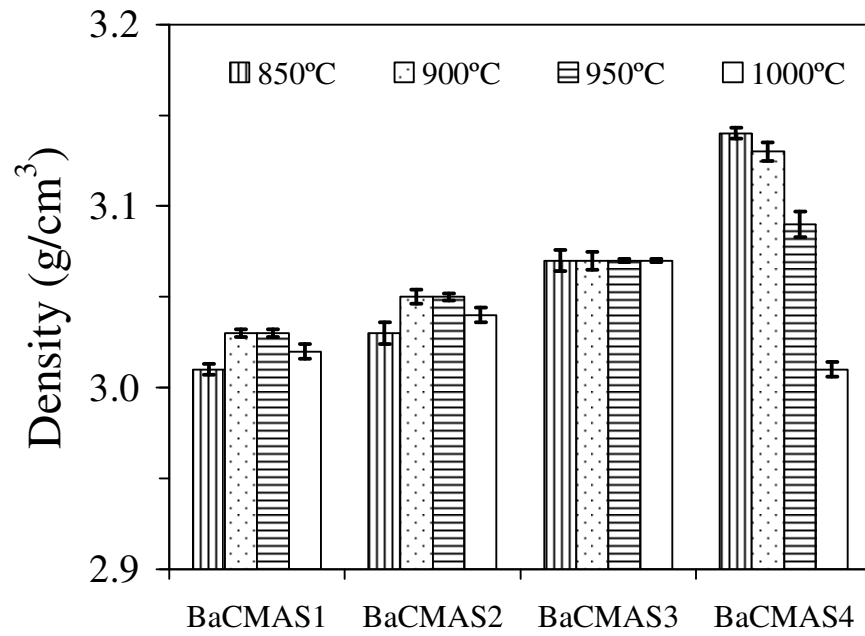


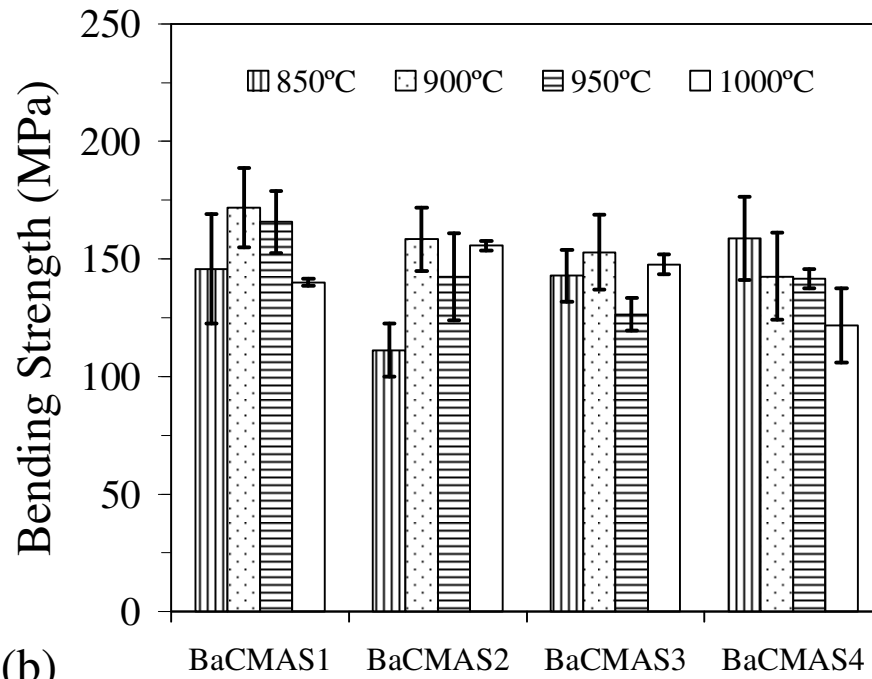
Fig. 4.29 X-ray diffractograms of glass-powder compacts after heat treatment at 900 °C for 300 h. (Please see the comments in the legend of Fig. 4.25).

#### 4.3.7 Properties of BaO-containing sintered glass-ceramics

Well-sintered dense glass-powder compacts were obtained after heat treatment at 850 °C. The appearance of the samples did not change at higher temperatures. There was no evidence of detrimental effects, such as deformation or formation of open porosity, in the temperature interval of 850-1000 °C. The highest values of shrinkage (with SD less than 5%) were reached at 850 °C for the compositions BaCMAS3 (17.17%) and BaCMAS4 (16.64%), and at higher temperatures (900 °C) for BaCMAS1 (16.91%) and BaCMAS2 (16.10%). Shrinkage systematically decreased in BaCMAS4 GCs at temperatures higher than 900 °C, but practically did not in the B-free GCs. In accordance with shrinkage measurements, BaCMAS4 GCs had the highest density among the four investigated compositions, with a maximum of  $3.14 \text{ g cm}^{-3}$  at 850 °C, which however, dramatically decreased at higher temperatures (Fig. 4.30a). The most stable GCs, with regards to smaller density variations at different temperatures, were those of BaCMAS3 composition, exhibiting a high density of about  $3.07 \text{ g cm}^{-3}$  in the temperature interval of 850-1000 °C.



(a)



(b)

Fig. 4.30 Density (a) and bending strength (b) of glass-powder compacts sintered at different temperatures for 1 h.

The highest densities of BaCMAS1 ( $3.03 \text{ g cm}^{-3}$ ) and BaCMAS2 ( $3.05 \text{ g cm}^{-3}$ ) were reached in the temperature interval of 900-950 °C. Increasing BaO-content should plausibly cause a density increase, as was also seen for the bulk glass samples (Table 4.13). Nevertheless, higher BaO-content generally degraded bending strength of the produced GCs (Fig. 4.30b). The Di/CaTs solid solutions seemingly play a key role in the constitution and strengthening of the investigated GCs. In the temperature interval of 900-1000 °C, BaCMAS1 ( $\text{Ca}_{0.95}\text{Ba}_{0.05}\text{Mg}_{0.8}\text{Al}_{0.4}\text{Si}_{1.8}\text{O}_6$ ) possessed the highest bending strength (140-172 MPa) among the investigated GCs, while the corresponding BaO-free composition  $\text{CaMg}_{0.8}\text{Al}_{0.4}\text{Si}_{1.8}\text{O}_6$  (DT1), studied earlier (Table 4.8), exhibited higher bending strength (166-189 MPa). These results of bending strength should be related to the sintering ability as reflected on the values of shrinkage and density, as well as on other inherent features of the developed crystalline phases at each specific temperature (Figs. 4.25 and 4.26). The decrease of bending strength with increasing BaO-content may be explained by possible transformations of  $\text{BaAl}_2\text{Si}_2\text{O}_8$  polymorphs, including reversible transformation of  $\alpha \leftrightarrow \beta$ -HC, accompanied by a detrimental volume change [148]. This suggestion is seemingly more realistic in GCs with high amounts of BaO, considering the slope changes in dilatation curves of the BaCMAS3 GC (sintered at either 950 °C for 1 h or at 900 °C for 300 h) recorded at about 300 °C. The BaCMAS1 and BaCMAS2 GCs did not show similar features, and hence they can be qualified for potential applications in products that must function in broader temperature ranges [149].

The CTE of the GCs sintered at 950 °C, determined by the slope of dilatometry curves, were  $8.75 \times 10^{-6} \text{ K}^{-1}$ ,  $10.10 \times 10^{-6} \text{ K}^{-1}$ ,  $9.78 \times 10^{-6} \text{ K}^{-1}$ , and  $9.83 \times 10^{-6} \text{ K}^{-1}$  (along the respective order of BaCMAS1, BaCMAS2, BaCMAS3 and BaCMAS4). The GCs produced after prolonged isothermal heat treatment at 900 °C for 300 h had CTE of  $9.01 \times 10^{-6} \text{ K}^{-1}$ ,  $9.01 \times 10^{-6} \text{ K}^{-1}$ ,  $9.02 \times 10^{-6} \text{ K}^{-1}$ , and  $8.92 \times 10^{-6} \text{ K}^{-1}$ , respectively (i.e. CTE a slightly increased in BaCMAS1 and slightly decreased for the other three GCs). It is noteworthy that GC BaCMAS3 featured a jump in the thermal expansion curves at about 300 °C and then the slope also changed. Thus, for this composition, the above CTE values correspond to the temperature interval of 300-600 °C, while for other three GCs to 200-600 °C interval. The important point is that the above values match fairly well the CTE of

zirconia-based solid electrolytes, varying in the range of  $9.8\text{-}10.4 \times 10^{-6} \text{ K}^{-1}$  at SOFC operation temperatures.

The experimental results of wetting experiments suggest strong interfacial adhesion between the four investigated compositions and 8YSZ at  $900 \text{ }^\circ\text{C}$  (100 h, air). In particular, good wetting regime was observed (i.e. contact angle  $< 90^\circ$ ) and continuous interfaces, with no cracks or gaps, were revealed after cross section and polishing. There was no evidence of reaction at the interface, except in the case of BaCMAS4, where a thin reaction layer was observed, probably due to a B-rich liquid phase formed during heat treatment, favouring diffusion of components. No reaction products were also determined by XRD analysis of compact samples made of powder mixtures of glasses and 8YSZ similarly heat treated (i.e.  $900 \text{ }^\circ\text{C}$ , 100 h), where the augite, OC, HC and cubic zirconia were the only identified phases. It should be also underlined that glass devitrification, which occurred under these conditions, did not jeopardize the good adhesion. The chemical etching (with 2 Vol.% HF) of polished cross-sectioned interfaces confirmed the formation of crystals in the glass side of the interface (Fig. 4.31 corresponds to the case of BaCMAS1 composition, but similar features were also observed for the cases of the other compositions).

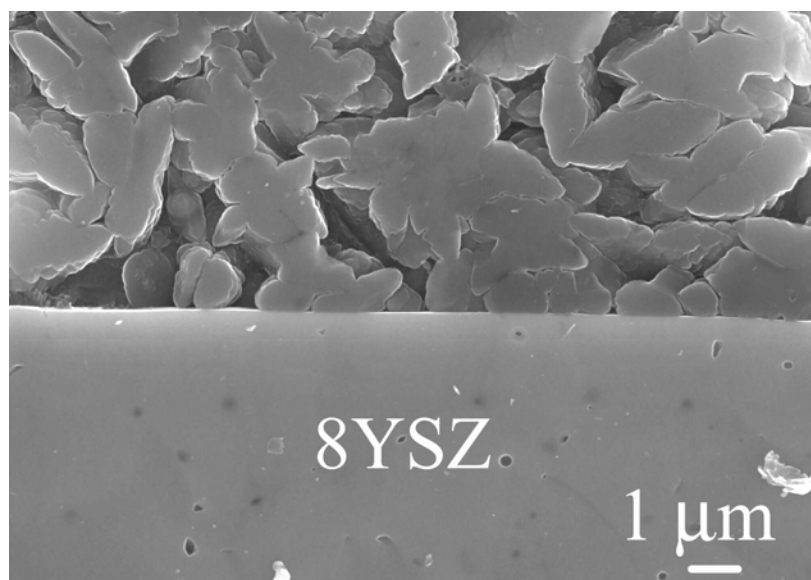


Fig. 4.31 Microstructure of solidified interface between zirconia (8YSZ) and glass BaCMAS1, developed after heat treatment at  $900 \text{ }^\circ\text{C}$  for 100 h in air.

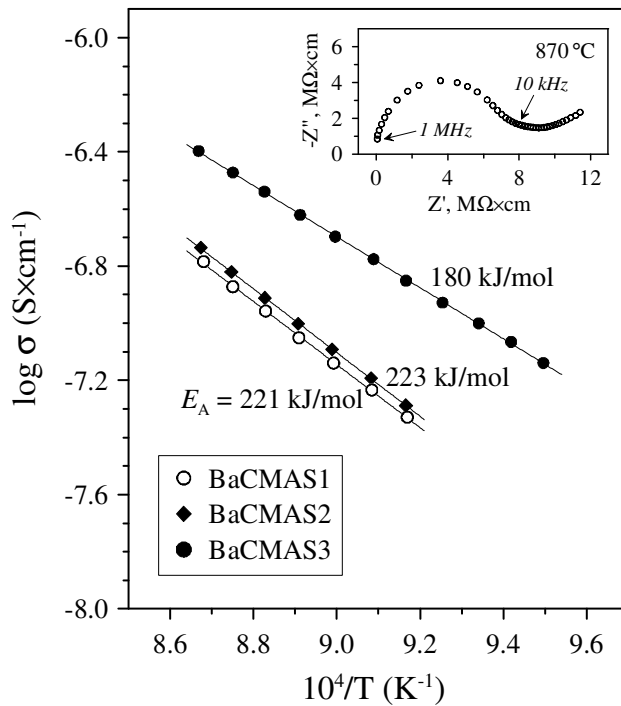


Fig. 4.32 Total conductivity of the investigated glass-ceramics in air. The inset shows a typical example of impedance spectrum for BaCMAS1.

The impedance spectra and the level of total conductivity (Fig. 4.32) are all typical for GCs free of mobile alkaline cations. The impedance spectra consist of two contributions attributed to the bulk (high-frequency) and the electrode (low-frequency). The total conductivity ( $\sigma$ ) was calculated from the intermediate-frequency intercept. Note that the presence of electrode signal suggests a dominant ionic contribution to the conductivity, in agreement with the e.m.f. data (Fig. 4.33). No degradation of electrical properties over time was detected at 650-890 °C.

The e.m.f. measurements confirmed that, as expected [116], the role of electrode polarization resistance in the oxygen concentration cells with GC membranes is essential, making it impossible to determine the ion transference numbers simply from the measured voltage using the Nernst equation. Figure 4.33 compares the ratio of measured and theoretical voltages ( $E_{obs}/E_{th}$ ), the true values of ion transference numbers determined by the modified e.m.f. technique, and the ratio of polarization and ionic resistances ( $R_{\eta}/R_i$ ) for BaCMAS1 composition. This composition was selected for detailed characterization due to

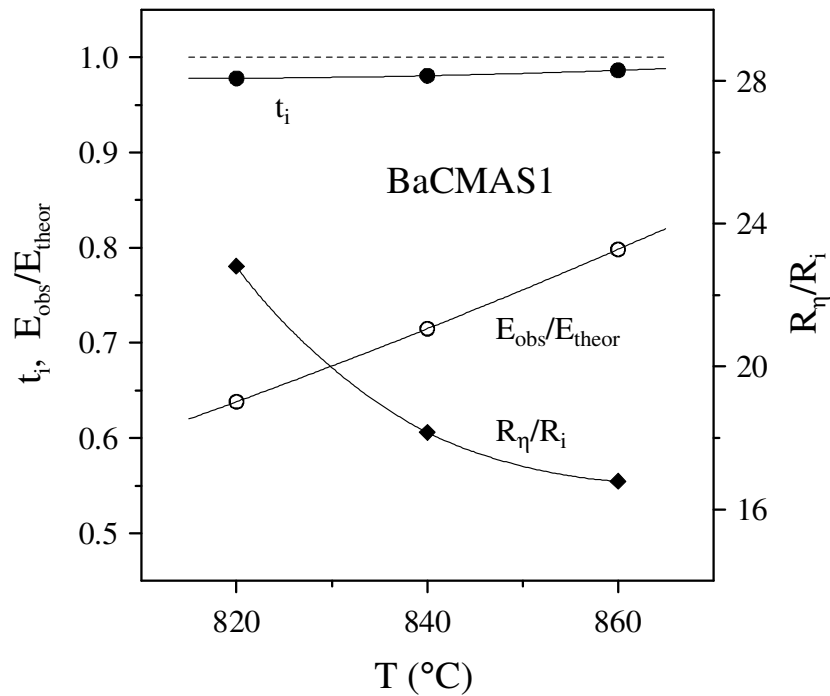


Fig. 4.33 Ion transference numbers, ratio between the observed and the theoretical e.m.f. values, and  $R_{\eta}/R_i$  ratio for BaCMAS1 glass-ceramics with Pt electrodes under air / ( $\text{H}_2$ - $\text{H}_2\text{O}$ - $\text{N}_2$ ) gradient.

the lowest conductivity and minimum Ba content, making it possible to expect minimum reactivity with SOFC components, in the investigated series of GCs. The sum of the electrode polarization resistances is considerably higher than the resistance to ionic transport. Such a behavior is well-known for Si-containing GCs [116] and results from conglutination of Pt particles forming the electrodes due to the high surface diffusivity of silica. Consequently, the  $E_{\text{obs}}/E_{\text{th}}$  values vary in the range 0.6-0.8, whilst the ionic contribution to total conductivity of the GCs is close to 100%. However, the e.m.f. measurements can not indicate the exact ionic charge carriers when an oxide membrane is placed under an oxygen chemical potential gradient and equilibrium is achieved at the electrodes. Therefore, the transference numbers shown in Fig. 4.33 correspond to the total ionic transport, irrespective of the nature of mobile anions and/or cations. As the content of alkaline metal impurities in the investigated materials is lower than the detection limits of available analytical techniques, the mobile charge carriers may include oxygen ions and/or protons.

The data on oxygen permeation (Fig. 4.34) confirm that the ionic conduction is contributing, at least in a significant extent, to the migration of oxygen ions. Indeed, the observed level of oxygen permeation fluxes can be only explained in terms of oxygen diffusion, either in ionic or in molecular form. This process can also involve ambipolar transport of  $O^{2-}$  and  $OH^-$  anions, migrating in opposite directions. These fluxes should compensate each other, resulting in zero current density through the GCs. The ambipolar

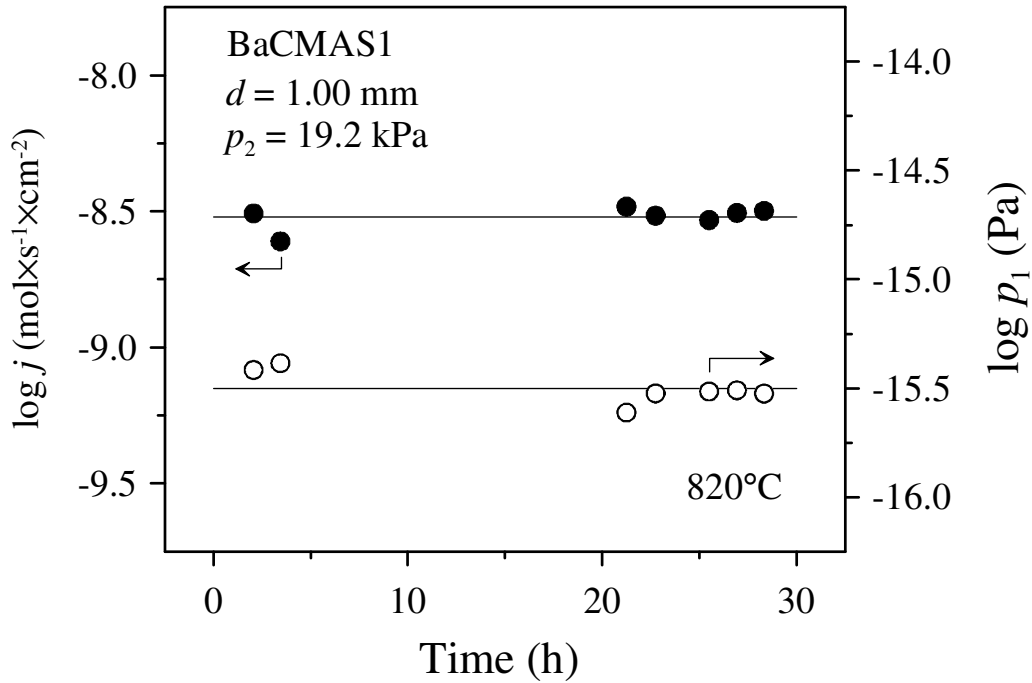


Fig. 4.34 Oxygen permeation flux and the corresponding permeate-side oxygen partial pressure for dense BaCMAS1 membrane (thickness of 1.0 mm), under air / ( $H_2+H_2O+N_2$ ) gradient at 820 °C.

steam permeation is well-known for oxide materials where the conductivity is mixed protonic and oxygen-ionic [150], and may occur without participation of electronic charge carriers. Compared to oxygen permeation caused by mixed oxygen-ionic and electronic conduction, the later mechanism may be preferential for the investigated materials, where the total and electronic conductivities are both very low (Figs. 4.32 and 4.33). Notice also that the oxygen fluxes are higher than those predicted theoretically from the data on total conductivity and ion transference numbers by the Wagner equation, ignoring possible protonic contribution. This indicates a key influence of microstructure-related factors,

including closed porosity, microcracks, grain boundaries, and various extended defects. A similar conclusion has been drawn out earlier for other sealant materials [116].

In general, the level of total conductivity (Fig. 4.32) and oxygen permeation (Fig. 4.34) is similar or even lower compared to RO-BaO-SiO<sub>2</sub> (R= Mg, Zn) GCs, recently considered as potential SOFC sealants [116]. In spite of the transport mechanisms discussed below, these data clearly show that the investigated GCs possess good insulating properties in the whole range of intermediate-temperature SOFC operation conditions. This finding, in conjunction with the negligible reaction between the investigated glasses and 8YSZ as well as their good CTE matching, suggest that the investigated materials may exhibit serious advantages. Certainly, long-term stability tests (2000-5000 h) at high temperatures are necessary to ensure the absence of chemical reactions with other SOFC components, such as stainless steel- or LaCrO<sub>3</sub>-based interconnects. Attention should be also directed to possible surface diffusivity of silica.

Finally, one should mention that BaCMAS3 exhibits a higher conductivity compared to BaCMAS1 and BaCMAS2 (Fig. 4.32). The activation energies calculated by the standard Arrhenius equation,  $\sigma = \sigma^0 \times \exp[-E_a/RT]$ , where  $\sigma^0$  is a pre-exponential factor, are  $221 \pm 2$  kJ mol<sup>-1</sup> for BaCMAS1,  $223 \pm 1$  kJ mol<sup>-1</sup> for BaCMAS2, and  $180 \pm 1$  kJ mol<sup>-1</sup> for BaCMAS3. That behaviour may be associated with the bigger size of Ba<sup>2+</sup> cations compared to Ca<sup>2+</sup>, which increases the specific free volume and decreases energetic barrier for ion jumps. Note that, although increasing barium content may also promote water intercalation, the difference in cation composition of BaCMAS2 and BaCMAS3 is moderate with respect to the conductivity variations. Furthermore, the Arrhenius curves of the total conductivity exhibit no deviations from linearity, indicative of progressive water intercalation on cooling. Therefore, the higher total conductivity of BaCMAS3 should be primarily related to the different phase composition.

.....

## 4.4 Influence of MO (Ba, Sr) and R<sub>2</sub>O<sub>3</sub> (R = B, Cr, La) on sintering, crystallization behaviour and properties of diopside based glasses and glass-ceramics

### 4.4.1 Designing of glass compositions

The aim of the present study is to investigate the effect of M<sub>2</sub>O<sub>3</sub> (M = B, Al, Cr, La) on the thermal, crystallization behaviour and properties of Di (CaMgSi<sub>2</sub>O<sub>6</sub>) based glasses and GCs in order to qualify them for sealing in SOFC. La<sub>2</sub>O<sub>3</sub> is known to control the viscosity and CTE of the silicate glasses and GCs [151] while Cr<sub>2</sub>O<sub>3</sub> additions decrease the crystallization temperature by acting as a nucleating agent [147] and reduce the surface tension of the glass [152]. Therefore, La<sub>2</sub>O<sub>3</sub> was added with the aim of altering the thermal characteristics of the glasses and the resultant GCs, whereas Cr<sub>2</sub>O<sub>3</sub> was introduced with the primary aim of assessing its influence on the physicochemical and electrical properties. Accordingly, Table 4.15 presents four new glass compositions investigated in the present work. The composition 7A was derived by the complex substitution of 0.2Ca<sup>2+</sup> + 0.1Si<sup>4+</sup> ↔ 0.1Ba<sup>2+</sup> + 0.1La<sup>3+</sup> + 0.1Al<sup>3+</sup> while glass 7B was derived by molar substitution 0.2Ca<sup>2+</sup> + 0.1Mg<sup>2+</sup> + 0.2Si<sup>4+</sup> ↔ 0.1Ba<sup>2+</sup> + 0.1Al<sup>3+</sup> + 0.1La<sup>3+</sup> in the pure Di system. The glasses 7A-Cr and 7B-Cr were derived by the addition of 0.5 wt.% Cr<sub>2</sub>O<sub>3</sub> in glasses 7A and 7B, respectively. 1wt.% of NiO was added to all the glasses in order to improve the adhesion behaviour of the glasses [152].

Furthermore, the decrease in viscosity and crystallization tendency of the silicate glasses (both of which are favourable properties) with the addition of B<sub>2</sub>O<sub>3</sub> is well known. According to Sohn *et al.* [153], B<sub>2</sub>O<sub>3</sub>/SiO<sub>2</sub> ratio plays an important role in tailoring the properties of the GC sealants as the CTE of the glasses has been observed to increase with increase in B<sub>2</sub>O<sub>3</sub>/SiO<sub>2</sub> ratio. However, the disadvantage of adding B<sub>2</sub>O<sub>3</sub> is that, at operating temperatures, B<sub>2</sub>O<sub>3</sub> forms volatile compounds with water vapour leading to seal degradation [8]. Therefore, high amount of B<sub>2</sub>O<sub>3</sub> in the sealants is not seen with alacrity. Thus, considering the previously reported results, an attempt has been made to tailor the properties of the La<sub>2</sub>O<sub>3</sub> containing diopside based glasses and GCs (7A) by the addition of varying amounts of B<sub>2</sub>O<sub>3</sub> to the parent glass (Ca<sub>0.8</sub>Ba<sub>0.1</sub>MgAl<sub>0.1</sub>La<sub>0.1</sub>Si<sub>1.9</sub>O<sub>6</sub>, labelled as 7A) in a systematic manner. The first five compositions were derived from the glass composition 7A by the addition of different amounts of B<sub>2</sub>O<sub>3</sub> to it varying between 2-20 wt.%. In order to be consistent, these compositions are labelled as 7-2B, 7-5B, 7-10B, 7-

15B and 7-20B, respectively, where, 2B, 5B, 10B, 15B and 20B designate the amount of B<sub>2</sub>O<sub>3</sub> incorporated into the parent glass, as listed in Table 4.15.

Table 4.15 Batch compositions of the glasses (wt.%)

| Glass                                       | MgO   | CaO   | BaO  | SrO  | SiO <sub>2</sub> | Al <sub>2</sub> O <sub>3</sub> | La <sub>2</sub> O <sub>3</sub> | B <sub>2</sub> O <sub>3</sub> | Cr <sub>2</sub> O <sub>3</sub> | NiO |
|---------------------------------------------|-------|-------|------|------|------------------|--------------------------------|--------------------------------|-------------------------------|--------------------------------|-----|
| All the glasses were melted in Pt-crucibles |       |       |      |      |                  |                                |                                |                               |                                |     |
| 7A                                          | 16.90 | 18.82 | 6.43 | -    | 47.88            | 2.14                           | 6.83                           | -                             | -                              | 1   |
| 7B                                          | 14.52 | 17.95 | 6.14 | -    | 43.28            | 4.08                           | 13.04                          | -                             | -                              | 1   |
| 7A-Cr                                       | 16.82 | 18.72 | 6.40 | -    | 47.64            | 2.13                           | 6.80                           | -                             | 0.5                            | 1   |
| 7B-Cr                                       | 14.44 | 17.86 | 6.11 | -    | 43.06            | 4.06                           | 12.97                          | -                             | 0.5                            | 1   |
| 7-2B                                        | 16.56 | 18.44 | 6.30 | -    | 46.91            | 2.09                           | 6.70                           | 2                             | -                              | 1   |
| 7-5B                                        | 16.05 | 17.87 | 6.11 | -    | 45.46            | 2.03                           | 6.49                           | 5                             | -                              | 1   |
| 7-10B                                       | 15.20 | 16.92 | 5.78 | -    | 43.04            | 1.92                           | 6.14                           | 10                            | -                              | 1   |
| 7-15B                                       | 14.34 | 15.97 | 5.46 | -    | 40.62            | 1.81                           | 5.80                           | 15                            | -                              | 1   |
| 7(Sr)-2B                                    | 16.92 | 18.83 | -    | 4.35 | 47.92            | 2.14                           | 6.84                           | 2                             | -                              | 1   |
| 7(Sr)-5B                                    | 16.40 | 18.25 | -    | 4.22 | 46.44            | 2.07                           | 6.63                           | 5                             | -                              | 1   |

It has been widely accepted that the BaO from glass reacts with Cr from the metallic interconnect under oxidizing environment so as to produce BaCrO<sub>4</sub> which is highly detrimental for the SOFC stack [98]. Significant content of BaO may also promote interaction with water vapour, leading to slow sealant degradation under SOFC operating conditions. Thus, in order to avoid such a condition, replacement of BaO by SrO has been attempted, in the present study, as an alternative, and various properties of the as produced glasses and GCs have been investigated. Previously, Ley *et al.* [94] studied the glass and GC system of SrO–Al<sub>2</sub>O<sub>3</sub>–La<sub>2</sub>O<sub>3</sub>–SiO<sub>2</sub>–B<sub>2</sub>O<sub>3</sub>. The CTE values of the as-made materials were in the range of 8–13 × 10<sup>-6</sup> K<sup>-1</sup>, while the long-term stability was not reported. Recently, Brochu *et al.* [154] compared the performance of the BaO- and SrO-based borate glass composites for sealing materials in SOFCs and reported the formation of low CTE crystalline phase, BaZrO<sub>3</sub>, on interaction with 8YSZ, for BaO containing glass-composites.

However, in case of SrO based glass-composites, formation of strontium zirconates was observed, which has CTE similar to 8YSZ. Kumar *et al.* [155] studied the MgO/SrO based borosilicate glasses and observed that SrO containing glasses had higher CTE in comparison to MgO based glasses. In a recent study, Mahapatra *et al.* [156] investigated the thermophysical properties and devitrification behaviour of the glasses in the system  $(25-X)\text{SrO}-20\text{La}_2\text{O}_3-(7+X)\text{Al}_2\text{O}_3-40\text{B}_2\text{O}_3-8\text{SiO}_2$  (mol.%) ( $X = 0-10$ ). However, as mentioned above, high boron seals proposed in earlier studies [94, 154-156] are apt to eventually corrode under humidified hydrogen environments (common in fuel cell operation) over time.

In the present investigation, two SrO-containing glass compositions were derived from compositions 7-2B and 7-5B by replacement of BaO for SrO and are labelled as 7(Sr)-2B and 7(Sr)-5B. Table 4.15 presents the details of the all the compositions investigated in the present work.

#### 4.4.2 Casting ability of glasses

The compositions containing 0, 2, 5 and 10 wt.%  $\text{B}_2\text{O}_3$  (Table 4.15) were prone to easy casting after 1 h of melting (in the temperature range 1550-1580 °C), resulting in homogenous transparent glasses with brown colour. The melting temperature of glass batch was reduced with the addition of  $\text{B}_2\text{O}_3$ . A similar brown coloured glass but with a dull appearance was obtained for the composition containing 15 wt.%  $\text{B}_2\text{O}_3$  (7-15B). For composition containing 20 wt.%  $\text{B}_2\text{O}_3$  (7-20B), we obtained a light brown coloured opaque glass. The amorphous nature of as cast and annealed glasses was confirmed by XRD analysis.

The SEM images of the bulk glasses (heated at 700 °C for 1 h) (Fig. 4.35a-c) showed the existence of phase separation in  $\text{B}_2\text{O}_3$  containing glasses. However, the type of phase separation seems to change with the variation in boron content in the glasses. The glasses with 2 wt.%  $\text{B}_2\text{O}_3$  (Fig. 4.35a) showed nucleated droplet phase separation while spinodal decomposition was observed with addition of 5 wt.%  $\text{B}_2\text{O}_3$  (7-5B) (Fig. 4.35b). Further, with an increasing  $\text{B}_2\text{O}_3$  in the glasses, nucleated droplet phase separation was observed (Fig. 4.35c). A large number of homogeneously distributed round shaped droplets of size 150-200 nm were observed in as cast and annealed glass 7-20B (Fig. 4.35d). Due to lack of

transparency and strong tendency for phase separation, this particular composition was not considered for further investigation.

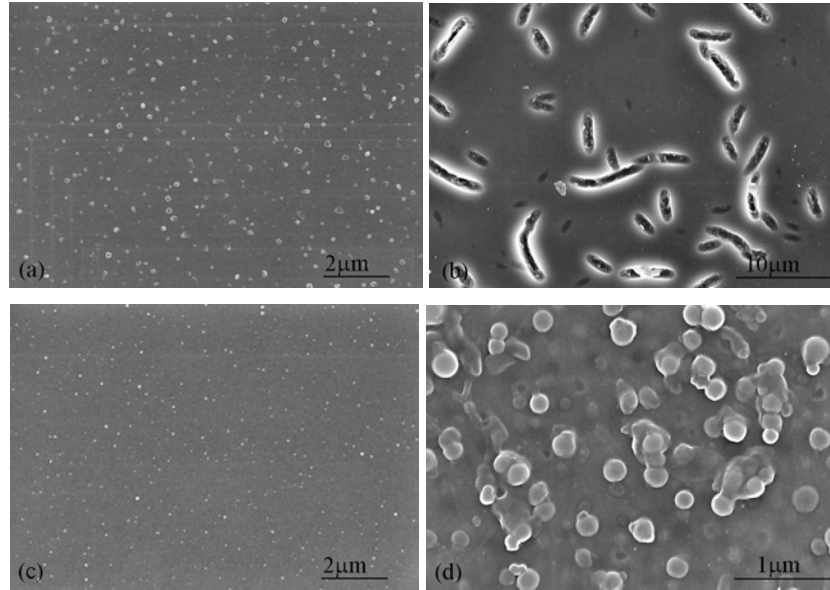


Fig. 4.35 SEM images of glasses (a) 7-2B, (b) 7-5B, (c) 7-10B after heat treatment at 700 °C for 1 h, respectively and (d) 7-20B (as casted and annealed at 550°C for 1h).

#### 4.4.3 Density measurements

The experimental results showed an increase in the apparent density of the glasses with increasing  $\text{La}_2\text{O}_3$  content because the latter has almost two times the density of CaO. However, the addition of  $\text{Cr}_2\text{O}_3$  did not show any considerable affect on these parameters (Table 4.16). Further, addition of  $\text{B}_2\text{O}_3$  led to a decrease in the density ( $\rho$ ) of the glasses (Table 4.16). Since, density of a glass is an additive property and density of  $\text{B}_2\text{O}_3$  is the lowest among all the constituents of the glasses ( $\rho = 2.55 \text{ g cm}^{-3}$ ) except that of  $\text{SiO}_2$  ( $\rho = 2.53 \text{ g cm}^{-3}$ ), therefore, a decrease in density with increasing  $\text{B}_2\text{O}_3$  contents is logical. SrO-containing glasses exhibit lower density than their BaO-containing counterparts because density of SrO ( $\rho = 5.10 \text{ g cm}^{-3}$ ) is lower in comparison to that of BaO ( $\rho = 5.72 \text{ g cm}^{-3}$ ). The molar volume ( $V_m$ ) and excess volume ( $V_e$ ) of glass 7B are higher than glass 7A. Among  $\text{B}_2\text{O}_3$ -containing glasses, the highest values of  $V_m$  and  $V_e$  were obtained for glass 7-15B and the lowest for glass 7-2B. The values of  $V_m$  and  $V_e$  for the glasses under

investigation are higher than the parent glass composition, 7A (Table 4.16). The  $V_m$  for SrO-containing glasses is lower while  $V_e$  is higher than their BaO-containing analogs (7-2B and 7-5B), respectively. The incorporation of  $B_2O_3$  increases the covalent nature of the glasses. Owing to the formation of directional bonds in the structural skeleton of the glass with the increasing  $B_2O_3$  contents, molar volume and excess volume increases [145].

#### 4.4.4 Dilatometry

The  $T_{dg}$  of the glass 7A is higher than the BaO-containing Di-CaTs based glasses investigated in our previous study (section 4.3) (Table 4.16). Since the composition of Di-CaTs based glasses were very similar to the glasses presently under investigation, therefore, it is evident that  $T_{dg}$  increased with the incorporation of  $La_2O_3$  in the glasses (7A). However, with further addition of  $La_2O_3$  (glass 7B), the  $T_{dg}$  was observed to decrease. The CTE of all the four B-free glasses was higher than the previously studied Di-CaTs based glasses (Table 4.13).

In general,  $T_{dg}$ ,  $T_s$  and CTE decreased considerably with introduction of  $B_2O_3$  in the parent glass composition, 7A (Table 4.16). This trend in variation of  $T_{dg}$  and  $T_s$  may be explained on the basis of two competing mechanisms: (a)  $B_2O_3/SiO_2$  ratio in the glasses and (b) conversion of three-coordinated boron ( $B_3$ ) to four-coordinated boron ( $B_4$ ) (as will also be discussed in section 4.4.5). The decrease in  $T_{dg}$  with increase in  $B_2O_3$  content may be attributed to the increasing  $B_2O_3/SiO_2$  ratio in the glasses.  $B_2O_3/SiO_2$  ratio has been reported to have a significant effect on the  $T_g$  and  $T_s$  of the glasses [94, 153]. The activation energies of viscous flow for  $SiO_2$  and  $B_2O_3$  are  $710 \text{ kJ mol}^{-1}$  (1100-1400 °C) and  $347 \text{ kJ mol}^{-1}$ -  $50 \text{ kJ mol}^{-1}$  (26 °C-1300 °C), respectively [157]. Since,  $T_g$  of a glass is a function of its viscosity, therefore, decreasing viscosity implies a decrease in  $T_g$ . Even though, conversion of  $B_3$  to  $B_4$  must have occurred with increasing  $B_2O_3$  content, however, it seems that until glass 7-15B, the concentration of  $B_3$  dominated. Further experimental studies related to the quantification of  $B_3$  and  $B_4$  structural units in these glasses are required to obtain a better insight on the structure of these glasses. The  $T_{dg}$  and  $T_s$  for SrO-containing glasses were lower in comparison to their BaO-containing analogs (Table 4.16)

Table 4.16 Properties of the glasses

|                                                      | 7A    | 7A-Cr | 7B    | 7B-Cr | 7-2B  | 7-5B  | 7-10B | 7-15B | 7(Sr)-2B | 7(Sr)-5B |
|------------------------------------------------------|-------|-------|-------|-------|-------|-------|-------|-------|----------|----------|
| $\rho \pm 0.002$ (g cm <sup>-3</sup> )               | 3.08  | 3.08  | 3.20  | 3.21  | 3.06  | 3.02  | 2.96  | 2.91  | 3.02     | 2.98     |
| $V_m \pm 0.015$ (cm <sup>3</sup> mol <sup>-1</sup> ) | 19.71 | 19.77 | 20.39 | 20.36 | 19.88 | 20.22 | 20.51 | 21.24 | 19.74    | 20.08    |
| $V_e \pm 0.01$ (cm <sup>3</sup> mol <sup>-1</sup> )  | 0.24  | 0.28  | 0.34  | 0.29  | 0.28  | 0.41  | 0.36  | 0.74  | 0.30     | 0.44     |
| $\beta = 5$ K min <sup>-1</sup>                      |       |       |       |       |       |       |       |       |          |          |
| CTE x 10 <sup>6</sup> K <sup>-1</sup> (200-500 °C)   | 8.69  | 8.48  | 8.50  | 8.78  | 7.91  | 7.79  | 7.56  | 7.50  | 7.99     | 8.08     |
| T <sub>dg</sub> ± 2 (°C)                             | 685   | 675   | 630   | 672   | 580   | 575   | 530   | 490   | 533      | 545      |
| T <sub>s</sub> ± 5 (°C)                              | 716   | 721   | 700   | 720   | 710   | 698   | 680   | 665   | 665      | 672      |
| T <sub>FS</sub> ± 5 (°C)                             | 783   | -     | 790   | -     | 776   | 754   | -     | -     | 769      | -        |
| T <sub>MS</sub> ± 5 (°C)                             | 834   | -     | 844   | -     | 829   | 809   | -     | -     | 832      | -        |
| T <sub>c</sub> ± 2 (°C)                              | 882   | 871   | 908   | 886   | 863   | 845   | 823   | 819   | 857      | 840      |
| T <sub>p</sub> ± 2 (°C)                              | 912   | 895   | 951   | 916   | 896   | 874   | 859   | 855   | 891      | 871      |
| T <sub>D</sub> ± 5 (°C)                              | 883   | -     | 884   | -     | 885   | 842   | -     | -     | 850      | -        |
| T <sub>HB</sub> ± 5 (°C)                             | 1307  | -     | 1257  | -     | 1278  | 1239  | -     | -     | 1286     | -        |
| T <sub>F</sub> ± 5 (°C)                              | 1323  | -     | 1312  | -     | 1318  | 1308  | -     | -     | 1355     | -        |
| A/A <sub>0</sub>                                     | 0.68  | -     | 0.64  | -     | 0.64  | 0.66  | -     | -     | 0.67     | -        |
| E <sub>c</sub> (kJ mol <sup>-1</sup> )               | 300   | 213   | 274   | 198   | 255   | 236   | 207   | 184   | 266      | 260      |
| <n>                                                  | 1.85  | 2.16  | 2.03  | 2.18  | 2.22  | 1.77  | 1.78  | 2.21  | 1.82     | 1.67     |

due to the decrease in polymerization of silicate glass network, as discussed in section 4.4.5.

The CTE value decreased with increasing  $B_2O_3$  contents, while the CTE values for glasses 7(Sr)-2B and 7(Sr)-5B were higher in comparison to glasses 7-2B and 7-5B, respectively. According to Ojovan and Lee [124], addition of  $B_2O_3$  up to 15 wt.% in a borosilicate glass decreases the CTE of the glass. The change in the CTE of the glasses with variation of boron content and replacement of Sr for BaO has been explained with the help of FTIR and MAS-NMR analysis of the glasses in the section 4.4.5. However, it should be noted that this anomalous thermal expansion of the glasses with change in  $B_2O_3$  content should not be attributed to the existence of phase separation in these glasses [158]. Similar results have also been reported in glazes where lower amount of boron oxide prevents crazing in glazes, while addition of more than 15 wt.%  $B_2O_3$  shows an opposite effect because the resilience of glazes decreases with high amount of  $B_2O_3$ . This behavior of  $B_2O_3$  in glazes is termed as boracitis [159].

With respect to the development of a suitable GC sealant, optimization of  $T_{dg}$  of the glass is a crucial step, as above  $T_{dg}$  the mechanical properties of the glass change from brittle to elastic. However, the brittle nature of the glass below this temperature makes the seal vulnerable to cracking. Therefore, it is necessary to obtain the seal with low  $T_{dg}$  and  $T_s$ . The  $T_{dg}$  and  $T_s$  values obtained in the present investigation for glasses containing  $\leq 10$  wt.%  $B_2O_3$  are appropriate for sealant application in SOFC.

#### 4.4.5 Structure of glasses

The structural analysis was made on  $B_2O_3$  containing glasses in order to study the influence of increasing  $B_2O_3$  concentration on the structure of glasses and co-relate it with other properties.

##### 4.4.5.1 FTIR analysis

The room temperature FTIR transmittance spectra of all the  $B_2O_3$  containing glasses along with  $B_2O_3$ -free parent glass (7A) are shown in Fig. 4.36. All spectra (except for glass 7A) exhibit four broad transmittance bands in the region of  $300-1500\text{ cm}^{-1}$ . This lack of sharp features is indicative of the general disorder in the silicate network mainly due to a wide distribution of  $Q^n$  (polymerization in the glass structure, where  $n$  denotes the

number of bridging oxygens) units occurring in these glasses. The most intense bands lie in the 800-1300  $\text{cm}^{-1}$  region, the next between 300-600  $\text{cm}^{-1}$  and 1350-1500  $\text{cm}^{-1}$ , while the least intensive lies between 650-800  $\text{cm}^{-1}$ . The broad bands in the 800-1300  $\text{cm}^{-1}$  are assigned to the stretching vibrations of the  $\text{SiO}_4$  tetrahedron with a different number of bridging oxygen atoms, while the bands in the 300-600  $\text{cm}^{-1}$  region are due to bending vibrations of Si-O-Si and Si-O-Al linkages [122, 123]. The transmittance bands in 800-1300  $\text{cm}^{-1}$  region for  $\text{B}_2\text{O}_3$ -containing glasses were registered at considerably lower wave numbers than those observed for  $\text{B}_2\text{O}_3$ -free parent glass, 7A. Thus, it is evident that the introduction of  $\text{B}_2\text{O}_3$  breaks up  $Q^3$  units and favours the formation of  $Q^2$  units. These results are in accordance with those of Ojovan and Lee [124], according to whom, the introduction of boron in the silicate glass leads to the breaking up of  $Q^3$  units and the formation of  $Q^2$ ,  $Q^4$  and small amounts of  $Q^1$  units. A slight shift towards lower wave numbers has been registered in the 800-1300  $\text{cm}^{-1}$  band with the replacement of Ba by Sr. This suggests that the SrO- depolymerizes the silicate glass network in an efficient manner in comparison to BaO. The transmittance bands in the 650-800  $\text{cm}^{-1}$  region are related to the stretching vibrations of the Al-O bonds with  $\text{Al}^{3+}$  ions in four-fold coordination [122]. Aluminum is known to create  $Q^3$  bands at the expense of  $Q^2$  and  $Q^4$  units in the silicate glasses [125]. The transmittance band in the region 1350-500  $\text{cm}^{-1}$  corresponds to B-O vibrations in  $[\text{BO}_3]$  triangle [125]. As is evident from Fig. 2, an increase in  $\text{B}_2\text{O}_3$  content did not affect the silicate glass network. This may be due to the conversion of boron from  $\text{B}_3$  to  $\text{B}_4$  in the presence of alkaline earth ions. In a borosilicate glass, alkali or alkaline earth metals may associate either with silicon, creating non-bridging oxygen (NBO), or with boron, presumably converting a  $\text{BO}_3$  to  $\text{BO}_4$  and creating no NBOs in the process [160]. The bond between a bivalent ion and the centres of two boron-oxygen tetrahedrons is stronger than the bond between outside oxygens of silicon-oxygen tetrahedrons (as is also the case with alkali ions). Therefore, it can be presumed that alkaline earth ions prefer to be associated with the borate component. This increase in connectivity causes the CTE to decrease. This effect has also been observed in alkali-borosilicate glasses and was attributed to the commonly known 'boron anomaly' [160]. Since, the IR band for  $[\text{BO}_4]$  tetrahedron (about 1000  $\text{cm}^{-1}$ ) overlaps with that of stretching vibrations of  $\text{SiO}_4$ , it could not therefore be observed in the present investigation.

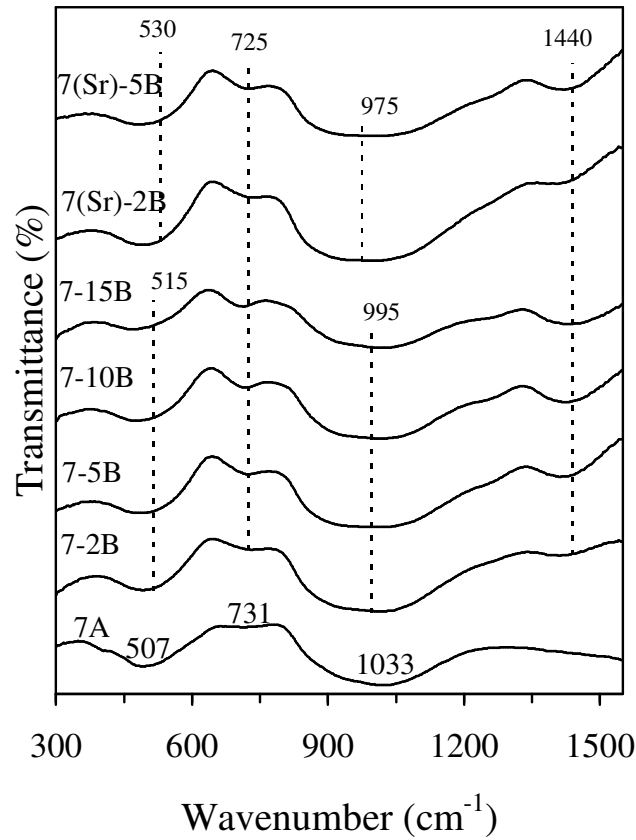


Fig. 4.36 FTIR spectra of the investigated glasses

The results obtained from dilatometry and FTIR analysis show that the network structure of experimental boron containing glasses is complex, containing mostly silicon  $Q^n$  as well as boron  $BO_3$  and  $BO_4$  groups. Due to preferential association of alkaline earth ions with the borate component, conversion of boron from  $BO_3$  to  $BO_4$  occurs with increasing  $B_2O_3$  content, causing the CTE to decrease. This interpretation supports the trends previously observed in borosilicate glasses [124]. Nevertheless, further experimentation including NMR measurements of the concentration  $Q^n$  silicate and borate units is required to better understand the structure of these multicomponent glasses and the composition-property trends observed in the present investigation (section 4.45.2). The above discussed results are in agreement with the results obtained from the calculations of  $V_m$  and  $V_e$ . No other band could be resolved in the spectra of the glasses.

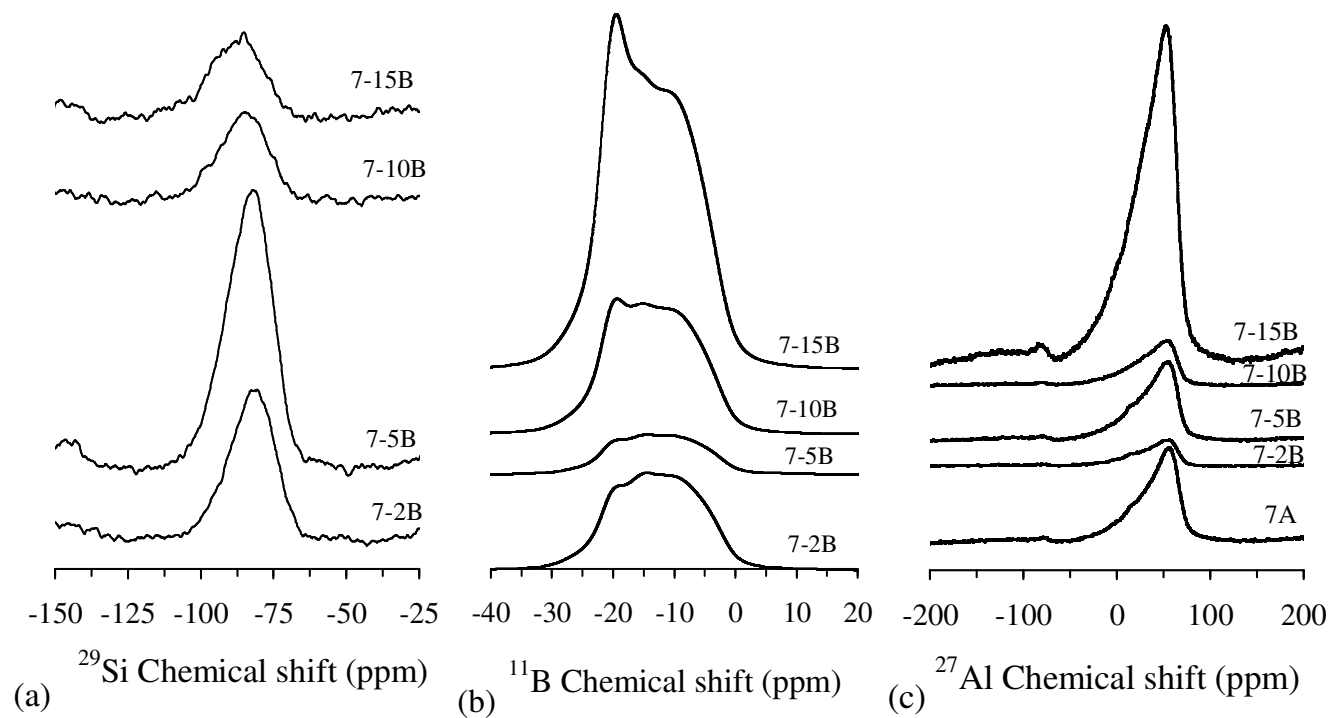


Fig. 4.37 (a)  $^{29}\text{Si}$  MAS-NMR spectra, (b)  $^{11}\text{B}$  MAS-NMR spectra, (c)  $^{27}\text{Al}$  MAS-NMR spectra of the investigated glasses.

#### 4.4.5.2 MAS-NMR structural characterization

Fig. 4.37a depicts the  $^{29}\text{Si}$  MAS-NMR spectra of the glasses 7-2B, 7-5B, 7-10B and 7-15B, all showing a broad resonance band from Si typically found in glasses. The resonance bands of 7-2B and 7-5B glasses are centred at -82 ppm, while the spectra of 7-10B and 7-15B glasses clearly present a little wider resonance bands and slightly shifted down to -85 ppm. These chemical shift values are indicative of a major amount of  $Q^2$ -type silica tetrahedra present in the glass network. The high field shifting and slight broadening of the resonance bands in 7-10B and 7-15B glasses might be interpreted as re-polymerization of the silica glass sub-network as boron content increases in the glasses.

The  $^{11}\text{B}$  MAS-NMR spectra of the same series of glasses is shown in Fig. 4.37b. The broad resonance bands can be observed within the chemical shift range between 0 and -25 ppm. This higher field chemical shift could be attributed to the higher ionic field strength (I.F.S.) of the modifier elements,  $\text{Mg}^{2+}$ ,  $\text{Ca}^{2+}$  and  $\text{Ba}^{2+}$ , when compared to alkaline ones. The spectra of the 7-2B and 7-5B glasses present resonance bands with typical of quadrupolar boron atoms in three-fold coordination, i.e.  $\text{BO}_3$  triangles, meanwhile they do not allow to infer any presence of Gaussian-shape bands corresponding to four-fold coordinated boron atoms, i.e.  $\text{BO}_4$  units. However, 7-10B and 7-15B NMR spectra show an increase in the resonance contribution at -20 ppm, Gaussian type, which could indicate the appearance of a signal due to  $\text{BO}_4$  units as the boron content increased in the glasses.

Fig. 4.37c depicts the  $^{27}\text{Al}$  MAS-NMR spectra of glass 7A and other  $\text{B}_2\text{O}_3$ -containing glasses. All the spectra show an asymmetric and very broad resonance bands typical for quadrupolar aluminium atoms, between 100 and -50 ppm, centred at around 60 ppm. At this level of magnetic field the resolution does not allow to discriminate between different aluminium coordination. According to the chemical shift, most of aluminium atoms would be four-fold coordinated, i.e. forming  $\text{AlO}_4$  tetrahedra. A small shoulder can also be appreciated at around 20 ppm for the glasses 7A, 7-2B and 7-5B, which is not clearly seen in glasses 7-10B and 7-15B, indicating that part of aluminium could be of the type Al(V) for the 7A glass and glasses with low boron contents, disappearing for further boron additions.

#### 4.4.6 Sintering and crystallization behaviour by HSM and DTA

Sealing is usually applied on the surface (ceramic or metallic) to be sealed using powder glass mixed with a binder. The GC formation involves the sintering of glass powders, followed by crystallization at a higher temperature. In order to obtain a good sealing, the sintering stage should precede crystallization as dense and low-porosity materials are desired for obtaining a gas-tight GC seal [139]. Further, crystallization is needed to increase the seal viscosity and improve the chemical and mechanical durability of the sealant, which has to maintain the bulk stability and not flow during operation at high temperature. Therefore, for the development of a suitable GC sealant, it is necessary to understand the sintering and crystallization behaviour of the glass system [93].

During the sintering of a GPC with a size distribution of glass particles, small particles get sintered first as shown by Prado *et al.* [161]. Thus, sintering kinetics at first shrinkage is dominated by the neck formation among smallest particles by viscous flow and is best described by the Frenkel model of sintering [162]. Maximum shrinkage is reached when larger pores (pores formed from cavities among larger particles) have disappeared due to viscous flow that reduces their radii with time. This region of sintering kinetics may be described by the Mackenzie-Shuttleworth model of sintering [163]. However, various physical processes (entrapped insoluble gases, crystallization) occurring at the very end of sintering process might affect the densification kinetics. A comparison between DTA and HSM results under the same heating conditions can be useful to investigate the effect of glass composition on sintering and devitrification phenomena. In general, two different trends can be observed related to the sintering and crystallization behaviour of the glasses [139]. In the first case, the beginning of crystallization ( $T_c$ ) occurs after the final sintering stage. Thus, under such circumstances, sintering and crystallization are independent processes. However, in other case,  $T_c$  appears before maximum density has been reached. In this case, the crystallization process starts before complete densification, thus, preventing further sintering.

On the basis of the relation between the temperatures measured by HSM and their corresponding viscosities, the following characteristic viscosity points have been defined [112]:

(a) *First shrinkage or sintering* ( $T_{FS}$ ): the temperature at which the pressed sample starts to shrink ( $\log \eta = 9.1 \pm 0.1$ ), where  $\eta$  is the viscosity.

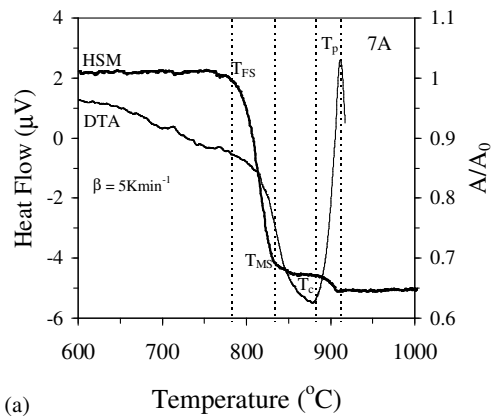
(b) *Point of maximum shrinkage* ( $T_{MS}$ ): the temperature at which maximum shrinkage of the glass powder compact takes place before it starts to soften ( $\log\eta = 7.8 \pm 0.1$ ).

(c) *Softening point* ( $T_D$ ): the temperature at which the first signs of softening are observed. This is generally shown by the disappearance or rounding of the small protrusions at the edges of the sample ( $\log\eta = 6.3 \pm 0.1$ ).

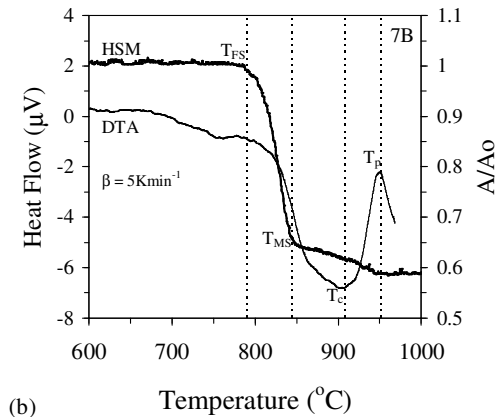
(d) *Half ball point* ( $T_{HB}$ ): the temperature at which the section of the sample observed forms a semicircle on the microscope grid ( $\log\eta = 4.1 \pm 0.1$ ).

(e) *Flow point* ( $T_F$ ): the temperature at which the maximum height of the drop of the molten glass corresponds to a unit on the microscopic scale ( $\log\eta = 3.4 \pm 0.1$ ).

Since, it was observed that glasses with  $B_2O_3 > 5 \text{ wt}\%$  showed poor sinterability and the resultant GCs were highly porous (will be discussed in section 4.4.8), thus rendered unfit for sealing applications in SOFC; therefore, glasses with  $B_2O_3 > 5 \text{ wt}\%$  were excluded from HSM investigation in the present study. Also, since the molar concentration of BaO in 7-2B and 7-5B is equal to that of SrO in 7(Sr)-2B and 7(Sr)-5B, respectively. Therefore, in order to observe the effect of replacement of BaO by SrO on the sintering ability and crystallization of the glass powders, glass 7(Sr)-2B was chosen and the results were compared with those of glass 7-2B. Further, influence of  $Cr_2O_3$  on the sintering behaviour of glasses will be presented while discussing next series of glasses (section 4.5).



(a)



(b)

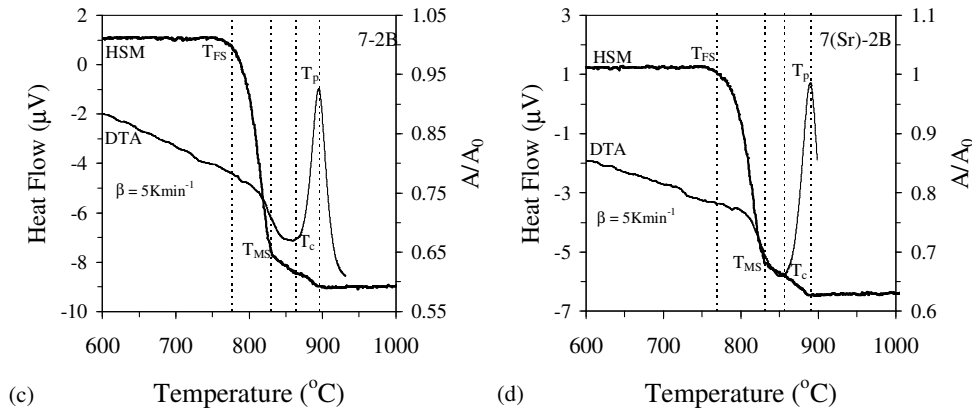


Fig. 4.38 Comparison of DTA and HSM curves on the same temperature scale for compositions (a) 7A, (b) 7B, (c) 7-2B, (d) 7(Sr)-2B.

Therefore, in the present investigation, HSM data in conjunction with DTA data will be used to study the effect of  $\text{La}_2\text{O}_3$  and  $\text{B}_2\text{O}_3$  ( $\leq 5$  wt.%) on the sintering ability of diopside based GC sealants. However, a detailed analysis of crystallization kinetics on all the 10 glass compositions will be presented and discussed in this section. The variation in the relative area and heat flow with respect to temperature as obtained from HSM and DTA, respectively for glasses 7A, 7B, 7-2B and 7(Sr)-2B at heating rate ( $\beta$ ) =  $5 \text{ K min}^{-1}$  is presented in Fig. 4.38 while Fig. 4.39 presents photomicrographs of the changes in geometric shape of the glasses 7A, 7B, 7-2B and 7-5B with respect to temperature, as obtained from HSM. Table 4.16 lists the characteristic temperatures for all the 5 glasses as obtained by HSM ( $T_{FS}$ ,  $T_{MS}$ ,  $T_D$ ,  $T_{HB}$ ,  $T_F$ ) and DTA ( $T_c$ ,  $T_p$ ).  $A/A_0$  corresponds to the ratio of final area /initial area of the glass powder compact.  $A/A_0 \approx 0.65$  at  $T_{MS}$  (as presented in Table 4.16) implies towards good densification (95-98%) [139].

#### 4.4.6.1 Effect of $\text{La}_2\text{O}_3$

Fig. 4.38a and 4.38b present the DTA and HSM data for glasses 7A and 7B, respectively while their characteristic temperatures are listed in Table 4.16. It is evident that  $T_{dg}$  considerably decreases, while  $T_c$  increases with increasing  $\text{La}_2\text{O}_3$  content. Therefore, the difference between  $T_c$  and  $T_{dg}$  (i.e.  $T_c - T_{dg}$ ) is higher for glass 7B in comparison to glass 7A implying towards an increase in glass stability versus crystallization. Sinterability parameter, as defined by  $T_c - T_{MS}$  [139] is also higher for 7B

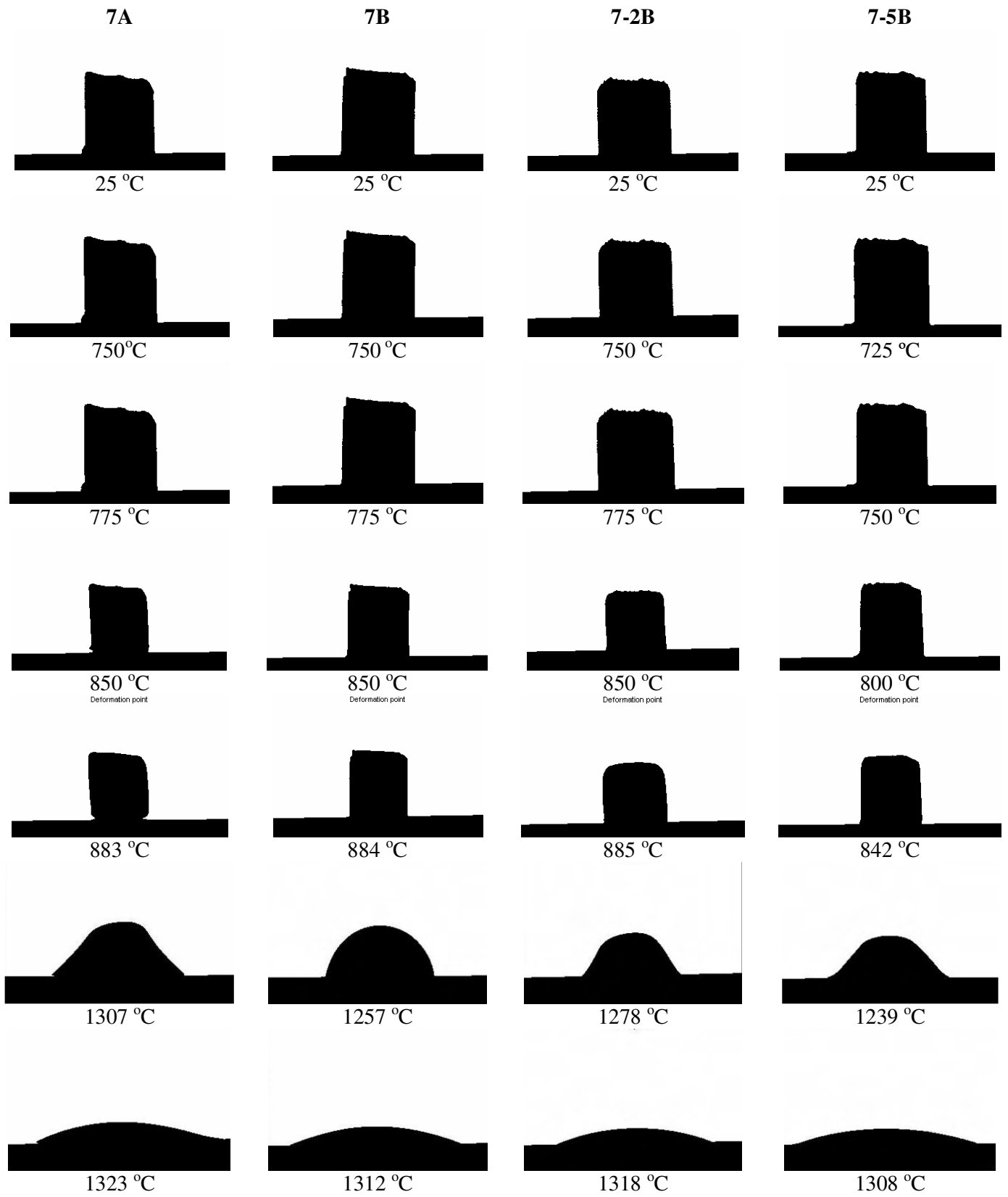


Fig. 4.39 HSM images of glasses on alumina substrates at various stages of heating cycle.

( $T_c - T_{MS} = 64$ ) in comparison to 7A ( $T_c - T_{MS} = 48$ ). These two factors are indicative of a better sintering-crystallization behaviour of 7B composition. The  $T_D$  for both the compositions was almost unaffected by the  $La_2O_3$  content (Table 4.16). With further increase in temperature, half ball ( $T_{HB}$ ) was formed for glass 7B at 1257 °C, which is 50 °C lower than for glass 7A (Fig. 4.39). This was followed by the complete flow of glass 7B at lower temperature than that for glass 7A. The decrease in  $T_{HB}$  and  $T_F$  for composition 7B may be attributed to the presence of low melting crystalline phase calcium lanthanum oxide silicate (ICDD: 01-071-1368) along with augite (ICDD: 01-078-1392) instead of a mono-mineral GC with augite as the only crystalline phase, as will be discussed in section 4.4.8.

#### 4.4.6.2 Effect of $B_2O_3$

With respect to a comparison between sintering behaviour of glasses 7A, 7-2B and 7-5B, the temperature for initiation of sintering ( $T_{FS}$ ) decreases with increase in  $B_2O_3$  content in the glasses (Table 4.16). The temperature for maximum shrinkage ( $T_{MS}$ ) showed a small decrease with initial addition of  $B_2O_3$  for glass 7-2B (Fig. 4.38c) in comparison to glass 7A (Fig. 4.38a) while it decreased considerably with addition of 5 wt.%  $B_2O_3$  in glass 7-5B. In all the three investigated glass compositions, sintering and crystallization act as independent processes. The  $T_c$ ,  $T_p$ ,  $T_D$  and  $T_{HB}$  values decreased with increase in  $B_2O_3$  content in the glasses (Table 4.16, Fig. 4.39). The  $T_F$  decreased with addition of  $B_2O_3$  in the parent glass 7A; however, the decrease was not as significant as it was in case of  $T_{HB}$ . When increasing the temperature, boron tends to diminish the coordination index forming triangular units from tetrahedral units, provoking an additional diminution of viscosity at elevated temperatures joined to the thermal effect. This effect is more pronounced when greater is the proportion of boron oxide in the glass composition.

#### 4.4.6.3 Effect of replacement of BaO by SrO

The  $T_{dg}$  value decreased considerably with replacement of BaO (7-2B) by SrO (7-5B) which leads to a greater glass stability ( $T_c - T_{dg}$ ) for the glass with SrO. Similar trend was observed during initiation of sintering as sintering started ( $T_{FS}$ ) in glass composition 7(Sr)-2B at slightly lower temperature than 7-2B (Table 4.16). Sintering preceded crystallization in both the glass compositions. A slight decrease was observed for  $T_c$ ,  $T_p$  and  $T_D$  due to

replacement of BaO by SrO while temperatures for  $T_{HB}$  and  $T_F$  for 7(Sr)-2B were almost similar.

It should be mentioned that sintering preceded crystallization in all the glass compositions in accordance with wide  $T_c$ - $T_{dg}$  range for all the five compositions and no considerable change in the shape of the samples was observed in the range of SOFC operating temperature i.e. 850-1000 °C. Moreover, on the basis of the viscosity criteria defined by Pascual *et al.* [112], viscosity of the investigated sealants at SOFC operation temperature comes out to be in the range of  $10^6$ - $10^8$  dPas. These are the properties expected from good sealant materials. However, still there is need to tailor the flow properties of these GC sealants by reducing half ball and flow temperatures.

#### 4.4.7 Crystallization kinetics of glasses by DTA

Although numerous sealants have been proposed for SOFC [98], very few studies related with crystallization kinetics of GC sealants have been reported in literature [93, 164-166]. Crystallization process plays an important role in determining the properties and applications of GC sealants. For example, an installation process for the Siemens-SOFC required that the sealing glass should be partially viscous at 950 °C for 2-3 h to allow small displacement of the single stack elements after joining at 1000 °C. This can be achieved by using a slow crystallizing glass [167]. Also, the viscosity of GC sealants is affected by the crystallization of parent glasses. Sakaki *et al.* [168] observed an increase in seal viscosity at about 950 °C because of bulk crystallization of wollastonite ( $CaSiO_3$ ) in  $CaO-Al_2O_3-SiO_2$  glass system. Moreover, as discussed in the previous section, sintering should precede crystallization in order to obtain a dense material suitable for a SOFC seal. Uncontrolled crystallization during the initial sintering process can adversely affect the SOFC operation.

In the present study, an intermediate crystallization mechanism (both surface and bulk) has been observed in all the investigated glasses (Table 4.16). The glass composition 7A showed the highest  $E_c$  value among all the investigated sealant compositions. The  $E_c$  of  $La_2O_3$  containing Di-based GC sealants is lower than BaO-containing Di-CaTs GC sealants (Table 4.13) while  $E_c$  decreases with further increase in  $La_2O_3$  content. This decrease in  $E_c$  with increase in  $La_2O_3$  may be due to the network modifying effect and clustering of  $La^{3+}$  ions (La-O-La linkages) in the glass structure [169-171]. The  $E_c$  decreased with addition of  $Cr_2O_3$  in the glasses can be ascribed to the nucleation effect of

the former. The  $E_c$  values decreased consistently with increase in  $B_2O_3$  amount in the glasses with glass 7-15B showing the lowest  $E_c$  value. The decrease in  $E_c$  with  $B_2O_3$  addition may be attributed to the lower activation energy of viscous flow of  $B_2O_3$  which allows the crystallization to occur at lower temperature. The replacement of BaO by SrO led to an increase in the  $E_c$  values of glass 7(Sr)-2B and 7(Sr)-5B in comparison to glasses 7-2B and 7-5B. The  $E_c$  value for glass 7A is higher in comparison to barium calcium aluminium silicate (BCAS) GC sealant while  $E_c$  values for glasses 7-2B and 7-5B are lower than BCAS GC sealant [93]. The  $E_c$  values for all the glasses investigated in present study are much lower than that reported for 19.2CaO-18.5SrO-13.2ZnO-1.9B<sub>2</sub>O<sub>3</sub>-2.9Al<sub>2</sub>O<sub>3</sub>-2.0TiO<sub>2</sub>-42.2SiO<sub>2</sub> (mol.%) GC sealant proposed by Zhang *et al.* [165] and by Lahl *et al.* [174] for their sealing glasses.

#### ***4.4.8 Crystalline phase analysis, microstructure and properties of sintered glass powder compacts***

The GPCs (rectangular bars with dimensions of 4x5x50 mm<sup>3</sup> for  $B_2O_3$ -free compositions and circular disc shaped pellets with Ø 20 mm and thickness ~3 mm for  $B_2O_3$ -containing compositions) were sintered and crystallized in accordance with the data obtained from HSM and DTA studies. The  $B_2O_3$ -free glass compositions were sintered and crystallized at three different temperatures i.e. 800, 900 and 1000 °C while  $B_2O_3$  containing compositions were sintered at 800 and 850 °C, for 1 h, respectively.

Further in order to evaluate long term stability of crystalline phases,  $B_2O_3$ -free GC compositions already sintered at 900 °C for 1 h were further heat treated at 900 °C for 300 h while in case of  $B_2O_3$ -containing compositions, GPCs already sintered at 850 °C for 1 h were heat treated at 800 °C for 300 h.

##### ***4.4.8.1 B<sub>2</sub>O<sub>3</sub>-free compositions***

Well-sintered dense GPCs were obtained after heat treatment at 800 °C. There was no evidence of detrimental effects, such as deformation or formation of open porosity, in the temperature interval of 800-1000 °C. Figure 4.40 shows the evolution of crystalline phases in GPCs between 800-1000 °C. The samples were still amorphous after heat treatment at 800 °C. Augite (designated as Aug; ICDD card: 01-078-1392) was developed after 900 °C for 1 h as also confirmed by the SEM images (Fig. 4.41). Calcium lanthanum oxide silicate

(ICDD: 01-071-1368), whose most intensive peaks ( $2\theta = 30.917^\circ$ ) overlap with a peak of augite ( $2\theta = 30.914^\circ$ ), was revealed in the 7B and 7B-Cr as the secondary phase. It is worth noting that monomineral GCs of augite were developed in both 7A and 7A-Cr (Fig. 4.40a and 4.40b) although in the former one the low intensive peak at  $2\theta=19.04^\circ$  was not resolved.

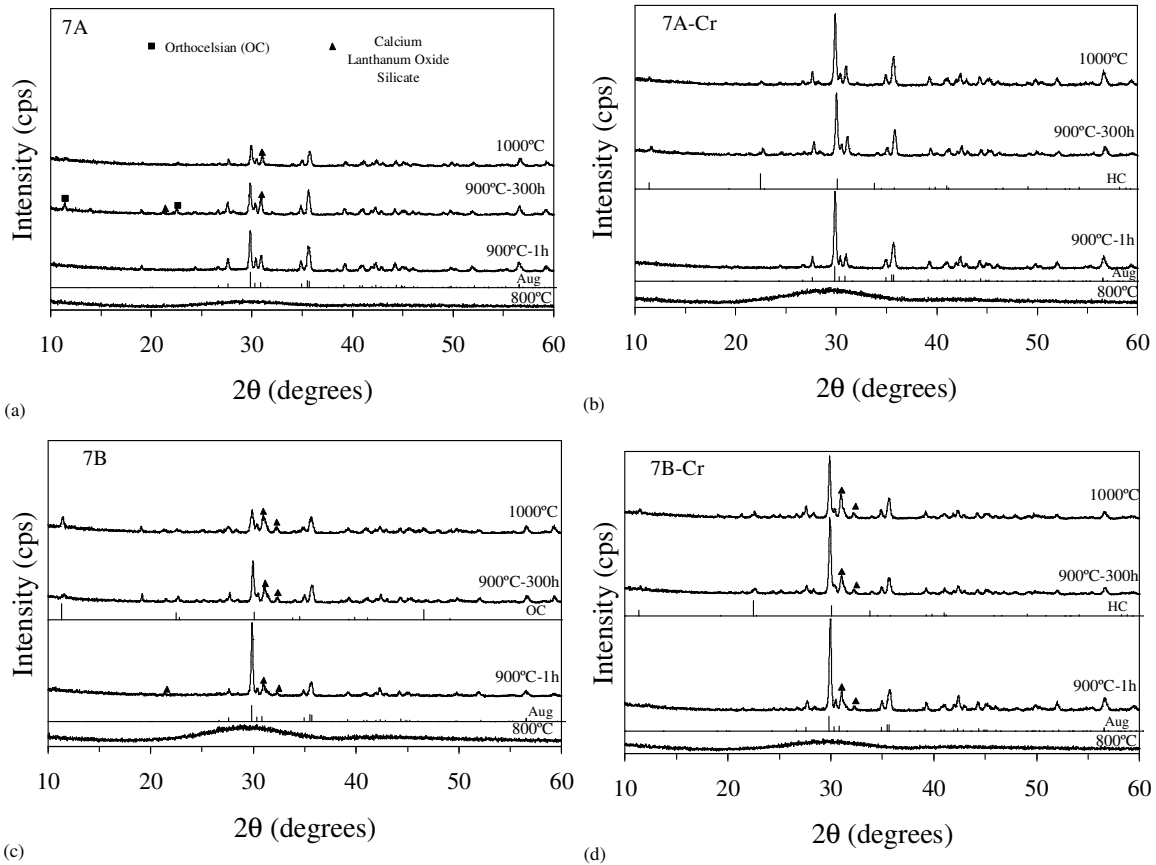


Fig. 4.40 X-ray diffractograms of glass-powder compacts of (a) 7A, (b) 7A-Cr, (c) 7B and (d) 7B-Cr after heat treatment at different temperatures for 1 h and at 900 °C for 300 h. (The spectra have not been normalized. Full scale of intensity axes 7500 cps).

A similar crystalline regime is generally suggested from the XRD patterns at 1000 °C (Fig. 4.40), but the intensity of the crystalline phases in the chromium-free compositions considerably decayed (more in 7A) due to dissolution effect. Moreover, calcium lanthanum

oxide silicate phase was apparently more developed in 7B. From the overall analysis of

Prolonged heat treatment at 900 °C for 300 h did not cause significant decrease in the intensities of the augite phase in the diffractograms of the GCs (Fig. 4.40). Two polymorphs of  $\text{BaAl}_2\text{Si}_2\text{O}_8$ , hexacelsian (designated as HC; ICDD card: 01-088-1048) and orthocelsian (designated as OC; ICDD card: 00-012-0725) were formed in chromium-containing (7A-Cr and 7B-Cr) and in chromium-free (7A and 7B) compositions, respectively. Calcium lanthanum oxide silicate appeared as a newly developed phase in 7A and was registered in all the compositions except 7A-Cr. The peak at  $2\theta=19.04$  was not resolved in both 7A and 7B. XRD patterns for chromium-containing GCs featured highest intensity of the Aug, indicating improved crystallinity with  $\text{Cr}_2\text{O}_3$  doping, as well demonstrated from SEM images presented in Fig. 4.41c, d.

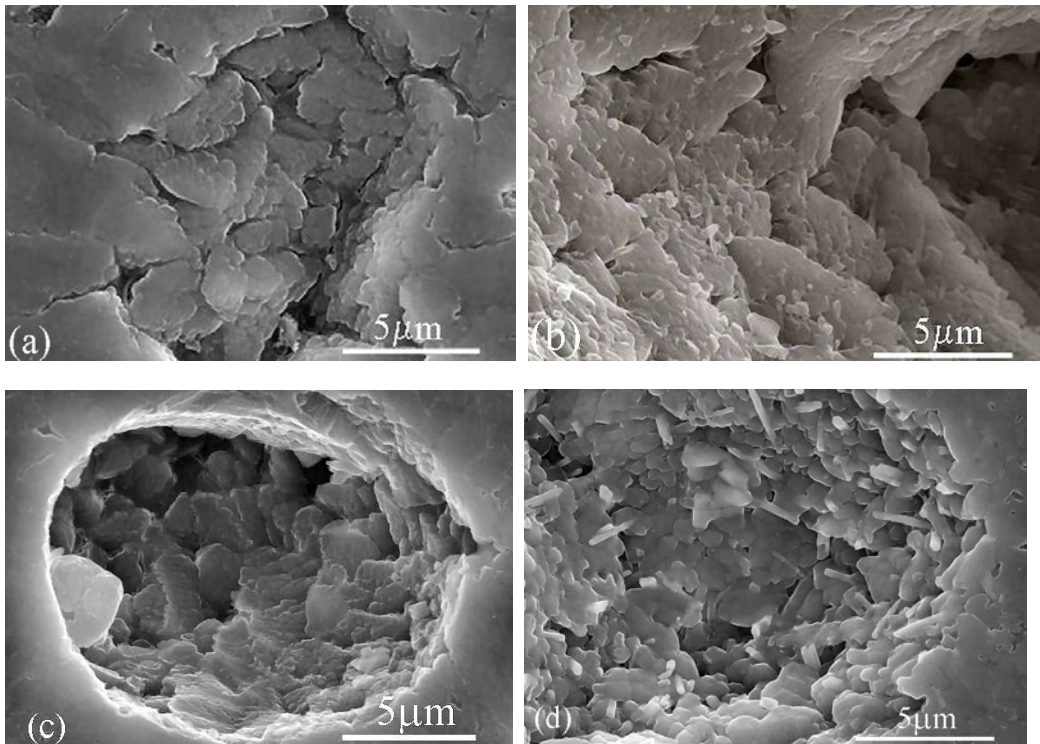


Fig. 4.41 Microstructure (revealed via SEM imaging after chemical etching of polished surfaces with 2 vol.% HF solution) of the glass-ceramics 7A heat treated at (a) 900 °C and (b) 1000 °C; 7B at 900 °C and (d) 1000 °C.

Table 4.17 Properties of the sintered glass-ceramics produced from GPCs after heat treatment at different temperatures for 1 h.

| Composition                        | 800 °C         | 900 °C         | 1000 °C        |
|------------------------------------|----------------|----------------|----------------|
| <i>Shrinkage (%)</i>               |                |                |                |
| 7-A                                | 15.52 ± 0.13   | 16.58 ± 0.41   | 16.60 ± 0.43   |
| 7A-Cr                              | 14.87 ± 0.25   | 15.30 ± 0.21   | 15.29 ± 0.31   |
| 7-B                                | 15.72 ± 0.24   | 16.90 ± 0.56   | 17.50 ± 0.58   |
| 7B-Cr                              | 14.73 ± 0.37   | 15.55 ± 0.29   | 15.86 ± 0.27   |
| <i>Density (g cm<sup>-3</sup>)</i> |                |                |                |
| 7A                                 | 3.05 ± 0.002   | 3.19 ± 0.005   | 3.19 ± 0.004   |
| 7A-Cr                              | 3.07 ± 0.005   | 3.14 ± 0.004   | 3.15 ± 0.003   |
| 7-B                                | 3.19±0.005     | 3.28 ± 0.006   | 3.29 ± 0.005   |
| 7B-Cr                              | 3.19 ± 0.005   | 3.25 ± 0.008   | 3.25 ± 0.005   |
| <i>Bending strength (MPa)</i>      |                |                |                |
| 7-A                                | 94.67 ± 15.90  | 136.31 ± 13.59 | 162.51 ± 8.44  |
| 7A-Cr                              | 103.36 ± 18.59 | 148.73 ± 9.19  | 154.61 ± 12.52 |
| 7-B                                | 99.48 ± 17.07  | 145.35 ± 9.47  | 134.29 ± 2.07  |
| 7B-Cr                              | 104.18 ± 16.76 | 149.27 ± 13.77 | 177.84 ± 13.78 |

The linear shrinkage of the samples increased with an increase in temperature as the highest values of shrinkage (with SD less than 5%) for all the compositions were reached between the temperature interval of 900 °C and 1000 °C (Table 4.17). In terms of composition, shrinkage systematically decreased for Cr<sub>2</sub>O<sub>3</sub> containing GCs in comparison to Cr-free analogues. In accordance with shrinkage measurements, all GCs showed the highest density between the temperature interval of 900 °C and 1000 °C (Table 4.17). In general, the density of the GCs increased with the increase in La<sub>2</sub>O<sub>3</sub> content; however, the Cr<sub>2</sub>O<sub>3</sub> containing compositions had the lower density values in comparison to their Cr-free counterparts at any specific temperature. It is worth noting that all the GCs showed good

stability in terms of small density variations with temperature increasing in the range 900-1000 °C. In general, the bending strength increased with the increase in the temperature, irrespective of the compositions of the glasses or GCs. Nevertheless, La<sub>2</sub>O<sub>3</sub>-content had a mixed effect on the bending strength of the produced GCs (Table 4.17). For composition 7A, a maximum value (163 MPa) was observed at 1000 °C. However, for 7B, that maintained higher strength than 7A at 800 and 900 °C, it decreased at 1000 °C. The Cr<sub>2</sub>O<sub>3</sub>-containing compositions generally possessed higher bending strength in comparison to their Cr<sub>2</sub>O<sub>3</sub>-free analogues and GC 7B-Cr showed highest bending strength in comparison to other compositions, 178 MPa after sintering at 1000 °C.

Table 4.18 CTE×10<sup>6</sup> (K<sup>-1</sup>) of the GCs produced under different conditions together with the CTE of yttria stabilized cubic zirconia (8YSZ).

| Composition | 900 °C, 1 h | 1000 °C, 1 h | 900 °C, 300 h |
|-------------|-------------|--------------|---------------|
| 7-A         | 9.50        | 9.54         | 9.69          |
| 7A-Cr       | 9.62        | 9.62         | 9.62          |
| 7-B         | 9.49        | 9.34         | 8.28          |
| 7B-Cr       | 10.28       | 9.68         | 9.41          |
| 8YSZ        |             | 10.01        |               |

The CTE values of the GCs sintered at 900 °C and 1000 °C for 1 h are presented in Table 4.18. The GCs sintered at 900 °C showed higher CTE than those sintered at 1000 °C except composition 7A-Cr which featured a stable CTE value at all investigated temperatures (9.62×10<sup>-6</sup> K<sup>-1</sup>). La<sub>2</sub>O<sub>3</sub> content did not affect significantly the CTE of the GCs, however, Cr<sub>2</sub>O<sub>3</sub> addition increased the CTE of the GCs. The highest CTE was calculated for composition 7B-Cr sintered at 900 °C. The CTE values of both 7B and 7B-Cr decreased considerably after prolonged isothermal heat treatment at 900 °C for 300 h while the CTE of the GC 7A slightly increased. Generally, CTE values of 7A, 7A-Cr and 7B-Cr match fairly well the CTE of 8YSZ that varies in the range (9.8-10.4)×10<sup>-6</sup> K<sup>-1</sup> at the SOFC operation temperatures. In this work, the CTE (200-600 °C) of 8YSZ was determined as 10.01×10<sup>-6</sup> K<sup>-1</sup>.

The electrical conductivity of 7A and 7B GCs is as low as  $(1.1-1.3)\times 10^{-7}$  S cm<sup>-1</sup> at 780 °C and  $(2.2-2.5)\times 10^{-7}$  S cm<sup>-1</sup> at 880 °C, and tends to decrease with lanthanum additions. The introduction of 0.5 wt.% Cr<sub>2</sub>O<sub>3</sub> results in 1.6-2.0 times higher conductivity. Nonetheless, the latter GCs exhibit better insulating properties if compared to the La- and Cr-free analogue, Ca<sub>0.8</sub>Ba<sub>0.2</sub>Mg<sub>0.8</sub>Al<sub>0.4</sub>Si<sub>1.8</sub>O<sub>4</sub> (Table 4.13). At the same time, the conductivity remains dominantly ionic, as for the BaO-doped materials. Due to very low conductivity of the studied GCs, the contribution of electrode polarization resistance ( $R_{\eta}$ ) to the overall cell resistance was small, lower than 5% with respect to the sample bulk. This indicates that deviations of the cell e.m.f. from the theoretical Nernst voltage cannot be attributed to electrode polarization. The incorporation of variable-valence chromium cations leads, hence, to a moderate increase of the electronic conductivity. One should note that the e.m.f. measurements cannot indicate the exact type of ionic charge carriers when an oxide membrane is placed under an oxygen or metal chemical potential gradient and equilibrium is achieved at the electrodes. The measured transference numbers correspond to the total ionic transport, irrespective of the nature of mobile anions and/or cations. As the content of alkaline metal impurities in the studied GCs is lower than the detection limits of the available analytical techniques, the mobile ionic charge carriers may include alkaline-earth cations such as Mg<sup>2+</sup> and Ca<sup>2+</sup>, oxygen anions and protons. Exact identification of the migrating ionic species by electrochemical methods, such as Faradic efficiency measurements [115], is impossible due to very high resistivity of the studied GCs. However, previous studies of the steady-state oxygen permeation through Ca<sub>0.95</sub>Ba<sub>0.05</sub>Mg<sub>0.8</sub>Al<sub>0.4</sub>Si<sub>1.8</sub>O<sub>6</sub> GCs under air/(H<sub>2</sub>-H<sub>2</sub>O-N<sub>2</sub>) gradient indicated a significant oxygen-ion diffusion and possible protonic contribution; similar mechanisms of the ionic transport are expected in the studied GCs. The activation energy for the total conductivity ( $E_A$ ) calculated by the standard Arrhenius equation,  $\sigma = \frac{\sigma^0}{T} \exp\left(-\frac{E_A}{RT}\right)$ , where  $\sigma^0$  is the pre-exponential factor, has similar values for all studied GCs, varying in the narrow range 172-183 kJ mol<sup>-1</sup> at 780-880 °C (Table 4.19). This fact indicates that, despite the moderate increase of the electronic transport, the conductivity mechanism remains essentially unchanged for all compositions and is similar to that in the BaO-doped GCs. One particular conclusion is that minor diffusion of chromium from the SOFC interconnects should not result in the sealant degradation.

Table 4.19 Activation energy for the total conductivity of glass-ceramics in air.

| Composition                                                                                 | $E_A$ , kJ mol <sup>-1</sup><br>(780-880 °C) |
|---------------------------------------------------------------------------------------------|----------------------------------------------|
| 7A                                                                                          | 172 ± 3                                      |
| 7A-Cr                                                                                       | 180 ± 1                                      |
| 7B                                                                                          | 175 ± 2                                      |
| 7B-Cr                                                                                       | 183 ± 3                                      |
| $\text{Ca}_{0.8}\text{Ba}_{0.2}\text{Mg}_{0.8}\text{Al}_{0.4}\text{Si}_{1.8}\text{O}_6$ [6] | 180 ± 2                                      |

#### 4.4.8.2 $\text{B}_2\text{O}_3$ -containing compositions

In accordance with HSM results, well-sintered dense GPCs were obtained after heat treatment at 800 °C for compositions containing  $\text{B}_2\text{O}_3 \leq 10$  wt.%. Sintering preceded crystallization and the appearance of the samples did not change at higher temperatures. There was no evidence of detrimental effects, such as deformation or formation of open porosity, in the temperature interval of 800-850 °C. At a particular temperature, the shrinkage of BaO- containing compositions increased with addition of  $\text{B}_2\text{O}_3$  content up to 5 wt.% (Table 4.20). Further addition of  $\text{B}_2\text{O}_3$  (7-10B and 7-15B) led to a decrease in shrinkage of the GCs, thus, evidencing poor sinterability. The shrinkage of SrO-containing GCs is almost similar to its BaO-containing counterparts. Among all the investigated compositions, 7-5B showed the highest shrinkage (17.26%) after sintering at 800 °C, while the lowest was exhibited by GC 7-15B (8.35%). The shrinkage results indicate that addition of  $\text{B}_2\text{O}_3$  up to 5 wt.% in the glasses improves the sintering ability of the GPCs, which will further reduce the porosity of the resultant GCs and improve their mechanical strength.

The evolution of crystalline regime of the GPCs at 800 °C and 850 °C (for 1 h) is demonstrated in the X-ray diffractograms of Fig. 4.42, while characteristic microstructures observed by SEM) are shown in Fig. 4.43. The glass compositions 7A, 7-2B and 7(Sr)-2B were highly amorphous after heat treatment at 800 °C. The addition of 2 wt.%  $\text{B}_2\text{O}_3$  in 7A (7-2B) led to the initiation of crystallinity in the resultant GC 7-2B, which was confirmed

Table 4.20 Properties of the sintered GCs produced from GPCs after heat treatment at different temperatures for 1 h.

| Composition                        | 800 °C                    | 850 °C       |
|------------------------------------|---------------------------|--------------|
| <i>Shrinkage (%)</i>               |                           |              |
| 7-2B                               | 16.30 ± 0.28              | 16.69 ± 0.36 |
| 7-5B                               | 17.26 ± 0.34              | 17.08 ± 0.25 |
| 7-10B                              | 16.61 ± 0.31              | 16.97 ± 0.56 |
| 7-15B                              | 8.35 ± 0.15               | 8.35 ± 0.15  |
| 7(Sr)-2B                           | 16.45 ± 0.05              | 16.80 ± 0.49 |
| 7(Sr)-5B                           | 17.20 ± 0.18              | 17.15 ± 0.46 |
| <i>Density (g cm<sup>-3</sup>)</i> |                           |              |
| 7-2B                               | 3.04 ± 0.006              | 3.15 ± 0.001 |
| 7-5B                               | 3.11 ± 0.004              | 3.09 ± 0.002 |
| 7-10B                              | 3.02 ± 0.002              | 3.00 ± 0.001 |
| 7-15B                              | Samples are highly porous |              |
| 7(Sr)-2B                           | 3.01 ± 0.003              | 3.09 ± 0.001 |
| 7(Sr)-5B                           | 3.05 ± 0.001              | 3.04 ± 0.005 |

by the existence of very low intensity XRD peaks of augite (designated as Aug; ICDD card: 01-078-1392) (Fig. 4.42a). However, with further increase in B<sub>2</sub>O<sub>3</sub> content and, increase in temperature to 850 °C, augite precipitated out to be the only crystalline phase in all the resultant GCs (Fig. 4.42). No boron containing phases were observed for any of the compositions after sintering for 1 h at 800 °C and 850 °C. However, the intensity of the XRD peaks of the augite was observed to depend on the B<sub>2</sub>O<sub>3</sub> content in the parent glass and was found to be maximum for GC 7-5B at both the temperatures (Fig. 4.43a). The GCs with B<sub>2</sub>O<sub>3</sub> content higher than 5 wt.% showed a considerable decrease in the intensity of the XRD peaks of augite (Fig. 4.42 and Fig. 4.43b), with the GCs containing 15 wt.% B<sub>2</sub>O<sub>3</sub> showing the lowest intensity (Fig. 4.43c) among all the investigated compositions,

implying towards the stabilization of amorphous phase in the GCs. Similar results have recently been reported by Hillers *et al.* [173] where they showed that an aluminosilicate E-glass containing 7 wt.% B<sub>2</sub>O<sub>3</sub> crystallized slowly in comparison to the glass containing 2 wt.% B<sub>2</sub>O<sub>3</sub>. They also did not detect any boron containing crystalline phases; however, crystal growth rate was significantly decreased with the addition of boron in the glasses [173]. The intensity of the XRD peaks of augite in GCs 7(Sr)-2B and 7(Sr)-5B (Fig. 4.42) were lower in comparison to BaO-containing GCs 7-2B and 7-5B, respectively due to the higher activation energy of crystallization of SrO-containing glasses.

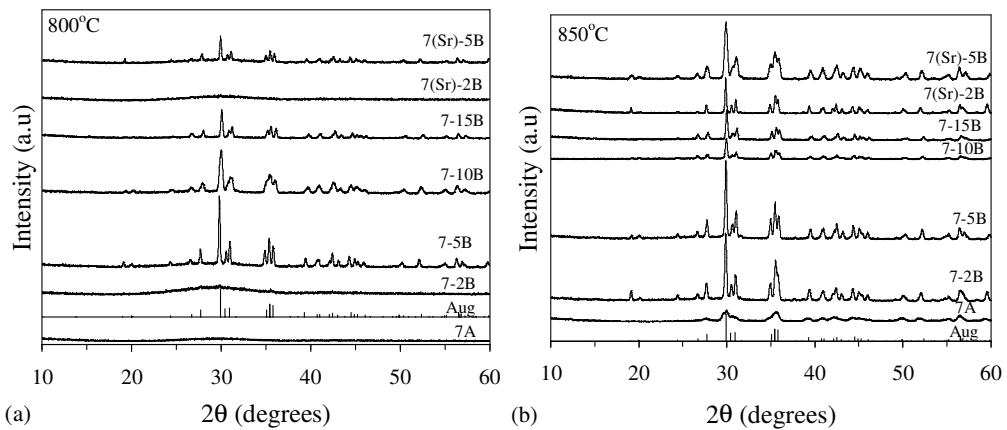


Fig. 4.42 X-ray diffractograms of glass-powder compacts sintered at (a) 800 °C, (b) 850 °C, for 1 h.

The density of the GCs was considerably affected by the extent of crystallinity in the GCs. With respect to temperature, GC 7-5B showed the highest density among all the investigated GCs after sintering at 800 °C, while GC 7-2B exhibited the highest density among all the GCs sintered at 850 °C (Table 4.20). The higher density of GC 7-2B at 850 °C and for 7-5B at 800 °C is in accordance with the shrinkage results and may be explained on the basis of increase in the crystallinity in the GCs at a particular temperature, as is evident from the XRD (Fig. 4.42). We could not measure the density of the GCs from composition 7-15B as these GCs were highly porous in nature. The density of GCs 7(Sr)-2B and 7(Sr)-5B was lower than GCs 7-2B and 7-5B at any particular temperature (Table 4.20). This may be due to the lower density of SrO in comparison to BaO and lower crystallinity in SrO containing GCs in comparison to BaO-containing GCs, as revealed by XRD (Fig. 4.42).

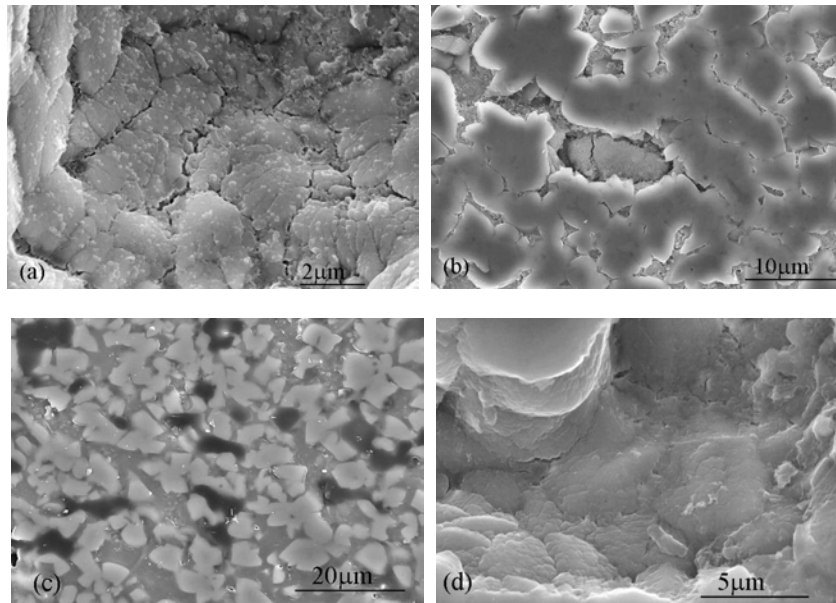


Fig. 4.43 Microstructure (revealed via SEM imaging after chemical etching of polished surfaces with 2 vol.% HF solution) of the GCs (a) 7-5B heat treated at 850 °C (b) 7-10B heat treated at 800 °C (c) 7-15B heat treated at 800 °C and (d) 7(Sr)-2B heat treated at 850 °C for 1 h, respectively.

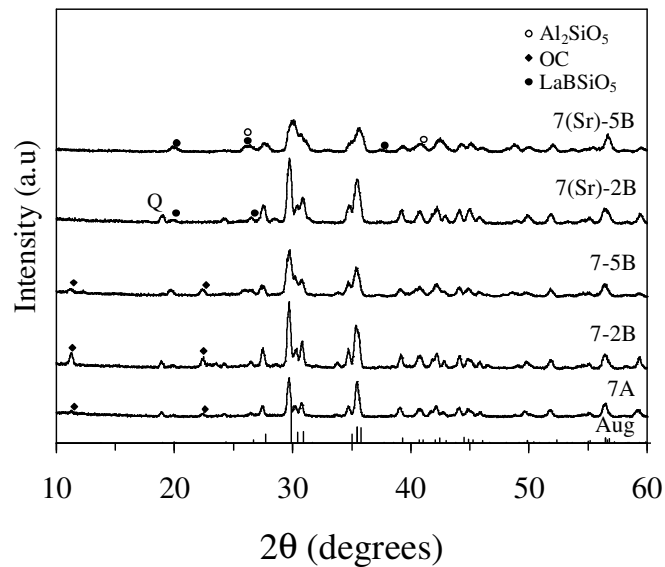


Fig. 4.44 X-ray diffractograms of sintered GCs (850 °C, 1 h) after heat treatment at 800 °C for 300 h.

The results obtained from density and shrinkage measurements indicate that compositions containing 2 and 5 wt.%  $B_2O_3$  exhibit good sintering ability in comparison to higher  $B_2O_3$  content GCs, which is a desirable result with respect to optimization of GC

sealant [98]. Also, as discussed above, glass and GC sealants with high content of B<sub>2</sub>O<sub>3</sub> will degrade the seal. Further more, addition of low amount of B<sub>2</sub>O<sub>3</sub> in the glass will aid in wetting and flowability properties [174].

Prolonged heat treatment of GCs (already sintered at 850°C for 1 h) at 800 °C for 300 h caused a significant variation in the intensities of the augite phase in the BaO-containing GCs (Fig. 4.44). The intensity of augite for GC 7A became almost twice the intensity of the parent GC (sintered at 850 °C for 1 h), while it reduced to half for GC 7-5B after heat treatment at 800 °C for 300 h. No considerable effect on the intensity of augite in GC 7-2B could be observed after long term heat treatment. An orthorhombic polymorph of BaAl<sub>2</sub>Si<sub>2</sub>O<sub>8</sub> (designated as OC; ICDD card: 00-012-0726) was formed in BaO-containing GCs. Interestingly, no considerable effect on the intensity of augite could be observed in SrO-containing GCs after prolonged heat treatment. A boron containing crystalline phase, namely lanthanum boron silicate (designated as LaBSiO<sub>5</sub>; ICDD card: 00-019-0650) was detected in both 7(Sr)-2B and 7(Sr)-5B GCs. No polymorph of Sr-containing celsian in both the SrO-containing GCs was observed. However, minor peaks for SiO<sub>2</sub> (designated as Q; ICDD card: 01-073-3437) and sillimanite (designated as Al<sub>2</sub>SiO<sub>5</sub>; ICDD card: 01-083-1562) were detected in GCs 7(Sr)-2B and 7(Sr)-5B, respectively. It is noteworthy that no monoclinic celsian was detected in any of the investigated compositions even after 300 h of heat treatment.

Table 4.22 CTE×10<sup>6</sup> (K<sup>-1</sup>) (200-600 °C) of the GCs produced under different conditions.

| Composition | 850 °C, 1 h | 800 °C, 300 h |
|-------------|-------------|---------------|
| 7A          | -           | 9.42          |
| 7-2B        | 9.14        | 9.34          |
| 7-5B        | 9.57        | 9.18          |
| 7-10B       | 8.60        | -             |
| 7-15B       | 9.06        | -             |
| 7(Sr)-2B    | 9.69        | 8.99          |
| 7(Sr)-5B    | 9.23        | 8.85          |

The CTE values of the GCs sintered at 850 °C for 1 h and at 800 °C (GCs already sintered at 850 °C for 1h) for 300 h are presented in Table 4.22. Among the GCs sintered at

850 °C for 1 h, the highest value of CTE was shown by 7(Sr)-2B ( $9.69 \times 10^{-6} \text{ K}^{-1}$ ) while the lowest was shown by GC 7-10B ( $8.60 \times 10^{-6} \text{ K}^{-1}$ ). It is noteworthy that the CTE values presented in Table 4.22 are in the temperature range 200–600 °C, while the SOFC operating temperature is in the range 700–850 °C. The selection of this temperature range 200–600 °C was due to the fact that GCs with  $\text{B}_2\text{O}_3$  content  $\geq 5$  wt.% showed an abnormal thermal expansion behaviour in the temperature region 650–750 °C (Fig. 4.45). Also, it should be mentioned that the change in slope of thermal expansion curve was highly prominent in BaO-containing GCs in comparison to SrO based GCs. Recently, similar abnormal thermal expansion behaviour was observed for the GCs obtained from

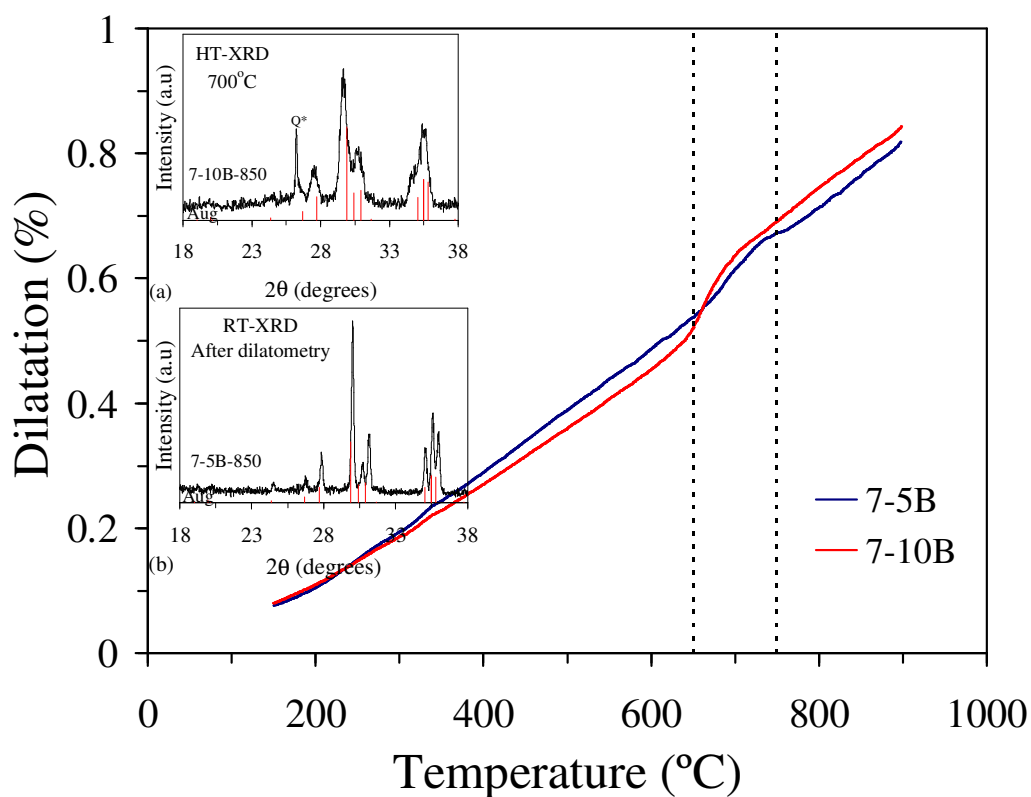


Fig. 4.45 Thermal expansion curve of GCs 7-5B and 7-10B after sintering and crystallization at 850 °C for 1h. Inserts: (a) *In-situ* HT-XRD for GC 7-10B at 700 °C, (b) XRD for GC 7-5B after dilatometry at room temperature.

barium calcium aluminosilicate (BCAS) GC sealant [100]. BCAS GC sealant (contains 10 mol.%  $\text{B}_2\text{O}_3$ ) is the most extensively investigated sealant and has been seen with alacrity

by the SOFC researchers worldwide [98]. The CTE of the BCAS GCs was obtained from room temperature (R.T) to 550 °C, which is far below the SOFC operating temperature [100] and no results pertaining to such abrupt changes in thermal expansion of GCs were discussed. In our opinion, such abrupt changes in thermal expansion of GCs can cause unwanted stresses in the SOFC stack during its operation. According to Shelby [175], similar deviation of thermal expansion curve from linear behaviour can be obtained for a phase separated glass containing two glassy phases, where the more viscous phase is continuous and if the immiscibility temperature for the glass lies above the  $T_g$  of the more viscous phase. The thermal expansion curves of this type have been observed for lead borate and barium silicate glasses, where the immiscibility temperature is greater than the  $T_g$  of either phase [175]. However, in the present investigation, such behaviour has been observed for GCs and not glasses. Therefore, in quest of the reason for the change in the thermal expansion of the GCs in the temperature range 650-750 °C, *in-situ* high temperature XRD was performed on the GCs with  $B_2O_3$  content  $\geq 5$  wt.%. It is worth to be noted that quartz (designated as Q\*, ICDD card: 01-089-8939) precipitated out along with augite in the investigated temperature region in all the GCs (Fig. 4.45, inset a). As shown in Fig. 4.35, the investigated glasses show tendency towards phase separation in to  $SiO_2$  and  $B_2O_3$  rich regions at 700 °C. Similar phase separated regions can also be expected in the glassy phase of the GCs, though with different composition in comparison to their parent glasses. This led to the precipitation of quartz from  $SiO_2$  rich glassy phase during heating of the GC (Fig. 4.45, inset a), consequently, changing the thermal expansion behaviour of the GC. However, according to RT-XRD results of the GCs obtained after dilatometry experiments, augite was the only crystalline phase in all the GCs (Fig. 4.45, inset b). Therefore, it can be suggested that during cooling, the glassy phase in the GC again regained its form, thus leading to the dissolution of previously formed quartz.

We are now in the process of analyzing the expansion behaviour of these GCs during cooling and crystalline phase evolution (through *in-situ* HT-XRD) after long term dwell at SOFC operating temperature.

The CTE value of SrO-containing GCs decreased considerably after prolonged isothermal heat treatment at 800 °C for 300 h due to the simultaneous presence of different crystalline phases while the CTE of the GC 7-2B slightly increased. Generally, CTE values

of 7A, 7-2B and 7-5B match fairly well the CTE of 8YSZ that varies in the range  $(9.8-10.4) \times 10^{-6} \text{ K}^{-1}$  at the SOFC operation temperatures.

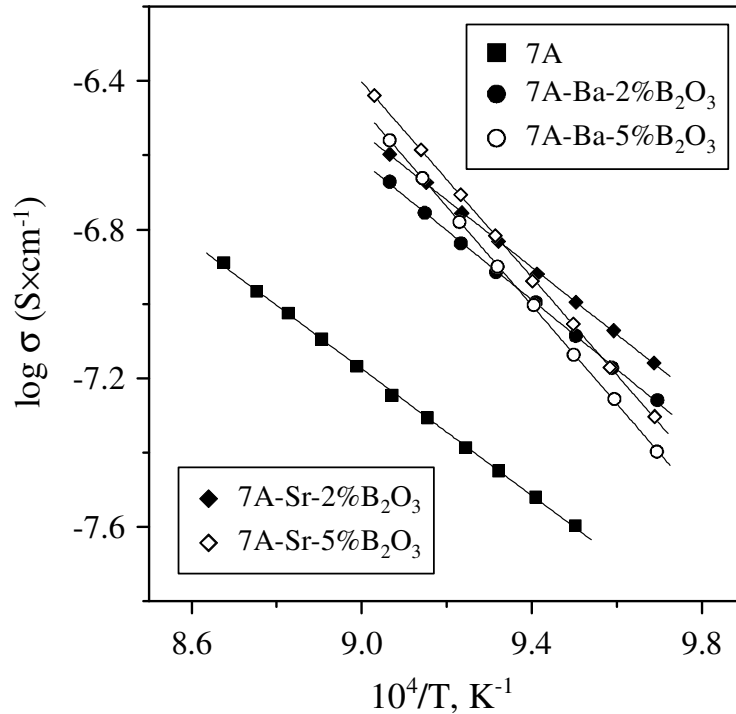


Fig. 4.46 Total conductivity of dense GCs in air. The data on 7A are shown for comparison. The error bars are smaller than the data point symbols.

Small additions of  $\text{B}_2\text{O}_3$  (2 wt.%) resulted in 3-4 times increase of the total conductivity of dense GCs compared to the boron-free GC (7A) (Fig. 4.46). Nevertheless, the conductivity is still as low as  $(2.1-2.5) \times 10^{-7} \text{ S cm}^{-1}$  at 830 °C and  $(5.5-6.9) \times 10^{-8} \text{ S cm}^{-1}$  at 760 °C. Also, the activation energy ( $E_A$ ) is similar to that of parent GC, 7A (Table 4.23), thus indicating that the conduction mechanism remains essentially unchanged. Further increase in the  $\text{B}_2\text{O}_3$  content up to 5 wt.% does not lead to significant variations of total conductivity in the studied temperature range, but results in substantially higher activation energy. Whatever the mechanisms, the results unambiguously show that the studied GCs can be used as sealants for intermediate-temperature SOFCs operating at temperatures below 780-800 °C. A negligible difference in  $E_A$  was observed when BaO was replaced with SrO in the GCs.

Table 4.23 Activation energy for the total conductivity of GCs in air.

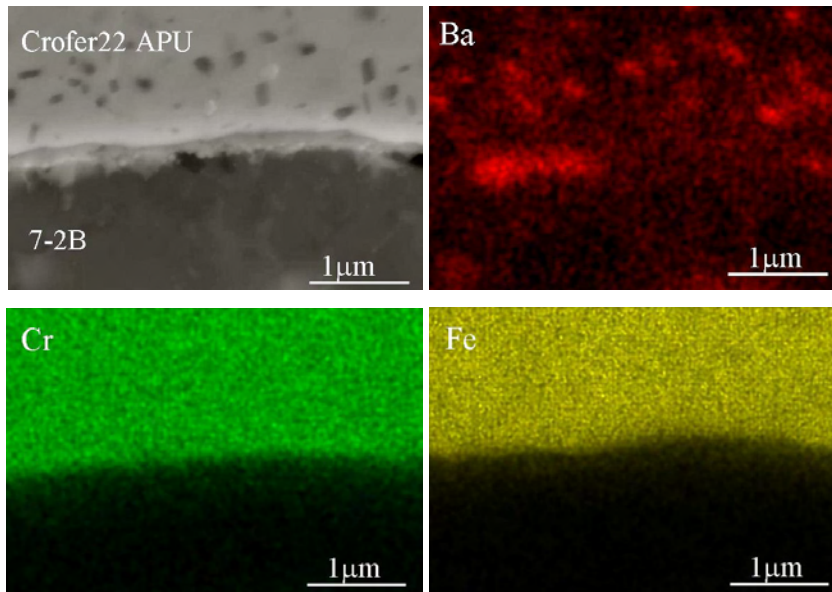
| Glass    | T (°C)  | E <sub>A</sub> (kJ mol <sup>-1</sup> ) |
|----------|---------|----------------------------------------|
| 7A       | 780-880 | 172 ± 3                                |
| 7-2B     | 760-830 | 188 ± 4                                |
| 7-5B     | 760-830 | 263 ± 3                                |
| 7(Sr)-2B | 760-830 | 182 ± 3                                |
| 7(Sr)-5B | 760-830 | 261 ± 3                                |

#### ***4.4.9 Interfacial adhesion, stability and electrical resistivity in contact with solid electrolyte and interconnect materials under different atmospheres***

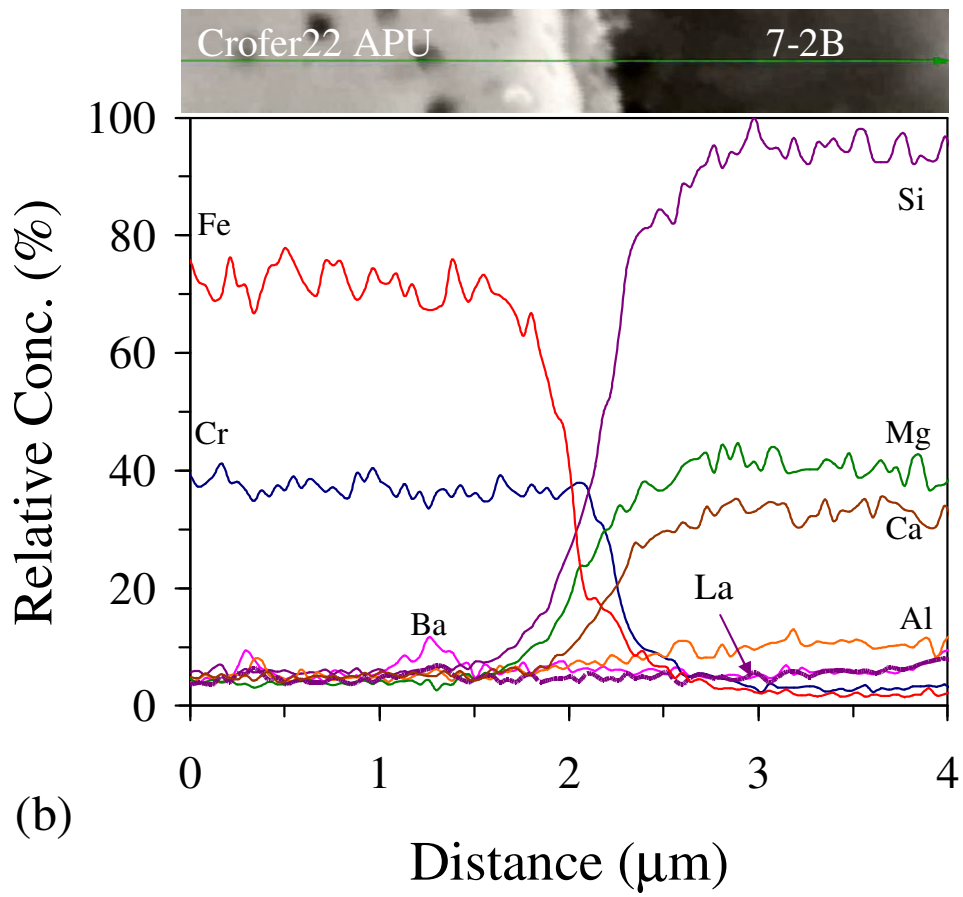
##### *4.4.9.1 In air*

The results of wetting experiments suggest strong interfacial adhesion between investigated compositions and 8YSZ. Good wetting regime was observed (i.e. contact angle < 90°) and continuous interfaces, no reaction zones, no cracks or gaps, were revealed after cross sectioning and polishing. No reaction products were also determined by XRD analysis of compact samples made of the powder mixtures of glasses and 8YSZ after heat treatment under the similar conditions (i.e. 850 °C, 1 h and then 800 °C, 300 h).

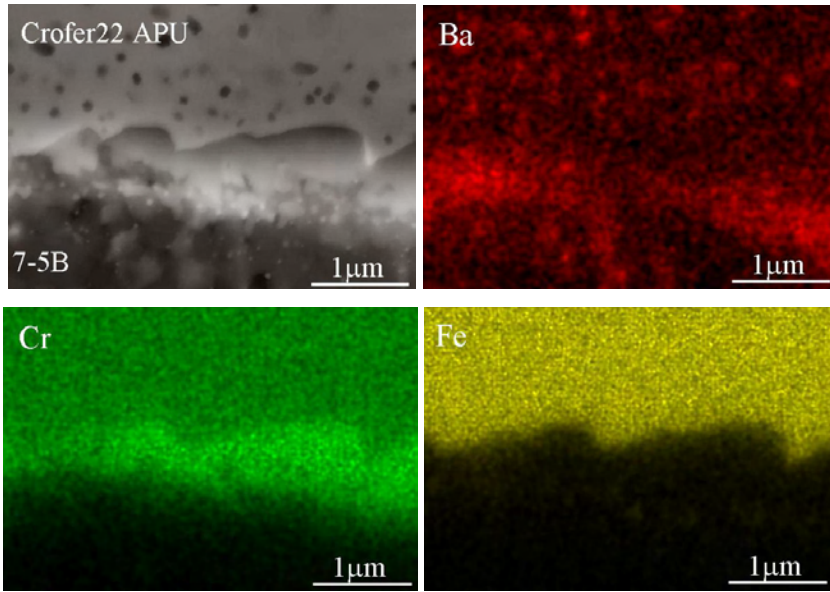
Two SOFC interconnect alloys, Crofer22 APU and Sanergy HT, were investigated for their chemical compatibility with the investigated glasses. All the sealing GCs bonded well to the metallic interconnect and no gaps were observed even at the edges of the joints. Fig. 4.47 shows the SEM images of the interface of interconnect/glass joins, respectively, after heat treatment at 850 °C for 1 h, followed by 800 °C for 300 h in air. The extent of diffusion of constituent elements from the alloy interconnects into the glass and vice versa (Fig. 4.47) has been observed through EDS element mapping and line scanning. As is evident from Fig. 4.47a, an interaction zone of less than submicron thickness, has been formed at the interface between Crofer22 APU and glass 7-2B. From the element mapping of Cr, Fe and Ba (Fig. 4.47a) and the elemental line profile of diffusion of elements (Fig. 4.47b), it is clear that the reaction zone is rich in Ba and Cr and poor in Fe. The concentration of Cr shows an increase at the interface (Fig. 4.47b)



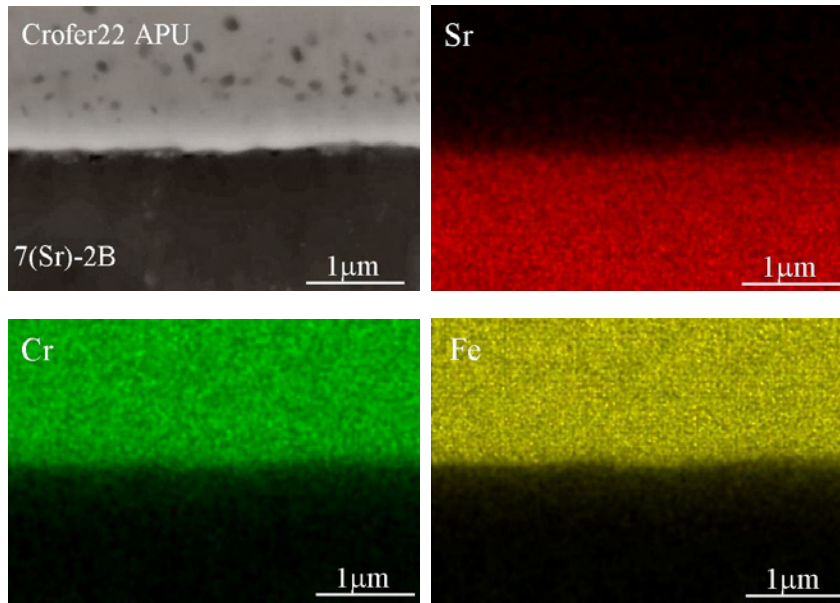
(a)



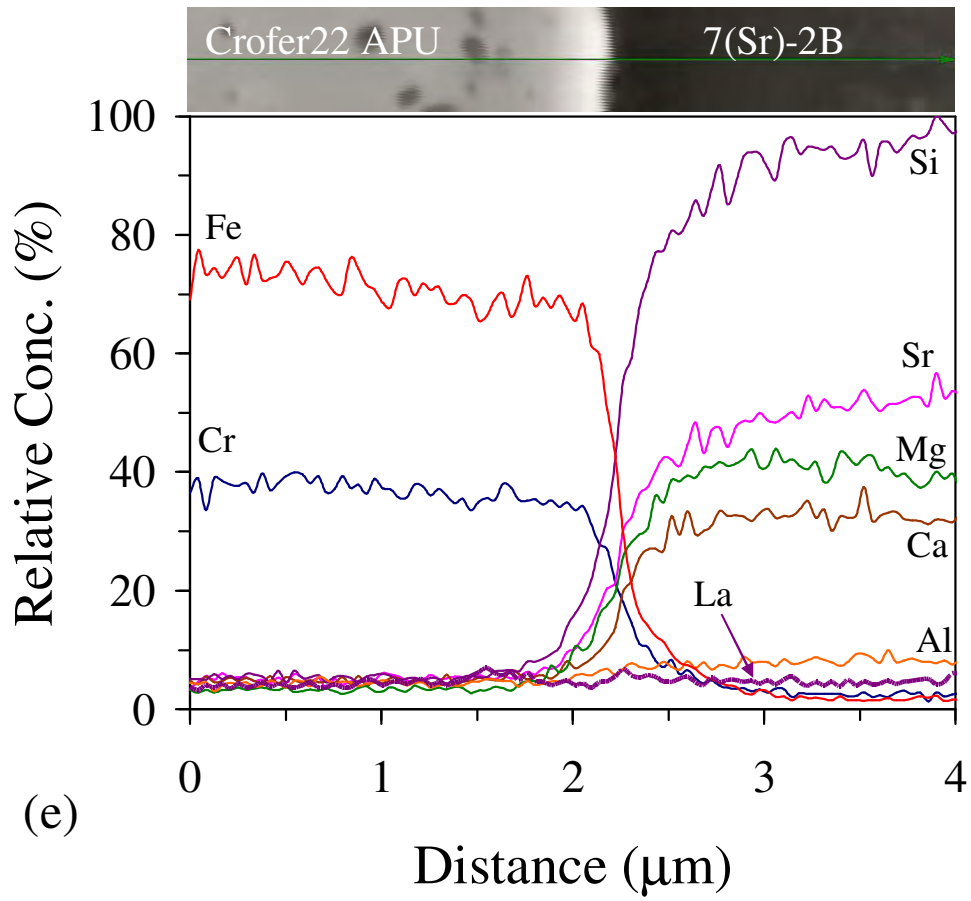
(b)



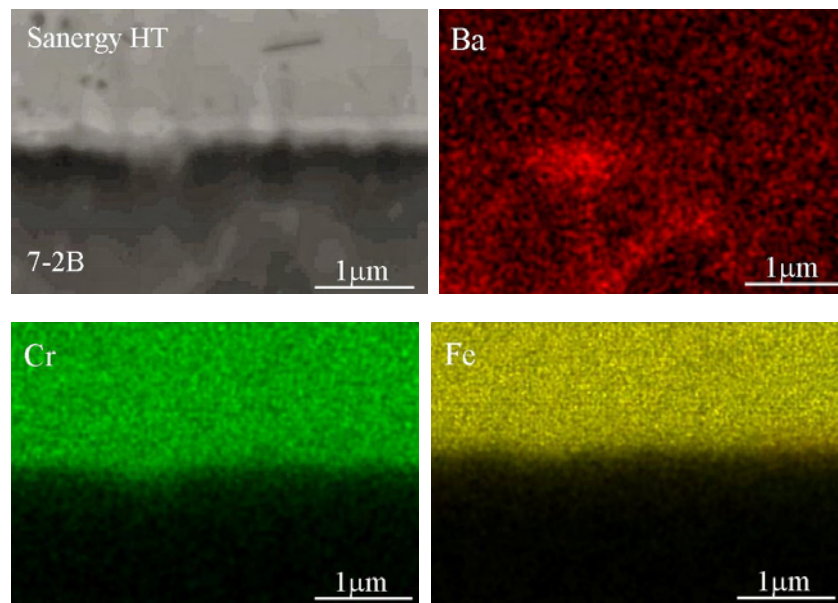
(c)



(d)



(e)



(f)

**Fig. 4.47** (a) Microstructure (SEM) and EDS element mapping of Ba, Cr and Fe at the interface between Crofer22 APU/glass 7-2B (b) EDS line profile for diffusion of various elements from glass 7-2B to Crofer22 APU and vice versa at their interface (c) microstructure (SEM) and EDS element mapping of Ba, Cr and Fe at the interface between Crofer22 APU/glass 7-5B (d) microstructure (SEM) and EDS element mapping of Ba, Cr and Fe at the interface between Crofer22 APU/glass 7(Sr)-2B (e) EDS line profile for diffusion of various elements from glass 7(Sr)-2B to Crofer22 APU and vice versa at their interface (f) microstructure (SEM) and EDS element mapping of Ba, Cr and Fe at the interface between Sanergy HT/glass 7-2B developed after heat treatment at 850 °C for 1 h and 800 °C for 300 h in air.

and then decreases considerably, while the relative concentration profile of Ba is approximately constant across the interface suggesting the absence of diffusion barriers for this element. The thickness of the Cr- and Ba-rich reaction zone at the interface between Crofer22 alloy and glass increased with increase in  $B_2O_3$  content to 5 wt.% (Fig. 4.47b), thus evidencing high reactivity. The EDS element mapping (Fig. 4.47a and c) revealed that the brown spots visible in the interconnect region above the interface are rich in Ba. It is noteworthy that the investigated glasses 7-2B and 7-5B contain 2.50 mol% BaO and 4.38 mol.%  $B_2O_3$  respectively, while the amount of BaO and  $B_2O_3$  in the barium aluminium silicate (BAS) based and BCAS based glass and GC sealing materials varies between 35-45 mol.% and 0-15 mol.%, respectively [98]. If, ~2.5 mol.% BaO in the presence of 4.38 mol.%  $B_2O_3$  can cause such an adverse reaction at the interface of glass/interconnect, then we can definitely expect adverse reaction products for glasses and GCs containing higher amount of BaO and  $B_2O_3$ . SrO-containing glasses, 7-2B and 7-5B showed highly stable interface with Crofer22 alloy (Fig. 4.47d) in comparison to BaO-containing glasses. A good wetting regime and continuous interfaces with minimal reaction zones, no cracks or gaps, were revealed after cross section and polishing. No significant diffusion of Sr into the Crofer22 alloy or formation of Cr-rich reaction product was observed (Fig. 4.47d and e). This shows that Cr rich interface was not formed in the absence of BaO. It has been reported earlier that BaO containing glasses interact chemically with chromia-forming alloys forming  $BaCrO_4$ , which leads to Ba depletion in

the GCs and to the separation of GCs from the alloy matrix due to thermal expansion mismatch [102]. In the present investigation, we did not observe any separation of GC from the alloy matrix after 300 h of heat treatment.

In comparison to Crofer22 APU, the investigated GCs showed a better compatibility with Sanergy HT interconnect alloy (Fig. 4.47f). A thin reaction zone of lower thickness in comparison to that observed with Crofer22 alloy was observed at the interface between glass/Sanergy HT joins. Also, the CTE of Sanergy HT is lower ( $11 \times 10^{-6} \text{ K}^{-1}$ ) than Crofer22 alloy ( $11.6 \times 10^{-6} \text{ K}^{-1}$ ) in the temperature range of 20-700 °C [118, 119], which is good for compatibility with GC sealants. Moreover, it was recently reported that higher amount of Si in the metallic interconnect enhances the rate of corrosion attack, leading to the degradation of the SOFC stack [176] and unfortunately, Crofer22 APU alloy contains higher Si content than Sanergy HT (Table 3.1). Therefore, Sanergy HT seems to be a better candidate as interconnect material in comparison to Crofer22 APU alloy.

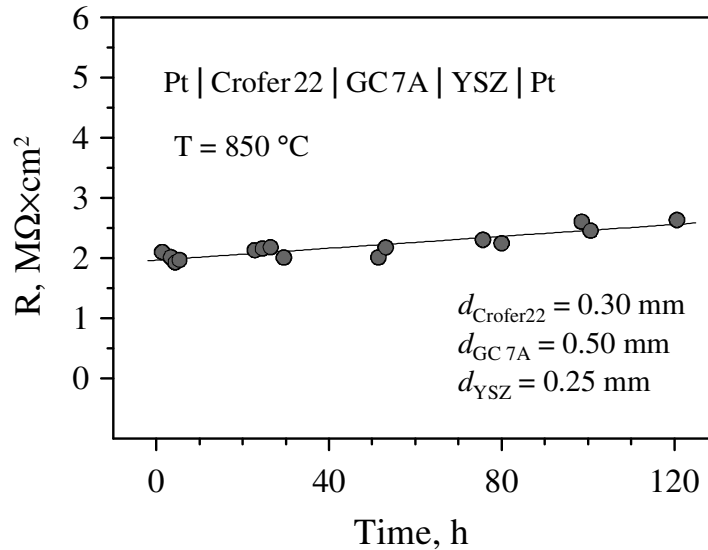


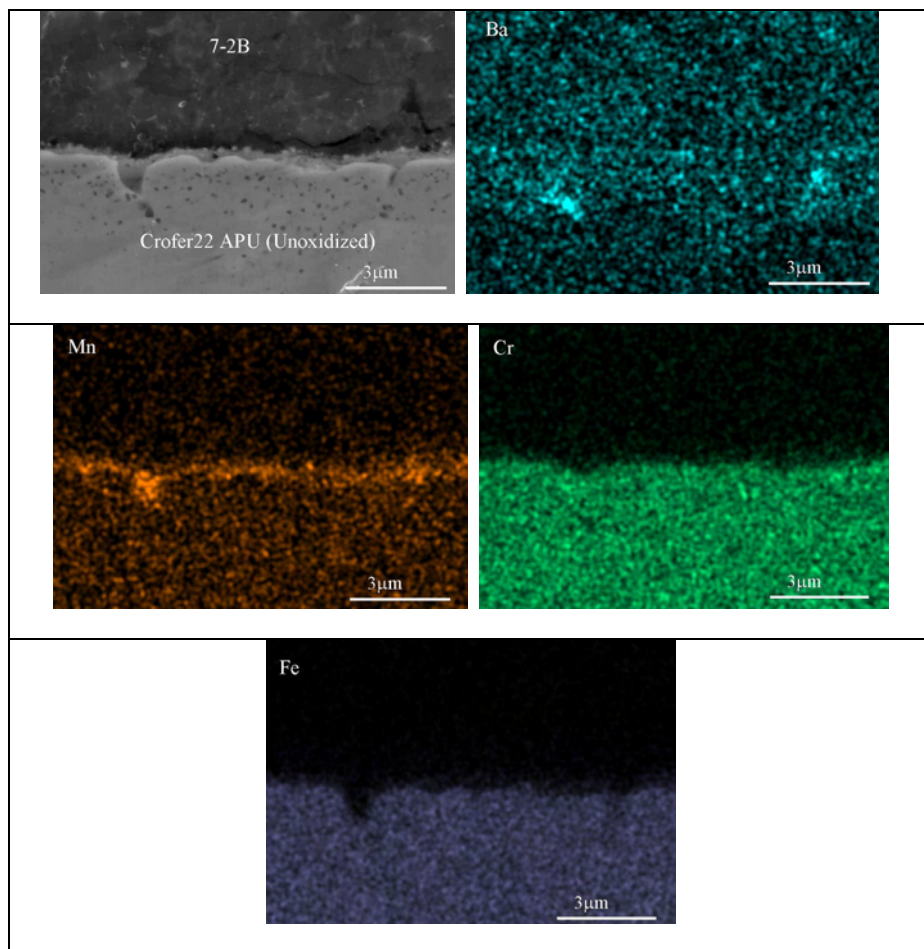
Fig. 4.48 Total electrical resistance of a model cell comprising Crofer 22 APU and YSZ plates joined by the 7A GC sealant.

In order to confirm good insulating properties of the GCs, the total electrical resistance of a model cell comprising Crofer 22 APU and YSZ plates joined by the 7A GC sealant, was examined by the impedance spectroscopy. The results showed a very high area-specific resistance, 1.7-2.6 MOhm cm<sup>2</sup> at 850 °C, which tends to slowly increase with

time due to surface oxidation of Crofer 22 APU (Fig. 4.48). This level of resistivity is very appropriate for practical electrochemical applications, such as SOFCs. At the same time, one should note that the total resistance of such cells is considerably higher than expected from the specific conductivities and thicknesses of all components. The latter may indicate formation of thin blocking layers at the interfaces, in particular at the GC| YSZ boundary, invisible by SEM.

#### 4.4.9.2 In humidified reducing atmosphere

Fig. 4.49 shows a SEM micrograph of the cross-section of interface between Crofer22 APU/7-2B GC sealant after 300 h of exposure to wet fuel gas atmosphere. The extent of diffusion of constituent elements from alloy interconnects into the glass and vice versa has been observed through EDS element mapping and line scanning. A rather smooth interface between GC sealant and steel is observed without the presence of iron-rich oxide products even at the edges. According to thermodynamic data available in the literature [177], the oxygen partial pressure required to oxidize iron to wustite (FeO) at 800 °C should exceed  $1.71 \times 10^{-19}$  atm. Therefore, we can expect the oxygen partial pressure to be lower than that which is required to oxidize iron. Furthermore, no substantial Ba-, Cr-rich oxide zone was observed at the interface (Fig. 4.49a) as was evident after heat treatment in air atmosphere. However, a Mn-rich oxide layer was formed at the steel side of the interface (Fig. 4.49a and 4.49b). Fig. 4.50 presents the SEM micrographs of the cross-section of interface between Sanergy HT/GC sealants 7A (Fig. 4.50a), 7-2B (Fig. 4.50b) and 7-5B (Fig. 4.50c), respectively. On the steel surface, formation of whisker like oxide products were formed for all the investigated diffusion couples, which were rich in Cr and Mn-oxides indicating towards the possible formation of manganese-chromium spinel. The oxygen partial pressure required to oxidize Cr has been reported to be  $6.91 \times 10^{-28}$  atm [177] which is much lower in comparison to that required for oxidation of Fe and led to the oxidation of chromium. The bonding/wetting behaviour of silicate glasses to metals is strongly dependent on the nature of the surface of the metal. Metallic surfaces often result in poor joining due to poor wetting, while an oxide layer on the metal surface tends to promote wetting which leads to improved chemical bonding. An Al-rich oxide layer was observed beneath this layer for Sanergy/ GC-7A diffusion couple (Fig. 4.50a). Similar Al-rich oxide layer was also observed by Haanappel *et al.* [178] at an interface between BCAS GC



(a)

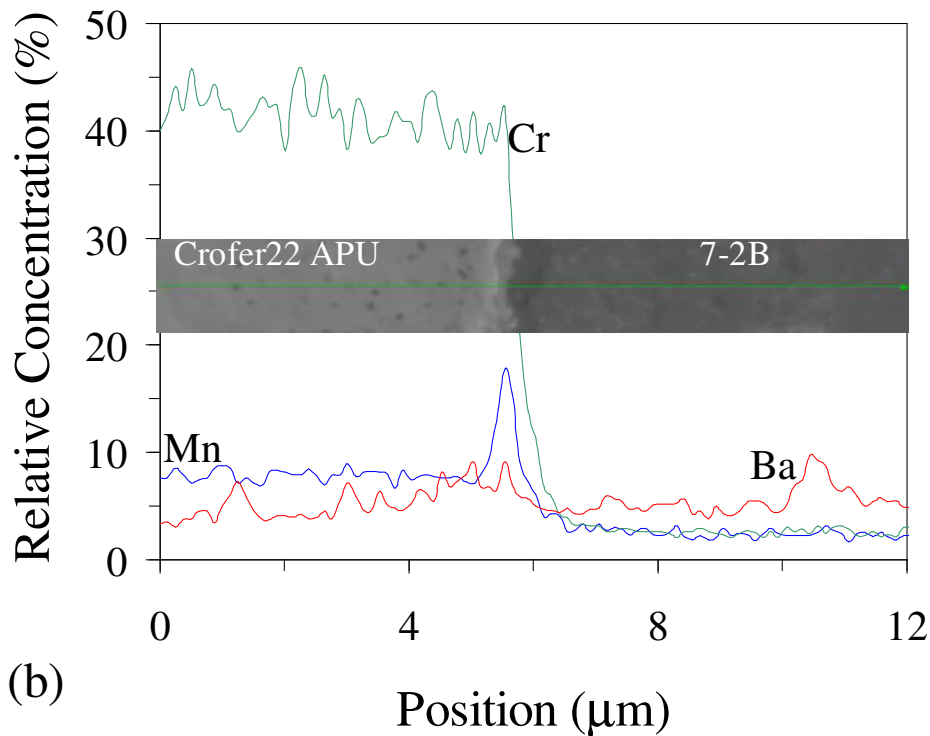


Fig. 4.49 (a) Microstructure (SEM) and EDS element mapping of Ba, Mn, Cr and Fe at interface between glass 7-2B and Crofer22 APU (b) EDS line profile for diffusion of Cr, Ba and Mn at the interface between glass 7-2B and Crofer22 APU developed after heat treatment at 850 °C for 1 h and 800 °C for 300 h in humidified reducing atmosphere. (The term ‘unoxidized’ refers to the usage of interconnect material in as received form. The alloy was not pre-oxidized).

sealant and chromia scale forming ferritic steel under wet fuel gas conditions. The concentration of impurities like Al and Si in metallic interconnect plays a significant role in the performance of SOFC stacks. It has been reported that higher amount of Si in metallic interconnect enhances the rate of corrosion attack due to internal oxidation, leading to the degradation of SOFC stack. However, no such degradation of SOFC stack has been reported due to internal oxidation of Al [178]. In the present investigation, no such Al-rich layer could be seen in any of the other diffusion couples else than Sanergy HT/GC-7A. All the investigated GC sealants showed highly stable interface with Sanergy HT and absence of any severe reaction products under humidified reducing atmosphere. No severe effect of increasing

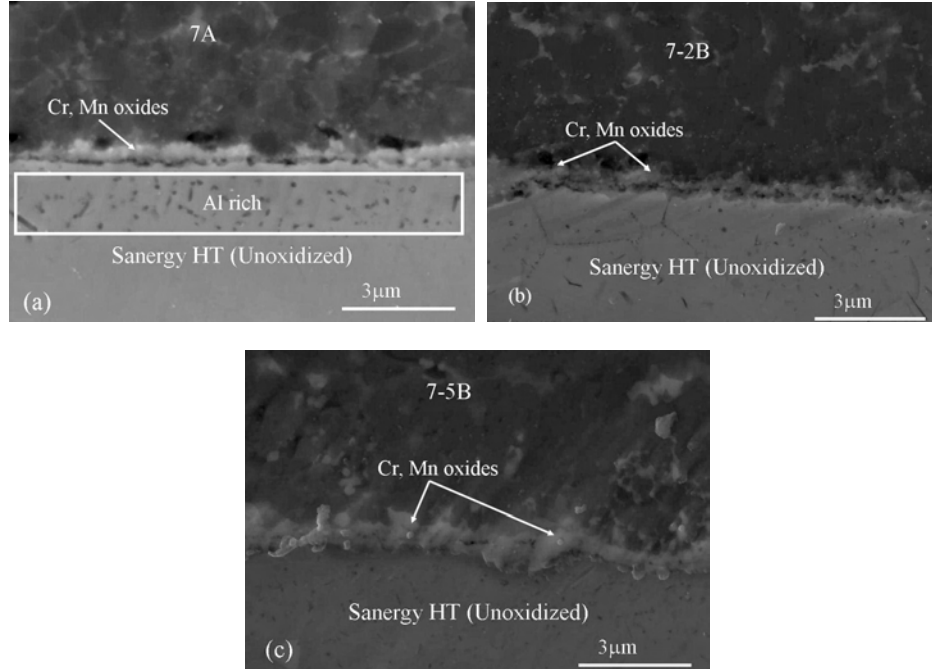


Fig. 4.50 SEM micrographs of the interface between (a) glass 7A and Sanergy HT, (b) glass 7-2B and Sanergy HT, (c) glass 7-5B and Sanergy HT developed after heat treatment at 850 °C for 1 h and 800 °C for 300 h in humidified reducing atmosphere. (The term ‘unoxidized’ refers to the usage of interconnect material in as received form. The alloy was not pre-oxidized.).

$B_2O_3$  content in the glass compositions could be observed on the reaction mechanism at the glass-steel interface in reducing conditions as was observed in air atmosphere. Although, the degradation of  $B_2O_3$ -containing seals under humidified reducing conditions due to the formation of volatile species has been well documented in literature [179], no such effects were observed in the present study owing to the very low concentration of  $B_2O_3$  in the glasses. Further, since no chromate formation was observed in any of the investigated diffusion couples, therefore, negligible chromium depletion can be expected at the three phase boundary (metal-GC-gas). As a consequence, no swelling of the metal with consequent bulging was observed. No significant differences were observed on the chemical interaction between sealant and steel after replacement of BaO by SrO in the GC sealant (not shown) as a layer of about 1 $\mu$ m thickness, rich in Cr and Mn oxides was observed at interface between GC sealant and metallic interconnect.

#### 4.4.10 Thermal shock resistance

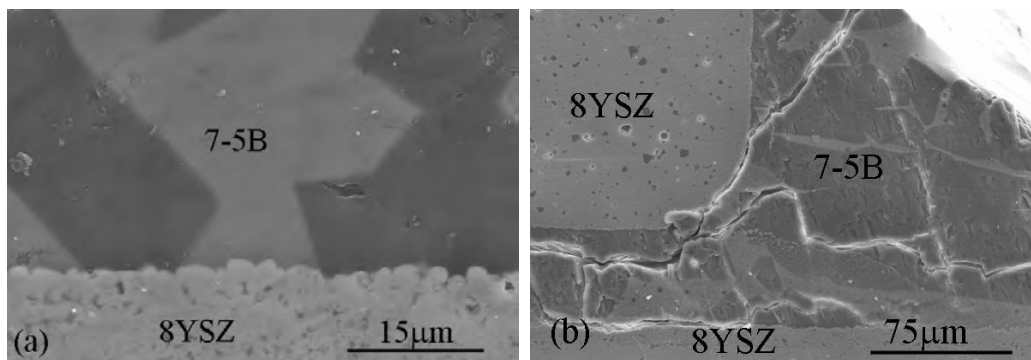


Fig. 4.51 SEM image of the 8YSZ-GC 7-5B pseudo cell after thermal shock resistance experiments in (a) air, (b) water, after 15 quenching cycles.

The thermal shock tests showed no crack development in the GCs, joining zirconia ceramics, after quenching in air (Fig. 4.51a). The sealants remained gas-tight, demonstrating an excellent thermal shock resistance and, thus, suitability of the GC sealants for any startup/shutdown protocols in SOFCs. Quenching in more severe conditions, namely in water, resulted in sealants cracking as illustrated by Fig. 4.51b. Although the mechanical properties of any Si-containing GCs may hardly be enhanced up to the level characteristic of zirconia-based materials, the specific crack-development patterns observed on water quenching suggests a possibility of further sealant optimization, in particular via the incorporation of nano- or submicron-sized crystalline additives such as tetragonal partially-stabilized zirconia (TZP).

.....

## 4.5 Optimization of diopside based glass-ceramic sealants for sealing applications in SOFC

### 4.5.1 Designing of glass compositions

On the basis of results obtained in our previous studies based on Di based glasses and GCs, particularly, in section 4.4, this study was attempted to optimize the sealing process of the glasses at temperatures close to working temperatures (800-850 °C) of the SOFC. Moreover, some adverse reactions were observed at the interface between Di based GC sealants and metallic interconnect leading to the formation of barium-chromium rich oxides (section 4.4.9). Also, still there is need to increase and stabilize the CTE of the diopside based GC sealants during long term heat treatment and to improve the flow behaviour of the resultant GCs in order to qualify those for the applications in SOFC stack. Thus, in the light of above mentioned perspective, the present study is also an attempt to design new GC sealants in order to tailor their CTE and reduce adverse chemical reactivity with metallic interconnect without compromising with their electrical and joining properties, so as to fulfil the criteria of a compliant sealing material required for SOFCs.

The structure, sintering process and crystallization kinetics of a new series of aluminosilicate glasses derived from substitution via scheme  $0.1 (\text{Ca}^{2+} + \text{Si}^{4+}) \leftrightarrow 0.1 (\text{La}^{3+} + \text{Al}^{3+})$  in pure  $\text{CaMgSi}_2\text{O}_6$  (diopside) system was examined. Further, partial substitution of CaO by BaO was attempted in the present study as depicted in [Table 4.24](#). The addition of 1 wt.% NiO and 2 wt.%  $\text{B}_2\text{O}_3$  was made in all the investigated glasses in order to improve adhesion behaviour of sealant to metal and decrease the viscosity and glass transition temperature, respectively. Furthermore, 0.5 wt.%  $\text{Cr}_2\text{O}_3$  was added in the parent glass in order to reduce the surface tension of the glass and decrease the temperature of crystallization. Moreover, it was observed in *section 4.4.8* that addition of minor amounts of  $\text{Cr}_2\text{O}_3$  promotes the formation of mono-mineral GCs in Di based glass compositions which further help in stabilizing the CTE and mechanical properties of sealant during long term SOFC operations. [Table 4.24](#) presents the compositions of all the investigated glasses.

Table 4.24 Batch compositions of the glasses

| Glass                |       | MgO   | CaO   | BaO   | SiO <sub>2</sub> | Al <sub>2</sub> O <sub>3</sub> | La <sub>2</sub> O <sub>3</sub> | B <sub>2</sub> O <sub>3</sub> | Cr <sub>2</sub> O <sub>3</sub> | NiO  |
|----------------------|-------|-------|-------|-------|------------------|--------------------------------|--------------------------------|-------------------------------|--------------------------------|------|
| Pt-crucible, 1550 °C |       |       |       |       |                  |                                |                                |                               |                                |      |
| 10                   | wt.%  | 17.27 | 21.63 | 0.00  | 48.93            | 2.18                           | 6.98                           | 2.00                          | 0.00                           | 1.00 |
|                      | mol.% | 25.01 | 22.51 | 0.00  | 47.52            | 1.25                           | 1.25                           | 1.68                          | 0.00                           | 0.78 |
| 10A                  | wt.%  | 17.19 | 21.52 | 0.00  | 48.67            | 2.17                           | 6.95                           | 2.00                          | 0.50                           | 1.00 |
|                      | mol.% | 24.96 | 22.46 | 0.00  | 47.42            | 1.25                           | 1.25                           | 1.68                          | 0.19                           | 0.78 |
| 10B                  | wt.%  | 16.48 | 18.34 | 6.27  | 46.67            | 2.08                           | 6.66                           | 2.00                          | 0.50                           | 1.00 |
|                      | mol.% | 24.93 | 19.94 | 2.49  | 47.37            | 1.25                           | 1.25                           | 1.75                          | 0.20                           | 0.82 |
| 10C                  | wt.%  | 16.14 | 16.85 | 9.21  | 45.73            | 2.04                           | 6.53                           | 2.00                          | 0.50                           | 1.00 |
|                      | mol.% | 24.92 | 18.69 | 3.74  | 47.34            | 1.25                           | 1.25                           | 1.79                          | 0.20                           | 0.83 |
| 10D                  | wt.%  | 15.83 | 15.41 | 12.04 | 44.82            | 2.00                           | 6.40                           | 2.00                          | 0.50                           | 1.00 |
|                      | mol.% | 24.90 | 17.43 | 4.98  | 47.32            | 1.25                           | 1.25                           | 1.82                          | 0.21                           | 0.85 |

#### 4.5.2 Casting ability of glasses

For all the investigated compositions (Table 4.24), heating at 1550 °C for 1 h was adequate to obtain bubble-free, homogenous transparent glasses. Absence of crystalline inclusions was confirmed by XRD and SEM analyses. The glass 10 (Cr<sub>2</sub>O<sub>3</sub> -free) was dark brown in colour (likely due to the presence of NiO) while the remaining four glasses had dark brown colour with greenish hue. The origin of this brown coloration in the glasses is due to the presence of nickel in five-coordination while greenish tinge in Cr<sub>2</sub>O<sub>3</sub> containing glasses implies towards the presence of chromium in Cr<sup>3+</sup> state [180].

#### 4.5.3 Density and dilatometry

The experimental results showed that the addition of Cr<sub>2</sub>O<sub>3</sub> led to a slight increase in the density ( $\rho$ ) of the investigated glasses in comparison to its parent glass, 10 (Table 4.25) since, the density of Cr<sub>2</sub>O<sub>3</sub> (5.2 g cm<sup>-3</sup>) is significantly higher in comparison to other constituents of glass (except BaO, La<sub>2</sub>O<sub>3</sub> and NiO). Further, the density of glasses increased with partial substitution of CaO by BaO due to higher density of BaO (5.72 g

cm<sup>-3</sup>) in comparison to CaO (3.34 g cm<sup>-3</sup>), thus, resulting in the highest density for glass 10D.

Table 4.25. Properties of the glasses

|                                                               | 10           | 10A          | 10B          | 10C          | 10D          |
|---------------------------------------------------------------|--------------|--------------|--------------|--------------|--------------|
| $\rho$ (g cm <sup>-3</sup> )                                  | 2.97 ± 0.004 | 2.98 ± 0.001 | 3.06 ± 0.006 | 3.10 ± 0.003 | 3.14 ± 0.002 |
| $V_m$ (cm <sup>3</sup> mol <sup>-1</sup> )                    | 19.68 ± 0.03 | 19.67 ± 0.01 | 19.94 ± 0.04 | 20.08 ± 0.02 | 20.17 ± 0.01 |
| $V_e$ (cm <sup>3</sup> mol <sup>-1</sup> )                    | 0.33 ± 0.02  | 0.30 ± 0.01  | 0.32 ± 0.04  | 0.32 ± 0.02  | 0.29 ± 0.01  |
| $T_g$ (± 5) (°C)                                              | 756          | 756          | 755          | 756          | 758          |
| (CTE ± 0.02) × 10 <sup>6</sup> K <sup>-1</sup><br>(200-600°C) | 8.39         | 8.43         | 8.40         | 8.71         | 9.04         |
| $T_c$ (± 2) (°C)                                              | 885          | 885          | 904          | 906          | 914          |
| $T_p$ (± 7) (°C)                                              | 920          | 920          | 937          | 946          | 955          |
| $N$                                                           | 1.80 ± 0.005 | 1.95 ± 0.004 | 1.97 ± 0.007 | 2.07 ± 0.009 | 2.15 ± 0.006 |
| $E_c$ (kJ mol <sup>-1</sup> )                                 | 487          | 473          | 459          | 395          | 412          |

$T_g$ ,  $T_c$  and  $T_p$  values are for  $\beta = 20$  K min<sup>-1</sup>; CTE values were obtained at  $\beta = 5$  K min<sup>-1</sup>.

The molar volume ( $V_m$ ) of the glass 10B is significantly higher than that of the B<sub>2</sub>O<sub>3</sub>-free glass (7A-Cr) with similar composition investigated in section 4.4.3. This may be attributed to the formation of directional bonds in the structural skeleton due to addition of B<sub>2</sub>O<sub>3</sub>.  $V_m$  increases while excess volume ( $V_e$ ) decreases with increase in BaO content in the glasses. However,  $V_e$  for glass 10B is higher than for BaO-free glass 10A owing to an increase in directional bonding in the structure of glass due to low ionic field strength of BaO in comparison to CaO. The decrease in  $V_e$  with increasing BaO content in the glasses implies that even though introduction of BaO in the glass structure (glass 10B) increased the polymerization (in comparison to glass 10A), further increase in BaO content depolymerized the glass network, as will be discussed in detail in section 4.5.4.

The CTE of the glasses as obtained from dilatometry is presented in Table 4.25. In general, the highest value of CTE was obtained for glass 10D while the lowest was for glass 10. The CTE increased slightly with addition of Cr<sub>2</sub>O<sub>3</sub> to parent glass (glass 10),

while it decreased slightly with the introduction of BaO in the glasses (10B). The decrease in CTE with introduction of BaO implies towards an increasing polymerization in the structure of glass 10B, as suggested by molar volume data and will also be discussed during FTIR analysis in section 4.5.4. However, CTE increased with further increase in BaO for glasses 10C and 10D due to decrease in  $V_c$  in the structural skeleton of the glass.

#### 4.5.4 FTIR analysis

The room temperature FTIR transmittance spectra of all the five investigated glasses are shown in Fig. 4.52. All spectra exhibit four broad transmittance bands in the region of 300-1500  $\text{cm}^{-1}$ . This lack of sharp features is indicative of the general disorder in the silicate network mainly due to a wide distribution of  $Q^n$  (polymerization in the

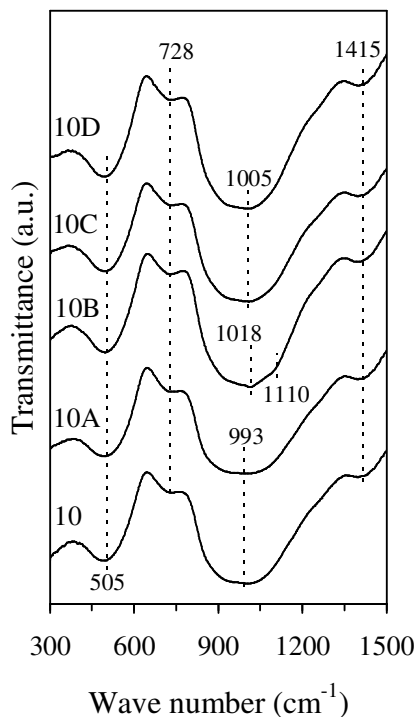


Fig. 4.52 FTIR of investigated glasses.

glass structure, where  $n$  denotes the number of bridging oxygens) units occurring in these glasses. The most intense bands lie in the 800-1300  $\text{cm}^{-1}$  region, the next between 300-600  $\text{cm}^{-1}$  and 1350-1500  $\text{cm}^{-1}$ , while the least intensive lies between 650-800  $\text{cm}^{-1}$ . The broad bands in the 800-1300  $\text{cm}^{-1}$  are assigned to the stretching vibrations of the  $\text{SiO}_4$  tetrahedron

with a different number of bridging oxygen atoms, while the bands in the 300-600  $\text{cm}^{-1}$  region are due to bending vibrations of Si-O-Si and Si-O-Al linkages [122, 123]. In the present study, the band for glass 10 in 800-1300  $\text{cm}^{-1}$  region was registered at almost similar position as was observed in our previous investigation for  $\text{La}_2\text{O}_3$ -containing diopside based glasses (section 4.4.5.1). However, it is noteworthy that unlike glass 7-2B, the glass 10 in the present study is BaO-free. No considerable effect was observed in the position of bands due to addition of  $\text{Cr}_2\text{O}_3$ . The wave number values for transmittance bands in 800-1300  $\text{cm}^{-1}$  region for glass 10 and 10A ( $\sim 993 \text{ cm}^{-1}$ ) are indicative of a major amount of  $Q^2$ -type silicate species present in the glass network. The introduction of BaO (glass 10B) shifted this wave number to higher region ( $\sim 1018 \text{ cm}^{-1}$ ) implying towards an increasing polymerization in the silicate glass network. Further, a small shoulder was observed for glass 10B at  $\sim 1110 \text{ cm}^{-1}$  which corresponds to the presence of  $Q^3$ -type silicate species along with  $Q^2$ , thus pinpointing towards an increasing polymerization in the silicate glass network (Fig. 4.52). The increasing connectivity with introduction of BaO content implies that only part of BaO acts as network modifier. The remaining BaO might be acting as a network former and existing as interconnected  $\text{BaO}_4$  tetrahedra [181]. Similar network forming action of MgO due to formation of  $\text{MgO}_4$  tetrahedron has been reported for MgO- $\text{Na}_2\text{O}$ - $\text{B}_2\text{O}_3$  glasses [182]. With further increase in BaO, the wave number in the region 800-1300  $\text{cm}^{-1}$  decreased implying towards de-polymerization of silicate glass network. No band was resolved at  $\sim 1100 \text{ cm}^{-1}$  for glasses 10C and 10D indicating towards the presence of major amount of  $Q^2$ -type silica tetrahedra in the glass network and de-polymerized network in comparison to glass 10B. The transmittance bands in the 650-800  $\text{cm}^{-1}$  region are related to the stretching vibrations of the Al-O bonds with  $\text{Al}^{3+}$  ions in four-fold coordination [122]. The transmittance band in the region 1350-500  $\text{cm}^{-1}$  corresponds to B-O vibrations in  $[\text{BO}_3]$  triangle.

#### 4.5.5 Crystallization kinetics by DTA

Fig. 4.53 presents DTA thermographs of all the investigated glasses at a heating rate of 20  $\text{K min}^{-1}$ . The glass transition temperature ( $T_g$ ) remained almost constant for all the investigated glasses irrespective of any additions or substitutions made in the parent composition as presented in Table 4.25. These results are in good agreement with the results obtained by Sohn *et al.* [151] and Meinhardt *et al.* [101], according to whom,  $T_g$

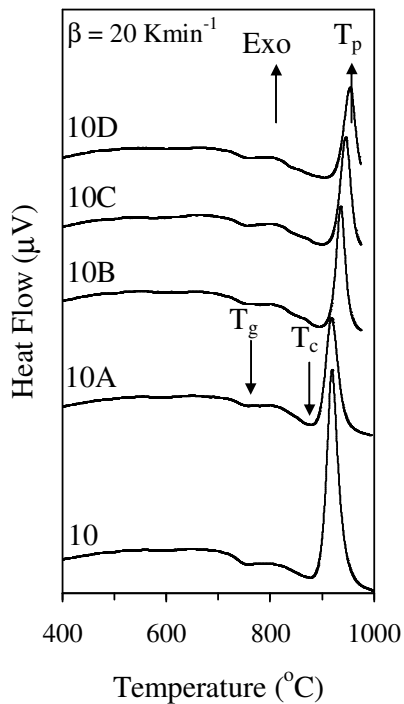


Fig. 4.53 DTA thermographs of glass powders at  $\beta = 20 \text{ K min}^{-1}$ .

and softening temperature ( $T_s$ ) are independent of BaO content in the glasses and are proportional to the  $\text{B}_2\text{O}_3/\text{SiO}_2$  ratio which is also valid for the glasses under investigation in the present study (Table 4.24). However, these results are in contradiction with the results of Ghosh *et al.* [102] as they report a decrease in  $T_g$  with increasing BaO contents in the glasses. It is noteworthy that along with an increase in the amount of BaO, a considerable decrease in  $\text{SiO}_2$  content in the glasses was also made by Ghosh *et al.* [102], while the exact amount of  $\text{B}_2\text{O}_3$  in the glasses was not disclosed. In the present investigation, the DTA plots of glasses exhibited single exothermic effects (Fig. 4.53) at all the heating rates which shifted towards higher temperatures with increasing the heating rate. This signifies that the GC is formed either as a result of single phase crystallization or of an almost simultaneous precipitation of different crystalline phases. The  $T_c$  and  $T_p$  values for glasses 10 and 10A were almost similar (Table 4.25) which implies that  $\text{Cr}_2\text{O}_3$  addition did not have any significant effect on the crystallization behaviour of the glasses. The  $T_c$  and  $T_p$  of the investigated glasses shifted towards higher temperature with increase in BaO content in the glasses with glass 10D showing the highest value of  $T_p$  among all the five glasses. The values of  $E_c$  and Avrami parameter,  $n$  for all the five glasses are listed in

**Table 4.25.** An intermediate crystallization mechanism (both surface and bulk) was observed in all the investigated glasses. The activation energy of crystallization ( $E_c$ ) slightly decreased with addition of  $\text{Cr}_2\text{O}_3$ . Lahl *et al.* [172] studied the crystallization behaviour of  $\text{MgO-Al}_2\text{O}_3\text{-B}_2\text{O}_3\text{-SiO}_2$  glasses and observed an increase in the  $E_c$  value due to addition of 0.6 mol.%  $\text{Cr}_2\text{O}_3$  in the glasses. This increase in  $E_c$  value was explained on the basis of dual role of  $\text{Cr}_2\text{O}_3$  (i.e. nucleating agent and glass network former) in the glasses. However, it is noteworthy that they did not calculate the mechanism of crystallization and assumed it to be surface crystallization, thus considering  $n = 1$ , which provides an uncertainty to their results. The addition of BaO in glasses 10B and 10C further led to decrease in the value of  $E_c$  while it slightly increased with further increase in BaO content in glass 10D. The  $E_c$  values for all the glasses investigated in present study compare well with those reported by Zhang *et al.* [165] and Lahl *et al.* [172] for their sealing glasses.

#### **4.5.6 Sintering and crystallization process of glasses**

In the present investigation, sintering preceded crystallization in all the five glass compositions as depicted in Fig. 4.54. Fig. 4.55 presents the photomicrographs of all the five glass compositions depicting the variation of sample dimensions with increase in temperature. As it is evident from the photomicrographs, densification started at  $\sim 800$  °C. The sintering initiated ( $T_{FS}$ ) at  $\sim 775\text{-}800$  °C in all the compositions while maximum shrinkage ( $T_{MS}$ ) was achieved well before the onset of crystallization ( $T_c$ ) (Fig. 4.54). Similar results were obtained from the sintering and crystallization experiments of the GPCs (rectangular bars) heat treated at 800 and 850 °C for 1 h, respectively. Well-sintered, dense but amorphous glass-powder compacts were obtained after heat treatment at 800°C for all the investigated compositions. A considerable increase in mechanical strength and density was observed for composition 10A after sintering at 800 °C due to the introduction of  $\text{Cr}_2\text{O}_3$  (Table 4.26) in parent composition (glass 10). This shows that addition of  $\text{Cr}_2\text{O}_3$  improved the sinterability of the parent glass. Further, with the initial substitution of BaO for CaO (glass 10B), the linear shrinkage and mechanical strength of the GPCs decreased while they increased with further increase in BaO content for composition 10C after sintering at 800 °C. The highest value of linear shrinkage and mechanical strength after

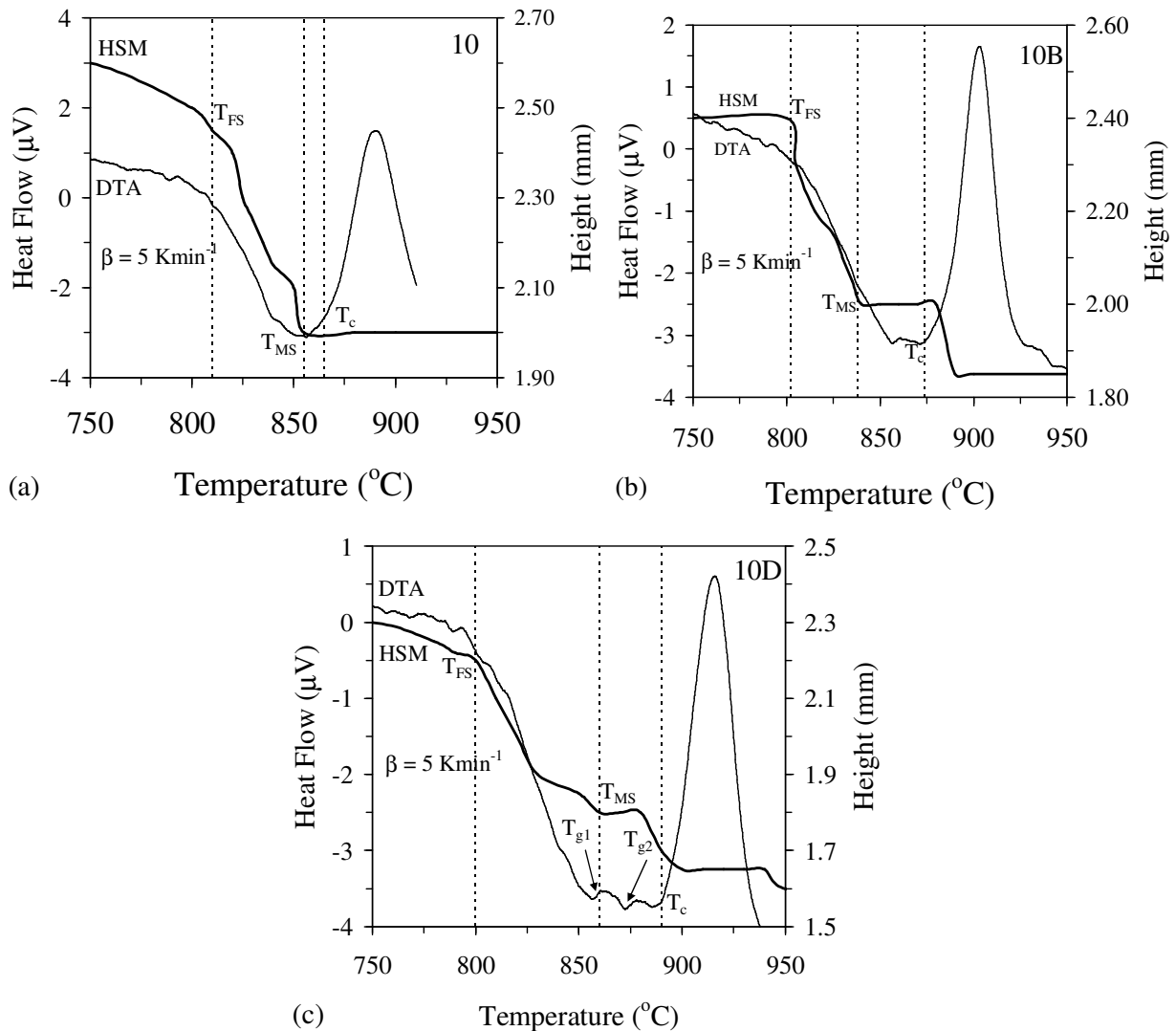


Fig. 4.54 Comparison of DTA and HSM curves on the same temperature scale for compositions (a) 10, (b) 10B and (c) 10D.

sintering at 800 °C were observed for compositions 10A (14.95%) and 10C (~115 MPa), respectively. In accordance with HSM and DTA results (Fig. 4.54 and Fig. 4.55), well sintered but crystallized GPCs were obtained after heat treatment at 850 °C for 1 h. The photomicrographs of GPCs at 850 °C (Fig. 4.55) show considerable shrinkage in their dimensions signifying densification. The evolution of crystalline regime of the GPCs (rectangular bars) heat treated at 850 °C for 1 h is demonstrated in the X-ray diffractograms of Fig. 4.56. Augite ( $\text{Ca}(\text{Mg}_{0.85}\text{Al}_{0.15})(\text{Si}_{1.70}\text{Al}_{0.30})\text{O}_6$ ), ICDD card:01-078-1391)

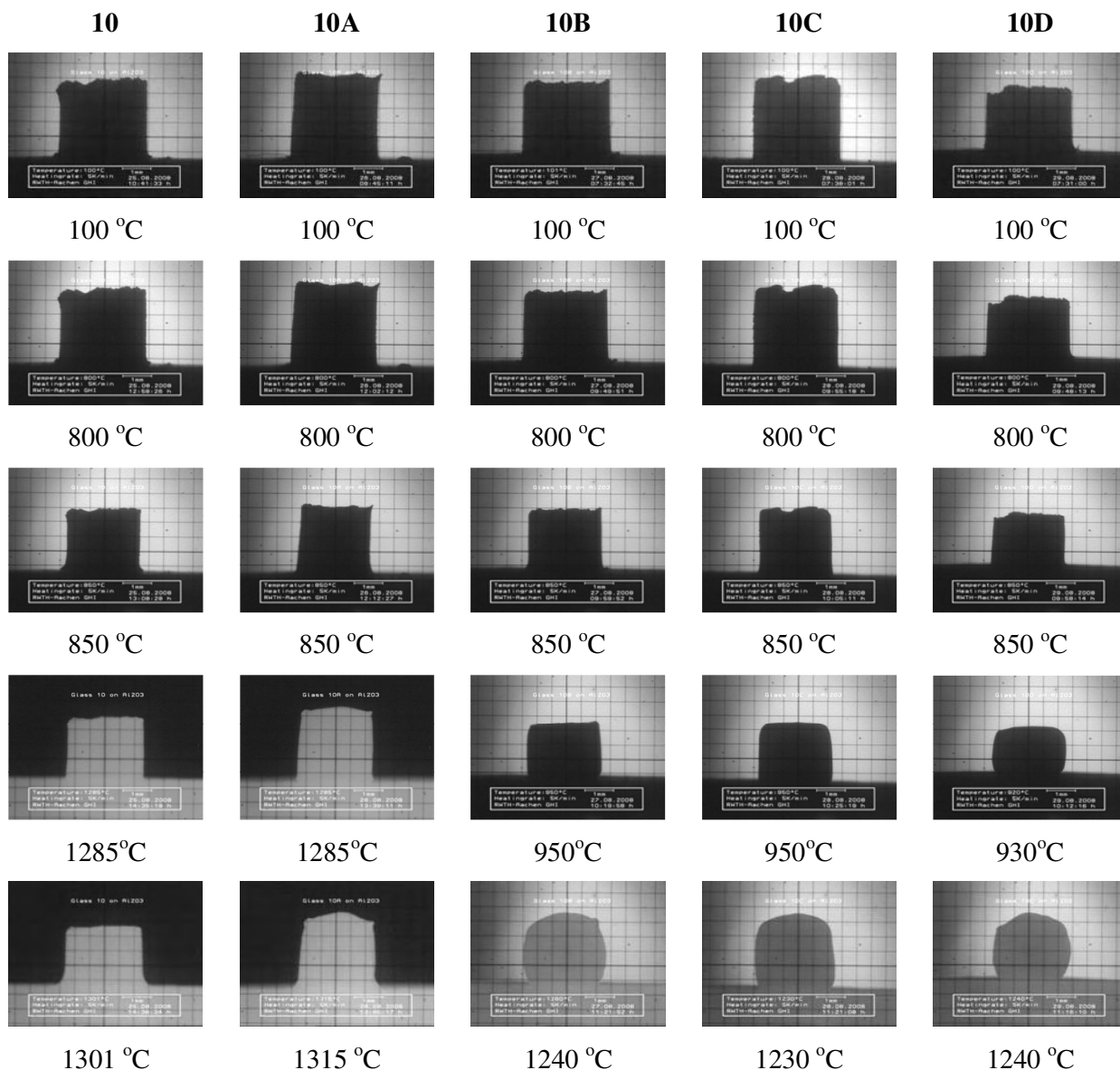


Fig. 4.55 HSM images of glasses on alumina substrates at various stages of heating cycle.

crystallized as primary phase in all the investigated compositions along with diopside ( $\text{CaMgSi}_2\text{O}_6$ ; ICDD card: 01-078-1390) as minor phase (except GC 10A). The quantitative analysis of crystalline phases in the GCs (Fig. 4.57, Table 4.27) reveals that addition of  $\text{Cr}_2\text{O}_3$  increases the degree of crystallinity in GC 10A and suppresses the crystallization of diopside, thus, leading to the formation of a complete solid solution which in turn leads to an increase in mechanical strength of resultant GC (166 MPa).

Table 4.26 Properties of the sintered glass-ceramics produced from glass-powder compacts after heat treatment at different temperatures for 1 h

| Composition                        | 800 °C        | 850 °C        |
|------------------------------------|---------------|---------------|
| <i>Density (g cm<sup>-3</sup>)</i> |               |               |
| 10                                 | 2.96 ± 0.005  | 3.02 ± 0.002  |
| 10A                                | 2.98 ± 0.001  | 3.03 ± 0.005  |
| 10B                                | 3.05 ± 0.005  | 3.17 ± 0.002  |
| 10C                                | 3.10 ± 0.002  | 3.22 ± 0.002  |
| 10D                                | 3.13 ± 0.007  | 3.27 ± 0.003  |
| <i>Flexural strength (MPa)</i>     |               |               |
| 10                                 | 97.69 ± 10.89 | 156.04 ± 6.09 |
| 10A                                | 102.16 ± 3.44 | 166.30 ± 7.83 |
| 10B                                | 87.96 ± 11.71 | 142.63 ± 9.21 |
| 10C                                | 115.41 ± 8.61 | 158.33 ± 5.15 |
| 10D                                | 89.43 ± 9.23  | 130.50 ± 6.82 |

The introduction of BaO in GCs disturbs the formation of solid solution by promoting the formation of diopside along with augite while an increase in BaO content further led to the dissolution of augite leading to an increasing amount of amorphous glassy phase in the GCs (Table 4.27). A two step shrinkage behaviour was observed for BaO-containing compositions as observed from HSM data (Fig. 4.54b and 4.54c). This second step of shrinkage was not observed in BaO free glass compositions, 10 and 10A (Fig. 4.54a) and tendency towards glass-in-glass phase separation as is evident from existence of two glass transition temperatures ( $T_{g1}$  and  $T_{g2}$ ) in DTA curves of BaO containing glasses (Fig. 4.54c) [183]. Thus, shrinkage continued also during crystallization stage of BaO-containing compositions as can also be seen from photomicrographs presented in Fig. 4.55, while BaO-free glass compositions (10 and 10A) depict no significant changes in the dimensions of samples until ~1285 °C while BaO-containing compositions (10B, 10C and 10D) reveal a softening and deformation, thus leading to a considerable shrinkage at

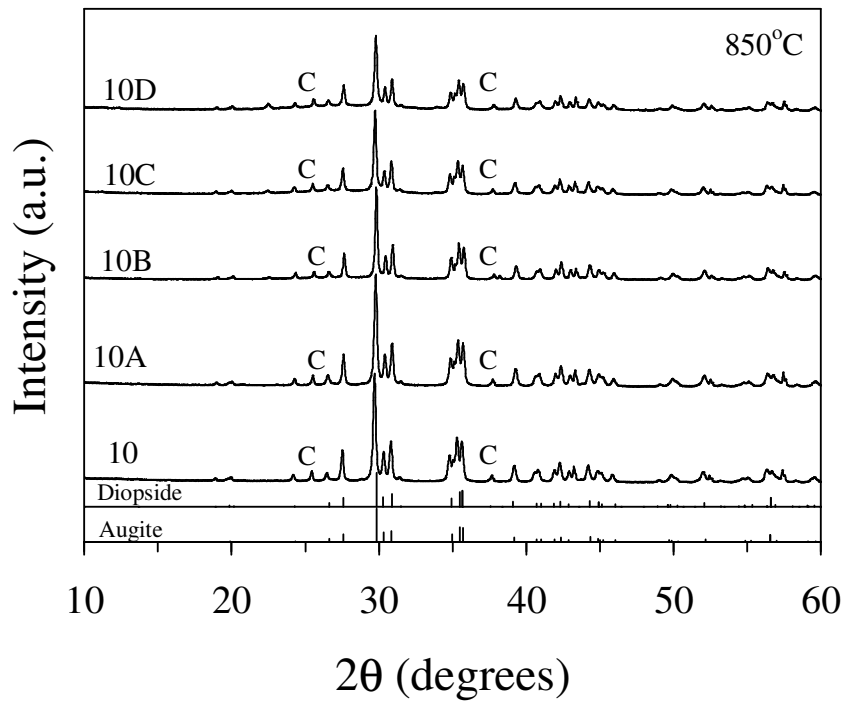


Fig. 4.56 Powder X-ray diffractograms of GCs sintered at 850 °C for 1 h mixed with corundum (internal standard). (Label: C: Corundum)

~950 °C. These results show that addition of BaO improves the flow behaviour of the diopside based GC sealants. Moreover, on the basis of the viscosity criteria defined by Pascual *et al.* [113], viscosity of the BaO-containing investigated sealants is calculated to be in the range of  $10^6$ - $10^8$  dPas at SOFC operation temperature. These are the properties expected from good sealant materials.

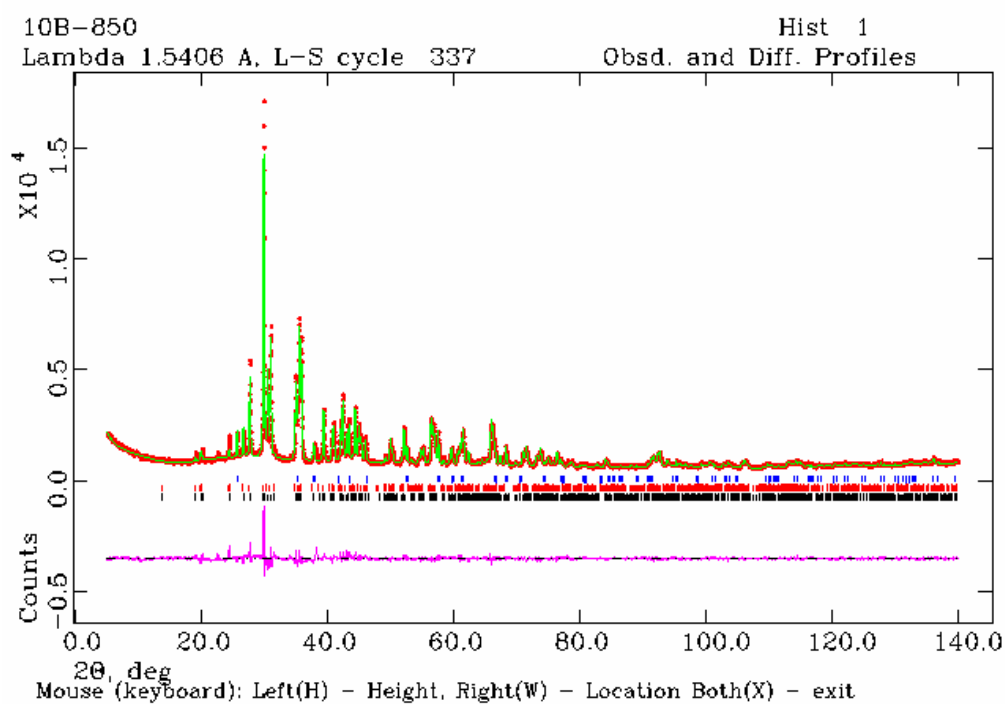


Fig. 4.57 Observed (crosses), calculated (continuous line), and difference curve from the Rietveld refinement of the GC 10B treated at 850 °C for 1 h in air. Markers representing the phase reflections correspond to corundum, diopside, and augite (from top to bottom).

Table 4.27 Results of Rietveld-R.I.R quantitative analysis

|                 | 10        | 10A       | 10B       | 10C       | 10D       |
|-----------------|-----------|-----------|-----------|-----------|-----------|
| Augite          | 83.33 (1) | 94.08 (1) | 92.39 (1) | 79.48 (1) | 70.26 (1) |
| Diopside        | 7.78 (5)  | -         | 5.09 (3)  | 5.38 (3)  | 15.41 (4) |
| Glass           | 8.89 (6)  | 5.92 (1)  | 2.52 (4)  | 15.14 (4) | 14.33 (5) |
| Total           | 100       | 100       | 100       | 100       | 100       |
| $\chi^2$        | 3.77      | 5.08      | 3.35      | 3.55      | 4.51      |
| R <sub>wp</sub> | 0.059     | 0.067     | 0.057     | 0.056     | 0.063     |
| R <sub>p</sub>  | 0.045     | 0.050     | 0.043     | 0.044     | 0.049     |

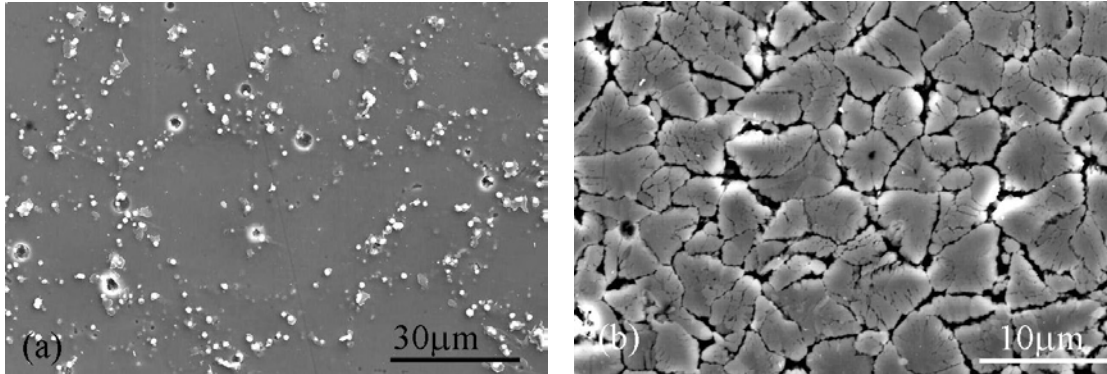


Fig. 4.58 Microstructure (revealed via SEM imaging after chemical etching of polished surfaces with 2 vol.% HF solution) of the GCs (a) 10A heat treated at 800 °C (b) 10B heat treated at 850 °C for 1 h, respectively.

Fig. 4.58 presents the microstructure of the glass powder compacts sintered at 800 and 850 °C for 1 h. In consistence with XRD results (Fig. 4.56), the sintering of glasses in close proximity to  $T_{FS}$  (~800 °C) led to the softening and fusion of glass particles resulting in a dense and amorphous glass powder compact with small amount of porosity (Fig. 4.58a). However, sintering of glasses at 850 °C resulted in dense and crystalline microstructure for all the investigated compositions (Fig. 4.58b). These observations are consistent with the relative importance of two main stages of densification (i.e. first shrinkage and maximum shrinkage).

#### 4.5.7 Isothermal heat treatment, 800 °C (300 h)

The crystalline phase evolution after prolonged heat treatment of GCs (already sintered at 850 °C for 1 h) at 800 °C for 300 h is presented in Fig. 4.59. Augite crystallized as the only phase in GC 10 and 10A while hexacelsian (HC;  $BaAl_2Si_2O_8$ ; ICDD: 01-088-1048) appeared as secondary phase along with augite in GC 10B and 10C. The intensity of XRD peaks was lower for all the investigated GCs after 300 h of heat treatment in comparison to GC sintered at 850 °C for 1 h. After heat treatment of 300 h, the intensity of XRD peaks for GCs 10 and 10A was almost similar while GC 10C showed the XRD peaks with highest intensity implying towards higher crystallinity. In GC 10D, two more minor phases, namely,  $LaBO_3$  (ICDD: 00-013-0571) and a solid solution isostructural to  $Cr_5O_{12}$

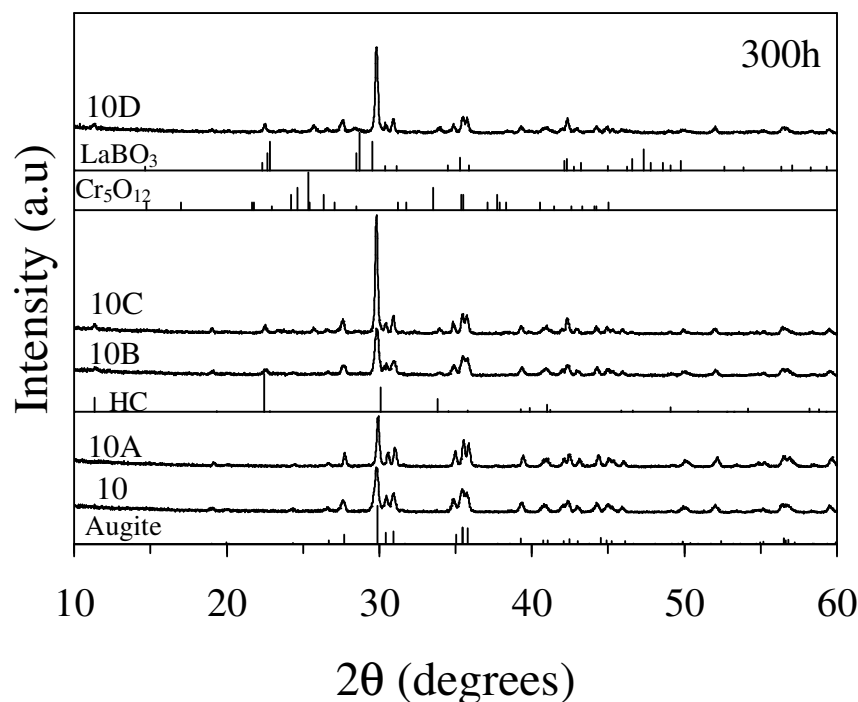


Fig. 4.59 X-ray diffractograms of GPCs sintered at 850 °C for 1 h followed by 800 °C for 300 h.

(ICDD: 00-018-0390) crystallized out along with augite and HC. Similar crystalline phase ( $\text{LaBO}_3$ ) was also observed by Mahapatra et al. [156] during devitrification of  $(25 - X)\text{SrO}-20\text{La}_2\text{O}_3-(7 + X)\text{Al}_2\text{O}_3-40\text{B}_2\text{O}_3-8\text{SiO}_2$  (mol%), where  $X = 0-10$  mol% and explained it on the basis of tendency of  $\text{La}^{3+}$  to coordinate with triangular coordinated boron due to the high electrostatic bond strength of the former. In the present investigation, this phase was observed only for the GC with highest amount of BaO (10D).

#### 4.5.8 Properties of sintered glass powder compacts

The CTE (200-600 °C) values of the GCs sintered at 850 °C for 1 h are presented in Table 4.28. The CTE values decreased with addition of  $\text{Cr}_2\text{O}_3$  while increased with an increase in BaO content in the glasses until composition 10C. However, with further replacement of CaO by BaO in composition 10D, the CTE decreased considerably. The highest CTE value for the GCs was observed for composition 10C ( $9.49 \times 10^{-6} \text{ K}^{-1}$ ) while the lowest was observed for composition 10D ( $8.79 \times 10^{-6} \text{ K}^{-1}$ ).

The CTE (200-600 °C) values for the GCs heat treated at 800 °C for 300 h are presented in Table 4.28. The CTE values for all the GCs decreased after prolonged heat

treatment in comparison to the parent GC compositions (sintered at 850 °C for 1 h) due to the decrease in crystallinity of the GCs. In accordance with the results obtained for parent GCs, the CTE values increased with an increase in BaO content until composition 10C. The highest CTE was obtained for GC 10C ( $9.19 \times 10^{-6} \text{ K}^{-1}$ ) while the lowest were obtained for GCs 10A ( $8.96 \times 10^{-6} \text{ K}^{-1}$ ) and 10D ( $8.99 \times 10^{-6} \text{ K}^{-1}$ ), respectively.

The results of impedance spectroscopy (Fig. 4.60) confirmed excellent insulating properties of the GC materials in spite of the conductivity increase caused by  $\text{B}_2\text{O}_3$  addition as reported in our previous work (section 4.4.8). At 830 °C, the maximum conductivity observed in the studied system for the parent composition, Glass 10, is as low as  $4 \times 10^{-7} \text{ Scm}^{-1}$ . This level ensures an absence of short circuiting between the SOFC stack components, especially in the intermediate temperature range. Barium additions lead to a substantial decrease in the total conductivity and to an increase of the corresponding activation energy calculated by the standard Arrhenius equation (Table 4.29).

Table 4.28 CTE $\times 10^6$  ( $\text{K}^{-1}$ ) (200-600 °C) of the GCs produced under different conditions

| Composition | 850 °C, 1 h | 800 °C, 300 h |
|-------------|-------------|---------------|
| 10          | 9.23        | 8.82          |
| 10A         | 9.14        | 8.96          |
| 10B         | 9.38        | 9.17          |
| 10C         | 9.49        | 9.19          |
| 10D         | 8.79        | 8.99          |

At temperatures below 780-800 °C, the conductivity of all Ba-containing GCs (10B, 10C and 10D) becomes similar within the limits of experimental uncertainty. These trends suggest an absence of significant protonic transport induced by barium doping, at least at 700-830°C. Whilst introducing  $\text{Ba}^{2+}$  cations might be expected to promote water incorporation in the oxide materials, the appearance of any significant protonic contribution should be reflected by higher total conductivity and lower  $E_A$  values (for example: Ref. 184); however, the experiments revealed opposite tendencies (Fig. 4.60).

Indeed, testing of the GCs in humidified air atmosphere confirmed that water incorporation can be neglected as no conductivity changes were observed within the

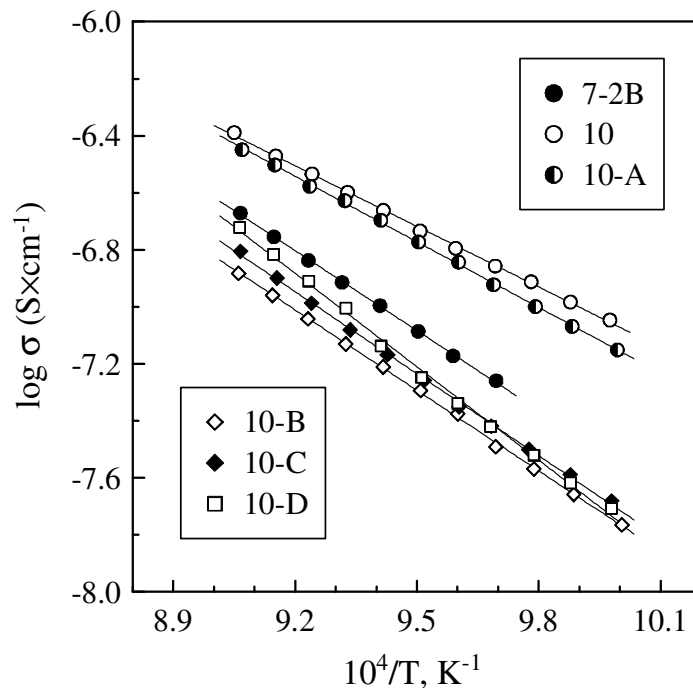


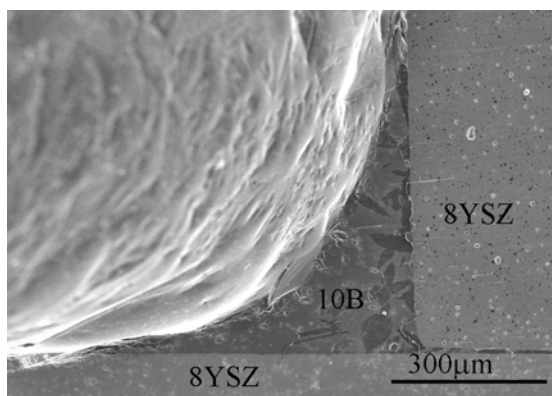
Fig. 4.60 Total conductivity of dense GCs in air. The data on 7-2B are shown for comparison. The error bars are smaller than the data point symbols.

Table 4.29 Activation energy for the total conductivity (730-830°C) of GCs in air

| Glass    | $E_A$ (kJ mol <sup>-1</sup> ) |
|----------|-------------------------------|
| 7-2B [5] | 188 ± 4                       |
| 10       | 144 ± 3                       |
| 10A      | 156 ± 3                       |
| 10B      | 189 ± 3                       |
| 10C      | 192 ± 4                       |
| 10D      | 218 ± 8                       |

limits of experimental error. Assessment of the conductivity mechanisms by the modified e.m.f. method under air/10% $H_2$ -90% $N_2$  gradient displayed a predominantly ionic transport as the ion transference numbers are higher than 0.93. As discussed earlier (*section 4.3.7*), these transference numbers correspond to the sum of all ionic charge carriers, irrespective of their nature. As the content of alkaline metal impurities in the studied GCs is lower than the detection limits of the available analytical techniques, the ionic charge carriers may include alkaline-earth cations with relatively small size (e.g.  $Mg^{2+}$  and  $Ca^{2+}$ ) and/or oxygen anions. The mobility of  $Ba^{2+}$  cations, which are much larger than any hypothetical bulk-diffusion pathway comparable to the average metal-oxygen bond distance, is very unlikely. Moreover, the incorporation of  $Ba^{2+}$  may block migration of smaller cations, such as  $Mg^{2+}$ , if their diffusion indeed occurs. The latter situation seems observed experimentally (*Fig. 4.60*), although the oxygen-ionic contribution to the total conductivity may still be significant, in agreement with previous results (*section 4.3.7*).

*Fig. 4.61* presents the SEM micrograph of GC 10B-8YSZ pseudo cell after thermal shock experiments in air. No cracks development in the GCs was observed; sealing remained gas-tight, demonstrating an excellent thermal shock resistance and, thus, suitability of the GC sealants for any start-up/shutdown protocols in SOFCs. The quenching in water resulted, however, in embrittlement and cracking of the GCs.



*Fig. 4.61* SEM image of the 8YSZ-GC 10B pseudo cell after thermal shock resistance experiments in air after 15 quenching cycles.

All the sealing GCs bonded well to the metallic interconnect and no gaps were observed even at the edges of the joints. *Fig. 4.62* shows the SEM image of the interface of

Crofer22 APU/glass 10 join after heat treatment at 850 °C for 1 h, followed by 800 °C for 300 h in air. A rather smooth interface between GC 10 and Crofer22 APU was observed without the presence of iron-rich oxide products. Also, the formation of Mn, Cr-rich oxides could not be seen at the interface. However, presence of a Ti rich zone near the interface was the main feature that was observed in all the diffusion couples between GCs (10, 10A, 10B, 10C) and Crofer22 APU except GC 10D/Crofer22 APU diffusion couple (Fig. 4.62 and Fig. 4.63). This formation of titanium oxide layer may have several positive effects; first of all, since the outer layer contains no Cr, the migration of Cr to the cathode which poisons its effectiveness would be expected to be greatly reduced if not

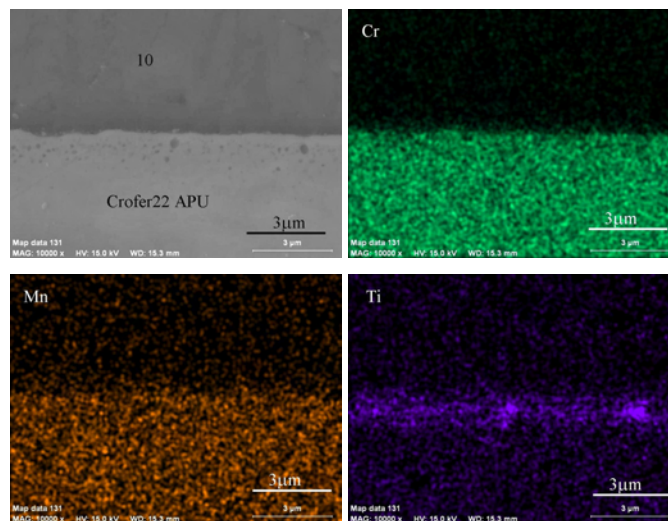
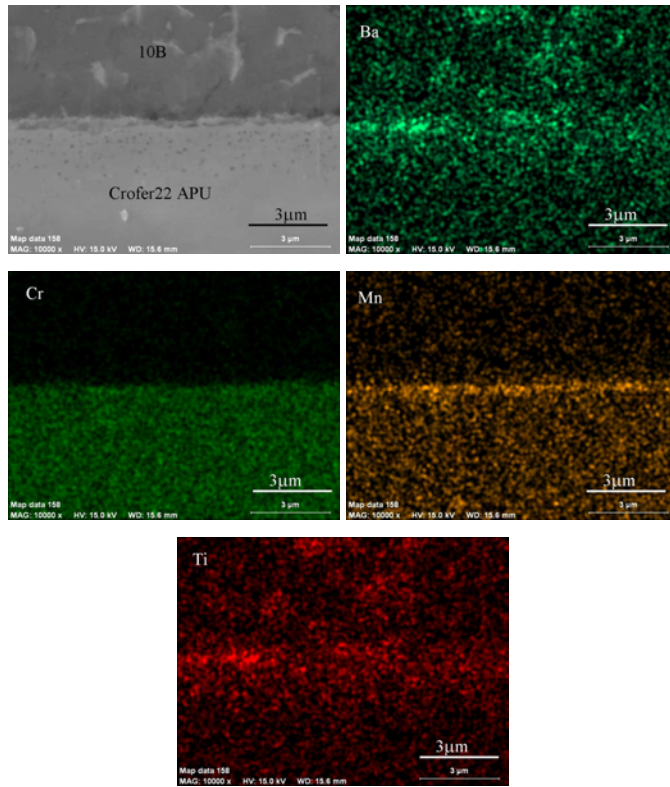
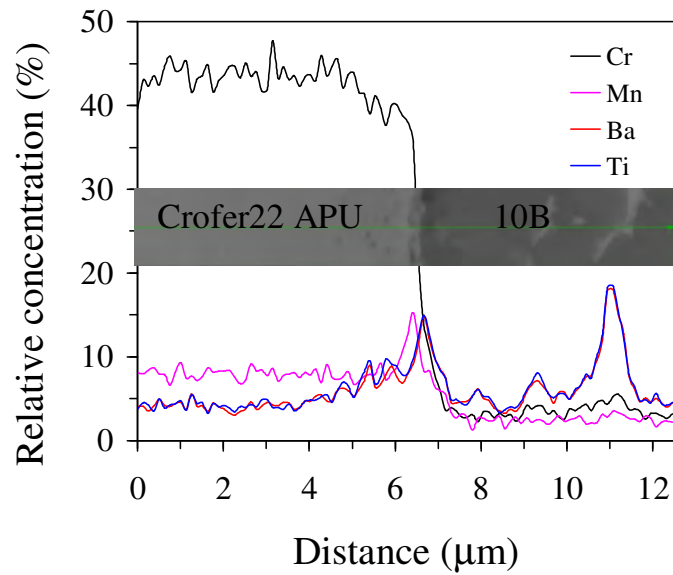


Fig. 4.62 Microstructure (SEM) and EDS element mapping of Cr, Mn, and Ti at interface between GC 10 and Crofer22 APU developed after heat treatment at 850 °C for 1 h and 800 °C for 300 h in air.



(a)



(b)

Fig. 4.63 (a) Microstructure (SEM) and EDS element mapping of Ba, Cr, Mn and Ti at the interface between GC 10B and Crofer22 APU (b) EDS line profile for diffusion of Ba, Cr, Mn and Ti from GC 10B to Crofer22 APU

and vice versa at their interface developed after heat treatment at 850 °C for 1 h and 800 °C for 300 h in air.

eliminated [185, 186]. A similar observation was reported by Jablonski and Alman [187] for a steel containing 22 wt% Cr and 1 wt% Ti when surface treated by CeO<sub>2</sub> while untreated steel samples did not show formation of Ti-enriched protecting layers. According to Jablonski and Alman [187], the formation of titanium oxides is much more favorable from thermodynamic point of view, in comparison to the other Cr, Mn-rich oxidizing species. Further, as is evident from Fig. 4.63a and 4.63b, substantial segregation of manganese takes place along with Ti at the oxidized interface of diffusion couple between GC 10B (also for GC 10C) and metallic interconnect. These results may indicate towards the (a) possible formation of Mn-rich oxides along with titanium oxide or (b) formation of Mn, Ti-oxides. Since, the standard Gibbs energy for formation of Mn,Ti-oxides at 800°C (for example: MnTiO<sub>3</sub> = 298 kJ mol<sup>-1</sup>, Mn<sub>2</sub>TiO<sub>4</sub> = 276 kJ mol<sup>-1</sup>) is significantly higher than Mn-oxides (for example: MnO = 217 kJmol<sup>-1</sup>, MnO<sub>2</sub> = 208 kJ mol<sup>-1</sup>, Mn<sub>2</sub>O<sub>3</sub> = 221 kJ mol<sup>-1</sup>, Mn<sub>3</sub>O<sub>4</sub> = 224 kJ mol<sup>-1</sup>) [187], possible formation of the latter seems to be more feasible in reducing atmospheres where Mn<sup>2+</sup> cations exist; in air, when Mn<sup>3+</sup> and Mn<sup>4+</sup> oxidation states prevail, formation of binary oxides mixture is more likely. Another necessary comment is that Ba rich zones could be observed while no Cr-rich zones were found along the interface of the diffusion couples. The EDS element profile (Fig. 4.63b) depicts the occurrence of Ba along with Ti at the interface pinpointing towards the possible formation of a BaTiO<sub>3</sub> based solid solution. BaTiO<sub>3</sub> is a relatively stable phase with respect to the redox behaviour and thermo-mechanical properties, and should have no detrimental impact on the SOFC performance. No Cr-rich zones could be seen all along the interface, therefore, occurrence of any adverse reaction between Ba and Cr could be neglected which is, again, highly favourable for sealing application. With an increase in BaO content (GC 10D), a thin zone rich in Cr and Mn was observed at the interface between GC 10D and Crofer22 APU implying towards the formation of Mn, Cr-spinel while no adverse reactions were observed between BaO and Cr<sub>2</sub>O<sub>3</sub>.

.....

## 4.6 Influence of nucleating agents ( $\text{Cr}_2\text{O}_3$ , $\text{Fe}_2\text{O}_3$ and $\text{CaF}_2$ ) on the crystallization kinetics of diopside and Di-CaTs based glasses

### 4.6.1 Designing of glass compositions

As mentioned in Chapter 1, *Introduction*, GCs are ceramic materials formed through the controlled nucleation and crystallization of glass. Glasses are melted, fabricated to shape, and thermally converted to predominantly crystalline ceramic. The basis of controlled internal crystallization lies in efficient nucleation that allows the development of fine, randomly oriented grains without voids, micro-cracks, or other porosity. In the absence of internal nucleation process as a precursor to crystallization, devitrification is initiated at lower energy surface sites.

In practice, surface crystal nucleation occurs more easily than internal crystal nucleation and is observed in most compositions. In order to achieve internal crystal nucleation, it is often necessary to add nucleating agents. Pyroxene based GCs are a typical example of surface crystallized GCs. As shown in previous sections, En based and Di based glasses are prone to surface crystallization. Therefore, clinopyroxene based glasses are the ideal system for investigating the effect of nucleating agents on the crystallization kinetics of the glasses.

In order to obtain bulk nucleation in the glasses of  $\text{SiO}_2\text{-Al}_2\text{O}_3\text{-CaO-MgO}$  and related systems,  $\text{Cr}_2\text{O}_3$  has been recommended as one of the most efficient nucleating agents. However still there is an open debate on the exact role of  $\text{Cr}_2\text{O}_3$  in these glass systems [188-190]. In our study pertaining to crystallization behaviour and properties of  $\text{La}_2\text{O}_3$ -containing diopside based glasses (section 4.4), we also found 0.5 wt.%  $\text{Cr}_2\text{O}_3$  to be an ineffective nucleating agent. Therefore, as also discussed in the Chapter 2, *State of the art*, an attempt was made to achieve volume nucleation by using a mixture of 3 wt.%  $\text{Fe}_2\text{O}_3$  and 0.7 wt.%  $\text{Cr}_2\text{O}_3$  as nucleating agents in Di-CaTs based glass with theoretical composition corresponding to 75 mol.% Di – 25 mol.% CaTs (glass 8). Further, second composition, 8A was derived by substitution of  $0.1\text{Ca}^{2+} + 0.1\text{Mg}^{2+} \leftrightarrow 0.1\text{La}^{3+} + 0.1\text{Li}^+$  in the parent composition. The compositions of both the glasses are depicted in [Table 4.30](#).

Another attempt was made to induce volume nucleation in the Di based glasses by using  $\text{CaF}_2$  as a nucleating agent. The glass composition 7A (studied in section 4.4) was

chosen as the parent composition and different amounts of CaF<sub>2</sub> (3, 5 and 8 wt.%) was added to it. Table 4.31 presents the detailed compositions of these glasses.

Table 4.30 Batch compositions of glasses 8 and 8A (wt.%)

| Glass                                                                                                                              | MgO   | CaO   | Li <sub>2</sub> O | SiO <sub>2</sub> | Al <sub>2</sub> O <sub>3</sub> | La <sub>2</sub> O <sub>3</sub> | Fe <sub>2</sub> O <sub>3</sub> | Cr <sub>2</sub> O <sub>3</sub> |
|------------------------------------------------------------------------------------------------------------------------------------|-------|-------|-------------------|------------------|--------------------------------|--------------------------------|--------------------------------|--------------------------------|
| Pt-crucible                                                                                                                        |       |       |                   |                  |                                |                                |                                |                                |
| 8 (CaMg <sub>0.75</sub> Al <sub>0.5</sub> Si <sub>1.75</sub> O <sub>6</sub> )                                                      | 13.42 | 24.89 | -                 | 46.67            | 11.31                          | -                              | 3                              | 0.7                            |
| 8A (Ca <sub>0.9</sub> Mg <sub>0.65</sub> Li <sub>0.1</sub> Al <sub>0.5</sub> La <sub>0.1</sub> Si <sub>1.75</sub> O <sub>6</sub> ) | 11.21 | 21.59 | 0.64              | 44.98            | 10.91                          | 6.97                           | 3                              | 0.7                            |

Table 4.31 Batch compositions of CaF<sub>2</sub> containing glasses (wt.%)

| Glass       | MgO   | CaO   | BaO  | SiO <sub>2</sub> | Al <sub>2</sub> O <sub>3</sub> | La <sub>2</sub> O <sub>3</sub> | CaF <sub>2</sub> | NiO |
|-------------|-------|-------|------|------------------|--------------------------------|--------------------------------|------------------|-----|
| Pt-crucible |       |       |      |                  |                                |                                |                  |     |
| 7-0         | 16.90 | 18.82 | 6.43 | 47.88            | 2.14                           | 6.83                           | -                | 1   |
| 7-3         | 16.39 | 18.25 | 6.24 | 46.43            | 2.07                           | 6.63                           | 3                | 1   |
| 7-5         | 16.05 | 17.87 | 6.11 | 45.46            | 2.03                           | 6.49                           | 5                | 1   |
| 7-8         | 15.54 | 17.30 | 5.91 | 44.01            | 1.97                           | 6.28                           | 8                | 1   |

The glasses have been labelled according to the amount of CaF<sub>2</sub>, i.e. parent glass (Ca<sub>0.8</sub>Ba<sub>0.1</sub>MgAl<sub>0.1</sub>La<sub>0.1</sub>Si<sub>1.9</sub>O<sub>6</sub>) will be labelled as 7-0 (0 wt.% CaF<sub>2</sub>). Similarly, glasses with 3 wt.%, 5wt.% and 8 wt.% CaF<sub>2</sub> will be labelled as 7-3, 7-5 and 7-8 respectively. Although, the results pertaining to the parent glass composition (7-0) have been already presented in section 4.4, they will also be presented and discussed along the manuscript for the purpose of comparison.

The main aim behind this work was to test the effectiveness of different nucleating agents in order to induce volume nucleation in Di based GCs so as to qualify them for their potential applications in technological areas where sintering and crystallization approach could not be exploited, such as nuclear waste immobilization.

#### 4.6.2 Casting ability of glasses

The glass composition 8 was melted at 1580 °C for 1 h while all other glasses (8A and CaF<sub>2</sub>-containing glasses) were melted at 1550 °C. Homogenous transparent, bubble-free glasses with a dark brown colour were obtained. The absence of any crystalline inclusions was confirmed by XRD analysis. It should be noted that no glass frits were obtained by quenching in water during this study as nucleation and crystallization studies were made on monolithic glass blocks.

Table 4.32 Properties of CaF<sub>2</sub> -containing glasses

| Glass                                                    | 7-0           | 7-3           | 7-5           | 7-8           |
|----------------------------------------------------------|---------------|---------------|---------------|---------------|
| Density (g cm <sup>-3</sup> )                            | 3.08 ± 0.001  | 3.10 ± 0.003  | 3.11 ± 0.002  | 3.12 ± 0.005  |
| V <sub>m</sub> (cm <sup>3</sup> mol <sup>-1</sup> )      | 19.71 ± 0.012 | 19.70 ± 0.014 | 19.72 ± 0.010 | 19.60 ± 0.020 |
| V <sub>e</sub> (cm <sup>3</sup> mol <sup>-1</sup> )      | 0.24 ± 0.012  | 0.11 ± 0.02   | 0.063 ± 0.012 | -0.18 ± 0.036 |
| T <sub>dg</sub> (°C)                                     | 685           | 657           | 617           | 592           |
| T <sub>s</sub> (± 5) (°C)                                | 716           | 695           | 686           | 677           |
| CTE x 10 <sup>6</sup> (K <sup>-1</sup> )<br>(200-500 °C) | 8.69          | 8.69          | 8.87          | 9.31          |
| T <sub>p</sub> (°C)                                      | 912           | 908           | 895           | 875           |
| <i>n</i>                                                 | -             | 2.08 ± 0.01   | 1.98 ± 0.005  | 1.94 ± 0.002  |
| E <sub>c</sub> (kJ mol <sup>-1</sup> )                   | 300           | 328           | 339           | 342           |

#### 4.6.3 Density and dilatometry measurements

##### 4.6.3.1 CaF<sub>2</sub> containing glasses

The density of the glasses varied between 3.08-3.12 g cm<sup>-3</sup> and was found to increase with an increase in CaF<sub>2</sub> content in the glasses (Table 4.32). The values of V<sub>m</sub> and V<sub>e</sub> decreased with an increase in CaF<sub>2</sub> content in the glasses (Table 4.32). This decrease in V<sub>m</sub> and V<sub>e</sub> may be attributed to the high ionic character of CaF<sub>2</sub>. Since, the ionic bonds are non-directional in nature, increasing CaF<sub>2</sub> will lead to the collapse of the structural skeleton into a closer packing, thus, decreasing the excess volume (V<sub>e</sub>) [145] and, therefore, increasing the CTE and decreasing T<sub>dg</sub> and T<sub>s</sub> of the glasses (Table 4.32). The values of V<sub>m</sub>, as obtained for all the glasses under investigation, are lower than their B<sub>2</sub>O<sub>3</sub>-containing analogues investigated in section 4.4.3. This is due to the fact that unlike CaF<sub>2</sub>,

B<sub>2</sub>O<sub>3</sub> is covalent in nature and thus, promotes directional bonding in the glass structural network.

#### 4.6.3.2 Di-CaTs based glasses containing Fe<sub>2</sub>O<sub>3</sub> and Cr<sub>2</sub>O<sub>3</sub>

The experimental results showed that substitution of 0.1Ca<sup>2+</sup> + 0.1Mg<sup>2+</sup> ↔ 0.1La<sup>3+</sup> + 0.1Li<sup>+</sup> caused an increase in the density of the glass 8A (3.00 ± 0.007 g cm<sup>-3</sup>) in comparison to the parent glass 8 (2.89 ± 0.006 g cm<sup>-3</sup>). Since, the density of Li<sub>2</sub>O (2.01 g cm<sup>-3</sup>) is the lowest among all the constituent oxides of the glass, thus, this increase in density of glass 8A is due to the higher density of La<sub>2</sub>O<sub>3</sub> (6.5 g cm<sup>-3</sup>).

The  $V_m$  for glasses, 8 and 8A was calculated to be 20.50 ± 0.043 g cm<sup>-3</sup> and 21.03 ± 0.006 g cm<sup>-3</sup>, respectively while  $V_e$  for both the glasses was obtained to be 0.85 ± 0.029 g cm<sup>-3</sup> and 0.73 ± 0.006 g cm<sup>-3</sup>, respectively. An increase in  $V_m$  of glass 8A in comparison to glass 8 may be attributed to the lower ionic field strength of Li<sup>+</sup> (0.23) in comparison to all the constituent oxides in the glass, particularly Mg<sup>2+</sup> (0.45) and Ca<sup>2+</sup> (0.35), while the ionic field strength of La<sup>3+</sup> (0.46) is compared to Mg<sup>2+</sup> (0.45). However, a decrease in  $V_e$  of glass 8A in comparison to glass 8 may be explained on the basis of optical basicity ( $\Lambda$ ) concept [191]. The optical basicity of Li<sub>2</sub>O ( $\Lambda = 0.87$ ) and La<sub>2</sub>O<sub>3</sub> ( $\Lambda = 1.07$ ) is higher than MgO ( $\Lambda = 0.69$ ) and CaO ( $\Lambda = 1$ ) [192, 193]. Therefore, substitution of MgO and CaO by Li<sub>2</sub>O and La<sub>2</sub>O<sub>3</sub> will lead to an increase in the theoretical optical basicity ( $\Lambda_{th}$ ) of the glass, since  $\Lambda_{th}$  serves in the first approximation as a measure of the ability of oxygen to donate a negative charge in the glasses. It can be used to classify the covalent/ionic ratios of the glasses since an increasing  $\Lambda_{th}$  indicates decreasing covalency. Since ionic bonds are non-directional in nature, introduction of Li<sub>2</sub>O and La<sub>2</sub>O<sub>3</sub> will lead to the collapse of the structural skeleton into a closer packing, thus, decreasing the excess volume of the glass [145].

The  $T_{dg}$  values of glasses 8 and 8A, determined from these curves, are 615 °C and 584 °C, while their softening points are 715 °C and 698 °C, respectively. From the slope of the linear part of these curves (i.e. between 200-500 °C), the CTE values of the two glasses were calculated as 7.42 x 10<sup>-6</sup> K<sup>-1</sup> and 7.56 x 10<sup>-6</sup> K<sup>-1</sup>, respectively. The slight increase in CTE and decrease in  $T_{dg}$  of glass 8A can be explained on the basis of decrease in the excess molar volume ( $V_e$ ) owing to the collapse of directional bonds in the skeleton of the glass.

#### 4.6.4 FTIR analysis

##### 4.6.4.1 CaF<sub>2</sub> containing glasses

The room temperature FTIR transmittance spectra of all the investigated glasses are shown in Fig. 4.64. All spectra exhibit three broad transmittance bands in the region of 300-1300 cm<sup>-1</sup>. This lack of sharp features is indicative of the general disorder in the silicate network mainly due to a wide distribution of  $Q^n$  (polymerization in the glass

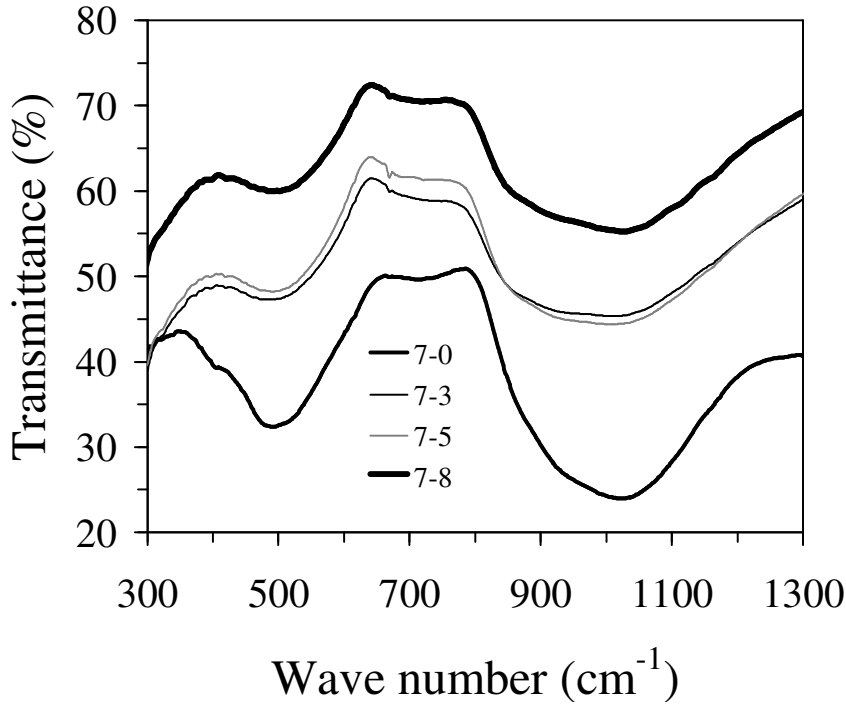


Fig. 4.64 FTIR spectra of CaF<sub>2</sub> containing glasses.

structure, where  $n$  denotes the number of bridging oxygens) units occurring in these glasses. The most intense bands in the 800-1300 cm<sup>-1</sup> region correspond to the stretching vibrations of the SiO<sub>4</sub> tetrahedron with a different number of bridging oxygen atoms while bands in the 300-600 cm<sup>-1</sup> region are due to bending vibrations of Si-O-Si and Si-O-Al linkages [123, 125]. The least intensive bands in the region 650-800 cm<sup>-1</sup> are related to the stretching vibrations of the Al-O bonds with Al<sup>3+</sup> ions in four-fold coordination [123]. The transmittance bands in 800-1300 cm<sup>-1</sup> region for CaF<sub>2</sub> containing glasses are registered at considerably lower wave numbers than those observed for CaF<sub>2</sub>-free parent glass (7-0). Thus, it is evident that the introduction of fluoride ions breaks up  $Q^3$  units and favours the formation of  $Q^2$  units. This depolymerization of glass network and formation of NBOs

leads to decrease in the  $T_{dg}$  of glasses (Table 4.32). The band in the region  $650\text{-}800\text{ cm}^{-1}$  shifted towards lower wave number with the addition of  $\text{CaF}_2$ . This may be due to the overlapping of band corresponding to the stretching vibrations of Al-O binds with that of F<sup>-</sup> as the characteristic band for F<sup>-</sup> lies around  $\sim 740\text{ cm}^{-1}$  [20].

#### 4.6.4.2 Di-CaTs based glasses containing $\text{Fe}_2\text{O}_3$ and $\text{Cr}_2\text{O}_3$

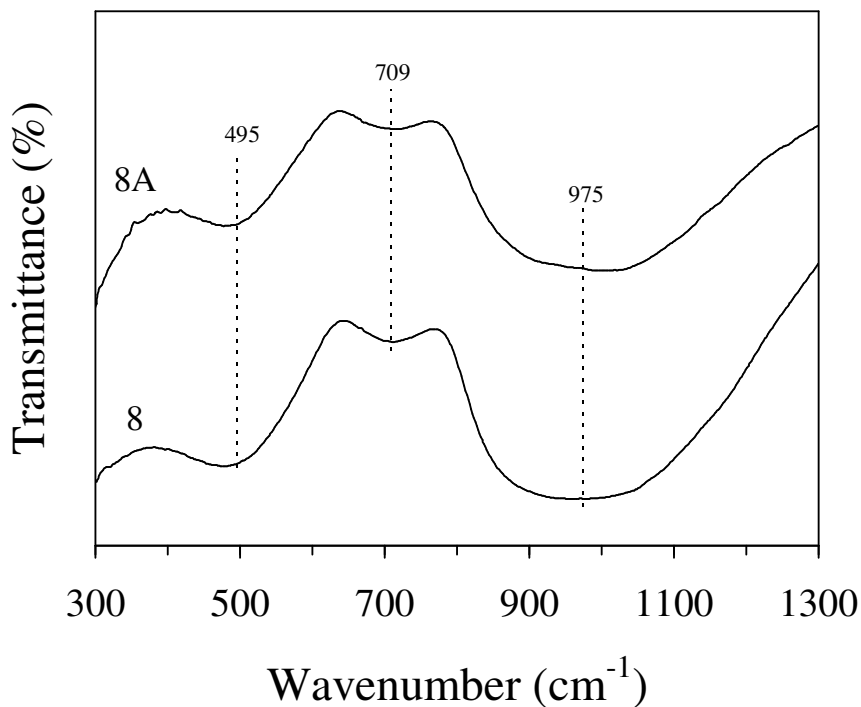


Fig. 4.65 FTIR spectra of glasses 8 and 8A.

The room temperature FTIR transmittance spectra of both the investigated glasses are shown in Fig. 4.65. Both spectra exhibit three broad transmittance bands in the region of  $300\text{-}1300\text{ cm}^{-1}$ . This lack of sharp features is indicative of the general disorder in the silicate network mainly due to a wide distribution of  $Q^n$  units occurring in these glasses. The bands in  $800\text{-}1300\text{ cm}^{-1}$  region, for both the glasses, were registered at  $\sim 975\text{ cm}^{-1}$ , which is considerably lower wave number than those observed for Di-CaTs glass investigated in section 4.2. This indicates the distribution of  $Q^n$  units around  $Q^2$  which suggests that addition of  $\text{Cr}_2\text{O}_3$  and  $\text{Fe}_2\text{O}_3$  led to the formation of non-bridging oxygens (NBOs) in the silicate glass network.

#### 4.6.5 Crystallization kinetics by DTA, XRD and SEM

##### 4.6.5.1 CaF<sub>2</sub> containing glasses

The DTA (NETZSCH 402 EP, Germany) plots of all the CaF<sub>2</sub>-containing glasses exhibit single exothermic effects at all the heating rates which shifted towards higher temperatures with increase in heating rate. The existence of a single crystallization exotherm signifies that either the GC formed as a result of crystallization is mono-mineral or different crystalline phases appear from the glass matrix almost simultaneously and the crystallization curve is the resultant of all the crystallization curves formed due to the appearance of different crystalline phases.

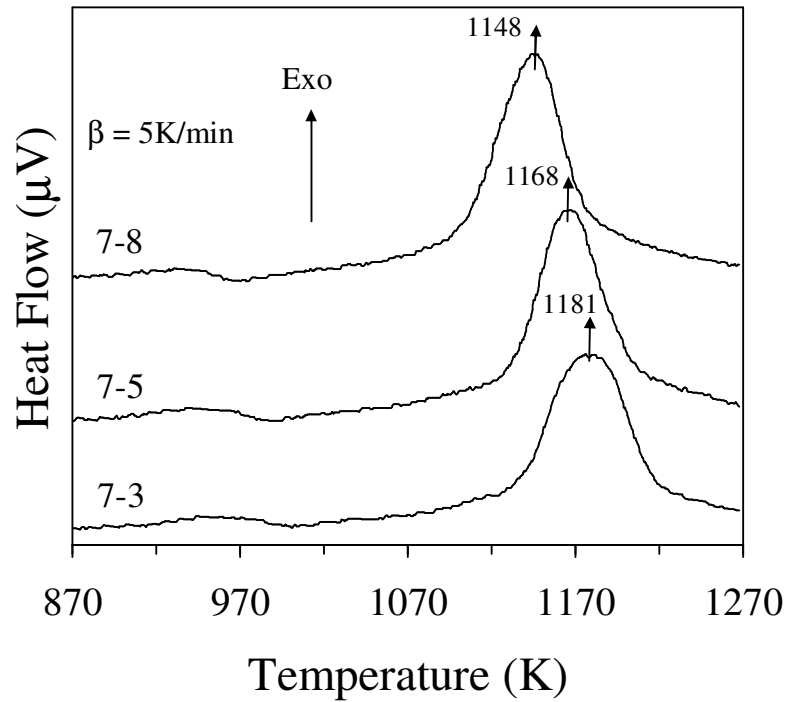


Fig. 4.66 DTA thermographs of CaF<sub>2</sub>-containing glasses.

The peak temperature of crystallization,  $T_p$  decreased with an increase in CaF<sub>2</sub> content in the glasses as shown in Fig. 4.66. XRD results of the heat treated glasses reveal that addition of CaF<sub>2</sub> in the parent glass, Ca<sub>0.8</sub>Ba<sub>0.1</sub>MgAl<sub>0.1</sub>La<sub>0.1</sub>Si<sub>1.9</sub>O<sub>6</sub> disturbed the formation of pyroxene solid solution and led to the crystallization of diopside (ICDD card: 01-078-1390; CaMgSi<sub>2</sub>O<sub>6</sub>) and La<sub>2</sub>O<sub>3</sub>-containing crystalline phase named, britholite (01-076-0340; La<sub>9.31</sub>(Si<sub>1.04</sub>O<sub>4</sub>)<sub>6</sub>O<sub>2</sub>) in all the thermal cycles except that of heat treatment at 800

°C. All the investigated glasses were amorphous after heat treatment at 800 °C. No fluorine containing phase could be detected after any thermal treatment evidencing that the F<sup>-</sup> ions were accumulated in the glassy phase. Fig. 4.67a shows the microstructural image of glass 7-8 after heat treatment at 700 °C for 1 h and presents a clear evidence of phase separation in the glasses in the form of network like structures with the introduction of fluoride ions in the glasses. The tendency to form such structures increased with an increase in the concentration of fluoride ions. Further, after heat treatment at 800 °C (Fig. 4.67b), though the glasses were XRD amorphous, nucleation occurred on the edge of the glasses through rosette morphology, evidencing the initiation of surface nucleation. Fig. 4.67c shows the

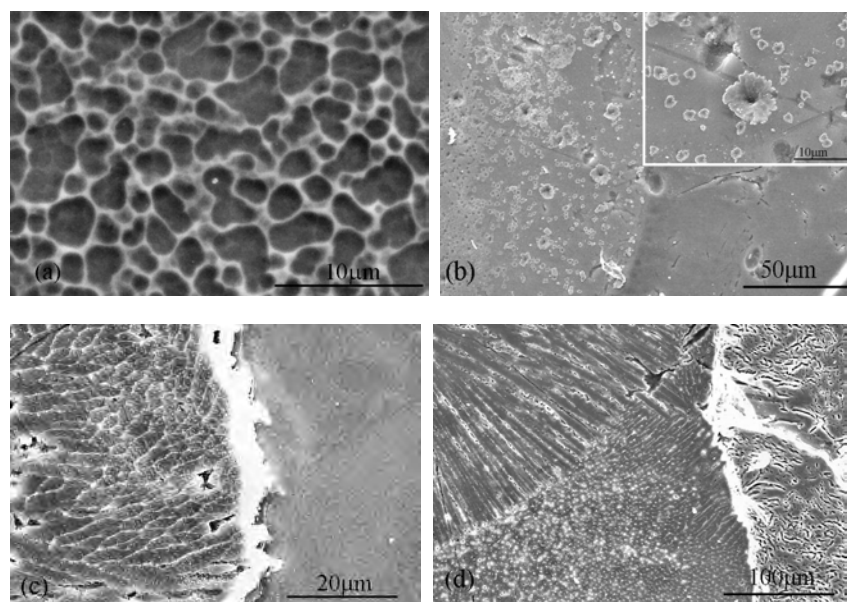


Fig. 4.67 Microstructure of the glass-ceramics (a) 7-8 (step1), (b) 7-5 (step 2), (c) 7-3 (step 5) (d) 7-5 (step 6) after etching in 2 vol% HF for 2 min.

initiation of crystallization from the surface of sample signifying the presence of surface crystallization while Fig. 4.67d shows the existence of crystalline phases with different microstructure in the GCs confirming the XRD results. Also, it is noteworthy that all the obtained GCs had either an amorphous glass or a hollow cavity in the core of the GC, thus pointing towards the existence of surface crystallization mechanism. The heating of glasses at different nucleating temperatures (step 4 and step 5) followed by heating them at final

crystallization temperature was also ineffective in achieving three-dimensional bulk crystallization in any of the investigated glass compositions. The Avrami parameters for all the three CaF<sub>2</sub>-containing glasses were calculated to be in the range 1.93-2.0 (Table 4.32), signifying towards the two-dimensional crystal growth and intermediate (i.e. simultaneous surface and bulk crystallization) mechanism of crystallization. The activation energy of crystallization (E<sub>c</sub>) increased with addition of CaF<sub>2</sub> in the parent glass (7-0) and varied between 300-342 kJ mol<sup>-1</sup> (Table 4.32, Fig. 68).

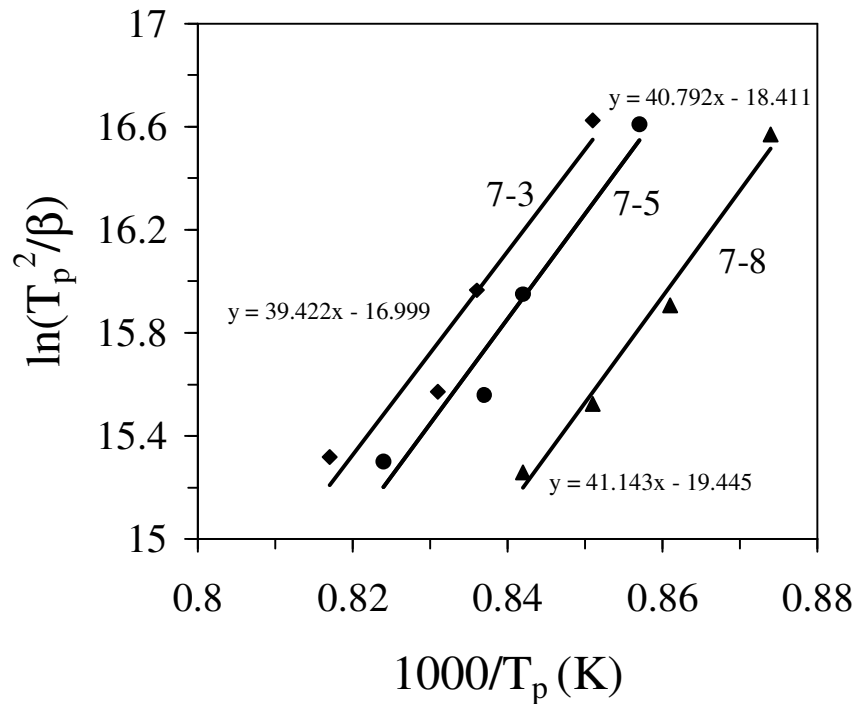


Fig. 4.68 Plot of  $\ln(T_p^2/\beta)$  v/s  $1/T_p$  in order to calculate the  $E_c$  for the investigated glasses.

#### 4.6.5.2 Di-CaTs based glasses containing Fe<sub>2</sub>O<sub>3</sub> and Cr<sub>2</sub>O<sub>3</sub>

The DTA plots of both the glasses exhibit single exothermic effects at all the heating rates which shifted towards higher temperatures with increasing heating rates (Table 4.33). This signifies that either the GC formed as a result of crystallization is monomineral or different crystalline phases precipitate from the parent glass almost simultaneously. The introduction of Li<sub>2</sub>O and La<sub>2</sub>O<sub>3</sub> caused a decrease in T<sub>p</sub> of glass 8A in comparison to glass 8 (Table 4.33).

Table 4.33 Variation in  $T_p$  ( $^{\circ}\text{C}$ ) with heating rate

| Heating rate ( $\beta$ ) | Glass 8 | Glass 8A |
|--------------------------|---------|----------|
| 5                        | 950     | 905      |
| 20                       | 982     | 947      |
| 30                       | 992     | 960      |
| 40                       | 1005    | 974      |

The values of Avrami parameter,  $n$ , for glasses 8 and 8A are  $1.41 \pm 0.01$  and  $1.76 \pm 0.01$ , respectively, while the  $E_c$  for these glasses are  $490 \text{ kJ mol}^{-1}$  and  $355 \text{ kJ mol}^{-1}$  (Fig. 4.69), respectively. The  $E_c$  value for glass 8 is almost similar to that for its parent composition (Di/Ca-Ts = 75/25 (mol.%), without  $\text{Cr}_2\text{O}_3$  and  $\text{Fe}_2\text{O}_3$ ), investigated in section 4.2. However, the crystallization mechanism in the parent composition (section 4.2) was bulk crystallization with two-dimensional growth of crystals [195, 196], while in the present study, the value of Avrami parameter,  $n$ , for glass 8 suggests three dimensional growth of crystals with polyhedron-like morphology indicating bulk crystallization with a constant number of nuclei with diffusion controlled crystal growth rate [195, 196]. This implies that the addition of appropriate amounts of  $\text{Cr}_2\text{O}_3$  and  $\text{Fe}_2\text{O}_3$  in the pyroxene based glasses does not affect the crystallization behaviour of the glasses but alters their crystallization mechanism. The  $E_c$  for glass 8A decreased considerably in comparison to glass 8 due to the substitution of  $0.1\text{Ca}^{2+} + 0.1\text{Mg}^{2+} \leftrightarrow 0.1\text{La}^{3+} + 0.1\text{Li}^+$  while value of  $n$  increased. The Avrami parameter for glass 8A suggests the simultaneous existence of two different crystallization mechanisms: (1) diffusion controlled, three dimensional growth of crystals with polyhedron-like morphology indicating bulk crystallization with a constant number of nuclei, (2) interface reaction mechanism with two-dimensional growth of bulk crystallization with a constant number of nuclei [195, 196]. It is worth mentioning that GCs produced from monolithic glass 8A after heat treatment at  $950 \text{ }^{\circ}\text{C}$  and  $1000 \text{ }^{\circ}\text{C}$  had at least one small hole(s) on its surface, however, it did not extend to the core of the GC. Such existence of holes/cavities was completely absent in GCs produced from glass 8. The

existence of these small holes/cavities in GC 8A while their absence in GC 8 supports the crystallization mechanism data obtained from crystallization kinetics studies. Thus, it may

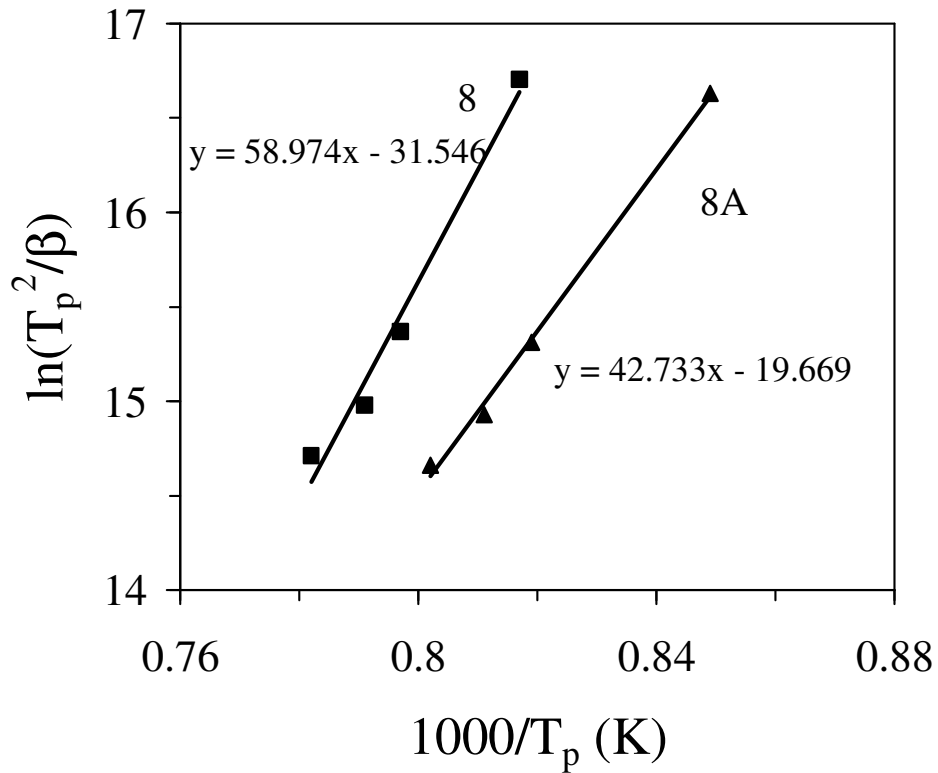


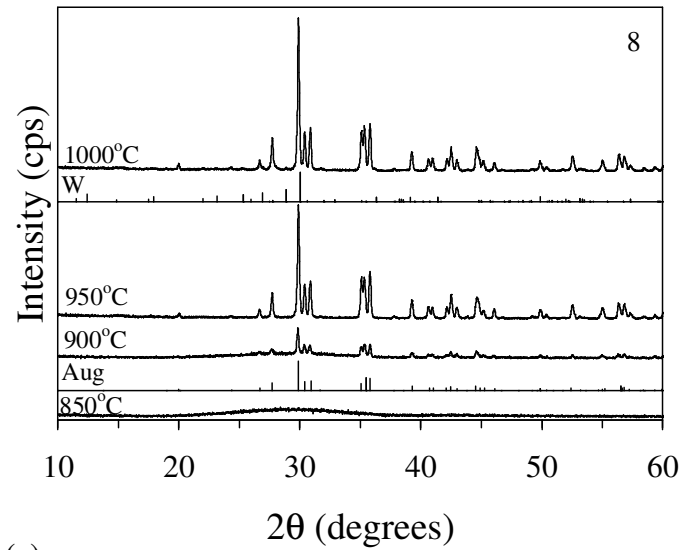
Fig. 4.69 Plot of  $\ln(T_p^2/\beta)$  v/s  $1/T_p$  in order to calculate the  $E_c$  for the investigated glasses

8 and 8A.

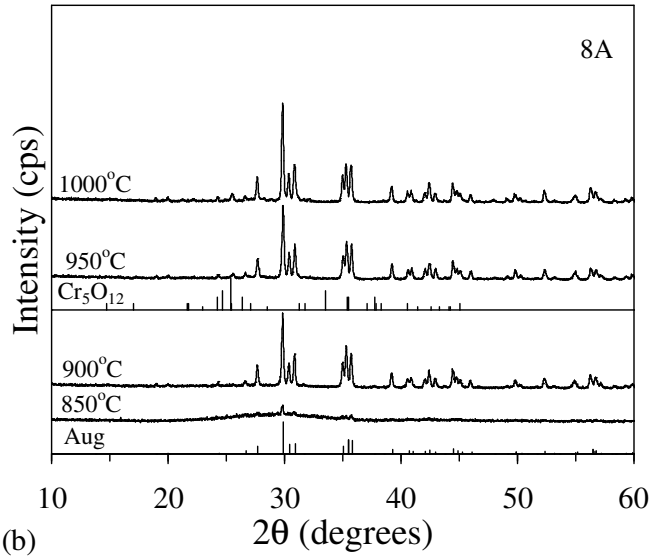
be concluded that 3 wt.%  $Fe_2O_3$  and 0.7 wt.%  $Cr_2O_3$  are effective nucleating agents for pure Di-Ca-Ts glass systems while substitutions in these glass systems alter the crystallization mechanism in the resultant GCs. The  $T_p$  and  $E_c$  values obtained for glasses 8 and 8A are considerably lower than their parent compositions (section 4.2), thus proving that the mixture of  $Cr_2O_3$  and  $Fe_2O_3$  acted as an effective nucleating agent in these glasses.

According to XRD results (Fig. 4.70), no-crystalline phase was observed in composition 8 after heat treatment at 800 and 850 °C. In consistence with the behaviour observed for glass 8, composition 8A was also amorphous at 800 °C, however, unlike to composition 8, very low intensity peaks of augite (Aug;  $Ca(Mg_{0.70}Al_{0.30})(Si_{1.70}Al_{0.30})O_6$ ; ICDD card: 01-078-1392) were recorded in composition 8A after heat treatment at 850 °C, thus, initiating the devitrification in the glass. The early initiation of crystallization in glass

8A is also supported by its low  $E_c$  value in comparison to glass 8. The intensity of the XRD peaks for augite increased significantly with increasing temperature in GC 8 and was found to be maximum at 1000 °C (Fig. 4.70a) while no significant effect was observed on the intensity of XRD peaks for Aug in GC 8A in the temperature interval 900-1000 °C (Fig. 4.70b). It is noteworthy that mono-mineral GCs were obtained for both compositions 8 and 8A until 950 °C and 900 °C, respectively. After heat treatment at 1000°C, wollastonite (W; ICDD: 00-042-0550;  $\text{CaSiO}_3$ ) crystallized out as a minor phase in GC 8, while Aug still predominated as the primary crystalline phase. No chromium- or iron- containing phases



(a)



(b)

Fig. 4.70 X-ray diffractograms of GCs (a) 8 and (b) 8A heat treated at different temperatures.

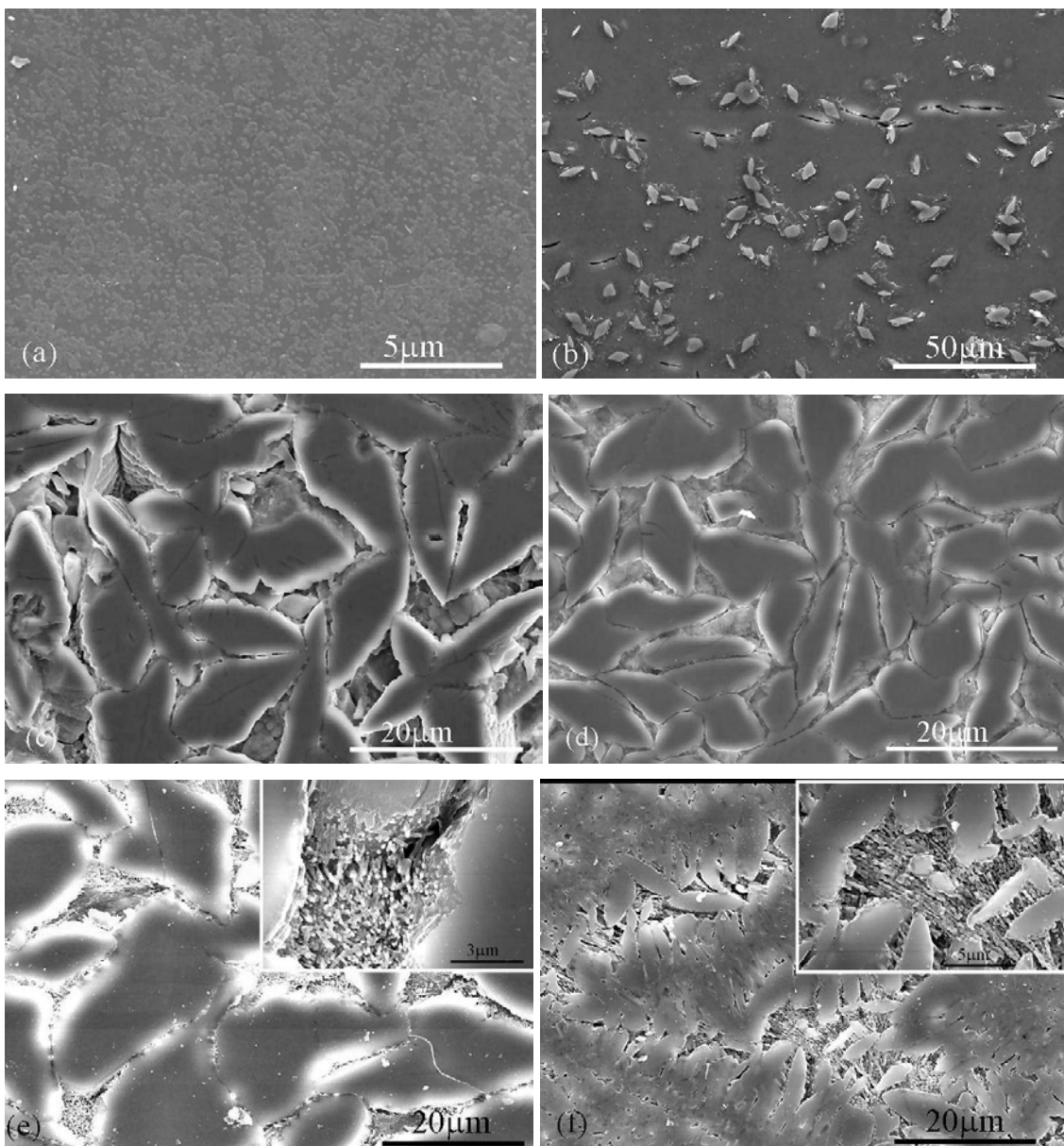


Fig. 4.71 SEM images of GCs (revealed after etching in 2 vol.% HF) (a) 8A after heat treatment at 700 °C for 2 h followed by heat treatment at 800 °C for 1 h, (b) 8A after heat treatment at 700 °C for 2 h followed by 850 °C, (c) 8 after heat treatment at 700 °C for 2 h followed by heat treatment at 900 °C for 1 h (d) 8A after heat treatment at 700 °C for 2 h followed by heat treatment at 900 °C for 1 h (e) 8A after heat treatment at 700 °C for 2 h followed by heat treatment at 950 °C for 1 h (f) 8A after heat treatment at 700 °C for 2 h followed by heat treatment at 1000 °C for 1 h.

were observed for GC 8 at any of the investigated temperatures. In the case of GC 8A, orthorhombic chromium oxide ( $\text{Cr}_5\text{O}_{12}$ ; ICDD: 00-018-0390) precipitated out after heat treatment at 950 and 1000 °C. However, unlike to GC 8, wollastonite could not be detected at any of the investigated temperatures. We did not observe any unidentified XRD peak at  $2\theta \approx 19^\circ$  in GC 8, as was observed for Di-CaTs based GCs in section 4.3. However, a small intensity peak at  $2\theta \approx 19^\circ$  was observed for GC 8A.

Fig. 4.71 shows some SEM images of the GCs investigated in the present study. The formation of segregated zones, amorphous in nature (as shown by XRD), can be seen in composition 8A after heat treatment at 800 °C, leading to the nucleated-droplet phase separation in the glasses (Fig. 4.71a). These zones probably acted as nucleating centres to induce bulk crystallization in the investigated glasses. Although, it has been shown earlier that pyroxene based glasses are prone to phase separation, however, the formation of such intense segregated zones before the initiation of devitrification may be attributed to the presence of  $\text{Cr}_2\text{O}_3$  and  $\text{Fe}_2\text{O}_3$  in the glasses. In accordance with the XRD results, further increase in temperature to 850 °C led to the formation of small crystals of augite from the amorphous glassy matrix and complete absence of the phase separated zones (Fig. 4.71b). The microstructure revealed by GC 8 and 8A was almost similar as is evident from Fig. 4.71c and Fig. 4.71d, where fully grown disc shaped Aug crystals can be seen in both the GCs after heat treatment at 900 °C. Fig. 4.71e and Fig. 4.71f depict the microstructure of GC 8A after heat treatment at 950 and 1000 °C, respectively, featuring intense crystallization of augite at both the temperatures.

.....

## **CHAPTER V: Conclusions**

## 5.1 Enstatite-Diopside join: Magnesium-metasilicate (MgSiO<sub>3</sub>) based glasses and glass-ceramics

The influence of partial substitutions in cation and anion sublattice of Mg-metasilicate on the properties and the crystallization of the investigated glasses and GCs is summarized as follows.

- a) The compositions 2a, 2b, 3a and 3b results in homogenous transparent glasses after melting at 1600 °C for 1 h, whereas longer melting is required for glasses of the composition 1. The value of kinetic fragility index (F) of these glasses feature lower glass forming tendency in comparison to diopside based glasses.
- b) The infrared spectroscopy reveals that the symmetric and the anti-symmetric stretching modes of the Si-O-Si bonds of the Q<sub>n</sub> units in the glass silicate network are distributed around Q<sup>2</sup> and Q<sup>3</sup>. The addition of BaO and Al<sub>2</sub>O<sub>3</sub> causes a change in the proportion of Q<sup>2</sup> and Q<sup>3</sup> units, which leads to a decrease in the connectivity of the silicate glass network.
- c) The suggested Y-substitution for Mg in composition 2b causes stabilization of OE and CE, while addition of Al<sub>2</sub>O<sub>3</sub> affects the diffusion mechanism in the glass powder compacts resulting in well sintered MgSiO<sub>3</sub>-based GCs. The poor sintering ability of Al<sub>2</sub>O<sub>3</sub>-free glasses, 2a and 3a, has been attributed to their higher activation energy of viscous flow.
- d) The value of Avrami parameter, *n* calculated for Al<sub>2</sub>O<sub>3</sub>-free glasses indicates that surface nucleation and crystallization mechanism dominates in these glasses. CE and OE are the predominant phases in the GCs 2a while BaO stabilizes PE in GCs 3a. Addition of Al<sub>2</sub>O<sub>3</sub> in glass 3b led to the formation of HC along with PE, CE and OE.

From the technological application point of view, enstatite based glasses/GCs are not suitable for application as sealants in SOFC due to their relatively low CTE. However, they can be potential candidates for the job of ceramic insulators and standoff resistors. Particularly, compositions 2b and 3b exhibited good sintering ability resulted in higher mechanical strength. Specially, the absence of metastable PE in GC 2b may be considered as an important step towards the prevention from aging of steatite ceramics and the increasing stability of the system during exploitation

.....

## 5.2 Diopside-Ca-Tschermak join

Four glasses with nominal compositions corresponding to Di/CaTs mole ratios of 80/20 (DT1), 75/25 (DT1a), 70/30 (DT1b), and 65/35 (DT1b) were investigated for their structure, thermal stability, crystallization behaviour and properties of resultant GCs. The results obtained are concluded as follow:

- a) The infrared spectroscopy reveals that the symmetric and the anti-symmetric stretching modes of the Si-O-Si bonds of the  $Q^n$  units in the glass silicate network are distributed around  $Q^2$  and  $Q^3$ .
- b) The phenomenon of glass-in-glass phase separation exists in the glasses due to the presence of  $Ca^{2+}$  and  $Mg^{2+}$  ions. The values of various thermal parameters around glass transition reveal that the glass composition corresponding to Di/ CaTs = 70/30 (DT1b) is thermally most stable.
- c) The Avrami parameter for the glass powders decreases from 2.11 to 1.96 with decrease in Di/CaTs ratio, which shows that the crystallization did not occur on the fix number of nuclei and the crystallization mechanism is intermediate (i.e. both bulk and surface crystallization) in all the glasses, which shifts more towards surface crystallization with decrease in Di/CaTs ratio.
- d) The threshold of CaTs dissolution in Di is c.a. 30 mol% between 850 °C and 1000 °C. This is important for obtaining mono-mineral GCs of augite and their properties, such as densification, mechanical, and thermal properties.
- e) The above experimental results in conjunction with the good matching of CTE and adherence of the investigated compositions with cubic zirconia (8YSZ) reveal promising perspectives for their potential as SOFC sealants. Destabilization of augite and CTE decrease after prolong heat treatment seem to be two drawbacks needed for thorough consideration in future investigations, but in the light of the general trend for decreasing SOFC operation temperatures (that are presently between 750 °C and 800 °C), the investigated compositions exhibit promising prospects as candidate SOFC sealants.

.....

### 5.3 Influence of ZnO and BaO on the crystallization behaviour and properties of Di-CaTs based glasses

The role of ZnO and BaO on the crystallization behaviour of the Di-CaTs based glasses and properties of their sintered GCs has been investigated. The results are summarized below:

- a) The glass DT-Zn2 is thermally most stable in the glass transition region, in comparison to the other three (ZnO-containing) investigated glasses. The activation energy for crystallization decreases with the increase in ZnO content while an intermediate type of crystallization mechanism was observed in all the four glasses. Well sintered and dense GCs were obtained for all the compositions. Augite precipitated out as the primary phase in all the compositions. However, depletion of MgO accelerates the formation of wollastonite and addition of 3.68 wt. % ZnO (DT-Zn2) leads to the formation of Zn-containing hardystonite as the secondary phases in the GCs.
- b) The molar volume and density of BaO-containing glasses are higher than BaO-free and ZnO-containing Di-CaTs glasses. The Avrami parameter for BaO-containing glasses varies between 2.03-2.12, which shows the existence of two-dimensional growth of crystals with constant number of nuclei in all the investigated glasses. The addition of B<sub>2</sub>O<sub>3</sub> retards the crystallization rate by stabilizing the amorphous phase in the glass, thus, leading to higher activation energy of crystallization. Well-sintered GCs comprising of ortho- (OC) and hexacelsian (HC) along with Di/CaTs solid solutions were obtained after sintering at 850 °C - 900 °C for 1 h. Pronounced decrease of augite X-ray peaks intensity and formation of monocelsian were observed in GCs BaCMAS4 after heat treatment at 900 °C for 300 h. Augite dominated in BaCMAS1 with OC as a secondary phase, while the most intensive peaks of Au and OC had similar intensities in BaCMAS2, and OC predominated in BaCMAS3. The density of the GCs increased and the bending strength decreased with the increase of BaO-content. Although BaCMAS3 exhibited a higher conductivity compared to BaCMAS1 and BaCMAS2, all glass-ceramics exhibit good insulating properties. At 850 °C, the total conductivity values vary in the

range of  $(0.9 \times 10^{-7} - 2.4 \times 10^{-7})$  S/cm. The low level of oxygen permeation fluxes under air / ( $\text{H}_2 + \text{H}_2\text{O} + \text{N}_2$ ) gradient indicates that in typical conditions for SOFC operation, no significant leakages may be expected. These properties, in conjunction with the negligible interfacial reaction with cubic zirconia (8YSZ) and the good matching of CTEs, qualifying the investigated materials as potential candidate SOFC sealant materials.

.....

#### **5.4 Influence of B<sub>2</sub>O<sub>3</sub>, BaO, SrO, Cr<sub>2</sub>O<sub>3</sub> and La<sub>2</sub>O<sub>3</sub> on sintering, crystallization behaviour and properties of diopside based glasses and glass-ceramics**

The effect of B<sub>2</sub>O<sub>3</sub>, BaO, SrO, Cr<sub>2</sub>O<sub>3</sub> and La<sub>2</sub>O<sub>3</sub> on structure, sintering behaviour, crystallization kinetics and properties of La<sub>2</sub>O<sub>3</sub>-containing Di based GC sealants has been studied and the interfacial adhesion along with chemical stability between GC sealants and metallic interconnects has been investigated under different atmospheres. The results obtained are as summarized below:

- a) Infrared spectroscopy along with MAS-NMR results reveals that Si atoms would be likely centered on  $Q^2$  units. No significant change on the structure of silicate network was observed with the addition of B<sub>2</sub>O<sub>3</sub> in the glasses. Boron tends to exist predominantly in BO<sub>3</sub> units while an increase in BO<sub>4</sub> units was found with an increase in B<sub>2</sub>O<sub>3</sub> concentration in the glasses. Al was found to be dominantly coordinated in AlO<sub>4</sub> units.
- b) An increase in glass transition temperature and CTE has been observed with the initial substitution of La<sub>2</sub>O<sub>3</sub> in comparison to La<sub>2</sub>O<sub>3</sub> free glasses while an opposite effect was observed with increase in B<sub>2</sub>O<sub>3</sub> concentration.
- c) Sintering precedes crystallization in all the GCs with B<sub>2</sub>O<sub>3</sub> content varying between 0 -5 wt.% and well sintered GPCs were obtained. GCs containing > 5 wt.% B<sub>2</sub>O<sub>3</sub> were highly porous, thus, rendering them unfit for sealing application in SOFC. The addition of La<sub>2</sub>O<sub>3</sub> improved the sintering behaviour of glasses while decreasing the activation energy of crystallization. An increase in B<sub>2</sub>O<sub>3</sub> decreased the half ball, flow temperature and activation energy of crystallization of all the glasses. The viscosity of all the GC sealants at SOFC operation temperature is appropriate for sealant applications. The addition of Cr<sub>2</sub>O<sub>3</sub> in the glasses decreased the activation energy of crystallization while it increased with replacement of BaO by SrO. However, 0.5 wt.% of Cr<sub>2</sub>O<sub>3</sub> was not found to be an effective nucleating agent in order to induce bulk nucleation in Di based glasses.
- d) Augite crystallized as the primary phase in all GCs after sintering in the temperature interval of 800 – 1000°C for 1 h. Monoclinic celsian did not crystallize in any of the GCs after heat treatment of 300 h at SOFC operating temperatures.

- e) Although the electrical conductivity of the GCs increased with the addition of  $\text{Cr}_2\text{O}_3$  and initial addition of  $\text{B}_2\text{O}_3$ , all the GCs still exhibited good insulating properties.

From the results concluded above, it is evident that  $\text{La}_2\text{O}_3$ -BaO- containing Di based GCs with  $\text{B}_2\text{O}_3$  content  $\leq 5$  wt.% exhibited essential features with respect to sealant applications in SOFC namely, good sintering behaviour at  $800^\circ\text{C}$ - $850^\circ\text{C}$ , absence of detrimental monoclinic celsian phase, long-term CTE stability, good insulating properties, bonding to the metallic interconnects, high area-specific resistance and excellent thermal shock resistance in air.  $\text{La}_2\text{O}_3$ -SrO-containing diopside based GCs, 7(Sr)-2B and 7(Sr)-5B, also exhibited general similar features, but the absence of any severe interface reactions conferred enhanced interface stability to the glass/metallic joins. However, their long-term CTE stability needs to be somewhat improved. Therefore, further experimentation on  $\text{La}_2\text{O}_3$ - diopside based GCs as candidate SOFC sealant material has to be continued.

.....

## 5.5 Optimization of diopside based glass-ceramic sealants for sealing applications in SOFC

The structural characteristics along with sintering behaviour along with crystallization kinetics of a new series of Di based glasses has investigated in order to develop a suitable GC sealing composition for SOFC. Further, the electrical properties, thermal shock resistance of GCs and chemical interactions between GC sealants and metallic interconnect materials has been discussed. The results obtained are summarized as follow:

- a) The investigated glasses showed a steady increase in density, CTE and molar volume with addition of  $\text{Cr}_2\text{O}_3$  and increasing BaO contents while no significant variation in  $T_g$  was observed. Infra-red spectroscopy reveals that Si atoms would be likely centred on  $Q^2$  units. The introduction of BaO led to an increase in the polymerization of glass network by formation of  $Q^3$  type silicate species along with  $Q^2$ . However, further increase in BaO de-polymerized the silicate glass network.
- b) An intermediate mechanism of crystallization has been obtained for all the glasses while the activation energy of crystallization decreased with addition of  $\text{Cr}_2\text{O}_3$  and with an increase in BaO until glass 10C.
- c) Sintering preceded crystallization in all the investigated glass compositions. BaO-free GPCs exhibited single stage sintering behaviour while two - step shrinkage behaviour was observed for BaO-containing glasses leading to improved flow behaviour of the glasses, thus making them suitable for sealing applications in SOFC operating in the temperature range of 800-1000 °C. The addition of  $\text{Cr}_2\text{O}_3$  improved the sintering ability of the glasses, increased the crystalline content, and promoted the formation of augite based solid solution in GC 10A, thus, resulting in highest mechanical strength (166 MPa). On the contrary, addition of BaO led to the dissolution of augite so as to increase the amount of amorphous phase in the GCs and encouraged the formation of diopside as a secondary phase along with augite which degraded the mechanical strength of the GCs.
- d) Well sintered GCs with augite as the primary crystalline phase were obtained in all the compositions. The addition of BaO led to a progressive decrease in the total conductivity of the GCs and to progressive increase of the activation energies, thus,

ensuring an absence of short circuiting between the SOFC stack components, especially in the intermediate temperature range. The addition of BaO increased the CTE of the resultant GCs which showed high thermal stability during long term heat treatments. The investigated GC sealants, 10B and 10C, demonstrated a good thermal shock resistance in air while cracks were only developed on quenching in water. Formation of Ti-rich oxide layers at the interface between GC sealants and Crofer22 APU was observed while no adverse reactions leading to the formation of BaCrO<sub>4</sub> were observed in any of the investigated diffusion couples.

.....

## 5.6 Influence of nucleating agents on the crystallization kinetics of diopside and Di-CaTs based glasses

In conclusion, effect of  $\text{CaF}_2$  addition and  $\text{Cr}_2\text{O}_3 + \text{Fe}_2\text{O}_3$  addition has been investigated on the structure and crystallization behaviour of clinopyroxene based glasses. The molar volume, excess volume and glass transition temperature decreases while density and CTE increases with an increase in fluoride ion content. The addition of fluoride ion causes the silicate glass network to break and thus led to the formation of  $Q^2$  units. The addition of  $\text{CaF}_2$  disturbed the solid solution formation and led to the formation of diopside and britholite. Three-dimensional bulk crystallization could not be achieved in any of the  $\text{CaF}_2$ -containing glasses. The activation energy of crystallization increased with an increase in  $\text{CaF}_2$  content in the glasses.

In case of  $\text{Cr}_2\text{O}_3 + \text{Fe}_2\text{O}_3$  containing glasses, the molar volume for glass 8A is higher than glass 8 while excess volume follows the opposite trend due to increasing ionic nature of the glass structure. FTIR suggests decreasing connectivity in the glass network with addition of  $\text{Cr}_2\text{O}_3$  and  $\text{Fe}_2\text{O}_3$ ; the symmetric and the anti-symmetric stretching modes of the Si-O-Si bonds of the  $Q^n$  units in the glass silicate network are distributed around  $Q^2$ . The crystallization kinetic studies on both the glasses indicate the presence of diffusion controlled three dimensional bulk crystallization mechanisms in glass 8 while two different types of bulk crystallization mechanisms have been found to exist in glass 8A.

.....

## **Future directions**

During past 4 years, an attempt has been made to prove the potential of clinopyroxene based GCs for functional applications. Though, we have succeeded in shedding some light on the fascinating characteristics of Di and En based glasses and GCs which render them suitable for further experimentation as potential candidates in various functional applications; a lot of job still needs to be accomplished before making them geared up for final application. Therefore, in our opinion, the future work in this area may be addressed to the following issues:

a) Enstatite based glasses and GCs

Influence of various additives other than  $\text{Al}_2\text{O}_3$  should be investigated on the sintering and crystallization behaviour of  $\text{MgSiO}_3$  based GCs. Further, electrical properties of these GCs will be of great interest as these GCs may find application in electronics industry

b) Development of a compliant sealant for SOFC

- It is necessary to tailor the properties (specially, CTE and flow properties) of Di based GCs by various additions/substitutions in the glass compositions.
- The chemical interaction between GC sealants and SOFC components should be studied after prolonged heat treatments (~ 3000 h) in SOFC operating conditions. The interfacial strength between sealant and SOFC components can be studied by nano-indentation technique while development of micro-cracks and flaws along the sealant-SOFC component join can be studied through acoustic emission.
- Temperature dependence of viscosity is another concern which should be addressed while improving the properties of sealant.
- Also, it will be necessary to study the influence of seal design on the thermal stresses in SOFC stack using finite elemental analysis technique which will include the development of three-dimensional model of SOFC stack.
- Before the final application of Di based GC sealant in SOFC stack, its performance should be evaluated in model cells. After successful experimentation in model cells, this sealant should be applied to SOFC stacks.

## References

- [1] N. Morimoto, Nomenclature of pyroxenes, *Am. Miner.* 73 (1988) 1123-1133.
- [2] D.U. Tulyaganov, R.Ya. Khodakovskaya, Glass-ceramic biomaterials based on the fluorapatite-anorthite and fluorapatite-diopside systems, *Glass Ceram.* 48 (1991) 221-222.
- [3] T. Nonami, S. Tsutsumi, Study of diopside ceramics for biomaterials, *J. Mater. Sci.: Mater. Med.* 10 (1999) 475-479.
- [4] P.N. De Aza , Z.B. Luklinska, M. Anseau, Bioactivity of diopside ceramic in human parotid saliva, *J. Biomed. Mater. Res. B* 73B (2005) 54 – 60.
- [5] W. Xue, C. Ding, C. Cao, Y. Dong, Bioactivity of Plasma-sprayed Diopside Coating In Vitro, *Key Eng. Mater.* 288-289 (2005) 319-322.
- [6] A. Goel, D.U. Tulyaganov, V.V. Kharton, A.A. Yaremchenko, S. Agathopoulos, J.M.F. Ferreira, The influence of BaO on the phase formation and properties of aluminous clinopyroxenes in the Diopside-Ca-Tschermak system, *J. Am. Ceram. Soc.* 90 (2007) 2236-2244.
- [7] A. Goel, D.U. Tulyaganov, V.V. Kharton, A.A. Yaremchenko, S. Eriksson, J.M.F. Ferreira, Optimization of La<sub>2</sub>O<sub>3</sub>-containing diopside based glass-ceramic sealants for fuel cell applications, *J. Power Sources* 189 (2009) 1032-1043.
- [8] A. Goel, D.U. Tulyaganov, M.J. Pascual, F. Munoz, E.R. Shaaban, J.M.F. Ferreira, Development and performance of La<sub>2</sub>O<sub>3</sub>-containing diopside based glass-ceramics for sealing applications in solid oxide fuel cells, *J. Non-Cryst. Solids* (2009) *Submitted*.
- [9] A. Goel, D.U. Tulyaganov, V.V. Kharton, A.A. Yaremchenko, J.M.F. Ferreira, Electrical behaviour of aluminosilicate glass-ceramic sealants and their interaction with SOFC metallic interconnects *J. Power Sources* 195 (2010) 522-526.
- [10] I.W. Donald, B. L Metcalfe and R. N. J Taylor, The immobilization of high level radioactive wastes using ceramics and glasses, *J. Mater. Sci.* 32 (1997) 5851-5887.
- [11] I.W. Donald, Immobilisation of radioactive and non-radioactive wastes in glass-based systems: an overview, *Eur. J. Glass Sci. Technol. A* 48 (2007) 155–163.
- [12] W. Lutze, J. Borchardt, A.K. Dé, in “Scientific basis for nuclear waste management”, Vol. 1, edited by G.J. McCarthy (Plenum Press, New York, 1979) pp. 69-81.

- [13] W. Höland, G.N. Beall, *Glass-Ceramic Technology*, Am. Ceram. Soc., Westerville, Ohio, 2002.
- [14] W.E. Lee, A.H. Heuer, On the polymorphism of enstatite, *J. Am. Ceram. Soc.* 70 (1987) 349-60.
- [15] C.M. Huang, D.H. Kuo, Y.J. Kim, W. Kriven, Phase stability of chemically derived enstatite ( $\text{MgSiO}_3$ ) powders. *J. Am. Ceram. Soc.* 77 (1994) 2625-31.
- [16] G.H. Beall, *Glass-ceramics: Recent developments and applications*, *Ceram. Trans.* 30 (1993) 241-266.
- [17] F. Nestola, G.D. Gatta, T.B. Ballaran, The effect of Ca substitution on the elastic and structural behaviour of orthoenstatite, *Am. Miner.* 91 (2006) 809-815.
- [18] J.V. Smith, Crystal structure and stability of the  $\text{MgSiO}_3$  polymorphs: Physical properties and phase relations of Mg, Fe pyroxens, *Miner. Soc. Am. Spec. Pap.* 2 (1969) 3-29.
- [19] W. Mielcarek, D. Nowak-Wozny, K. Prociow, Correlation between  $\text{MgSiO}_3$  phases and mechanical durability of steatite ceramics, *J. Eur. Ceram. Soc.* 24 (2004) 3817-3821.
- [20] V.L. Balkevich, *Technical Ceramics*. Moscow: Stroiizdat, 1984 (in Russian).
- [21] R.F. Cooper, W.Y. Yoon, J.H. Perepezko, Internal nucleation of high undercooled magnesium metasilicate melts, *J. Am. Ceram. Soc.* 74 (1991) 1312-1319.
- [22] D.U. Tulyaganov, S. Agathopoulos, V.V. Kharton, F.M.B. Marques, *Glass-ceramics in the former Soviet Union: A review on industry-oriented developments*, *Ind. Ceram.*, 23 (2003) 101-115.
- [23] E.A. Takher, T.I. Fedoseeva, V.Yu Kellerman, R.Ya Popilsky, High-strength steatite ceramics with broad range of the sintering stage, *Glass Ceram.* 2 (1974) 19-21.
- [24] E.A. Takher, R.Ya Popilsky, V.Yu Kellerman, A.G. Sokolnikova, Dielectric steatite ceramics, *Glass Ceram.* 10 (1975) 19-21.
- [25] G.N. Beall, Refractory glass-ceramic containing enstatite. US patent 4 687 749, 18<sup>th</sup> August 1987.
- [26] L.M. Echeverria, G.N Beall, Enstatite Ceramics; Glass and Gel routes, in: K.M. Nair (Ed.), *Glasses for Electronic applications*, *Ceram. Trans.* Vol. 20, American Ceramic Society, Westerville, OH, 1991, pp. 235-244.

- [27] G. Partridge, M.I. Budd, Toughened glass-ceramics. U.K. patent GB 2172282, 17 September 1986.
- [28] G. Partridge, Elyard, M.I. Budd, Glass-ceramics in substrate applications, in: M.H. Levis (Ed.), *Glasses and Glass-Ceramics*, Chapman and Hall, London, U.K., 1989, pp. 226-271.
- [29] M.I. Budd, Sintering and crystallization of a glass powder in the MgO- Al<sub>2</sub>O<sub>3</sub>-SiO<sub>2</sub>-ZrO<sub>2</sub> system, *J. Mater. Sci.* 28 (1993) 1007-1014.
- [30] M. Tribaudino, A transmission electron microscope investigation of the C2/c→P2<sub>1</sub>/c phase transition in clinopyroxenes along the diopside-enstatite (CaMgSi<sub>2</sub>O<sub>6</sub>-Mg<sub>2</sub>Si<sub>2</sub>O<sub>6</sub>) join, *Am. Miner.* 85 (2000) 707-715.
- [31] T. Gasparik, A thermodynamic model for the enstatite-diopside join, *Am. Miner.* 75 (1990) 1080-1091.
- [32] Y. Ohashi, C.W. Burnham, L.W. Finger, The effect of Ca-Fe substitution on the clinopyroxene crystal structure, *Am. Miner.* 60 (1975) 423-434.
- [33] V.I. Vereshchagin, E.P. Tzymbalyuk, B.P. Romanov, Correlation between crystalline structure and physico-technical properties of solid solutions in the system clinoenstatite-diopside, in: *Nucleated Crystallization of Glasses*, State Institute of Glass, Moscow, 1982, pp. 95-100 (in Russian).
- [34] M. Tribaudino, F. Nestola, C. Meneghini, Rietveld refinement of clinopyroxenes with intermediate Ca-content along the join diopside-enstatite, *Can. Mineral.* 43 (2005) 1411-1421.
- [35] R. L. Flemming, R. W. Luth, <sup>29</sup>Si MAS NMR study of diopside–Ca-Tschermak clinopyroxenes: detecting both tetrahedral and octahedral Al substitution, *Am. Miner.* 87 (2002) 25–36.
- [36] D. Goeriot, J.C. Dubois, D. Merle, F. Thevenot, P. Exbrayat, Enstatite based ceramics for machinable prosthesis applications, *J. Eur. Ceram. Soc.* 18 (1998) 2045-2056.
- [37] M.L.F. Nascimento, E.B. Ferreira, E.D. Zanotto, Kinetics and mechanisms of crystal growth and diffusion in a glass-forming liquid, *J. Chem. Phys.* 121 (2004) 8924-8928.

- [38] S. Reinsch, M.L.F. Nascimento, R. Müller, E.D. Zanotto, Crystal growth kinetics in cordierite and diopside glasses in wide temperature ranges, *J. Non-Cryst. Solids* 354 (2008) 5386-5394.
- [39] R. Conradt, On the entropy difference between the vitreous and the crystalline state, *J. Non-Cryst. Solids* 355 (2009) 636-641.
- [40] F. Branda, A. Costantini, A. Buri, Non-isothermal devitrification behaviour of diopside glass, *Thermochim. Acta* 217 (1993) 207-212.
- [41] M.L. Öveçoglu, B. Kuban, H. Özer, Characterization and crystallization kinetics of a diopside-based glass-ceramic developed from glass industry raw materials, *J. Eur. Ceram. Society* 17 (1997) 957-962.
- [42] L. Barbieri, C. Leonelli, T. Manfredini, M. Paganelli, G.C. Pellacani, Kinetic study of surface nucleated MgO–CaO–Al<sub>2</sub>O<sub>3</sub>–SiO<sub>2</sub> Glasses, *J. Therm. Anal.* 38 (1992) 2639–2647.
- [43] L. Barbieri, C. Leonelli, T. Manfredini, M. Romagnoli, G.C. Pellacani, C. Siligardi, Non-isothermal kinetic equations applied to crystallization of glasses, *Thermochim. Acta* 227 (1993) 125–133.
- [44] L. Barbieri, A. Corradi, I. Lancellotti, A.P.N. De Oliveira, O.E. Alarcon, Nucleation and crystal growth of a MgO–CaO–Al<sub>2</sub>O<sub>3</sub>–SiO<sub>2</sub> glass with added steel fly ash, *J. Am. Ceram. Soc.* 85 (2002) 670–674.
- [45] G. Baldi, E. Generali, C. Leonelli, T. Manfredini, G.C. Pellacani, C. Siligardi, Effects of nucleating agents on diopside crystallization in new glass-ceramics for tile-glaze application, *J. Mater. Sci.* 30 (1995) 3251-3255.
- [46] L. Barbieri, A. B. Corradi, I. Lancellotti, C. Leonelli, M. Montorsi, Experimental and computer simulation study of glasses belonging to diopside – anorthite system, *J. Non-Cryst. Solids* 345-346 (2004) 724–729.
- [47] A.B. Corradi, F. Bondioli, V. Cannillo, A.M. Ferrari, I. Lancellotti, M. Montorsi, The anorthite – diopside system: structural and devitrification study. Part I: structural characterization by molecular dynamic simulations, *J. Am. Ceram. Soc.*, 88 (2005) 714–718.
- [48] L. Barbieri, F. Bondioli, I. Lancellotti, C. Leonelli, M. Montorsi, A.M. Ferrari, The anorthite–diopside system: structural and devitrification study. Part II: crystallinity analysis by the Rietveld–RIR Method, *J. Am. Ceram. Soc.* 88 (2005) 3131–3136.

- [49] V.M.F. Marques, D.U. Tulyaganov, S. Agathopoulos, V.Kh. Gataullin, G.P. Kothiyal and J.M.F. Ferreira, Low temperature synthesis of anorthite based glass-ceramics via sintering and crystallization of glass-powder compacts, *J. Eur. Ceram. Society* 26 (2006) 2503-2510.
- [50] V.M.F. Marques, D.U. Tulyaganov, S. Agathopoulos, J.M.F. Ferreira, Low temperature production of glass-ceramics in the anorthite-diopside system via sintering and crystallization of glass-powder compacts, *Ceram. Int.* 34 (2008) 1145-1152.
- [51] C. Leonelli, T. Manfredini, M. Paganelli, P. Pozzi, G.C. Pellacani, Crystallization of some anorthite-diopside glass precursors, *J. Mater. Sci.* 26 (1991) 5041–5046.
- [52] R.D. Rawlings, in “Glass-Ceramic Materials. Fundamentals and Applications”, edited by T. Manfredini, G.C. Pellacani and J. M. Rincon. (Mucchi Editore, Modena, Italy 1997) p. 115.
- [53] P.S. Rogers, J. Williamson, J.F. Bell, M. Cambell, Final Report, Contract No. EUR 10389 EN, Commission of the European Communities (1986).
- [54] P.S. Rogers, J. Williamson, J. F. Bell, M. Cambell, in Proc. Int. Seminar “Energy Conservation Industry” Vol.3, Applications and Technologies, edited by A. Strub and H. Ehringer (Commission of the European Communities/VDI, 1984) p. 280.
- [55] S. Carter, R.D. Rawlings, P.S. Rogers, *Brit. Ceram. Proc.* 43, “Advanced ceramics in chemical process engineering,” edited by B.C.H. Steele and D. P. Thompson (Inst. Ceram. London, 1989) 13.
- [56] S. Carter, C.B. Ponton, R.D. Rawlings, P.S. Rogers, Microstructure, chemistry, elastic properties and internal-friction of silceram glass-ceramics, *J. Mater. Sci.* 23 (1988) 2622-2630.
- [57] P.S. Rogers, J. Williamson, J. F. Bell, M. Cambell, Commission of the European Communities Contractors Meeting “Energy Conservation Industry - Applications and Technologies” (D. Rendel Publ. Co., 1983) 156.
- [58] S. Carter, R.D. Rawlings, P.S. Rogers, Abrasion testing of glass-ceramics, *Brit. Ceram. Trans.* 92 (1993) 31-34.
- [59] R.D. Rawlings, J.P. Wu, A.R. Boccaccini, Glass-ceramics: Their production from wastes - A Review, *J. Mater. Sci.* 41 (2006) 733–761.

- [60] W. Lutze, J. Borchardt, A.K. De, in “Scientific basis for nuclear waste management”, Vol. 1, edited by G. J. McCarthy (Plenum Press, New York, 1979) pp. 69-81.
- [61] M. Ninomiya, T. Yamanaka, T. Sakane, M. Hora, S. Nakamura, S. Kawamura, in Proceedings of the international seminar on chemistry and process engineering for high level liquid waste solidification, edited by R. Odoj and E. Mertz, Julich, Germany, 1981, pp. 675.
- [62] A. Karnis, L. Gautron, Promising Immobilization of cadmium and Lead inside Ca-rich Glass-Ceramics, Proceedings of World Academy of Science, Engineering and Technology, vol. 40 (2009) ISSN: 2070-3740.
- [63] B.J. Wood, J.D. Blundy, A.C. Robinson, The role of clinopyroxene in generating U-series disequilibrium during mantle melting, *Geochim. Cosmochim. Acta* 63 (1999) 1613-1620.
- [64] C.P. Yoganand, V. Selvarajan, L. Lusvarghi, O.M. Goudouri, K.M. Paraskevopoulos, M. Rouabhia, Bioactivity of CaO–MgO–SiO<sub>2</sub> glass ceramics synthesized using transferred arc plasma (TAP) process, *Mater. Sci. Eng. C* 29 (2009) 1759-1764.
- [65] M. Ashizuka, E. Ishida, Mechanical properties of silicate glass-ceramics containing tricalcium phosphate, *J. Mater. Sci.* 32 (1997) 185-188.
- [66] M. Kamitakahara, C. Ohtsuki, K. Yuko, S.-I. Ogata, M. Tanihara, T. Miyazaki, Preparation of porous glass-ceramics containing whitlockite and diopside for bone repair, *J. Ceram. Soc. Japan* 114 (2006) 82-86.
- [67] A. Goel, A.M. Ferrari, I. Kansal, M.J. Pascual, L. Barbieri, F. Bondioli, I. Lancellotti, M.J. Ribeiro, J.M.F. Ferreira, Sintering and crystallization behavior of CaMgSi<sub>2</sub>O<sub>6</sub>-NaFeSi<sub>2</sub>O<sub>6</sub> based glass-ceramics, *J. Appl. Phys.* (2009) Accepted.
- [68] K. Putirka, M. Johnson, R. Kinzler, J. Longhi, D. Walker, Thermobarometry of mafic igneous rocks based on clinopyroxene-liquid equilibria, 0–30 kbar, *Contrib. Miner. Petro.* 123 (1996) 92–108.
- [69] P. Nimis, A clinopyroxene geobarometer for basaltic systems based on crystal-structure modeling, *Contrib. Miner. Petro.* 121 (1995) 115– 125.

- [70] P. Nimis, Clinopyroxene geobarometry of magmatic rocks. Part 2. Structural geobarometers for basic to acid, tholeiitic and mildly alkaline magmatic systems, *Contrib. Miner. Petrol.* 135 (1999) 62–74.
- [71] P. Nimis, P. Ulmer, Clinopyroxene geobarometry of magmatic rocks. Part 1. An expanded structural geobarometer for anhydrous and hydrous, basic and ultrabasic systems, *Contrib. Miner. Petrol.* 133 (1998) 122–135.
- [72] K. Etzel, A. Benisek, E. Dachs, L. Cemic, Thermodynamic mixing behaviour of synthetic Ca-Tschermak–diopside pyroxene solid solutions: I. Volume and heat capacity of mixing, *Phys. Chem. Miner.* 34 (2007) 733–746.
- [73] A. Benisek, K. Etzel, L. Cemic, Thermodynamic mixing behaviour of synthetic Ca-Tschermak–diopside pyroxene solid solutions: II. Heat of mixing and activity-composition relationships, *Phys. Chem. Miner.* 34 (2007) 747–755.
- [74] K. Etzel, A. Benisek, Thermodynamic mixing behaviour of synthetic Ca-Tschermak–diopside pyroxene solid solutions: III. An analysis of IR line broadening and heat of mixing behaviour, *Phys. Chem. Miner.* 35 (2008) 399–407.
- [75] Y. Kushiro, Clinopyroxenes solid solutions. Part 1. The  $\text{CaAl}_2\text{SiO}_6$  component, *Jpn. J. Geol. Geography* 33 (1962) 2–4.
- [76] J.F. Schairer, H.S. Jr. Yoder, Crystal and liquid trends in simplified alkali basalts, *Year Book* 63 (1964) 64–74.
- [77] S.N. Salama, H. Darwish, H.A. Abo-Mosallam, Crystallization and properties of glasses based on diopside-Ca-Tschermak’s-fluorapatite system, *J. Eur. Ceram. Soc.* 25 (2005) 1133–1142.
- [78] S.N. Salama, H. Darwish, H.A. Abo-Mosallam, HA forming ability of some glass-ceramics of the  $\text{CaMgSi}_2\text{O}_6$ - $\text{Ca}_5(\text{PO}_4)_3\text{F}$ - $\text{CaAl}_2\text{SiO}_6$  system, *Ceram. Int.* 32 (2006) 357–264.
- [79] L.L. Hench, Ö. Andersson, “Bioactive Glass Coatings”; pp. 239–59 in *An Introduction to Bioceramics*. Edited by L.L. Hench and J. Wilson. World Scientific, Singapore, 1993.
- [80] K.C. Vasilopoulos, D.U. Tulyaganov, S. Agathopoulos, M.A. Karakassides, J.M.F. Ferreira, D. Tsipas, Bulk nucleated fine grained mono-mineral glass-ceramics from low-silica fly ash, *Ceram. Int.* 35 (2009) 555–558.

- [81] A. Alvarez-Méndez, L.C. Torres-González, N. Alvarez, L.M. Torres-Martínez, Kinetic thermal analysis of glass ceramics from industrial wastes, *J. Non-Cryst. Solids* 329 (2003) 73-76.
- [82] F.J. Torres, J. Alarcón, Mechanism of crystallization of pyroxene-based glass-ceramic glazes, *J. Non-Crystalline Solids* 347 (2004) 45-51.
- [83] V. Gomes, C.D.G. De Borba, H.G. Riella, Production and characterization of glass ceramics from steelwork slag, *J. Mater. Sci.* 37 (2002) 2581-2585.
- [84] A. Goel, D.U. Tulyaganov, S. Agathopoulos, M.J. Ribeiro, J.M.F. Ferreira, Crystallization behaviour of the glasses, structure and properties of sintered glass-ceramics in the Diopside-Ca-Tschermak system, *J. Eur. Ceram. Soc.* 27 (2007) 3231-3238.
- [85] M. Erol, U. Demirler, S. Kucukbayrak, A. Ersoy-Mericboyu, M.L. Ovecoglu, Characterization investigations of glass-ceramics developed from Seyitömer thermal power plant fly ash, *J. Eur. Ceram.Soc.* 23 (2003) 757-763.
- [86] M. Erol, A. Genc, M.L. Ovecoglu, E. Yucelen, S. Kucukbayrak, Y. Taptik, Characterization of a glass-ceramic produced from thermal power plant fly ashes, *J. Eur. Ceram. Soc.* 20 (2000) 2209-2214.
- [87] S.P.S. Badwal, K. Foger, Solid oxide electrolyte fuel cell review, *Ceram. Int.* 22 (1996) 257-265.
- [88] A. Lashtabeg, S.J. Skinner, Solid oxide fuel cells - a challenge for materials chemists?, *J. Mater. Chem.* 16 (2006) 3161-3170.
- [89] J. Hartvigsen, J. Milliken, S. Elangovan, A. Khandkar, *Ceram. Trans.* 65 (1996) 279.
- [90] T.-L. Wen, D. Wang, M. Chen, H. Tu, Z. Lu, Z. Zhang, H. Nie, W. Huang, Material research for planar SOFC stack, *Solid State Ionics* 148 (2002) 513-519.
- [91] M. Singh, T.P. Shpargel, R. Asthana, Brazing of stainless steel to yttria-stabilized zirconia using gold-based brazes for solid oxide fuel cell applications, *Int. J. Appl. Ceram. Technol.* 4 (2007) 119-133.
- [92] Y-S. Chou, J.W. Stevenson, Thermal cycling and degradation mechanisms of compressive mica-based seals for solid oxide fuel cells, *J. Power Sources* 112 (2002) 376-383.

- [93] N.P. Bansal, E.A. Gamble, Crystallization kinetics of a solid oxide fuel cell seal glass by differential thermal analysis, *J. Power Sources* 147 (2005) 107-115.
- [94] K. Ley, M. Krumplet, R. Kumar, J. Meiser, I. Bloom, Glass-ceramic sealants for solid oxide fuel cells: Part I. Physical properties, *J. Mater. Res.* 11 (1996) 1489-1493.
- [95] F. Smeacetto, M. Salvo, M. Ferraris, V. Casalegno, P. Asinari, A. Chrysanthou, Characterization and performance of glass-ceramic sealant to join metallic interconnects to YSZ and anode-supported-electrolyte in planar SOFCs, *J. Eur. Ceram. Soc.* 28 (2008) 2521-2527.
- [96] A. Goel, D.U. Tulyaganov, V.V. Kharton, A.A. Yaremmchenko, S. Eriksson, J.M.F. Ferreira, Optimization of  $\text{La}_2\text{O}_3$ -containing diopside based glass-ceramic sealants for fuel cell applications, *J. Power Sources* 189 (2009) 1032-1043.
- [97] S.R. Choi, N.P. Bansal, A. Garg, Mechanical and microstructural characterization of boron nitride nanotubes-reinforced SOFC seal glass composite, *Mater. Sci. Eng. A* 460-461 (2007) 509-515.
- [98] J.W. Fergus, Sealants for solid oxide fuel cells, *J. Power Sources* 147 (2005) 46-57.
- [99] P.H. Larsen, F.W. Poulsen, R.W. Berg, The influence of  $\text{SiO}_2$  addition to  $2\text{MgO}-\text{Al}_2\text{O}_3-3.3\text{P}_2\text{O}_5$  glass, *J. Non-Cryst. Solids* 244 (1999) 16-24.
- [100] S. Ghosh, A. Das Sharma, P. Kundu, S. Mahanty, R.N. Basu, Development and characterizations of  $\text{BaO}-\text{CaO}-\text{Al}_2\text{O}_3-\text{SiO}_2$  glass-ceramic sealants for intermediate temperature solid oxide fuel cell application, *J. Non-Cryst. Solids* 354 (2008) 4081-4088.
- [101] K.D. Meinhardt, D.-S. Kim, Y.-S. Chou, K.S. Weil, Synthesis and properties of a barium aluminosilicate solid oxide fuel cell glass-ceramic sealant, *J. Power Sources* 182 (2008) 188-196.
- [102] S. Ghosh, P. Kundu, A. Das Sharma, R.N. Basu, H.S. Maiti, Microstructure and property evaluation of barium aluminosilicate glass-ceramic sealant for anode-supported solid oxide fuel cell, *J. Eur. Ceram. Soc.* 28 (2008) 69-76.
- [103] Z. Yang, J.W. Stevenson, K.D. Meinhardt, Chemical interactions of barium-calcium-aluminosilicate-based sealing glasses with oxidation resistant alloys, *Solid State Ionics* 160 (2003) 213-225.

- [104] K.D. Meinhardt, J.D. Vienna, T.R. Armstrong, L.R. Pederson, Glass-ceramic material and method of making, U.S. Pat. 6430966 (Aug. 13, 2002).
- [105] P.H. Larsen, P.F. James, Chemical stability of MgO/CaO/Cr<sub>2</sub>O<sub>3</sub>-Al<sub>2</sub>O<sub>3</sub>-B<sub>2</sub>O<sub>3</sub>-phosphate glasses in solid oxide fuel cell environment, *J. Mater. Sci.* 33 (1998) 2499-2507.
- [106] W.A. Johnson, K.F. Mehl, Reaction kinetics in processes of nucleation and growth, *Trans. Am. Inst. Mining Eng.*, 135 (1939) 416-442.
- [107] M. Avrami, Kinetics of phase change. I General theory, *J. Chem. Phys.* 7 (1939) 1103-1112; Kinetics of phase change. II Transformation-Time relations for random distribution of nuclei, *J. Chem. Phys.* 8 (1940) 212; Granulation, phase change, and microstructure kinetics of phase change. III, *J. Chem. Phys.* 9 (1941) 177-184.
- [108] A. Goel, E.R. Shabaan, F.C.L. Melo, M.J. Ribeiro, J.M.F. Ferreira, Non-isothermal crystallization kinetic studies on MgO-Al<sub>2</sub>O<sub>3</sub>-SiO<sub>2</sub>-TiO<sub>2</sub> glass, *J. Non-Cryst. Solids* 353 (2007) 2383-2391.
- [109] A. Goel, E.R. Shabaan, F.C.L. Melo, M.J. Ribeiro, J.M.F. Ferreira, Influence of NiO on the crystallization kinetics of near stoichiometric cordierite glasses nucleated with TiO<sub>2</sub>, *J. Phys.: Cond. Matter.* 19 (2007) 386231.
- [110] H. Scholze, *Ver. Dtsch., Keram. Ges.* 391 (1962) 63.
- [111] M.J. Pascual, L. Pascual, A. Durán, Determination of the viscosity-temperature curve for glasses on the basis of fixed viscosity points determined by hot stage microscopy *Phys. Chem. Glasses* 42 (2001) 61-66.
- [112] M.J. Pascual, A. Durán, M.O. Prado, A new method for determining fixed viscosity points of glasses, *Phys. Chem. Glasses* 46 (2005) 512-520.
- [113] A.C. Larson, R.B. von Dreele, GSAS: General Structure Analysis System LANSCE, MS-H805; Los Alamos National Laboratory, Los Alamos, NM, 1998.
- [114] B.H. Toby, EXPGUI, a graphical user interface for GSAS, *J. Appl. Cryst.* 34 (2001) 210-213.
- [115] V.V. Kharton, F.M.B. Marques, Interfacial effects in electrochemical cells for oxygen ionic conduction measurements. I. The e.m.f. method, *Solid State Ionics* 140 (2001) 381-394.
- [116] M.J. Pascual, V.V. Kharton, E.V. Tsipis, A.A. Yaremchenko, C. Lara, A. Durán, J.R. Frade, Transport properties of sealants for high-temperature electrochemical

applications: RO-BaO-SiO<sub>2</sub> (R= Mg, Zn) glass-ceramics, J. Eur. Ceram. Soc. 26 (2006) 3315-3324.

- [117] M.W. Chase, “NIST-JANAF Thermochemical Tables, Fourth Edition,” J. Phys. Chem. Ref. Data, Monograph, **9**, 1-1951 (1998).
- [118] Crofer 22 APU, Material data sheet no. 4046, December 2006, Thyssen Krupp VDM, Germany.
- [119] Sanergy HT, Material data sheet, Sandvik Materials Technology, Sandvik, Sweden.
- [120] W.A. Weyl, Coloured Glasses, Soc. Glass Technol., (1951) 558 (fifth reprint 1999) ISBN 0-900683-06-X
- [121] G. Calas, L. Cormier, L. Galois, P. Jollivet, [Structure–property relationships in multicomponent oxide glasses](#), C. R. Chim. 5 (2002) 831-843.
- [122] S-L. Lin, C-S. Hwang, Structures of CeO<sub>2</sub>-Al<sub>2</sub>O<sub>3</sub>-SiO<sub>2</sub> glasses, J. Non-Cryst. Solids 202 (1996) 61-67.
- [123] J.T. Kohli, J.E. Shelby, J.S. Frye, A structural investigation of yttrium aluminosilicate glasses using Si-29 and Al-27 magic angle spinning nuclear-magnetic-resonance, Phys. Chem. Glasses 33 (1992) 73-78.

[124] M.I. Ojovan, W.E. Lee, **An Introduction to Nuclear Waste Immobilisation**

(ISBN: 978-0-08-044462-8), Elsevier Science Ltd., UK, (2005) Chap. 17.

- [125] L. Stoch, M. Sroda, Infrared spectroscopy in the investigation of oxide glasses structure, J. Mol. Struct. 511-512 (1999) 77-84.
- [126] A. Goel, D.U. Tulyaganov, V.V. Kharton, A.A. Yaremchenko, S. Agathopoulos, J.M.F. Ferreira, The influence of BaO on the phase formation and properties of aluminous clinopyroxenes in the Diopside-Ca-Tschermak system, J. Am. Ceram. Soc. 90 (2007) 2236-2244.
- [127] S. Mahadevan, A. Giridhar, A.K. Singh, Calorimetric measurements on As-Sb-Se glasses, J. Non-Cryst. Solids 88 (1986) 11-34.

- [128] O.A. Lafi, M.M.A. Imran, M.K. Abdullah, Glass transition activation energy, glass-forming ability and thermal stability of  $\text{Se}_{90}\text{In}_{10-x}\text{Sn}_x$  ( $x=2, 4, 6$  and  $8$ ) chalcogenide glasses, *Physica B* 395(2007) 69-75.
- [129] A. Goel, E.R. Shabaan, D.U. Tulyaganov, J.M.F. Ferreira, Study of crystallization kinetics in glasses along the diopside-Ca-Tschermak join, *J. Am. Ceram. Soc.* 91 (2008) 2690-2697.
- [130] K. Chebli, J.M. Saiter, J. Grenet, A. Hamou, G. Saffarini, [Strong-fragile glass forming liquid concept applied to GeTe chalcogenide glasses](#), *Physica B* 304 (2001) 228-236.
- [131] M.M. Wakkad, E Kh. Shokr, S.H. Mohamed, Optical and calorimetric studies of Ge–Sb–Se glasses, *J. Non-Cryst. Solids* 265 (2005) 157-166.
- [132] T.A. Vilgis, Strong and fragile glasses: A powerful classification and its consequences, *Phys. Rev. B* 47 (1993) 2882-2885.
- [133] R. Böhmer, C.A. Angell, Global and local relaxations in glass-forming materials, in: *Disorder effects on relaxational processes*, edited by R. Richert and A. Blumen (Springer, Berlin Heidelberg, 1994), p. 11-54
- [134] R. C. De. Vekey and A.J. Majumdar, “The effect of fabrication variables on the properties of cordierite based glass-ceramics,” *Glass. Tech.*, **15**, 71 (1974).
- [135] J.A. Macmillan, Kinetics of glass transformation by thermal analysis.I. Glycerol, *J. Chem. Phys.* 42 (1965) 3497-501.
- [136] N.S. Saxena, Phase transformation kinetics and related thermodynamic and optical properties in chalcogenide glasses, *J. Non-Cryst. Solids* 345-346 (2004) 161-68.
- [137] N. Mehta, R. S. Tiwari, A. Kumar, Glass forming ability and thermal stability of some Se–Sb glassy alloys, *Mater. Res. Bull.* 41 (2006) 1664-1672.
- [138] A.A. Francis, Non-isothermal crystallization kinetics of a blast furnace slag glass, *J. Am. Ceram. Soc.* 88 (2005) 1859-63.
- [139] C. Lara, M.J. Pascual, A. Durán, Glass-forming ability, sinterability and thermal properties in the systems  $\text{RO–BaO–SiO}_2$  ( $\text{R} = \text{Mg, Zn}$ ), *J. Non-Cryst. Solids* 348 (2004) 149-155.
- [140] G. Tünker and H. Scholze, *Glastech. Ber.* 55 (1982) 61.
- [141] Y. Hasegawa, *Glastech. Ber.* 59 (1986) 189.

- [142] Gmelin's Handbook of Inorganic Chemistry, Verlag Chemie, Leipzig 1992.
- [143] S. Sen and A. Ghosh, Structure and other physical properties of magnesium vanadate glasses, *J. Non-Cryst. Solids* 258 (1999) 29-33.
- [144] S. Sen, A. Ghosh, Structural properties of strontium vanadate glasses, *J. Mater. Res.* 15 (2000) 995-999.
- [145] J.W. Martin, Concise Encyclopedia of the Structure of Materials (ISBN: 978-0-08-045127-5), Elsevier Science Ltd., **UK, 2006.**
- [146] L.A. Zhunina, M.I. Kuzmenkov, V.N. Yaglov, *Pyroxene Glass-Ceramics* (Minsk, 1974).
- [147] L. Barbieri, C. Leonelli, T. Manfredini, G.C. Pellacani, C. Siligardi, Solubility, reactivity and nucleation effect of Cr<sub>2</sub>O<sub>3</sub> in the CaO-MgO-Al<sub>2</sub>O<sub>3</sub>-SiO<sub>2</sub> glassy system, *J. Mater. Sci.* 29 (1994) 6273-6280.
- [148] Y.M. Sung, S. Kim, Mechanical properties of off-stoichiometric BaO. Al<sub>2</sub>O<sub>3</sub>. 2SiO<sub>2</sub> glass-ceramic, *J. Mater. Sci. Lett.* 18 (1999) 1657-1660.
- [149] G.H. Beal, H.J. Holland, J.T. Kohli, Glass-ceramic containing a stabilized hexacelsian crystal structure, US patent 5910459, June 8, 1999.
- [150] W.G. Coors, Protonic ceramic fuel cells for high-efficiency operation with methane, *J. Power Sources* 118 (2003) 150-156.
- [151] S.-B. Sohn, S.-Y. Choi, G.-H. Kim, H.-S. Song, G.-D. Kim, Stable sealing glass for planar solid oxide fuel cell, *J. Non-Cryst. Solids* 297 (2002) 103-112.
- [152] T. Schwickert, R. Sievering, P. Geasee, R. Conradt, Glass-ceramic materials as sealants for SOFC applications, *Mat-Wiss U Werkstofftech* 33 (2002) 363-366.
- [153] S.-B. Sohn, S.-Y. Choi, Suitable glass-ceramic sealant for planar solid-oxide fuel cells, *J. Am. Ceram. Soc.* 87 (2004) 254-260.
- [154] M. Brochu, B.D. Gauntt, R. Shah, G. Miyake, R.E. Loehman, Comparison between barium and strontium-glass composites for sealing SOFCs, *J. Eur. Ceram.Soc.* 26 (2006) 3307-3313.
- [155] V. Kumar, A. Arora, O.P. Pandey, K. Singh, Studies on thermal and structural properties of glasses as sealants for solid oxide fuel cells, *Int. J. Hydrog. Energy* 33 (2008) 434-438.

- [156] M.K. Mahapatra, K. Lu, W.T. Reynolds Jr., Thermophysical properties and devitrification of SrO-La<sub>2</sub>O<sub>3</sub>-Al<sub>2</sub>O<sub>3</sub>-B<sub>2</sub>O<sub>3</sub>-SiO<sub>2</sub>-based glass sealant for solid oxide fuel/electrolyzer cells, *J. Power Sources* 179 (2008) 106-112.
- [157] R.H. Doremus, *Glass Science* 2<sup>nd</sup> Ed. (ISBN: 0-471-89174-6), John Wiley & Sons, Inc., USA, 1994 Chap. 6, pp. 103.
- [158] D.R. Uhlmann, R.R. Shaw, The thermal expansion of alkali borate glasses and the boric oxide anomaly, *J. Non-Cryst. Solids* 1 (1969) 347-359.
- [159] F. Hamer, J. Hamer, *The Potter's Dictionary* (ISBN: 0812238109), University of Pennsylvania Press, USA, 2004.
- [160] A.K. Varshneya, *Fundamental of Inorganic Glasses* (ISBN: 0-12-714970-8), Academic Press Inc., USA, 1994 chap. 5.
- [161] M.O. Prado, E.D. Zanotto, R. Muller, Model for sintering polydispersed glass particles, *J. Non-Cryst. Solids* 279 (2001) 169-178.
- [162] J. Frenkel, Viscous flow of crystalline bodies under the action of surface tension, *J. Phys. (USSR)* 9 (1945) 385-391.
- [163] J.K. Mackenzie, R. Shuttleworth, A phenomenological theory of sintering, *Proc. Phy. Soc. (London)* 62 (1949) 833-852.
- [164] A. Goel, D.U. Tulyaganov, I.K. Goel, E.R. Shaaban, J.M.F. Ferreira, Effect of BaO on the crystallization kinetics of the Diopside-Ca-Tschermak based glasses and glass-ceramics, *J. Non-Cryst. Solids* 355 (2009) 193-202.
- [165] T. Zhang, R.K. Brow, S.T. Reis, C.S. Ray, Isothermal Crystallization of a Solid Oxide Fuel Cell Sealing Glass by Differential Thermal Analysis, *J. Am. Ceram. Soc.* 91 (2008) 3235-3239.
- [166] M.J. Pascual, C. Lara, and A. Durán, Non-isothermal crystallisation kinetics of devitrifying RO-BaO-SiO<sub>2</sub> (R=Mg, Zn) glasses, *Phys. Chem. Glasses* 47 (2006) 572-581.

- [167] K. Eichler, G. Solow, P. Otschik, W. Schaffrath, BAS (BaO-Al<sub>2</sub>O<sub>3</sub>-SiO<sub>2</sub>)-glasses for high temperature applications, *J. Eur. Ceram. Soc.* 19 (1999) 1101-1104.
- [168] Y. Sakaki, M. Hattori, Y. Esaki, S. Ohara, T. Fukui, K. Kodera, Y. Kubo, Glass-ceramics sealants in CaO-Al<sub>2</sub>O<sub>3</sub>-SiO<sub>2</sub> system, Proceedings of the 5<sup>th</sup> International symposium on solid oxide fuel cells (SOFC-V), June 02-05, 1997 Aachen, Germany, 97 [40] (1997) 652-660.
- [169] T. Schaller, J.F. Stebbins, M.C. Wilding, Cation clustering and formation of free oxide ions in sodium and potassium lanthanum silicate glasses: nuclear magnetic resonance and Raman spectroscopic findings, *J. Non-Cryst. Solids* 243 (1999) 146-157.
- [170] M.C. Wilding, A. Navrotsky, High temperature calorimetric studies of the heat of solution of La<sub>2</sub>O<sub>3</sub> in silicate liquids, *J. Non-Cryst. Solids* 265 (2000) 238-251.
- [171] E.M. Larson, A.J.G. Ellison, F.W. Lytle, A. Navrotsky, R.B. Gregor, XAS study of lanthanum coordination environments in glasses of the system K<sub>2</sub>O-SiO<sub>2</sub>-La<sub>2</sub>O<sub>3</sub>, *J. Non-Cryst. Solids* 130 (1991) 260-272.
- [172] N. Lahl, K. Singh, L. Singheiser, K. Hilpert, D. Bahadur, Crystallisation kinetics in AO-Al<sub>2</sub>O<sub>3</sub>-SiO<sub>2</sub>-B<sub>2</sub>O<sub>3</sub> glasses (A = Ba, Ca, Mg), *J. Mater. Sci.* 35 (2000) 3089-3096.
- [173] M. Hillers, G. Matzen, E. Véron, M. Dutreilh-Colas, A. Douy, Application of in situ high-temperature techniques to investigate the effect of B<sub>2</sub>O<sub>3</sub> on the crystallization behaviour of aluminosilicate E-glass, *J. Am. Ceram. Soc.* 90 (2007) 720-726.
- [174] P.A. Lessing, A review of sealing technologies applicable to solid oxide electrolysis cells, *J. Mater. Sci.* 42 (2007) 3465-3476.**
- [175] J.E. Shelby, Introduction to Glass Science and Technology (ISBN: 0-85404-533-3), The Royal Soc. Chem., Cambridge, UK, 1997, Chap. 7.
- [176] P. Batfalsky, V.A.C. Haanappel, J. Malzbender, N.H. Menzler, V. Shemet, I.C. Vinke, R.W. Steinbrech, Chemical interaction between glass-ceramic sealants and interconnect steels in SOFC stacks, *J. Power Sources* 155 (2006) 128-137.
- [177] E.T. Turkdogan, Physical chemistry of high temperature technology, Academic Press, New York (1980) pp. 5-24.

- [178] V.A.C. Hannappel, V. Shemet, S.M. Gross, Th. Koppitz, N. Menzler, M. Zahid, W.J. Quadackers, Behaviour of various glass–ceramic sealants with ferritic steels under simulated SOFC stack conditions, *J. Power Sources* 150 (2005) 86-100.
- [179] T. Zhang, W.G. Fahrenholtz, S.T. Reis, R.K. Brow, Borate volatility from SOFC sealing glasses, *J. Am. Ceram. Soc.* 91 (2008) 2564-2569.
- [180] A. Bartecki and J. Burgess, “The colour of metal compounds,” Gordon and Breach Science Publishers, ISBN: 90-5699-250-3 (2001) pp. 202-205.
- [181] R. K. Mishra, V. Sudarsan, C. P. Kaushik, K. Raj, S. K. Kulshreshtha and A. K. Tyagi, Effect of BaO addition on the structural aspects and thermophysical properties of sodium borosilicate glasses, *J. Non-Cryst. Solids* 353 (2007) 1612-1617.
- [182] K. S. Kim, P. J. Bray,  $B^{11}$  NMR-Studies of glasses in system MgO-Na<sub>2</sub>O-B<sub>2</sub>O<sub>3</sub> *Phys. Chem. Glasses* 15 (1974) 47-51.
- [183] L. Lefebvre, L. Gremillard, J. Chevalier, R. Zenati and D. Bernache-Assolant, Sintering behaviour of 45S5 bioactive glass, *Acta Biomater.* 4 (2008) 1894-1903.
- [184] K.-D. Kreuer, Proton conductivity: Materials and applications, *Chem. Mater.* 8 (1996) 610-641.
- [185] Z. Yang, G. Xia, P. Singh, J.W. Stevenson, Electrical contacts between cathodes and metallic interconnects in solid oxide fuel cells, *J. Power Sources* 155 (2006) 246-252.
- [186] X. Chen, P.Y. Hou, C.P. Jacobson, S.J. Visco, L.C. De Jonghe, Protective coating on stainless steel interconnect for SOFCs: oxidation kinetics and electrical properties, *Solid State Ionics* 176 (2005) 425-433.
- [187] P.D. Jablonski, D.E. Alman, Oxidation resistance of novel ferritic stainless steels alloyed with titanium for SOFC interconnect applications, *J. Power Sources* 180 (2008) 433-439.
- [188] J. Williamson, The kinetics of crystal growth in an aluminosilicate glass containing small amounts of transition-metal ions, *Min. Mag.* 37 (1970) 759-770.
- [189] L. J. Shelestak, R. A. Chavez, J. D. Mackenzie, Glasses and glass-ceramics from naturally occurring CaO-MgO-Al<sub>2</sub>O<sub>3</sub>-SiO<sub>2</sub> materials (I) glass formation and properties, *J. Non-Cryst. Solids* 27 (1978) 75-81.

- [190] L. J. Shelestak, R. A. Chavez, J. D. Mackenzie, Glasses and glass-ceramics from naturally occurring CaO-MgO-Al<sub>2</sub>O<sub>3</sub>-SiO<sub>2</sub> materials (II) crystallization behaviour, *J. Non-Cryst. Solids* 27 (1978) 83-97.
- [191] J. A. Duffy, M. D. Ingram, S. Fong, Effect of basicity on chemical bonding of metal ions in glass and its relevance to their stability, *Phys. Chem. Chem. Phys.* 2 (2000) 1829-1833.
- [192] V. Dimitrov, S. Sakka, Electronic oxide polarizability and optical basicity of simple oxides .1, *J. Appl. Phys.* 79 (1996) 1736-1740.
- [193] T. Honma, Y. Benino, T. Fujiwara, T. Komatsu, R. Sato, V. Dimitrov, Electronic polarizability, optical basicity, and interaction parameter of La<sub>2</sub>O<sub>3</sub> and related glasses, *J. Appl. Phys.* 91 (2002) 2942-2950.
- [194] S. Kannan, J.M. Ventura, J.M.F. Ferreira, In situ formation and characterization of flourine-substituted biphasic calcium phosphate ceramics of varied F-HAP/ $\beta$ -TCP ratios, *Chem. Mater.* 17 (2005) 3065-3068.
- [195] I.W. Donald, Crystallization kinetics of a lithium zinc silicate glass studied by DTA and DSC, *J. Non-Cryst. Solids* 345-346 (2004) 120-126.
- [196] M. Romero, M. Kovacova, J. Ma. Rincon, Effect of particle size on kinetics crystallization of an iron-rich glass, *J. Mater. Sci.* 43 (2008) 4135-4142.